EP/L014106/1

Supergen Wind Hub

Sustainable Power Generation and Supply
- Wind Energy Technologies

D4.1: **Report on new approaches to condition monitoring to reduce cost of energy from wind farms in far-offshore locations**

Delivered by:	Durham University (contributions from Loughborough and Manchester Universities)		
Author(s):	Donatella Zappalá, Christopher J Crabtree, Simon Hogg		
Delivery date:	August 2019		
Distribution list:	Management Committee		
Version No	Status	Date	Checked by
1	Draft	12 July 2019	DZ
2	Final	2 August 2019	DZ

Durham University
Department of Engineering

Summary

As offshore wind turbines increase in physical size and capacity and operate in remote locations and harsh environments, the need for high reliability and low O&M costs is higher than for on-shore applications. Proactive maintenance strategies must be adopted if wind energy is to achieve a reduced cost of energy and such a maintenance strategy requires detection, diagnosis and prognosis information. For these reasons the development of reliable condition monitoring systems for wind turbines is essential to avoid catastrophic failures and to minimize costly corrective maintenance. Condition monitoring allows early detection of any degeneration in system components, facilitating a proper asset management decision, improving availability, minimizing downtime and maximizing productivity.

The work on this deliverable focuses on the research undertaken in developing practical condition monitoring approaches for electrical and mechanical drive train faults, with an emphasis on the higher impact subassemblies such as the generator, gearbox and power converter. The papers and chapter book in this deliverable discuss the application of novel monitoring sensors and signal processing algorithms that have been developed within the Supergen Wind Hub Work Package 4. Where possible advanced analytical models are validated against laboratory test-rig experimental results.

The deliverable is comprised of a number of papers published and submitted by Durham University, the University of Manchester and Loughborough University. The 13 journal publications are supported by a further 4 conference papers and a book chapter. Of these 18 publications, the 13 journal papers are discussed in this introduction. Note that two of these papers are still under review so are not finalised. All the 17 journal and conference papers are attached.

Paper 1: Brigham, K., Zappalá, D., Crabtree, C.J. & Donaghy-Spargo, C. (UNDER REVIEW). Simplified Automatic Fault Detection in Wind Turbine Induction Generators. *Wind Energy*.

This paper presents a simplified automated fault detection scheme for wind turbine induction generators with rotor electrical asymmetries. Fault indicators developed in previous works have made use of the presence of significant spectral peaks in the upper sidebands of the supply frequency harmonics; however, the specific location of these peaks may shift depending on the wind turbine speed. In this work, a method is proposed to bypass the issue of shifting frequency peaks by introducing a set of bandpass filters designed to capture the fault-related spectral information to train a classifier for automatic fault detection, regardless of the specific peak location. Experimental results show that this approach is robust against variable speeds, and further shows good generalisability in being able to detect faults at speeds and conditions that were not presented during training.

Paper 2: Zhang, G., Zappalá, D., Crabtree, C.J., Donaghy-Spargo, C., Hogg, S. & Duffy, A. (UNDER REVIEW). Validation of a non-contact technique for torque measurements in wind turbines using an enhanced transient FSV approach. *Measurement*.

In-service turbine monitoring is essential for maximizing the wind energy contribution to the global energy budget. Measurement of turbine shaft torque under transient wind conditions is fundamental to develop reliable condition monitoring techniques. Contact based measurements bring their own disadvantages and non-contactless measurements have many potential advantages. However, their performance needs to be validated against standard methods. This paper focuses on enhanced transient FSV (Feature Selective Validation) techniques developed to undertake this analysis with an emphasis on transient data processing. The FSV method is a reliability function-like heuristic, initially developed for validation of electromagnetic compatibility simulations. Open questions have existed for some time as to how transients should be dealt with. This paper (a) overcomes the limitations of previous approaches for step-function transient comparison and (b) presents analytical methods where the comparison is dominated by the transient function itself and not the length of the pre- and post-transient periods.

Paper 3: Zappalá, D., Crabtree, C.J. & Hogg, S. (2019). Investigating Wind Turbine Dynamic Transient Loads Using Contactless Shaft Torque Measurements. *The Journal of Engineering* 18: 4975-4979. https://doi.org/10.1049/joe.2018.9361

Accurate and reliable drive train mechanical torque measurements can be a very informative input for enhancing wind turbine condition monitoring capabilities as well as for adopting proactive solutions for extreme load mitigation. This work is significant because it experimentally investigates shaft dynamic, transient loads through a novel contactless torquemeter designed by the Authors. The implementation of the proposed sensor in the field would allow direct, cheap, real-time measurements of wind turbine drive train loads. This method allows to overcome the current limitations of the industrial implementation of torque measurements for performance monitoring, condition monitoring and control purposes. This paper was originally presented at the 7th IET International Conference on Renewable Power Generation (RPG 2018).

Paper 4: Smith, C.J., Zappalá, D., Crabtree, C.J., Lapiedra, J. & Mulholland, B. (2019). Power Converter Junction Temperature Measurement using Infra-red Sensors. *The Journal of Engineering* 17: 4452-4456. https://doi.org/10.1049/joe.2018.9361

Studies demonstrate that the power converter has one of the highest failure rates in a wind turbine, with a key failure driver being the power module junction temperature (T_j). This paper details an experimental setup for simplified emulation of wind turbine conditions on a power converter with infra-red sensing of IGBT T_j. Results are compared to previous simulation work for a PMSG wind turbine, with the same trend of increasing mean T_j with wind speed found, and the need to use an equivalent generator reactance in highlighted. A commercial-scale prototype for more accurate wind turbine converter emulation is also detailed. This paper was originally presented at the 9th IET International Conference on Power Electronics, Machines and Drives (PEMD 2018).

Paper 5: Sarma, N., Tuohy, P. M., Djurović, S. (2019). Modeling, Analysis and Validation of Controller Signal Interharmonic Effects in DFIG Drives. *IEEE Transactions on Sustainable Energy* (Early access). https://doi.org/10.1109/TSTE.2019.2904113

This paper presents the development of a doubly fed induction machine (DFIG) harmonic model in MATLAB/Simulink, which is used to examine the spectral content of DFIG controller signals and improve the understanding of their behavior and spectral nature. The reported DFIG harmonic model has the capability of representing the effects of higher order time and space harmonics and thus, allows detailed analysis of the controller signals embedded spectral effects. The model consists of a wound rotor induction machine (WRIM) harmonic model coupled with a stator flux oriented controller (SFOC) model. The WRIM space harmonic effects are represented using the conductor distribution function approach to enable the calculation of winding inductances as harmonic series. In addition, analytical expressions are derived to define the possible spectral content in the controller signals of DFIGs. Both the reported DFIG harmonic model and the analytical equations are validated by comparison with measurements taken from a purpose built vector controlled DFIG laboratory test-rig. The findings confirm the capability of the developed DFIG harmonic model in representing the controller signals embedded spectral effects, as well as the accuracy of the reported analytical expressions, and enable a much improved understanding of the spectral nature of the DFIG controller signals

Paper 6: Zappalá, D., Sarma, N., Djurović, S., Crabtree, C. J., Mohammad, A. & Tavner, P. J. (2019). Electrical & Mechanical Diagnostic Indicators of Wind Turbine Induction Generator Rotor Faults. *Renewable Energy* 131: 14-24. https://doi.org/10.1016/j.renene.2018.06.098

One of the main challenges currently facing the wind industry is to improve the reliability of diagnostic decisions, including component fault severity assessment. Generators make a significant contribution to wind turbine downtime. This paper presents a modelling and experimental investigation of electrical and mechanical signatures for wind turbine generators, identifying the best diagnostic reliability condition monitoring indicators. This is significant because it represents the first occasion in which such comprehensive approach has been presented for wind turbine induction generators, with healthy and faulty conditions at varying loads and level of fault.

Paper 7: Sarma, N., Tuohy, P. M., Apsley, J. M., Wang, Y., Djurović, S. (2018). DFIG stator flux-oriented control scheme execution for test facilities utilising commercial converter. *IET Renewable Power Generation* 12(12): 1366-1374. https://doi.org/10.1049/iet-rpg.2018.5195

The utilisation of conventional industrial converters for development of doubly-fed induction generator (DFIG) test facilities poses an attractive prospect as it would provide proprietary commercial protection and functionality. However, standard commercial converters present significant challenges in attainable DFIG operational capability. This is due to the fact that they are designed for execution of a limited set of pre-programmed common control modes. They typically do not cater for execution of complicated stator flux-oriented vector control (SFOC) schemes required for DFIG drive control. The research work presented in this study reports a methodology that enables effective implementation of SFOC on industrial converters through a dedicated external real-time platform and a velocity/position communication module. The reported scheme is validated in laboratory experiments on an experimental DFIG test-rig facility. The presented principles are general and are therefore applicable to conventional DFIG drive architectures utilising standard industrial converters.

Paper 8: Ibrahim, Raed K., Watson, Simon J., Djurović, Siniša & Crabtree, Christopher J. (2018). An Effective Approach for Rotor Electrical Asymmetry Detection in Wind Turbine DFIGs. *IEEE Transactions on Industrial Electronics* 65(11): 8872-8881. https://doi.org/10.1109/TIE.2018.2811373

Determining the magnitude of particular fault signature components (FSCs) generated by wind turbine (WT) faults from current signals has been used as an effective way to detect early abnormalities. WTs frequently operate close to the generator synchronous speed, resulting in FSCs manifesting themselves in the vicinity of the supply frequency and its harmonics, making their detection more challenging. To address this, the detection of rotor electrical asymmetry in WT generators has been investigated experimentally and an effective extended Kalman filter (EKF) based method is proposed to iteratively track the FSCs. The proposed approach has been compared with a continuous wavelet transform (CWT) and an iterative localized discrete Fourier-transform (IDFT). Experimental results demonstrate that the CWT and IDFT algorithms fail to track the FSCs at low load operation near-synchronous speed. In contrast, the EKF was more successful in tracking the FSCs magnitude in all operating conditions, unambiguously determining the severity of the faults over time and providing significant gains in both computational efficiency and accuracy of fault diagnosis.

Paper 9: Zappalá, D., Bezziccheri, M., Crabtree, C.J. & Paone, N. (2018). Non-intrusive torque measurement for rotating shafts using optical sensing of zebra-tapes. *Measurement Science and Technology* 29(6): 065207. https://doi.org/10.1088/1361-6501/aab74a

This paper presents a new method to use optical sensors and patterned shafts for non-contact measurement of torque. The paper was created from a new collaboration between Durham and Università Politecnica delle Marche, Ancona, Italy. Unlike state-of-the-art transducers, the proposed method does not require costly embedded sensors, electronics or wires to be installed on the rotating shaft. Its non-intrusive nature, adaptable design, simple installation and low cost make it suitable for a large variety of advanced engineering applications. The paper was picked up by the Italian wind turbine manufacturer MAIT, who are in discussions with the Authors about full-scale testing on an operational wind turbine.

Paper 10: Smith, C.J., Crabtree, C.J. & Matthews, P.C. (2017). Impact of wind conditions on thermal loading of PMSG wind turbine power converters. *IET Power Electronics Special Issue: Power Electronics Converters for Marine Renewable Energy Applications* 10(11): 1268-1278. https://doi.org/10.1049/iet-pel.2016.0802

Power converter reliability is critical for permanent magnet synchronous generator (PMSG) wind turbines. Converter failures are linked to power module thermal loading but studies often neglect turbine dynamics, control and the impact of wind speed sampling rate on lifetime estimation. This study addresses this using a 2 MW direct-drive PMSG wind turbine model, and simulating junction temperatures (T_j) using a power module thermal equivalent circuit under various synthetic wind speed conditions. Responses to square wave wind speeds showed that the lower the gust frequency, the higher ΔT_j becomes, demonstrating that low turbulence sites have greater thermal variation in the converter. In contrast, wind speed variations with frequencies >0.25 Hz deliver only small increases in ΔT_j. It is concluded that reasonable approximations of T_j profiles can be made with 0.25 Hz wind speed data, but that lower data rate wind measurements miss essential, damaging characteristics. This paper was selected for publication after being presented at the 8th IET International Conference on Power Electronics, Machines and Drives (PEMD 2016).

Paper 11: Rieg, C. A., Smith, C. J. & Crabtree, C. J. (2016). Monitoring Wind Turbine Loading Using Power Converter Signals. *Journal of Physics: Conference Series (JPCS)* 749(1): 012018. https://doi.org/10.1088/1742-6596/749/1/012018

The ability to detect faults and predict loads on a wind turbine drivetrain's mechanical components cost-effectively is critical to making the cost of wind energy competitive. In order to investigate whether this is possible using the readily available power converter current signals, an existing permanent magnet synchronous generator based wind energy conversion system model was modified to include a grid-side converter (GSC) for an improved converter model and a gearbox. The GSC maintains a constant DC link voltage via vector control. The gearbox was modelled as a 3-mass model to allow faults to be included. Gusts and gearbox faults were introduced to investigate the ability of the machine side converter (MSC) current (I_q) to detect and quantify loads on the mechanical components. In this model, gearbox faults were not detectable in the I_q signal due to shaft stiffness and damping interaction. However, a model that predicts the load change on mechanical wind turbine components using I_q was developed and verified using synthetic and real wind data. This paper was originally presented at the WindEurope Summit 2016.

Paper 12: Zappalá, D., Tavner, P.J., Crabtree, C.J. & Sheng, S. (2014). Side-band algorithm for automatic wind turbine gearbox fault detection and diagnosis. *IET Renewable Power Generation* 8(4): 380-389. https://doi.org/10.1049/iet-rpg.2013.0177

This paper, originally presented at the 2013 European Wind Energy Association Conference, was recommended by the Session Chairs & Co-Chairs for submission to a special issue of the IET Renewable Power Generation Journal. The paper experimentally investigates a fault detection algorithm for wind turbine gearbox, which has been shown to cause the longest machine downtime. This work is significant because it allows automatic data interpretation, timely detection and diagnosis of developing wind turbine gear defects. The experimental outcomes were validated using the Round Robin project data provided by the National Renewable Energy Laboratory (NREL).

Paper 13: Zaggout, M. N., Tavner, P. J., Crabtree, C. J. & Ran, L. (2014). Detection of Rotor Electrical Asymmetry in Wind Turbine Doubly-Fed Induction Generators. IET Renewable Power Generation 8(8): 878-886. https://doi.org/10.1049/iet-rpg.2013.0324

This study presents a novel method for detecting rotor faults in wind turbine doubly-fed induction generators (DFIGs), controlled by a stator field-oriented vector control scheme. Rotor electrical asymmetry faults are identified from the rotor-side inverter control loop, using the error signal. Simulation and experimental measurements of the proposed signals were carried out under steady-state operation for both healthy and faulty generator conditions. Stator current and power were also investigated for rotor electrical asymmetry detection and comparison made with rotor-side inverter control signals. An investigation was then performed to define the sensitivity of the proposed monitoring signals to fault severity changes and a comparison made with previous current, power and vibration signal methods. The results confirm that a simple spectrum analysis of the proposed control loop signals gives effective and sensitive DFIG rotor electrical asymmetry detection.

List of Publications

Journal Papers

[1] Brigham, K., Zappalá, D., Crabtree, C.J. & Donaghy-Spargo, C. (UNDER REVIEW). Simplified Automatic Fault Detection in Wind Turbine Induction Generators. *Wind Energy*.

[2] Zhang, G., Zappalá, D., Crabtree, C.J., Donaghy-Spargo, C., Hogg, S. & Duffy, A. (UNDER REVIEW). Validation of a non-contact technique for torque measurements in wind turbines using an enhanced transient FSV approach. *Measurement*.

[3] Zappalá, D., Crabtree, C.J. & Hogg, S. (2019). Investigating Wind Turbine Dynamic Transient Loads Using Contactless Shaft Torque Measurements. *The Journal of Engineering* 18: 4975-4979. https://doi.org/10.1049/joe.2018.9361

[4] Smith, C.J., Zappalá, D., Crabtree, C.J., Lapiedra, J. & Mulholland, B. (2019). Power Converter Junction Temperature Measurement using Infra-red Sensors. *The Journal of Engineering* 17: 4452-4456. https://doi.org/10.1049/joe.2018.9361

[5] Sarma, N., Tuohy, P. M., Djurović, S. (2019). Modeling, Analysis and Validation of Controller Signal Interharmonic Effects in DFIG Drives. *IEEE Transactions on Sustainable Energy* (Early access). https://doi.org/10.1109/TSTE.2019.2904113

[6] Zappalá, D., Sarma, N., Djurović, S., Crabtree, C. J., Mohammad, A. & Tavner, P. J. (2019). Electrical & Mechanical Diagnostic Indicators of Wind Turbine Induction Generator Rotor Faults. *Renewable Energy* 131: 14-24. https://doi.org/10.1016/j.renene.2018.06.098

[7] Sarma, N., Tuohy, P. M., Apsley, J. M., Wang, Y., Djurović, S. (2018). DFIG stator flux-oriented control scheme execution for test facilities utilising commercial converter. *IET Renewable Power Generation* 12(12): 1366-1374. https://doi.org/10.1049/iet-rpg.2018.5195

[8] Ibrahim, Raed K., Watson, Simon J., Djurović, Siniša & Crabtree, Christopher J. (2018). An Effective Approach for Rotor Electrical Asymmetry Detection in Wind Turbine DFIGs. *IEEE Transactions on Industrial Electronics* 65(11): 8872-8881. https://doi.org/10.1109/TIE.2018.2811373

[9] Zappalá, D., Bezziccheri, M., Crabtree, C.J. & Paone, N. (2018). Non-intrusive torque measurement for rotating shafts using optical sensing of zebra-tapes. *Measurement Science and Technology* 29(6): 065207. https://doi.org/10.1088/1361-6501/aab74a

[10] Smith, C.J., Crabtree, C.J. & Matthews, P.C. (2017). Impact of wind conditions on thermal loading of PMSG wind turbine power converters. *IET Power Electronics Special Issue: Power Electronics Converters for Marine Renewable Energy Applications* 10(11): 1268-1278. https://doi.org/10.1049/iet-pel.2016.0802

[11] Rieg, C. A., Smith, C. J. & Crabtree, C. J. (2016). Monitoring Wind Turbine Loading Using Power Converter Signals. *Journal of Physics: Conference Series (JPCS)* 749(1): 012018. https://doi.org/10.1088/1742-6596/749/1/012018

[12] Zappalá, D., Tavner, P.J., Crabtree, C.J. & Sheng, S. (2014). Side-band algorithm for automatic wind turbine gearbox fault detection and diagnosis. *IET Renewable Power Generation* 8(4): 380-389. https://doi.org/10.1049/iet-rpg.2013.0177

[13] Zaggout, M. N., Tavner, P. J., Crabtree, C. J. & Ran, L. (2014). Detection of Rotor Electrical Asymmetry in Wind Turbine Doubly-Fed Induction Generators. IET Renewable Power Generation 8(8): 878-886. https://doi.org/10.1049/iet-rpg.2013.0324

Conference Papers

[14] Brigham, K., Zappalá, D., Crabtree, C.J. & Donaghy-Spargo, C. (2018), Automated Fault Detection in Wind Turbine Induction Generators with Rotor Electrical Asymmetry, International Conference on Power Electronics, Machines and Drives. Liverpool, UK.

[15] Secker, M., Crabtree, C.J. & Zappalá, D. (2015), Wind Turbine Non-Intrusive Torque Monitoring, European Wind Energy Conference, Scientific Track. Paris, France, European Wind Energy Association.

[16] Zappalá, D., Crabtree, C.J., Vilchis-Rodriguez, D.S., Tavner, P.J., Djurović, S. & Smith, A.C. (2014), Advanced Algorithms for Automatic Wind Turbine Generator Fault Detection and Diagnosis, European Wind Energy Conference, Scientific Track. Barcelona, Spain, European Wind Energy Association.

[17] Crabtree, C.J., Zappalá, D., Tavner, P.J. & Hogg, S.I. (2014), Electrical Fault Detection Using Mechanical Signals, European Wind Energy Conference, Scientific Track. Barcelona, Spain, European Wind Energy Association.

Chapter in book

[18] Zappalá, D., Crabtree, C.J. & Tavner, P.J. (2016). Reliability and condition monitoring. In UK Wind Energy Technologies. Hogg, S. & Crabtree, C.J. Routledge. 76-136. https://www.dur.ac.uk/research/directory/staff/?mode=pdetail&id=8780&sid=8780&pdetail=104849

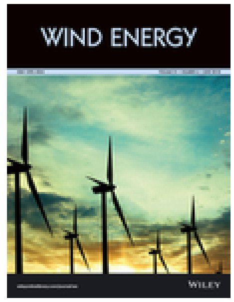

Simplified Automatic Fault Detection in Wind Turbine Induction Generators

Journal:	*Wind Energy*
Manuscript ID	WE-19-0203
Wiley - Manuscript type:	Research Article
Date Submitted by the Author:	23-Jun-2019
Complete List of Authors:	Brigham, Katharine; Durham University, Engineering; Zappalá, Donatella ; Durham University, Engineering Crabtree, Christopher; Durham University, Engineering Donaghy-Spargo, Christopher; Durham University, Engineering
Keywords:	fault detection, speed invariance, rotor electrical asymmetry, condition monitoring

Received: Added at production | Revised: Added at production | Accepted: Added at production

DOI: xxx/xxxx

ARTICLE TYPE

Simplified Automatic Fault Detection in Wind Turbine Induction Generators

Katharine Brigham* | **Donatella Zappalá** | **Christopher J. Crabtree** | **Christopher Donaghy-Spargo**

[1]Department of Engineering, Durham University, Durham, UK

Correspondence
*Katharine Brigham. Email: katharine.g.brigham@durham.ac.uk

Present Address
South Road, DH1 3LE, Durham, UK

Abstract

This paper presents a simplified automated fault detection scheme for wind turbine induction generators with rotor electrical asymmetries. Fault indicators developed in previous works have made use of the presence of significant spectral peaks in the upper sidebands of the supply frequency harmonics; however, the specific location of these peaks may shift depending on the wind turbine speed. As wind turbines tend to operate under variable speed conditions, it may be difficult to predict where these fault-related peaks will occur. To accommodate for variable speeds and resulting shifting frequency peak locations, previous works have introduced methods to identify or track the relevant frequencies, which necessitates an additional set of processing algorithms to locate these fault-related peaks prior to any fault analysis. In this work, a simplified method is proposed to instead bypass the issue of variable speed (and shifting frequency peaks) by introducing a set of bandpass filters that encompass the ranges in which the peaks are expected to occur. These filters are designed to capture the fault-related spectral information to train a classifier for automatic fault detection, regardless of the specific location of the peaks. Initial experimental results show that this approach is robust against variable speeds, and further shows good generalisability in being able to detect faults at speeds and conditions that were not presented during training. After training and tuning the proposed fault detection system, the system was tested on 'unseen' data and yielded a high classification accuracy of 97.4%, demonstrating the efficacy of the proposed approach.

KEYWORDS:
fault detection, speed invariance, rotor electrical asymmetry, condition monitoring

1 | INTRODUCTION

Reliable and efficient condition monitoring (CM) techniques play a crucial role in minimizing wind turbine (WT) operation and maintenance (O&M) costs for competitive development of offshore wind energy [1]. Current efforts in the wind industry are aimed at automating the data interpretation and improving the accuracy and the reliability of the diagnostic decisions to enable condition-based maintenance planning [2]. While alternatives are emerging, wound rotor induction generators (WRIGs), using a partially-rated power converter connected to the rotor side, remain the most widely-used machines in wind industry for medium and large size variable speed applications [3]. Reliability studies [4,5,6,7] have reported that generator faults contribute significantly to WT downtime. Rotor electrical asymmetry, caused by brush-gear degradation, slip-ring wear/faults or winding electrical faults, has been identified as one of the main contributors to WT generator failure rate [8,9]. Undetected generator faults may have a catastrophic effect on the turbine drive train resulting in costly repairs and long downtimes. Attention at the incipient fault stage is required to avoid fault escalation leading to breakdown.

Diagnosis methods to detect WRIG rotor failures, based on time domain and/or frequency domain techniques, have been researched extensively. Motor current signature analysis (MCSA) is a well-established signal-based technique, typically using non-invasive, spectral-based machine terminal quantity analysis, for detecting induction machine faults [10,11,12]. Stator current is commonly used in MCSA since it is sensitive to the rotor faults, and it is a suitable method to obtain a diagnostic index allowing the discrimination between faulty and healthy conditions [13]. Rotor asymmetry has been shown to induce a change in the generator stator current spectral content at slip-dependent sidebands of the dominant supply frequency harmonic components. Closed-form analytical expressions have been derived as to the specific locations of these sidebands [11,14,15,16,17,18] that can be monitored for diagnostic purposes for machine operating in steady state. MCSA was expansively investigated for rotor asymmetry detection in WRIGs under steady state conditions, ranging from analysis of experimental data only [19,20], to investigation based on both simulation and experimental data [21,22,23].

In the WT industry, electrical-signal-based CM has been gaining increasing attention, as it requires almost no additional capital expenditure [24]. This is due to the fact that electrical signals are already available in existing WT control and protection systems and no additional sensors or data acquisition devices are needed. However, despite the increasing concern about WT electrical component reliability and growing attention in electrical-signal-based CM, monitoring generator electrical faults has not yet become standard practice in the wind industry. The majority of WT CM systems (CMS) are mainly based on monitoring high-frequency vibration in gearbox and generator bearings [25]. In WT time-varying operating conditions, as the speed and then the slip changes, the frequency components associated with rotor faults are spread in a frequency range proportional to the operational speed variation range. This represents one of the main limitations associated to the effective implementation of MCSA techniques for WT generator CM as accurate information about the machine speed and specialist knowledge, with advanced signal analytics experience, are required to interpret large amounts of complex monitoring data [3]. Further to this, if the machine speed is unknown, it may not be possible to predict where these fault-related peaks will occur. In order to achieve a good spectral resolution, signal should be also sampled at high sampling rates, requiring large memory space for data storage and processing. To use CM information successfully for optimising the O&M strategies, systems that can automatically analyse and interpret large volumes of CM data are required.

Recent works have dealt with the problem of WRIG rotor fault detection under non-stationary conditions. Gritli *et al.* [26] and Vedreño *et al.* [27] proposed approaches based on detecting the faults through increases in signal energy in specific frequency ranges, including the fault component of interest. However, they rely on the use of the computationally intensive discrete wavelet transform (DWT) as filtering tool to isolate frequency intervals of interest and require the knowledge of the machine speed to identify in which band of the DWT decomposition the fault components appear. The harmonic order tracking analysis method presented by Sapena-Bano *et al.* [28] rearranges the information in the current time-frequency spectrograms into simplified graphs displaying a unique pattern for each type of fault. However, this methodology strictly relies on the knowledge of the rotor position in every sampling time, which is usually not available on operational wind turbines. All these approaches, besides requiring the knowledge of the machine speed or rotor position, imply complex additional calculations to characterize the machine fault signatures for every machine operating condition. This makes their industrial implementation difficult.

This paper proposes an automated fault detector of WT induction generator rotor electrical asymmetry that requires minimal prior knowledge of the machine operating conditions and is invariant to the issue of shifting slip-dependent fault-related peaks in the stator current spectral content. Building on previous research in [14,16,17,20,23], the proposed method is a simplified but effective approach that negates the need for supplementary processing to identify operational parameters and is based on the combination of simplified signal processing tools for feature extraction from the machine stator current signal and the use of a linear classifier for fault detection. Unlike previous works on AI-based algorithms for automatic induction motor fault detection, such as [29,30,31] and those reviewed in [12], tested under machine steady-state conditions, this work has been specifically developed to improve the fault diagnostic reliability during WT non-stationary load and speed operating conditions.

In general, the approach for developing an automated detection/classification system is to first extract a set of features from input data (e.g., images, speech signals), and then use these features to train a classifier [32]. Subsequent data can then be classified by applying the same feature extraction approach, and then inputting the features into the previously trained classifier to arrive at a decision about the class of the input data (e.g., healthy or faulty), or even a categorisation of the level of the fault severity, if a fault exists. The selection of an appropriate set of features is undoubtedly critical in this process towards implementing a successful detection system, as it is possible to extract features that do not contain information relevant for classification. Therefore, the suitability of the proposed set of features for automated fault detection is also investigated in this work, by applying a form of supervised dimensionality reduction to allow for both visual and numerical analyses of experimental healthy and faulty data. The applicability of the proposed approach to detecting different fault levels is experimentally validated in a laboratory test rig.

The main advantages of the proposed method are:

1. It does not require any speed measurement, and it has been experimentally validated under stationary and wind-like variable speed conditions;

2. It allows automatic classification of the WT generator condition without requiring expert knowledge in signal processing, significantly reducing the large degree of manual analysis currently required and facilitating reliable diagnostics;

3. It allows fault severity discrimination providing early generator rotor damage detection warnings as part of a predictive maintenance regime; and

4. It can be easily adapted to existing integrated monitoring systems and applied remotely to automatically monitor WT electrical signatures.

2 | PROPOSED METHODOLOGY

Previous work [14,17] has shown that WRIG rotor electrical asymmetry gives rise to additional frequency components in the stator current at characteristic slip-dependant frequencies, f^k, given by:

$$f^k = \left| j \pm \frac{k}{p}(1-s) \right| f \tag{1}$$

where f is the fundamental supply frequency, s is the induction generator fractional slip, p is the machine pole pair number, $k = 0, 1, 2, 3, \ldots$ and $j = 0, 1, 2, 3, \ldots$ relate to air-gap field space harmonics resulting from the layout of the machine and supply time harmonics in the current, respectively.

Given these findings regarding the manifestation of significant spectral peaks due to rotor asymmetry and the variability of the peak locations with the machine operating speed, the extracted features should incorporate information across the various frequency bands of interest. To this end, a set of bandpass filters is proposed (hereafter referred to as a filter bank), where the cutoff frequencies of the bandpass filters are determined based on an expected range of slip-dependent sideband peak locations, derived from both theory and actual experimentation. The average spectral magnitude contained in each frequency band of the filter bank is computed and concatenated to form a vector of features, whose length is equal to the number of bandpass filters.

With the introduction of these bandpass filters, any fault-related information contained within the frequency bands-of-interest can be found without the need for any frequency tracking or identification of the relevant spectral components. Each bandpass filter is expected to cover the range of where the relevant spectral peaks occur, and taking the average magnitude in each band reduces the spectral content contained in that range to a single metric in which the fault-related information is naturally captured. These metrics, which will be used as the 'features', can then be combined (i.e., concatenated) for usage in automatic classification.

2.1 | Feature Extraction

The mathematics for computing the features from the input signals are as follows. First, the frequency domain representation of the stator current signature is computed by taking the Discrete Fourier Transform (DFT) over a windowed data vector $\mathbf{x}_w[n] = \mathbf{h}[n] \odot \mathbf{x}[n]$, where $\mathbf{h}[n]$ is a windowing function (e.g., a Hamming window), and $\mathbf{x}[n]$ is the original data sample vector sampled at frequency f_s (Hz) over a window sample time of N_w (seconds).

For all data, the features are extracted using a filter bank approach on the stator current spectra whereby a set of R bandpass filters, H_r for $r = 1, \ldots, R$, are applied (i.e., multiplied by the spectrum). Each filter encompasses a frequency band of range $f_{range} = f_{r,max} - f_{r,min}$, which can discretely be represented as:

$$H_r[k] = \begin{cases} 1, & k = \lfloor f_{r,min} \cdot (N/f_s) \rfloor, \ldots, \lfloor f_{r,max} \cdot (N/f_s) \rfloor \\ 0, & \text{otherwise} \end{cases} \tag{2}$$

where $f_{r,min}$ and $f_{r,max}$ are the lower and upper cutoff frequencies, respectively, for the r^{th} bandpass filter, N is the length of the signal being analysed, where $N \geq N_w \cdot f_s$ (with the inequality accounting for optional zero-padding), and $k \in \mathbb{N}$. Application of these bandpass filters is essentially an extraction of the spectral content in the frequency range-of-interest (i.e., zeroing out the spectral content outside of the range of the bandpass filter, while 'passing', or multiplying by 1, the spectral content contained within the range of the bandpass filter). Different stator current bandpass filters are constructed under the guidance of work done by Zappalá [34], which states that in faulty spectra (compared to "healthy" spectra), higher amplitude peaks will appear at the 2sf upper sidebands of the supply frequency harmonics hf, where $h = 1, 2, 3\ldots$ is the supply harmonic order. Therefore, the filter bank will be constructed such that each bandpass filter encompasses this 2sf upper sideband of each supply frequency harmonic order h:

$$f_{r,min} = hf + f_{shift}; \text{ and} \tag{3}$$

$$f_{r,max} = hf + f_{shift} + f_{range} \tag{4}$$

where f_{shift} marks the start of the bandpass filter. The frequency range containing the sideband peaks, f_{range}, can be computed from the expected machine operational speed range. Note that while there could be an equivalence of $r \equiv h$ if there is a filter for each harmonic, in some cases it may not be necessary to have filters placed at each harmonic so that $r \neq h$ [23].

From the frequency spectra computed from each windowed signal, a feature vector, $\mathbf{v}$, will be constructed with each element in the vector $\mathbf{v}[r]$ representing information from each bandpass filter, and is generated by the following equation:

$$\mathbf{v}[r] = \frac{1}{k_2 - k_1 + 1} \sum_{k=k_1}^{k_2} X[k] H_r[k] \tag{5}$$

where $k_1 = \lfloor f_{r,\min}(N/f_s) \rfloor$ and $k_2 = \lfloor f_{r,\max}(N/f_s) \rfloor$ (i.e., the start and stop indices of the range in which the filter is nonzero), and $\mathbf{v}[r] \in \Re^R$. In this feature extraction approach, note that there are several parameters that can be varied:

- Length of the analysis time window; N_w
- Number of bandpass filters (interested harmonics); R
- Frequency range of the bandpass filters; f_{range}

During experimentation, these parameters will be tuned (i.e., the 'best' values will be determined) by classifying the data using a held-out development set (not to be used in testing), in part to quantify the effects of these parameters on the resulting classifications.

2.2 | Dimensionality Reduction and Classification

To investigate the suitability of these features for automatic fault detection, Fisher's Linear Discriminant (FLD) will be applied to the features since its usage permits visualisation of the proposed features in a lower dimensional subspace, and can help identify whether or not a distinct separation between healthy and faulty data can be attained. Note that although FLD is used and discussed herein, other popular classifiers such as Support Vector Machines or Artificial Neural Networks could also easily be applied, but the choice of classifier is not the primary focus of this work. FLD is merely used as a tool here to investigate the feasibility and demonstrate the efficacy of the proposed feature extraction approach. With FLD, the ability to achieve the desired distinctive separations can also be further analysed to determine whether or not such linear classifiers may be capable of detecting faults at multiple levels (e.g., the fault detector should ideally be capable of detecting various levels of rotor imbalances). FLD further provides an added benefit of dimensionality reduction, as the application of FLD computes a linear function of the input data as follows:

$$y = \mathbf{w}^T \mathbf{v} \tag{6}$$

where y is the (one-dimensional) FLD output, $\mathbf{w}$ is an R-dimensional weight (i.e., projection) vector, and $\mathbf{v}$ is an R-dimensional input vector (e.g., a feature vector derived from an input data sample). The weight vector $\mathbf{w}$ is determined using labelled 'training' data to solve an optimisation problem that minimises the *within-class variability* (i.e., spread of the data) and maximises the *between-class separation* of the projected output data. A derivation of FLD will be described here to provide additional details on how FLD works.

Mathematical representations should first be defined for two quantities-of-interest: the *within-class variability* and the *between-class separation* of the resulting projected FLD outputs. While FLD has a multi-class variant [32], for simplicity, the following description of FLD will be restricted to two classes. The within-class variability of the projected output from Equation (6) will be denoted as $\mathbf{S}_k^p$ and can be defined as the total sample variance, which is given by [32]:

$$\mathbf{S}_k^p = \sum_{n \in C_k} (\mathbf{y}_n - \mathbf{m}_k^p)^2 \tag{7}$$

where $\mathbf{y}_n$ is the projected data point of the n^{th} input vector for $n \in C_k$, where C_k is the class, and $k = \{1, 2\}$ is the class index, and $\mathbf{m}_k^p$ is the mean of the set of projected data points for class C_k.

The between-class separation of the projected data for classes C_1 (i.e., class 1) and C_2 (i.e., class 2) will be denoted as $\mathbf{m}_{12}^p$, and can be defined as a distance between the means of the projected data from each class:

$$\mathbf{m}_{12}^p = (\mathbf{m}_1^p - \mathbf{m}_2^p)^2 \tag{8}$$

where $\mathbf{m}_1^p$ and $\mathbf{m}_2^p$ are the means of the projected data belonging to C_1 and C_2, respectively, and are computed using their respective sample mean:

$$\mathbf{m}_k^p = \frac{1}{N_k} \sum_{n \in C_k} \mathbf{y}_n \tag{9}$$

where N_k is the number of samples in class C_k. To both maximise the between-class separation and minimise the within-class variability, a ratio between the two measures can be constructed to formulate the following optimisation function [32] for $\mathbf{w}$, the R-dimensional weight (i.e., projection) vector:

$$J(\mathbf{w}) = \frac{(\mathbf{m}_1^p - \mathbf{m}_2^p)^2}{\mathbf{S}_1^p + \mathbf{S}_2^p} \tag{10}$$

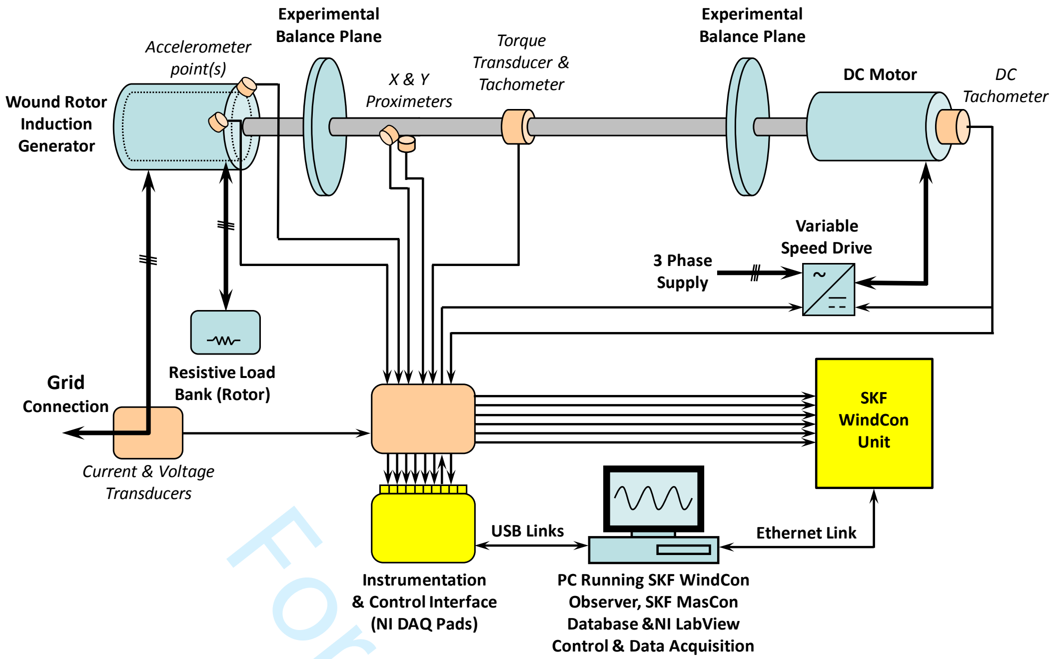

FIGURE 1 Schematic diagram of the wind turbine condition monitoring test rig [34].

where S_1^p and S_2^p are the variances of the projected data belonging to classes C_1 and C_2, respectively. The projected means and variances on the right-hand side of Equation (10) can be rewritten in terms of the original data and the weight vector $\mathbf{w}$ (making the dependence of the function on the weight vector explicit) to obtain the following final form of the desired optimisation function:

$$J(\mathbf{w}) = \frac{\mathbf{w}^T (\mathbf{m}_1 - \mathbf{m}_2)(\mathbf{m}_1 - \mathbf{m}_2)^T \mathbf{w}}{\mathbf{w}^T \mathbf{S}_W \mathbf{w}} \tag{11}$$

where $\mathbf{m}_1$ and $\mathbf{m}_2$ are the sample means of the input data (feature vectors) and are given by:

$$\mathbf{m}_k = \frac{1}{N_k} \sum_{n \in C_k} \mathbf{v}_n \quad \text{for } k = 1, 2 \tag{12}$$

where $\mathbf{v}_n$ is from Equation (6) but explicitly for $n \in C_k$, and $\mathbf{S}_W$ is the total *within-class* covariance:

$$\mathbf{S}_W = \sum_{n \in C_1} (\mathbf{v}_n - \mathbf{m}_1)(\mathbf{v}_n - \mathbf{m}_1)^T + \sum_{n \in C_2} (\mathbf{v}_n - \mathbf{m}_2)(\mathbf{v}_n - \mathbf{m}_2)^T \tag{13}$$

Maximizing $J(\mathbf{w})$ from Equation (11) with respect to $\mathbf{w}$ results in the following closed-form solution for $\mathbf{w}$ [32]:

$$\mathbf{w} = \mathbf{S}_W^{-1} (\mathbf{m}_1 - \mathbf{m}_2) \tag{14}$$

An optimal threshold for separating the classes after applying Equation (6) to the input (i.e., training) data using the weight vector $\mathbf{w}$ found from Equation (14) can subsequently be determined from the resulting input data projections.

2.3 | Experimental Rig and Data Curation

The proposed approach was tested using data collected from a small scale condition monitoring test rig used for WT drivetrain analysis. The rig was designed to act as a model for a WT drive train with the purpose of producing signals comparable to those encountered on an operational WT. It features a 54 kW DC motor, operated as a prime mover and simulating the WT rotor input, driving an industrial 4-pole, three-phase, 50 Hz, 30 kW WRIG. The WRIG is driven at either constant speed or non-stationary, variable speed conditions, to reflect the stochastic effects of wind torque driving, via a commercial DC machine drive. A schematic diagram of this experimental facility is shown in Fig. 1 and two photographs are shown in Fig. 2.

Details of the test rig are given in [33] and [34]. Seeded-fault conditions can be induced or removed from the test rig drive train as required enabling several electrical and mechanical faults to be implemented repeatedly on demand and under controlled driving conditions.

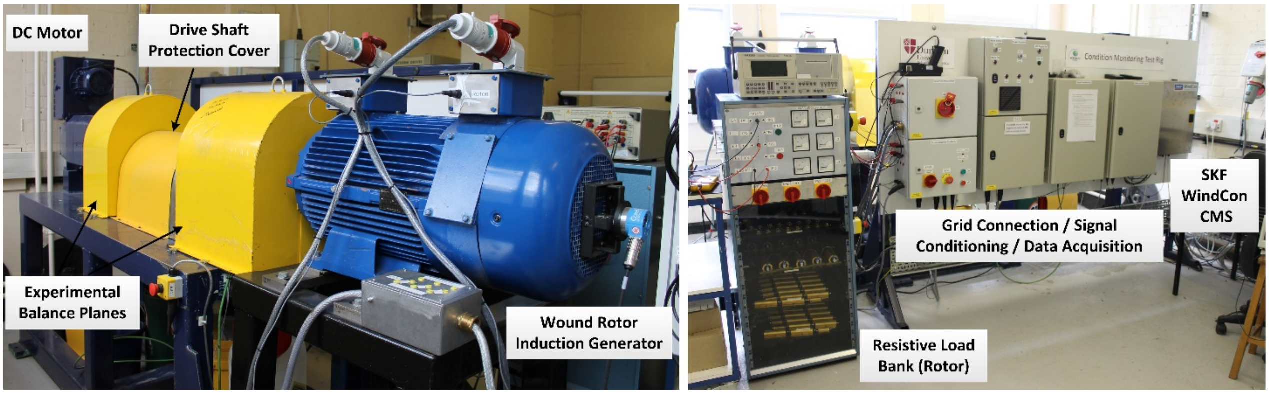

FIGURE 2 Wind turbine condition monitoring test rig: main components, instrumentation and control systems [34].

Rotor electrical asymmetry was simulated on the test rig WRIG by using a resistive load bank externally connected to the rotor circuit via the machine slip-rings to vary the resistance into one rotor phase winding circuit. For experimental purposes, to represent the development of rotor electrical faults on an induction generator, such as brush-gear or slip-ring wear, two seeded-fault levels were implemented on the test rig by successively adding two additional external resistances of 0.3Ω and 0.6Ω, respectively, to phase 1 of the rotor circuit through the external load bank. The corresponding levels of rotor electrical asymmetry, given as a percentage of the rotor balanced phase resistance, were 21% and 43%, respectively. These values compare very favourably with other studies [17,21].

Data was collected at both steady-state speeds, ranging from 1520 rpm to 1600 rpm, and at wind-like variable speeds. In each constant speed test the rig was driven for 300 seconds, while in each variable speed test it was driven for 450 seconds to allow for sufficient data acquisition. Variable speed machine testing was performed according to speed profiles derived from a 2 MW variable speed WT model. This model, developed by the University of Strathclyde, as part of the SUPERGEN Wind Energy Technologies Consortium, incorporates the properties of natural wind and the mechanical behaviour of a 2 MW variable speed WT operating under closed-loop conditions [33].

A variety of wind speeds and turbulence intensities, defined as the measure of the overall level of turbulence [35], were applied to the model. The driving conditions were then scaled to the test rig based on the generator speed data from the model as described in detail in [33]. The use of the 2 MW variable speed WT driving model has allowed the simulation of the different dynamic speed behaviors that a full-size WT 4-pole DFIG exhibits both below and above rated wind speed. The scaled generator variable speed signals used for testing, shown in Fig. 3, are:

1. 7.5 m/s mean, 6% turbulence intensity, representative of a low mean wind speed with low turbulence, with the WT operating at or below rated wind speed under generator speed control (hereafter denoted as '7.5m6t'); and

2. 15 m/s mean, 20% turbulence intensity, representative of a high mean wind speed with high turbulence, with the WT operating above rated wind speed under blade pitch control (hereafter denoted as '15m20t'). During the experiments, the signal acquisition of the stator line currents has been performed using a NI 6015 data acquisition pad at a rate of 5 kHz. The pad is in turn connected, via shielded USB connection, to the NI LabVIEW environment which also operates as control environment of the rig. Only one line current signal is presented and analysed here, as is usually the case for MCSA [33].

Three main sets of experimental data were curated and processed in this work that encompass a set of constant speeds spread across the experimental range and also includes variable-speed data. Table 1 shows the details of each experimental dataset. `TrainSet` is used to train FLD, `DevSet` is used to determine reasonable feature extraction parameters using the trained FLD weight vector, and `EvalSet` is used to test the final fault detection system. Note that `EvalSet` is never used during training or "development" phase (during which the system parameters are tuned); the idea is that at least one dataset should be held out to test the generalisability of the proposed detection system (i.e., how does the detection system perform on never-before-seen data). Also of note is that during training, only the 'healthy' and '21% rotor asymmetry' data is used. This is to test how well the proposed fault detector can distinguish between different levels of fault (e.g., '43% rotor asymmetry') even when the different fault levels are not present in the training data.

3 | RESULTS AND DISCUSSION

A single line current stator signal, captured using appropriate measurement hardware on the 30 kW test rig, has been used in the study of the proposed approach to WRIG fault detection. With an expected range of speeds between 1520-1600 rpm, each bandpass filter was designed to

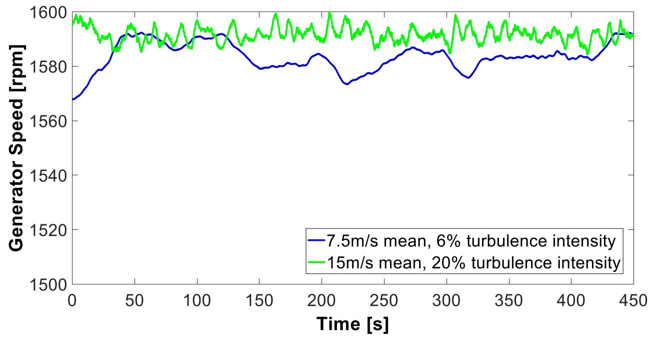

FIGURE 3 Wind turbine condition monitoring test rig variable speed test conditions [34].

TABLE 1 Speed and fault level details for the three curated datasets.

Dataset	Speed (rpm)	Fault Level
`TrainSet`	1520	none(healthy) 21% rotor asymmetry
`DevSet`	1525 1540 1553 1585 1600 variable (7.5m6t)	none (healthy) 21% rotor asymmetry 43% rotor asymmetry
`EvalSet`	1530 1555 1565 1590 variable (15m20t)	

start at each supply frequency harmonic + 1 Hz (i.e., for this set of experimental data, $f_{shift} = 1$ Hz) and have an f_{range} of 7 Hz, to capture the upper sideband. The number of bandpass filters used was initially (arbitrarily) selected to be 10 (i.e., one filter is placed at the upper sideband of the 1st through 10th supply frequency harmonics), along with a time window of $N_w = 10$s.

After extracting the proposed set of features and training the classifier, the training data (i.e., `TrainSet`) was projected to determine an appropriate threshold for classifying 'healthy' and 'faulty', which was selected as the halfway point between the means of each projected class. Numerical measures of the system performance were taken to be the system accuracy (i.e., the percentage of correctly identified samples) and the false positive rate (FPR) (i.e., the false 'alarm' rate), which is computed as the number of 'healthy' samples incorrectly categorized as 'faulty' over the total number of samples that were determined to be 'faulty'. The FPR is reported in addition to the system accuracy, as it is an important measure in health monitoring, since declaring a fault when the system is healthy would likely result in unnecessary expenditure of time and money to investigate a non-issue, and the FPR should be extremely low. The resulting classifications for the `DevSet` (categorizing both '21%' and '43%' as faulty) are shown in Table 2 for the initially selected feature extraction parameters.

TABLE 2 `DevSet` accuracy and FPR for the initial set of feature extraction parameters.

Feature Extraction		Accuracy	False Positive Rate (FPR)
Parameter	Value		
Time window	10s	98.8%	1.2%
# filters	10		
Freq. range	7 Hz		

The initial system accuracy and the FPR show the efficacy of the proposed solution in detecting faults in the stator current spectra as the resulting accuracy is quite high with a low false positive rate. However, it may be possible to achieve better system performance by 'tuning' the feature extraction parameters described in Section 2.1. Tables 3–5 show the system performance results for varying the length of the time window, the number of bandpass filters, and the frequency range of the bandpass filters, respectively.

TABLE 3 `DevSet` accuracy and FPR when varying the length of the time window.

Feature Extraction		Accuracy	False Positive Rate
Parameter	Value		(FPR)
Time window	1 s	76.6%	24.6%
	3 s	75.3%	5.9%
	4 s	83.2%	5.1%
	5 s	98.8%	1.5%
	7 s	98.8%	1.1%
	10 s	98.8%	1.2%

TABLE 4 `DevSet` accuracy and FPR when varying the number of bandpass filters.

Feature Extraction		Accuracy	False Positive Rate
Parameter	Value		(FPR)
# filters	1	81.6%	21.7%
	2	84.7%	18.7%
	5	96.2%	5.4%
	7	96.6%	2.0%
	10	98.8%	1.1%
	15	98.8%	1.1%
	20	99.4%	0.9%
	25	85.8%	1.4%

TABLE 5 `DevSet` accuracy and FPR when varying the frequency range of the bandpass filters.

Feature Extraction		Accuracy	False Positive Rate
Parameter	Value		(FPR)
Freq. range	5 Hz	69.2%	7.3%
	7 Hz	99.4%	0.9%
	9 Hz	89.8%	8.0%

Note that in Table 5 the lower cutoff frequency (i.e., the supply harmonic + 1 Hz) is the same for all frequency ranges; it is only the higher cutoff frequency that is varied. For the other parameters:

- in Table 3, 10 bandpass filters were used with a frequency range of 7 Hz each (i.e., initially selected feature extraction parameters);
- in Table 4, a 7 s time window was used, as this yielded a 'best' result shown in Table 3, and each filter had a frequency range of 7 Hz;
- in Table 5, a 7s time window was used with 20 bandpass filters, as this yielded a 'best' result shown in Table 4.

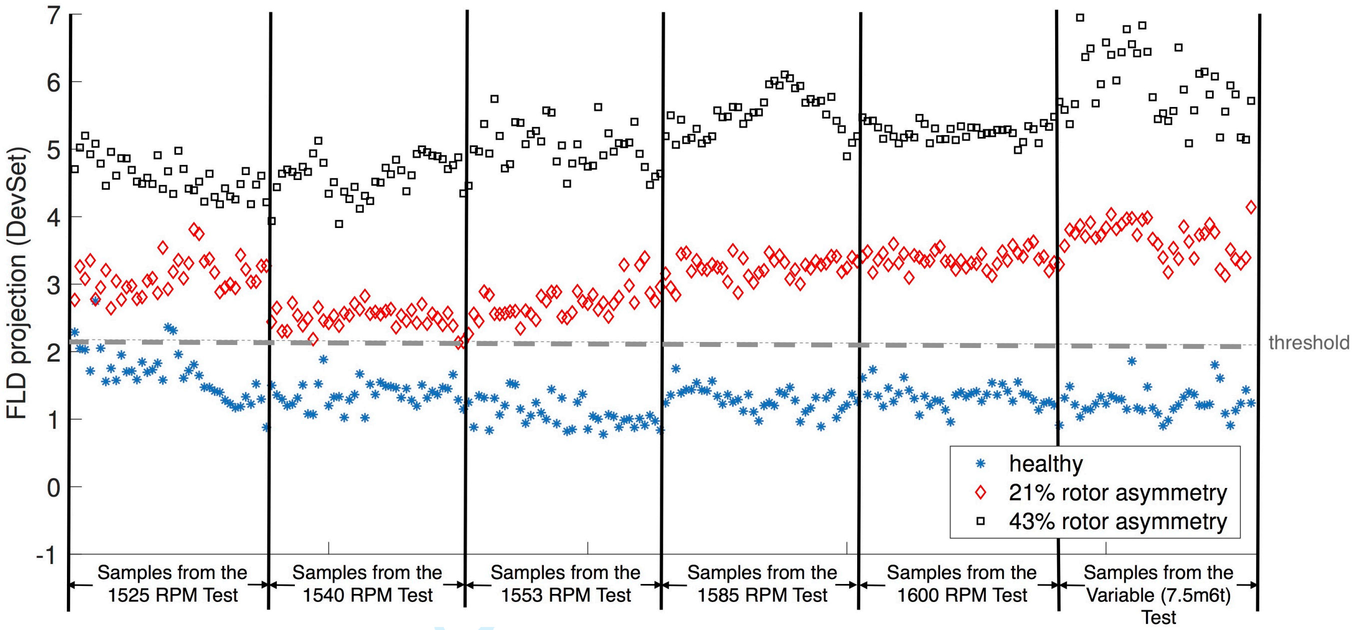

FIGURE 4 FLD projection of the average spectral magnitudes of the stator current spectra computed in each bandpass filter for the `DevSet` containing speeds ranging from 1525-1600 rpm, and a variable-speed dataset.

The resulting FLD projections for the `DevSet` are shown in Fig. 4. These features were extracted using a 7 second time window and 20 bandpass filters with a frequency range of 7 Hz. A clear delineation between the healthy and faulty data can be seen. Of interest is also the faulty data with 43% rotor asymmetry can be seen at even a different level (i.e., range of projected values) compared with the '21% rotor asymmetry' data even though the '43%' data was not included during training. This result further highlights the potential of the proposed approach to be generalised to detect alternate fault levels beyond those present during training.

Lastly, the proposed approach was tested on the remaining held-out `EvalSet` without any further system tuning. The resulting system performance is shown in Table 6, and the FLD projections for the `EvalSet` are shown in Fig. 5. Again, these features were extracted using a 7 second time window and 20 bandpass filters with a frequency range of 7 Hz.

TABLE 6 `EvalSet` accuracy and FPR for the final selected set of feature extraction parameters.

Feature Extraction Parameter	Value	Accuracy	False Positive Rate (FPR)
Time window	7s		
# filters	20	97.4%	3.6%
Freq. range	7 Hz		

The accuracy still remains relatively high, although the FPR has a significant increase. It can be seen in Fig. 5 that one particular set of test data included in the `EvalSet` (namely the data on the left-hand side of Fig. 5, which was collected at 1530 rpm) does not exhibit as much of a separation between classes as can be seen in the rest of the `EvalSet` data. It is possible that the data collected at this particular speed contains more noise than the others; future investigations may include noise reduction techniques and further analyses on potential overfitting.

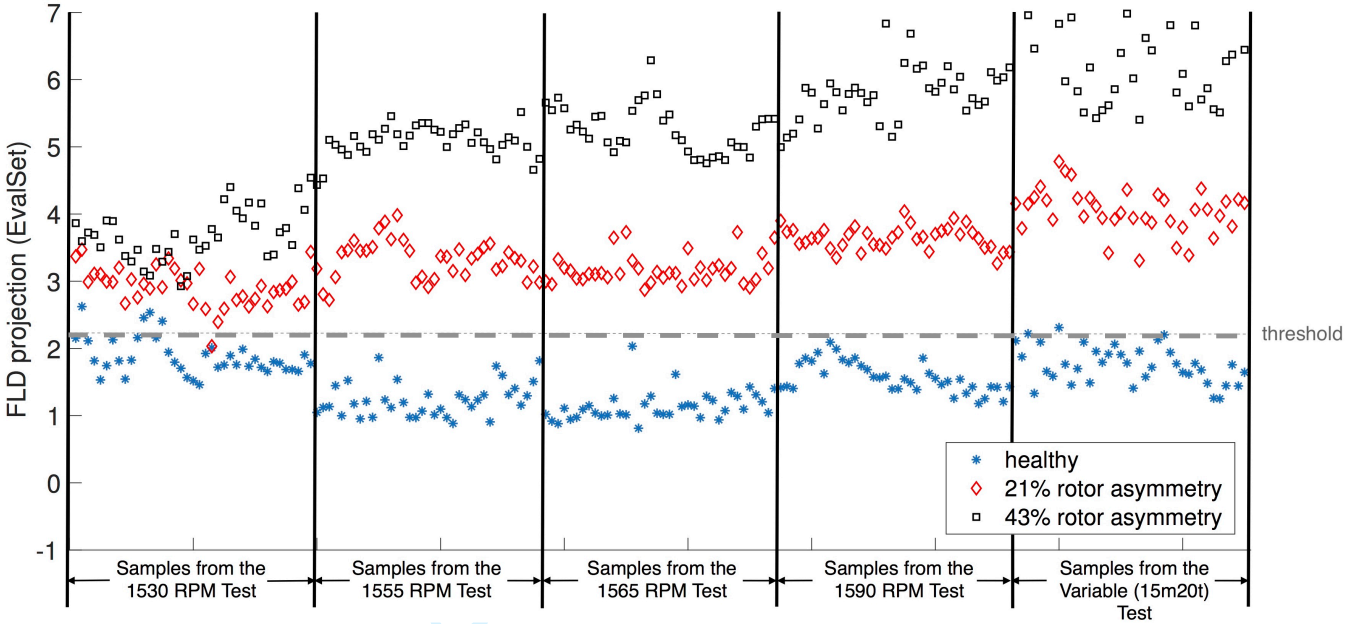

FIGURE 5 FLD projection of the average spectral magnitudes of the stator current spectra computed in each bandpass filter for the `EvalSet` containing speeds ranging from 1530-1590 rpm, and a variable-speed dataset.

4 | CONCLUSIONS

This paper proposes an automated WT induction generator fault detector that does not require frequency tracking or identification. The proposed methodology has been validated experimentally on a WT drive train test rig with two rotor fault levels under both constant and variable speed driving conditions, representative of WT generator field operation. The following specific conclusions arise:

- A set of bandpass filters is proposed to capture the stator current fault-related spectral information and to train a classifier, making the approach independent on the machine instantaneous speed.
- Unlike previous studies based on the analysis of single speed-dependent fault-related frequencies in stator current, this work is more robust as it draws information from multiple frequency components into a single fault indicator.
- The proposed approach can provide clear differentiation between healthy and faulty conditions, under both constant and variable speed operating conditions, even though the classifier has been only trained on a single fault level and a single constant speed condition.
- Experimental results have initially shown clear discrimination between fault levels, with an almost linear response, even at variable speed. This suggests the ability of the proposed approach to provide early fault detection of developing damage, crucial for effective maintenance optimization.
- The developed method can be easily implemented into WT CMSs for efficient real-time analysis of data captured without requiring expert knowledge.

Future work in this area includes further investigations into the robustness of the proposed approach, including the impact of different training data (e.g., training under variable-speed conditions) on the ability to differentiate between different fault levels and healthy data. A comparative study using other classification approaches may also be undertaken as these different training conditions are explored.

ACKNOWLEDGEMENTS

This work was supported by the EPSRC SUPERGEN Wind Hub [grant number EP/L014106/1].

References

1. Qiao W, Lu D. A survey on wind turbine condition monitoring and fault diagnosis - Part I: components and subsystems. *IEEE Trans. Ind. Electron.* 2015; 62 (10): 6536–6545.

2. Crabtree CJ, Zappalá D, Hogg SI. Wind energy: UK experiences and offshore operational challenges. *Proc. Inst. Mech. Eng. A*. 2015; 229 (7):727–746.

3. Tavner, PJ. *Offshore wind turbines: reliability, availability and maintenance*. 1st ed.: IET Press; 2012.

4. Carroll J, McDonald A, McMillan D. Failure rate, repair time and unscheduled O&M cost analysis of offshore wind turbines. *Wind Energy*. 2016;19(6):1107Đ1119.

5. Tavner, PJ, Faulstich S, Hahn B, *et al*. Reliability & availability of wind turbine electrical & electronic components. *EPE Journal*. 2010; 20(4):45–50.

6. Wilkinson M, Harman K, Hendriks B, *et al*. Measuring wind turbine reliability Đ results of the Reliawind project. *Proc. scientific track of the European Wind Energy Association conference*, Brussel, Belgium, March 2011, pp. 1–8.

7. Artigao E, Martín-Martínez S, Honrubia-Escribano A, *et al*. Wind turbine reliability: a comprehensive review towards effective condition monitoring development. *Appl. Energy*. 2018; 228:1569–1583.

8. Carroll J, McDonald A, McMillian D. Reliability comparison of wind turbines with DFIG and PMG drive trains. *IEEE Trans. Energy Convers.* 2015; 30(2):663–670.

9. Gritli Y, Rossi C, Casadei D, *et al*. A diagnostic space vector-based index for rotor electrical fault detection in wound-rotor induction machines under speed transient. *IEEE Trans. Ind. Electron.* 2017; 64(5):3892–3902.

10. Benbouzid MEH. A review of induction motors signature analysis as a medium for faults detection. *IEEE Trans. Ind. Electron.* 2000; 47(5):984–993.

11. Tavner PJ, Ran L, Penman J, *et al*. Condition monitoring of rotating electrical machines. 2nd ed. UK: IET Press; 2008.

12. Riera-Guasp M, Antonino-Daviu JA, Capolino GA. Advances in electrical machine, power electronic, and drive condition monitoring and fault detection: state of the art. *IEEE Trans. Ind. Electron.* 2015; 62(3):1746–1759.

13. Henao H, Capolino GA, Fernandez-Cabanas M, *et al*. Trends in fault diagnosis for electrical machines: a review of diagnostic techniques. *IEEE Ind. Electron. Mag.* 2014; 8(2):31–42.

14. Williamson S, Djurovic S. Origins of stator current spectra in DFIGs with winding faults and excitation asymmetries, *Proc. IEEE International Electric Machines and Drives Conference*, Miami, USA, May 2009, pp. 563–570.

15. Gritli Y, Stefani A, Chatti A, *et al*. The combined use of the instantaneous fault frequency evolution and frequency sliding for advanced rotor fault diagnosis in DFIM under time-varying condition. *Proc. 35th Annual Conference of IEEE Industrial Electronics*, Porto, Portugal, November 2009, pp. 3471–3476.

16. Djurovic S, Williamson S, Renfrew A. Dynamic model for doubly-fed induction machines with unbalanced excitation, both with and without winding faults. *IET Electr. Power Appl.* 2009;3(3):171–177.

17. Djurovic S, Crabtree CJ, Tavner PJ, *et al*. Condition monitoring of wind turbine induction generators with rotor electrical asymmetry. *IET Renewable Power Generation*. 2012; 6(4):207–216.

18. Pilloni A, Pisano A, Riera-Guasp M, *et al*. Fault detection in induction motors. In: Giri F, ed. *AC electric motors control: advanced design techniques and applications*. Wiley Press, 2013:275–309.

19. Vedreño-Santos F, Riera-Guasp M, Henao H, *et al*. Diagnosis of rotor and stator asymmetries in wound-rotor induction machines under nonstationary operation through the instantaneous frequency. *IEEE Trans. Ind. Electron.* 2014;61(9):4247–4259.

20. Ibrahim R, Watson S, Djurovic S, *et al*. An effective approach for rotor electrical asymmetry detection in wind turbine DFIGs. *IEEE Trans. Ind. Electron.* 2018; 65(11):8872–8881.

21. Stefani A, Yazidi A, Rossi C, *et al*. Doubly fed induction machines diagnosis based on signature analysis of rotor modulating signals. *IEEE Trans. Ind. Appl.* 2008;44(6):1711–1721.

22. Shah D, Nandi S, Neti P. Stator-Interturn-Fault detection of doubly fed induction generators using rotor-current and search-coil-voltage signature analysis. *IEEE Trans. Ind. Appl.* 2009; 45(5):1831–1842.

23. Zappalá D, Sarma N, Djurovic S, *et al*. Electrical & mechanical diagnostic indicators of wind turbine induction generator rotor faults. *Renewable Energy*. 2019; 131:14–24.

24. Yang W, Tavner PJ, Crabtree CJ, Feng Y, Qiu Y. Wind turbine condition monitoring: technical and commercial challenges. *Wind Energy*. 2014;17: 673-693.

25. Crabtree CJ, Zappalá D, Tavner PJ. Survey of commercially available condition monitoring systems for wind turbines. *Durham University and the SUPERGEN Wind Energy Technologies Consortium*, 2014, pp. 1–22.

26. Gritli Y, Zarri L, Rossi C, *et al*. Advanced diagnosis of electrical faults in wound-rotor induction machines. *IEEE Trans. Ind. Electron.* 2013; 60(9):4012–4024.

27. Vedreño-Santos F, Riera-Guasp M, Henao H, *et al*. Diagnosis of rotor and stator asymmetries in wound-rotor induction machines under nonstationary operation through the instantaneous frequency. *IEEE Trans. Ind. Electron.* 2014; 61(9):4947–4959.

28. Sapena-Bano A, Burriel-Valencia J, Pineda-Sanchez M, *et al*. The harmonic order tracking analysis method for the fault diagnosis in induction motors under time-varying conditions, *IEEE Trans. Energy Convers.* 2017; 32(1):244–256.

29. Fernandez-Temprano M, Gardel-Sotomayor PE, Duque-Perezet O, *et al*. Broken bar condition monitoring of an induction motor under different supplies using a linear discriminant analysis. *Proc. 9th IEEE International Symposium on Diagnostics for Electric Machines, Power Electronics and Drives (SDEMPED)*, Valencia, Spain, 2013, pp. 162–168.

30. Frosini L, Zanazzo S, Beccarisi F. Linear discriminant analysis for an automatic detection of stator faults in induction motor drives. *Proc. 11th IEEE International Symposium on Diagnostics for Electric Machines, Power Electronics and Drives (SDEMPED)*, Tinos, Greece, 2017, pp. 503–509.

31. Haroun S, Nait Seghir A, Touati S. Multiple features extraction and selection for detection and classification of stator winding faults. *IET Electric Power Applications*. 2018; 12(3):339–346.

32. Bishop CM. Pattern recognition and machine learning. Springer-Verlag Berlin, Heidelbergl; 2006.

33. Crabtree, CJ. Condition monitoring techniques for wind turbine. PhD thesis, Durham University, 2011.

34. Zappalá D. Advanced algorithms for automatic wind turbine condition monitoring. PhD thesis, Durham University, 2015.

35. Burton T, Sharpe D, Jenkins N, *et al*. Wind energy handbook. 2nd ed.: John Wiley & Sons; 2011.

Validation of a non-contact technique for torque measurements in wind turbines using an enhanced transient FSV approach

G. Zhang [a], D. Zappalá [b,*], C. Crabtree [b], C. Donaghy-Spargo [b], S. Hogg [b], A. Duffy [c]

[a] Harbin Institute of Technology, Harbin, China
[b] Department of Engineering, Durham University, South Road, Durham, UK
[c] School of Engineering and Technology, De Montfort University, Leicester, UK
[*] donatella.zappala@durham.ac.uk

Abstract:

In-service turbine monitoring is essential for maximizing the wind energy contribution to the global energy budget. Measurement of turbine shaft torque under transient wind conditions is fundamental to develop reliable condition monitoring techniques. Contact based measurements bring their own disadvantages and non-contactless measurements have many potential advantages. However, their performance needs to be validated against standard methods. This paper focuses on enhanced transient FSV (Feature Selective Validation) techniques developed to undertake this analysis with an emphasis on transient data processing. The FSV method is a reliability function-like heuristic, initially developed for validation of electromagnetic compatibility simulations. Open questions have existed for some time as to how transients should be dealt with. This paper (a) overcomes the limitations of previous approaches for step-function transient comparison and (b) presents analytical methods where the comparison is dominated by the transient function itself and not the length of the pre- and post-transient periods.

Keywords: Torque measurement, Wind Turbine, Transient analysis, Feature Selective Validation.

Declarations of interest: none

1. Introduction

As large-scale wind farms move further offshore, cost effective condition monitoring (CM) plays a crucial role in minimizing wind turbine (WT) operations and maintenance costs for a competitive development of wind energy [1,2]. WT component faults have usually distinguishable torque signatures and therefore can be diagnosed by using torque signals [3]. As the loading on the WT drive train components is highly variable, the study of transient conditions is fundamental to the development of reliable CM techniques. The potential benefits of adopting CM techniques based on WT mechanical torque measurement have been shown for the detection of generator electrical faults [4,5], drive train mass imbalance [6], gearbox failures [7], blade mass imbalance and aerodynamic asymmetry [8,9]. However, torque measurement on such large, inaccessible machines is impractical and economically infeasible, mainly due to limitations of the intrusive specialized equipment currently available. A contactless measurement system for direct, low-cost real-time measurement of WT drive train loads and speed has been presented in [10]. Unlike conventional in-line torque transducers [11-13], the proposed contactless measurement system does not require costly intrusive sensors and it can be designed to be fitted or retrofitted on any shaft diameter and material without mechanical interference. Its performance and accuracy have been experimentally demonstrated under dynamic, transient loads through conventional visual comparison and signal root mean square error (RMSE) calculations against measurements from an intrusive reference state-of-the art transducer [14]. This paper further validates the proposed contactless technique through an objective, quantified, comparison of the transient load and speed measurements based on an enhanced transient FSV (Feature Selective Validation) approach.

It is known that visual evaluation is the most subtle and widely used method of data comparison and validation [15,16]. Meanwhile, visual assessment is prone to many types of physical and psychological influences. For these reasons, the FSV method was established to support the validation of electromagnetic models by quantifying the agreement between the reference and the numerical results. Where the aim was to mirror, as far as possible, the opinion of a large group of expert users as a whole. This method has been incorporated as the central technique of IEEE STD 1597.1 and its associated Recommended Practice Guide, 1597.2 [17,18]. The details of the FSV method can be found in [19,20].

The FSV method was originally designed using a reliability function approach to overcome some of the key problems associated with validation of computational electromagnetic simulations for EMC (Electromagnetic Compatibility) problems. Key amongst those problems is that the complexity of the systems being analysed resulted in line graph data of, for example, the level of coupling versus frequency, which might have a serpentine envelope but many resonant-like features. The challenge was then further compounded by the challenges of the fact that simplifying assumptions are often required in the design of the simulations coupled with the fact that many of the experts would interpret the data slightly differently based on their backgrounds and expectations (for example, someone from an EMC measurement background may have a different interpretation of what 'good agreement' might be compared to someone from a radiofrequency design background). As a result, the FSV method provides a 'probability' density function that closely resembles that derived from a group of experts. From this, a mean or mode can be obtained to summarize the view of experts [16]. The original formulation was based on the comparison of x-y data with no meaning derived from the units of either axis. Data in the time domain was equally comparable with the standard method. A significant short-coming of the original FSV formulation was that the length of time included in the pre- and post-transient phases could inadvertently (or purposely) dominate the transient itself. A further shortcoming was identifying the start and end of the transient (for the purposes of comparison).

Meanwhile, the validation of transient data has become an increasingly interesting issue from the perspectives of FSV being used outside its 'home' domain of EMC, such as in Signal Integrity or, as is the case in this paper, health monitoring of equipment. A transient FSV algorithm was developed which looked at impulsive-like transients but was insufficient to adequately capture the effects of switching or step-like transients. However, for the emulated torque data of wind turbines, the comparison between step-function transients is essential and a new challenge for the FSV method. This paper develops the generalized FSV method to include an approach that satisfies the step-function requirements to allow transient data to be compared using standard FSV method.

The structure of this paper is as follows. In Section 2, the basic algorithms of FSV and the problems of transient FSV are reviewed. The generalized transient FSV approach is presented and validated in section 3. The proposed method is applied to emulated wind turbine torque data in Section 4.

2. Overview of the FSV Technique

2.1. Standard FSV method

The FSV method is based on decomposing the original comparison data, providing component-based comparison and recombining those measures into an overall quality metric. Of course, the application could dictate that only a sub-set of the data may be relevant but, in general, the complete (global) comparison is used.

With reference to Figure 1, which provides a graphical demonstration of the 'data flow'. The original data for comparison (Fig. 1(a)) is not required to conform to a particular set of axes: the method is domain-agnostic and so the data is shown with no x-axis or y-axis labelled to emphasize this. Three figures of merit are obtained to demonstrate data agreement from different perspectives in the FSV method. The Amplitude Difference Measure (ADM), Figure 1(b) shows the 'trend' difference, while the Feature Difference Measure (FDM), Figure 1(c), denotes the differences of details. Then the ADM and FDM are combined to give the Global Difference Measure (GDM), Figure 1(d). Further, in order to provide a direct link with visual assessment, the point-by-point FSV outputs are binned into a confidence histogram (usually labelled ADMc, FDMc and GDMc), Figure 1(e) shows the GDMc. This data can be used as a proxy for the qualitative assessment of a group of experts, Figure 1(f) compares the FSV output in the original bins with that from 50 engineers (the original data was EMC based). The data can also be represented as a density function, Figure 1(g), which can allow a statistical analysis of the comparison data [21] or further meta-comparisons, such as in Figure 1(d), where the cumulative density function is being used to verify with the K-S test the hypothesis that the visual and FSV data are from the same distribution (for this data D_{crit}, the value at which the difference in amplitude is such as to reject the null hypothesis, for 90% confidence is 0.17, so the null hypothesis can be accepted – a common trend when comparing FSV data and visual assessment).

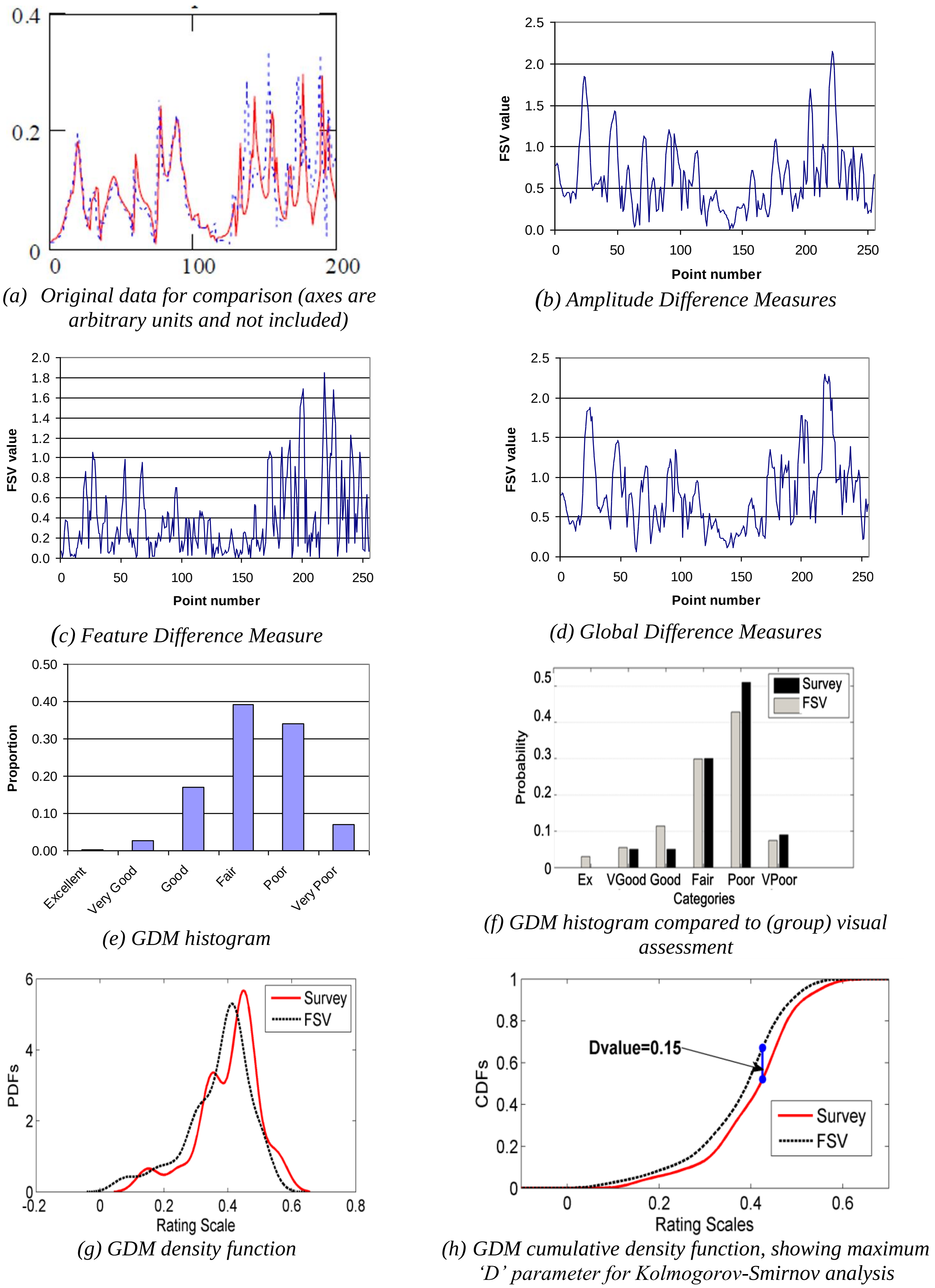

(a) Original data for comparison (axes are arbitrary units and not included)

(b) Amplitude Difference Measures

(c) Feature Difference Measure

(d) Global Difference Measures

(e) GDM histogram

(f) GDM histogram compared to (group) visual assessment

(g) GDM density function

(h) GDM cumulative density function, showing maximum 'D' parameter for Kolmogorov-Smirnov analysis

Figure 1. Summary of FSV.

FSV is a reliability function-like heuristic method, is heavily influenced by the approaches used by Zanazzi and Jona, van Hove, and Pendy [22]. The standard FSV procedures are as follows.

1) Data segmentation

The working datasets under comparison are first Fourier transformed. Then, the filter shown in Figure 2 is applied to the transformed working datasets to obtain the DC, Low-, and High-frequency components. The 'break-point' location, N_{bp}, is decided by

$$\sum_{i=N_{DC}+1}^{N_{40\%}} TDWS(i) \leq 0.4S \tag{1}$$

$$N_{bp} = N_{40\%} + 5 \tag{2}$$

where $TDWS(i)$ is the value of the i^{th} independent variable within the Fourier transformed data set; S is the sum of the values of the independent variable; N is the sum of the values of the independent variable; $N_{40\%}$ is the element containing the '40% location'. The 'break-point' location N_{bp} is five data points higher than the '40% location'. N_{DC} is set to 4. A "breakpoint" at five data points above $N_{40\%}$ allows a comfortable transition window between the low and the high results. The windowed frequency components are then inverse transformed to obtain DC, Low and High components, labeled as *DC*, *Lo* and *Hi*, respectively.

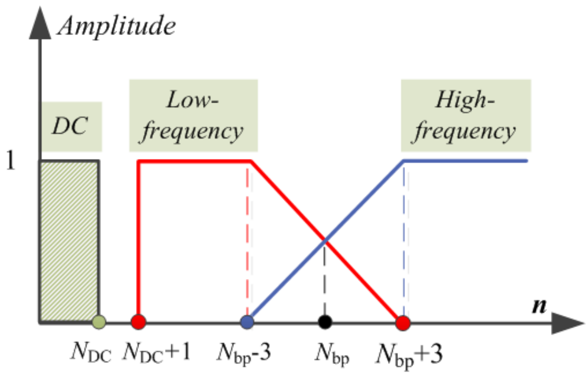

Figure 2. Filter used in the original FSV method [15].

2) The calculation of ADM

The ADM is calculated to show the difference between DC and low-frequency information in both of the datasets under comparison.

$$ADM(n) = \frac{\left||Lo_1(n)| - |Lo_2(n)|\right|}{\sum_{i=1}^{N}(|Lo_1(i)| + |Lo_2(i)|)} + ODM \tag{3a}$$

where

$$ODM(n) = \left|\frac{\chi}{\delta}\right| exp\left\{\left|\frac{\chi}{\delta}\right|\right\} \tag{4b}$$

$$\chi = (|DC_1(n)| - |DC_2(n)|) \tag{5c}$$

$$\delta = \frac{1}{N}\sum_{i=1}^{N}(|DC_1(i)| + |DC_2(i)|) \tag{6d}$$

where N is the sum of the values of the independent variable; n is the n^{th} data point. The FSV measures are generally based on a 'difference over sum' approach, except the ODM: the use of the exponential reflects the non-linear interpretation of offsets in data, where a small offset is frequently ignored but a large offset is regarded as significant, even if the original data is highly similar in shape.

3) The calculation of FDM

The scaling factors 2, 6, and 7.2 in equations (4), (5) and (6) are used to balance the internal sub-measures of the FDM, emphasizing either low level trends (broad peaks/troughs) or higher level features (narrow peaks/troughs).

$$FDM_1(n) = \frac{|Lo_1'(n)| - |Lo_2'(n)|}{\frac{2}{N}\sum_{i=1}^{N}(|Lo_1'(i)| + |Lo_2'(i)|)} \tag{4}$$

$$FDM_2(n) = \frac{|Hi_1'(n)| - |Hi_2'(n)|}{\frac{6}{N}\sum_{i=1}^{N}(|Hi_1'(i)| + |Hi_2'(i)|)} \tag{5}$$

$$FDM_3(n) = \frac{|Hi_1''(n)| - |Hi_2''(n)|}{\frac{7.2}{N}\sum_{i=1}^{N}(|Hi_1''(i)| + |Hi_2''(i)|)} \tag{6}$$

$$FDM(n) = 2(|FDM_1(n) + FDM_2(n) + FDM_3(n)| \tag{7}$$

where $Lo'_{\{1,2\}}$ and $Hi'_{\{1,2\}}$ are the first derivatives of the $Lo_{\{1,2\}}$ and $Hi_{\{1,2\}}$ components, respectively; $Hi''_{\{1,2\}}$ is the second derivative of the $Hi_{\{1,2\}}$ component. The sub-level difference measures in equations (4), (5), and (6) emphasize independent areas of the compared signals.

4) The Global Difference Measure (GDM) is obtained through combination of the ADM and FDM. The GDM gives an indication of the overall goodness-of-fit of both amplitude and feature differences between compared signals, quantifying the overall assessment of a comparison.

$$GDM(n) = \sqrt{ADM(n)^2 + FDM(n)^2} \tag{8}$$

5) The original development of FSV looked to bridge the gap between a quantitative assessment and the subjective, qualitative, assessment common in papers, presentations and reports thought the use of a natural language interpretations scale. The FSV interpretation scale is shown in Table 1. In this way, the form of qualitative result, xDMc (where x is A, F or G), becomes a six-category confidence histogram.

Table 1. FSV interpretation scale in [18].

FSV value y (quantitative)	FSV interpretation (qualitative)
$y \leq 0.1$	Excellent
$0.1 < y \leq 0.2$	Very Good
$0.2 < y \leq 0.4$	Good
$0.4 < y \leq 0.8$	Fair
$0.8 < y \leq 1.6$	Poor
$y > 1.6$	Very Poor

To some extent, this approach is being superseded by the use of density functions and distributions, which provide more options for analysis, particularly meta-comparison. However, the interpretation scale is still widely used and it is common to see such interpretations in papers where FSV is used. The qualitative interpretations are not intended to be absolute definitions of quality, they are merely a means to aid human communication.

2.2. Transient FSV method

The comparison of transient data, which may typically be simulation versus experimental data for validation purposes, is made more difficult by the indeterminate nature of the 'pre' and 'post' transient regions, as shown in Figure 3(a). In essence, a comparison could be dominated by the selection of the length of the tails either side of the transient event. This has recently received some attention [23-25] with the identification of weighting regimes to ensure that the transient event dominates any comparison and such a comparison is not skewed by arbitrary choice of duration. Reference [23] also provided some indication of where experienced users of transient data would place those boundaries.

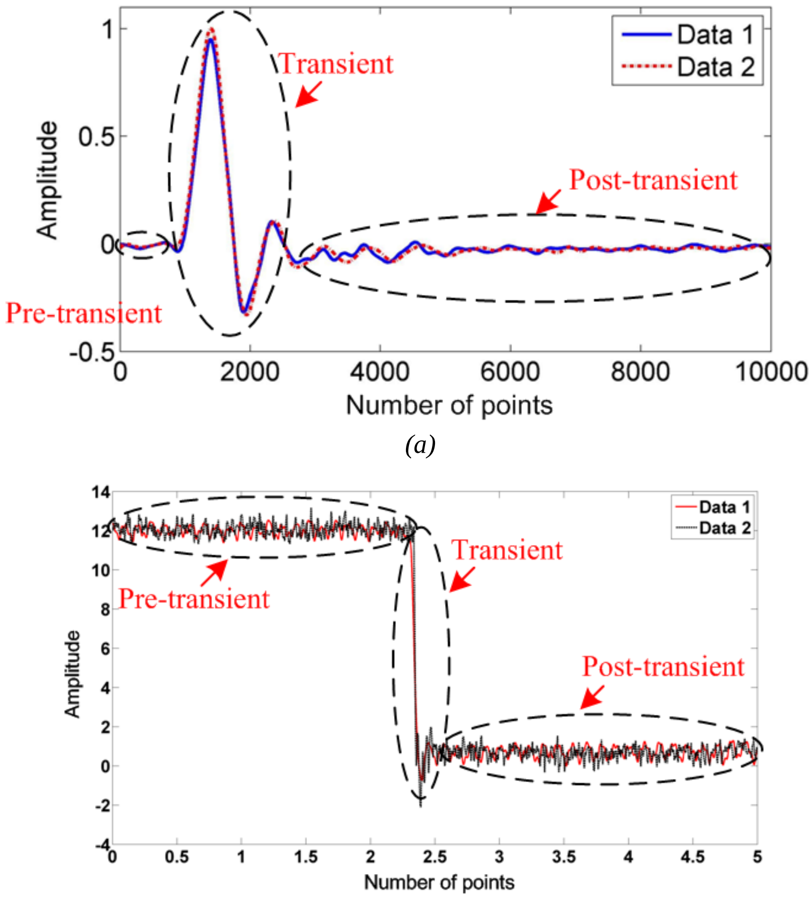

(a)

(b)

Figure 3. Illustration of the regions of transient event.

A segment approach was proposed in [23], algorithms were designed to divide the transient into three regions: pre-transient event, transient event and post-transient event. The FSV is applied in each region separately. Then, each region is weighted. The transient region was originally considered as ranging from the end of the pre-transient up to a point that contains 65% of the signal's energy. The energy is calculated by

$$Energy_{\{1,2\}}(n) = \sum_{i=1}^{n} \left(Data_{\{1,2\}}(i)\right)^2, \quad n = 1,2,3, \ldots \ldots N \tag{9}$$

where $Data_{\{1,2\}}$ is the set of the data to be compared ("1" is the first dataset and "2" the second dataset) and N is the length of $Data_{\{1,2\}}$.

It is clear that this approach is valid for the transient in Figure 3(a), but is invalid for the step transient in Figure 3(b) since the energy will be concentrated in the pre-transient region rather than the transient region (or vice versa). The approach to transients used in Figure 3(a) is based on the energy being concentrated in the transient region, something that does not happen with a step-function type transient.

3. Generalized Transient Data Method

To overcome the problems of transient FSV in applications, such as torque data comparison, a generalized transient FSV approach is required and such an approach is proposed and tested here. This generalized approach aims to compare the transient data using the standard FSV method after pre-processing. Meanwhile, the proposed approach is expected to be applicable to a wide variety of transient types, including those in Figure 3. The key is to develop a pre-processing method that allows a clear identification of the boundaries between the pre-transient/transient and the transient/post-transient regions.

3.1. *Generalized transient FSV method*

***Step 1*:** The boundaries of pre-transient, transient and post-transient regions are identified. To find the boundaries of "step transient signals", as shown in Figure 1, the derivative of datasets under comparison are calculated and the boundaries are determined according to the Cumulative Distribution Function (CDF) of data 1 and data 2.

1. The cumulative distribution is calculated by

$$E(n) = \sum_{i=1}^{n} \left(Data_1{}'(i)^2 + Data_2{}'(i)^2\right), \quad n = 1,2,3, \ldots \ldots N \tag{10}$$

where $Data_{\{1,2\}}{}'$ is the derivative of the data to be compared ("1" is the first dataset and "2" the second dataset). N is the length of $Data_{\{1,2\}}{}'$.

2. Then the least-squares fit of a straight line to the cumulative distribution, $E(n)$, is calculated. $E(n)$ is then de-trended by subtracting the resulting least-squares function from the original data. $E(n)$ is de-trended by

$$E_{detrend}(n) = E(n) - (an + b)\,, \quad n = 1,2,3, \ldots \ldots N \tag{11}$$

where a and b are the coefficients of a straight-line function (an+b) that fits $E(n)$.

3. Subsequently, the positions of the turning point (crest and trough of the de-trended data $E_{detrend}(n)$), N_{bp1} and N_{bp2}, are found and they are chosen as the pre- and post-transient boundaries.

Figure 4 shows the process to identify the breakpoints of a pair of step-transient data and Figure 5 does the same process for normal transient data.

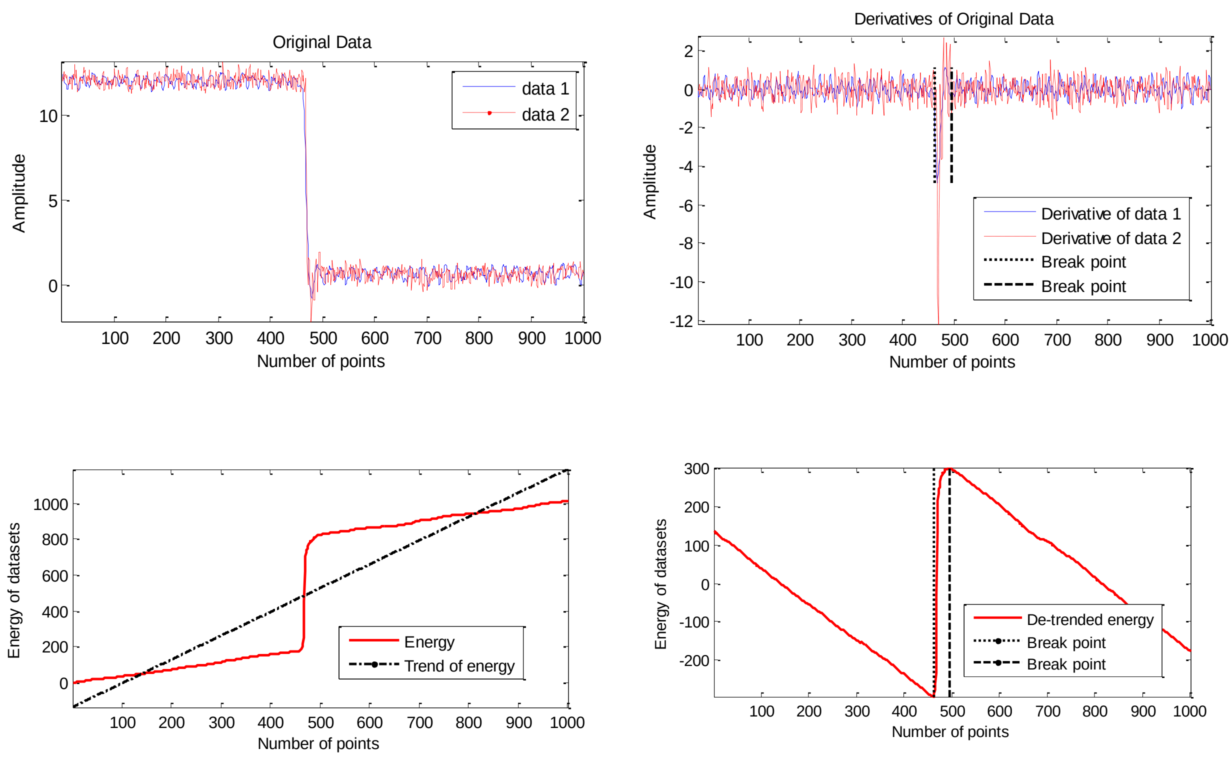

Figure 4. Break-point selection of the step transient data. Note the indication of the trends and break points.

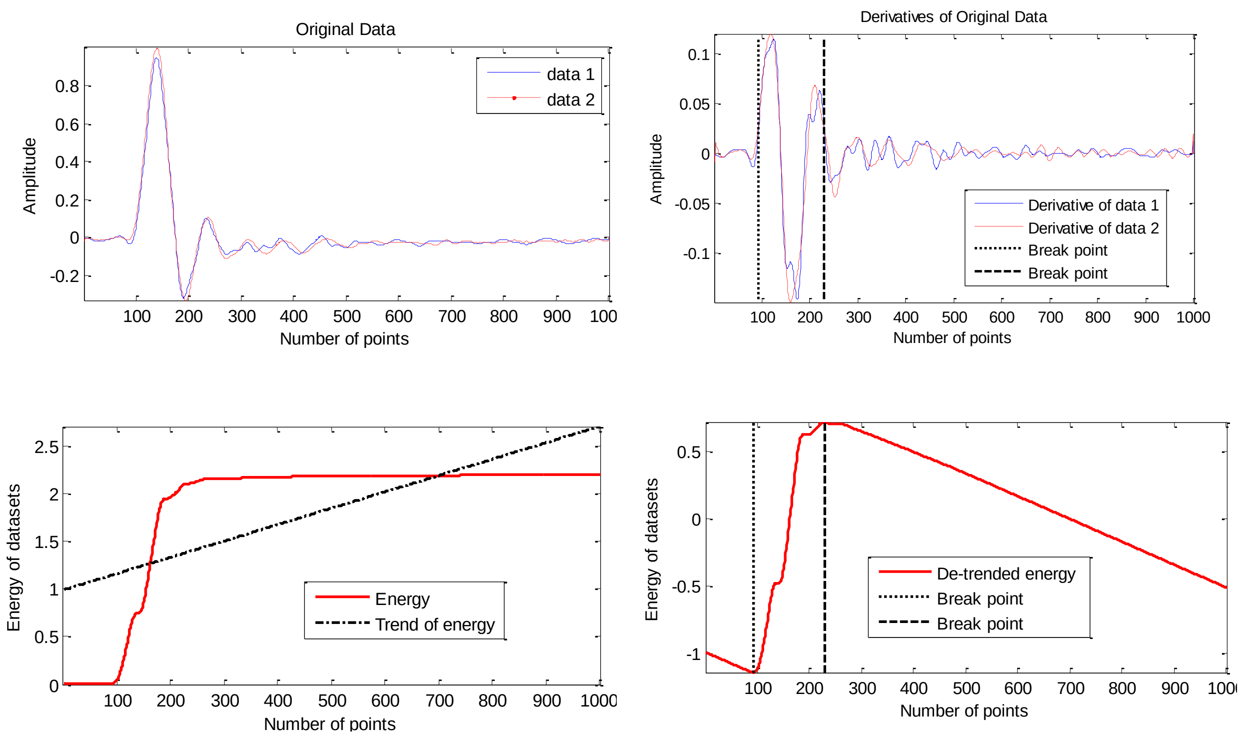

Figure 5. Break-point selection of the normal transient data. Note the indication of the trends and break points.

***Step 2*:** Instead of the weighting approach proposed in [23], a pre-emphasis approach that is based on interpolation of points in the three regions to match the weighting functions is proposed. Effectively the pre-transient, transient and post-transient regions are expanded or contracted to match the influence the regions have on the overall results. The lengths of pre-transient and post-transient regions are proposed to contributing 5% and 20% percent of the overall weighting of the comparison whole length, respectively, as shown in Figure 6.

The values of 5% and 20% are based on the experience of the authors and are values that can be subject to further investigation: the authors would welcome further research and contribution to this from the wider community. The “companded” data sets are then compared using the standard FSV method. The ADM and FDM results are shown in Figure 7, which also shows the re-mapping used to provide the emphasis of the regions just described. Hence, the pre-transient region is compressed (or expanded) to occupy 5% of the data points. In the example of Figure 7, this will be 50 points. The transient region is expanded (or compressed) to occupy 75% of the data points (750 points in this case) and the post-transient region will occupy the remaining 20% of the points.

This approach has the benefit of not requiring separate comparisons that are then ‘stitched’ back together but treats the overall comparison as a single uniform whole which can then be interpolated back to the original point distribution.

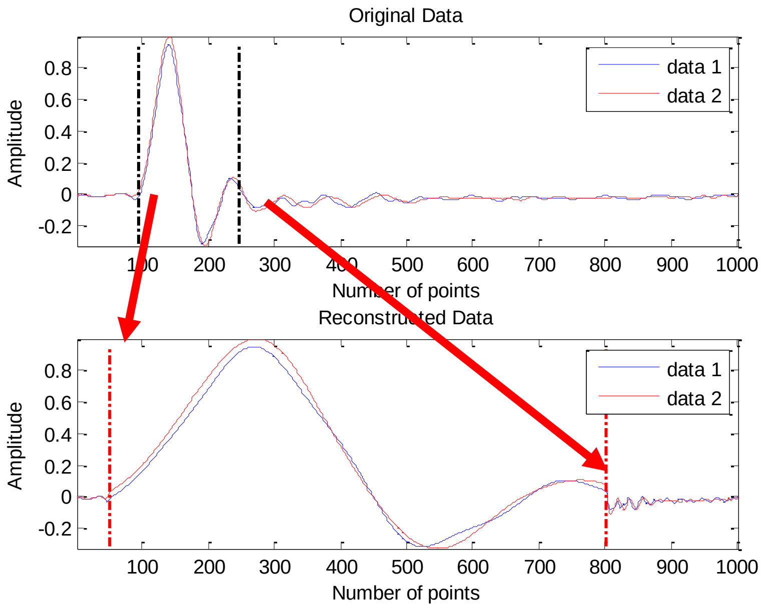

Figure 6. Illustration of the pre-emphasis approach to data based on interpolation of points in the three regions.

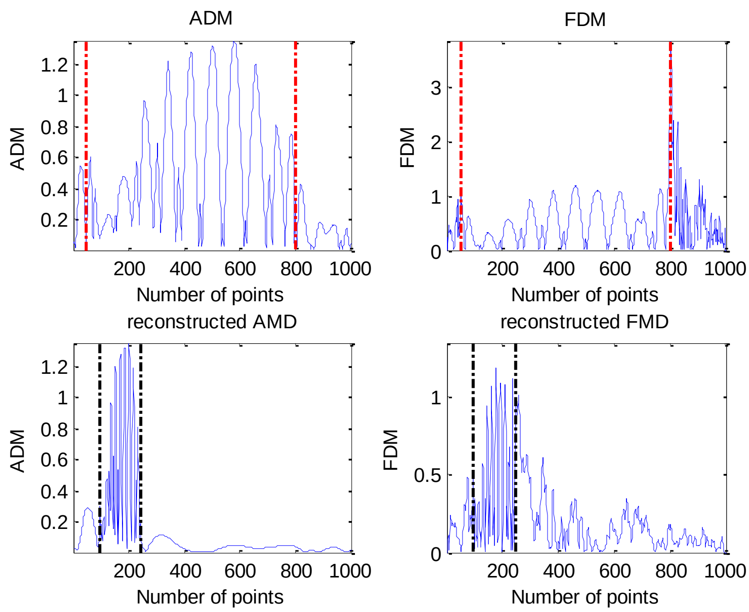

Figure 7. Re-mapping point by point FSV result back to the original data point.

Step 3**:** Re-mapping point by point data back to the original data point distribution using the interpolation in reverse. The reconstructed AMD and FDM are obtained by expanding (or compressing) the FSV results in pre-transient and post-transient regions. The amplitude of the

ADM and FDM in pre-transient and post-transient regions are proportionally varied. The proportionality factor is obtained by

$$P = \frac{Nc}{No} \tag{12}$$

where *Nc* is the length of the compressed (expanded) region and *No* is the length of the original region. Then the GDM is calculated by (8).

3.2. *Performance test*

The standard and transient FSV has used visual assessment surveys to verify its performance [23,26]. Since the survey results are qualitatively presented by natural language descriptors, the survey results are first transformed into quantitative results according to Table 1. After that, the statistics, mean and standard deviation, of GDM and survey results are calculated. The comparison between standard deviations indicates whether FSV and the visual assessments are within each other's range of expectation.

The generalized transient FSV method is tested using the transient data in [23] that comprises 7 typical transient structures. The results of standard FSV, transient FSV and the generalized transient FSV method proposed in this paper are compared in Figure 8 (in the same y-axis range). The mean and standard deviation values are presented by error bars.

It is demonstrated in Figure 8 that both the transient FSV and generalized FSV method could reduce the disagreement between FSV and visual assessment. Overall, there is little difference in the means of the comparisons between the original transient and the generalized transient approaches. Both are significantly better than the standard FSV approach itself.

Also, the performance of the new transient FSV method for the ordinary datasets in [26] were also tested, as shown in Figure 9. It is noted that the generalized FSV method has little influence on the assessment of the ordinary datasets, indicating that it can be more widely applied without it having any significant (detrimental) impact. This is attributed to the fact that the pre-processing of the generalized FSV has little influence on the ordinary datasets. The break points decided by *Step 1* may close to the 0% and 100% points when features are uniformly distributed in the range of data. Then the influence of pre-emphasis and re-mapping processes are reduced.

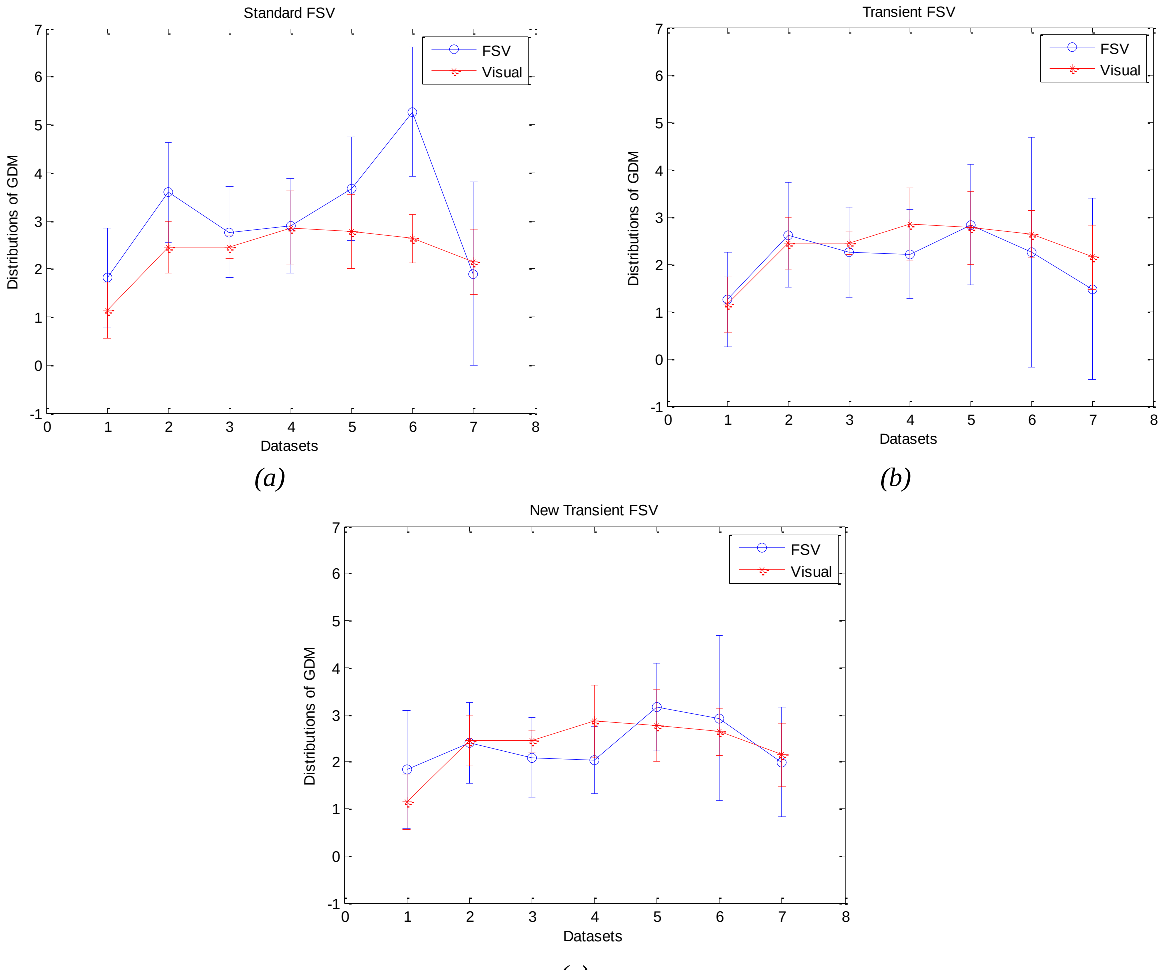

Figure 8. Comparison between 2011 survey and FSV results, (a) standard FSV, (b) transient FSV, (c) generalized FSV.

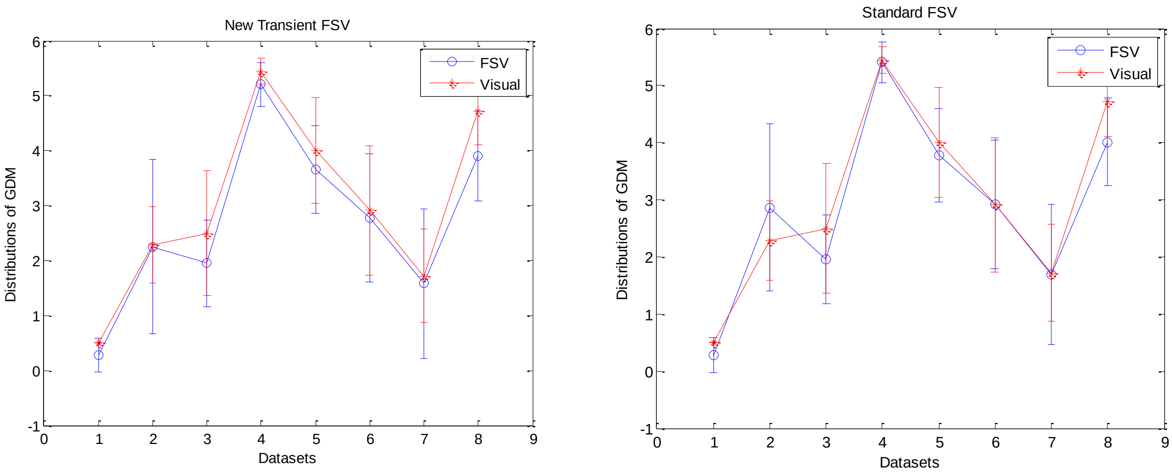

(a) *(b)*

Figure 9. Comparison between 2014 survey and FSV results, (a) generalized FSV, (b) standard FSV.

4. Results

Step-transient speed and torque data was experimentally obtained by emulating shaft dynamic transient loads experienced by a WT drive train on a small-scale test bench equipped with the contactless torque meter described in detail in [14]. The proposed technique instruments the drive shaft with two barcodes, one at each end of the shaft, and two optical sensors mounted on non-rotating supports. Torque and speed measurement is achieved by estimating the shaft twist angle through analysis of the barcode pulse train time shifts [10]. Figure 10(a) shows the effects of torque reversal due to a drastic reduction of the shaft load, as typically occurring in WT stopping events. The corresponding changes in speed, shown in Figure 11(a), are the result of the applied torque that was not countered by the variable speed drive connected to the rig induction motor. Both figures show the contactless torque meter measurements (in blue) compared with those of a reference in-line torque transducer (in red). In both cases, the data comparison visual evaluation shows good agreement between measurements with signal RMSE values of 0.53 Nm and 0.45 rpm, respectively.

Fig. 10(b) and Fig. 11(b) show the torque and speed data comparison, respectively, when applying the standard FSV, transient FSV and generalized FSV method. It is indicated that the results of generalized FSV are smaller than that of standard and transient FSV approach in the pre- and post-transient regions, which means the influence of noise is not exaggerated (as it is clearly the case for the speed FSV and (original) Transient FSV results in Fig. 11b). Table 2 compares the GDMtot values of these methods. It is noted that the standard and generalized FSV method could identify that the agreement between speed data is better than that of torque data, which could be visually verified by Fig. 10(a) and Fig. 11(a). However, the generalized FSV method results in FSV values that recognize the difference between the comparison between the speed and torque data. In contrast, the original transient FSV method is not as clear.

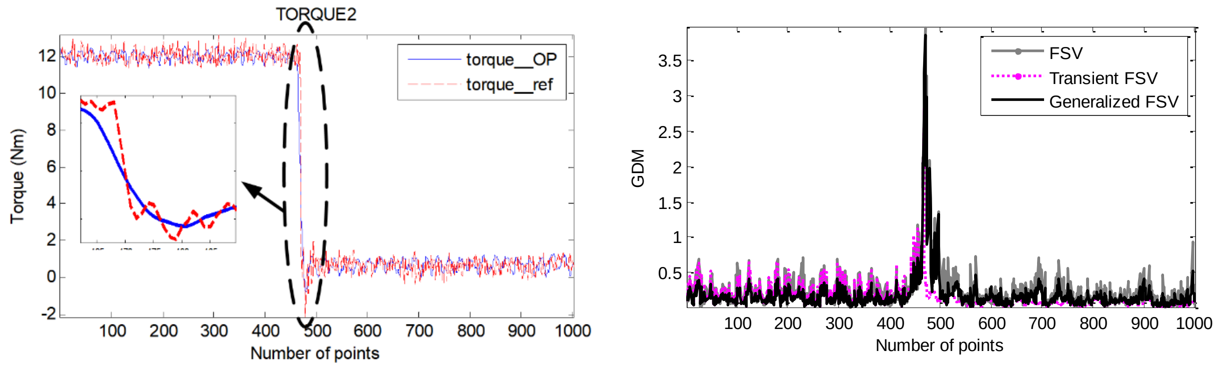

(a) *(b)*

Figure 10. (a) Experimental torque measurements; (b) Comparison of FSV results.

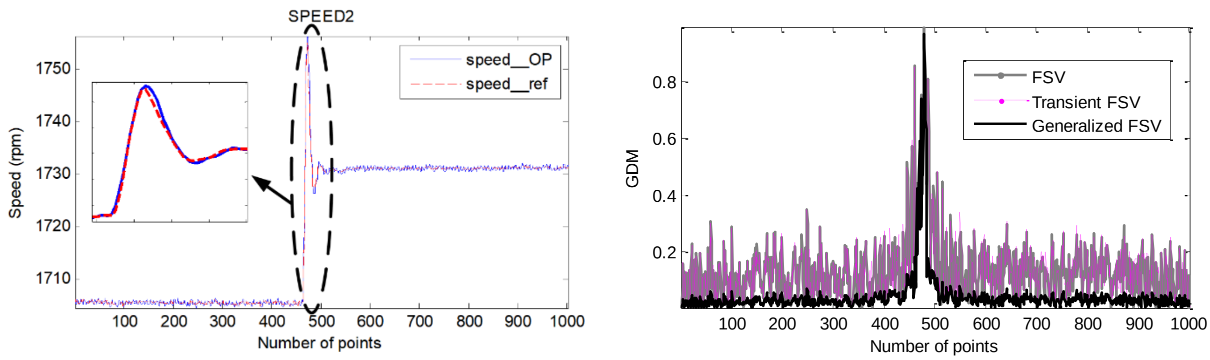

(a) *(b)*

Figure 11. (a) Experimental speed measurements; (b) Comparison of FSV results.

Table 2. Comparison of GDMtot results given by different FSV algorithms.

Data		Speed	Torque
GDMtot	Standard FSV	0.13	0.26
	Transient FSV	0.13	0.14
	Generalized FSV	0.04	0.18

5. Conclusions

A generalized FSV approach is proposed to validate step-function transient data in wind turbines measurement along with other data families. The approach is developed to overcome the limitations of previous standard and transient FSV methods. It is demonstrated that the proposed approach improves the performance of standard FSV method in the comparison of transient datasets and can be directly used in the comparison of ordinary (non-transient) datasets. Comparing with the transient FSV method, the generalized FSV method has been shown to adequately compare step-function transients. Further, the proposed approach ensures that the comparison is dominated by the transient function itself and not the length of the pre- and post- transient periods. Note that the ability to compare step-function transient behaviour opens up further application areas within the signal integrity and power integrity (SIPI) domain.

6. Acknowledgments

This work was in part supported by the EPSRC SUPERGEN Wind Hub (EP/L014106/1). The International Fund of Harbin Institute of Technology (HIT) has supported the collaboration between Zhang and Duffy.

7. References

[1] C.J. Crabtree, D., Zappalá, and S.I. Hogg, "Wind energy: UK experiences and offshore operational challenges," Proceedings of the Institution of Mechanical Engineers, Part A: Journal of Power and Energy, vol. 229, no. 7, pp. 727-746, 2015.

[2] W. Qiao, and D. Lu, "A survey on wind turbine condition monitoring and fault diagnosis - Part I: components and subsystems," IEEE Transactions on Industrial Electronics, vol. 62, no.10, pp. 6536-6545, 2015.

[3] W. Qiao, and D. Lu, "A survey on wind turbine condition monitoring and fault diagnosis - Part II: signals and signal processing methods," IEEE Transactions on Industrial Electronics, vol. 62, no.10, pp. 6546-6557, 2015.

[4] S. Djurović, D. Vilchis-Rodriguez, and A.C. Smith, "Vibration monitoring for wound rotor induction machine winding fault detection," in 2012 XXth International Conference on Electrical Machines, Marseille, 2012, pp. 1906-1912.

[5] D. Zappalá, N. Sarma, S. Djurović, C.J. Crabtree, A. Mohammad, and P.J. Tavner, "Electrical & Mechanical Diagnostic Indicators of Wind Turbine Induction Generator Rotor Faults," Renewable Energy 131, pp. 14-24, 2019.

[6] M. R. Wilkinson, F. Spinato, and P. J. Tavner, "Condition monitoring of generators & other subassemblies in wind turbine drive trains," in 2007 IEEE International Symposium on Diagnostics for Electric Machines, Power Electronics and Drives, 2007, pp. 388-392.

[7] H. Soker, S. Kieselhorst, and R. Royo. "Load monitoring on a main shaft. A case study," German Wind Energy Conference DEWEK, Wilhelmshaven, 2004.

[8] N. Perišić, P. H. Kirkegaard, and B. J. Pedersen, "Cost-effective shaft torque observer for condition monitoring of wind turbines," Wind Energy, vol. 18, no. 1, pp. 1-19, 2015.

[9] D. J. Gardels, W. Qiao, and X. Gong, "Simulation studies on imbalance faults of wind turbines, " in 2010 IEEE Power & Energy Society General Meeting, 2010, pp. 1–5.

[10] D. Zappalá, M. Bezziccheri, C.J. Crabtree, and N. Paone, "Non-intrusive torque measurement for rotating shafts using optical sensing of zebra-tapes," Measurement Science and Technology, vol. 29, n. 6, 065207, 2018.

[11] G. Wegener, and T. Bruns, "Traceability of torque transducers under rotating and dynamic operating conditions", Measurement, vol. 42, n. 10, 2009, pp. 1448-1453.

[12] R.S. Oliveira, S. Winter, H.A. Lepikson, T. Fröhlich, and R. Theska, "A new approach to test torque transducers under dynamic reference regimes", Measurement, vol. 58, 2014, pp. 354-362.

[13] M. Chandra Sekhar Reddy, and A.S.Sekhar, "Detection and monitoring of coupling misalignment in rotors using torque measurements", Measurement, vol. 61, 2015, pp. 111-122.

[14] D. Zappalá, C. J. Crabtree, and S. Hogg, "Investigating wind turbine dynamic transient loads using contactless shaft torque measurements," The Journal of Engineering, in press.

[15] D. E. Coleby, and A.P. Duffy, "A visual interpretation rating scale for validation of numerical models," Compel-the International Journal for Computation and Mathematics in Electrical and Electronic Engineering, vol. 24, no. 4, pp. 1078-1092, 2005.

[16] B. Archambeault, S. Connor, and A.P. Duffy, "Comparing FSV and human responses to data comparisons," in 2005 International Symposium on Electromagnetic Compatibility, 2005, vol. 1, pp. 284-289 Vol. 1.

[17] "IEEE Standard for Validation of Computational Electromagnetics Computer Modeling and Simulations," IEEE Std 1597.1-2008, pp. c1-41, 2008.

[18] "IEEE Recommended Practice for Validation of Computational Electromagnetics Computer Modeling and Simulations," IEEE Std 1597.2-2010, pp. 1-124, 2011.

[19] A.P. Duffy, A. Orlandi, and H. Sasse, "Offset Difference Measure Enhancement for the Feature-Selective Validation Method," IEEE Transactions on Electromagnetic Compatibility, vol. 50, no. 2, pp. 413-415, 2008.

[20] A.P. Duffy, A.J.M. Martin, A. Orlandi, G. Antonini, T.M. Benson, and M.S. Woolfson, "Feature selective validation (FSV) for validation of computational electromagnetics (CEM). part I-the FSV method," IEEE Transactions on Electromagnetic Compatibility, vol. 48, no. 3, pp. 449-459, 2006.

[21] G. Zhang, A.P. Duffy, H. Sasse, and L.X. Wang, "The Use of Probability Density Functions to Improve the Interpretation of FSV Results," in 2012 IEEE International Symposium on Electromagnetic Compatibility, 2012, pp. 675-679.

[22] A.J.M. Martin, "Quantitative data validation," Ph. D. dissertation, De Montfort Univ., Leicester, U.K., 1999.

[23] R. Jauregui, G. Zhang, J. Rojas-Mora, O. Ventosa, F. Silva, A. Duffy, and H. Sasse, “Analysing Transient Phenomena in the Time Domain Using the Feature Selective Validation Method,” IEEE Transactions on Electromagnetic Compatibility, vol. 56, no. 4, pp. 825–34, 2014.

[24] R. Jauregui, P.J. Riu, and F. Silva, “Transient FDTD simulation validation,” in Electromagnetic Compatibility (EMC), 2010 IEEE International Symposium on, 2010, pp. 257–262.

[25] R. Jauregui, J. Rojas-Mora, and F. Silva, “Study of transient phenomena with Feature Selective Validation Method,” in Progress in Electromagnetics Research Symposium (PIERS), 2011, pp. 2–6.

[26] A. Orlandi, A.P. Duffy, B. Archambeault, G. Antonini, D.E. Coleby, and S. Connor, “Feature selective validation (FSV) for validation of computational electromagnetics (CEM). part II-assessment of FSV performance,” Electromagnetic Compatibility, IEEE Transactions on, vol. 48, no. 3, pp. 460–467, 2006.

The Journal of Engineering

The 7th International Conference on Renewable Power Generation (RPG 2018)

eISSN 2051-3305
Received on 6th November 2018
Accepted on 9th January 2019
E-First on 1st July 2019
doi: 10.1049/joe.2018.9361
www.ietdl.org

Investigating wind turbine dynamic transient loads using contactless shaft torque measurements

Donatella Zappalá[1] ✉, Christopher J. Crabtree[1], Simon Hogg[1]
[1]*Department of Engineering, Durham University, Durham, UK*
✉ *E-mail: donatella.zappala@durham.ac.uk*

Abstract: The wind industry is showing increasing awareness about the importance of long-term direct shaft mechanical torque measurements to fully understand wind turbine (WT) dynamics, adopt proactive solutions for extreme load mitigation and enhance condition monitoring (CM) capabilities. Although torsional effects are important, torque measurement on such large, inaccessible machines is practically and logistically difficult, mainly because of the costly and intrusive specialised equipment currently available. This study details an experimental set-up for the investigation of shaft dynamic transient load and speed measurements through a contactless, low-cost torque meter. Results are obtained over a range of applied loads and compared with reference measurements from an in-line, invasive torque transducer. Average torque and speed root-mean-square error values of 0.53 Nm and 0.35 rpm, respectively, indicate good accuracy of the proposed contactless torque meter. Its implementation in the field would allow direct, cheap, real-time measurements of WT drive train loads for performance monitoring, control and CM purposes.

1 Introduction

As large-scale wind farms move further offshore, it is essential to keep a competitive cost of energy by achieving a high availability and capacity factor, and ensuring that loss of energy and wind turbine (WT) downtime are minimised. Offshore wind operations and maintenance (O&M) incur costs up to 25% of the total levelised cost of energy [1]. Unscheduled maintenance activity has been shown to account up to around 65% of O&M costs [2], resulting in unexpected WT downtime, reduced availability and lost revenue. Repair costs are not the only consequence of maintenance, as the WT downtime and revenue costs must also be considered. These issues highlight the importance of O&M strategy within economic viability evaluation of large offshore wind farms. The adoption of cost-effective condition monitoring (CM) techniques is crucial in reducing O&M costs, avoiding catastrophic failures and minimising costly unscheduled maintenance. As the loading on the WT drive train components is highly variable, the study of transient conditions is fundamental to the development of reliable CM techniques.

WTs experience a broader range of dynamic loads than most other large conventional rotating machines. Load variations originate from the grid/generator due, for example, to curtailments, grid loss, voltage changes, emergency stops, shutdowns etc., as well as from very frequent and occasionally extreme wind changes such as gusts, storms and sudden wind losses. Transient events, occurring during control actions or anomalous wind speed behaviour, can cause highly variable drivetrain loads. These can lead to unexpected torque reversals [3] that can be harmful to WT drive train components and reduce their expected life [4].

During extreme transient conditions, dynamic torsional loading causes rapid unloading/loading up of the drive train and loading up/unloading in the opposite direction. These occur in fractions of seconds, unlike the typical minute timescale captured by supervisory control and data acquisition (SCADA) systems. This creates oscillations affecting the entire turbine drive train system. Premature failures of some gearbox components have been associated with overloading experienced by the drive train [5]. Direct high-frequency real-time measurements of drive train loads can improve confidence in drive train design and allow the adoption of proactive solutions for extreme load mitigation.

Mechanical torque measurements are also relevant for efficient CM during turbine operational life, and for condition-based diagnosis for reliable and safe operation [6]. The potential of monitoring different WT drive train components using direct measurements of the shaft mechanical torque signal is significant, as it contains information on the mechanical response to wind before any generator effects. Recent studies have shown the potential benefits of adopting CM systems (CMSs) based on the measurement of WT shaft torque for the detection of rotor electrical asymmetry and machine winding faults [7–9], mass imbalance [10], gearbox failures [11], blade mass imbalance and aerodynamic asymmetry [12].

Owing to the costly and intrusive nature of measurement equipment [13], which is impractical for long-term use on operating WTs, there is currently a lack of insight into dynamic WT drivetrain behaviour. Furthermore, torque sensors are not currently used in commercial WT CMSs. This paper presents the experimental investigation of a novel contactless, low-cost torque meter for shaft load and speed measurements, with a focus on tracking transient conditions for use in a CMS. The adoption of the proposed technique would allow mechanical torque and speed measurement, and monitoring across the machine operational life. It relies on the instrumenting of its shaft with a set of two barcodes and optical probes, one at each end of the shaft, as outlined in the next section.

2 Contactless shaft torque measurement

The contactless torque meter proposed in this research consists of two black and white striped codes, with equal stripe pairs, directly glued around the shaft scanned by two optical sensors mounted on non-rotating supports. The operating principle of the contactless torque meter has been described in details in [14]. As schematically shown in Fig. 1, when a torque is applied to the rotating shaft, it produces a relative shaft twist, θ, resulting in a time shift, Δt, between the pulse trains generated by the optical probes. The measurements of Δt and of the pulse train period, τ, allow the calculation of the shaft absolute twist angle, θ_a, and rotational speed, n, as [15]

$$\theta_a = \frac{2\pi}{60} n \Delta t \tag{1}$$

$$n = \frac{60}{\tau \mathrm{ppr}} \tag{2}$$

where ppr is the number of pulses per shaft revolution. Owing to mounting misalignment between the two optical probes and/or the two zebra tapes, the shaft absolute twist angle, θ_a, could differ from the shaft relative twist angle, θ, which is calculated as

$$\theta = \theta_a - \theta_{a,0} \tag{3}$$

where $\theta_{a,0}$ is the shaft apparent angular shift at no-load conditions.

Shaft torque measurement can then be indirectly obtained from the known system calibration curve, that is, the relationship between the shaft relative twist angle, θ, and torque, T, for a given shaft and material, described by [16]

$$T = I\ddot{\theta} + C\ddot{\theta} + K\theta \tag{4}$$

where I is the rotating system moment of inertia, C is the shaft damping coefficient and K is the shaft torsional stiffness.

3 Experimental set-up

The contactless torque meter has been tested on the experimental test bench shown in Fig. 2. The rig features a 4-pole 5 kW grid-connected induction generator (IG) driven by a 4-pole 5 kW induction motor (IM). The shaft speed profile is controlled by an ABB drive. A variable transformer connected to the IG allows variation of the stator voltage and hence of the torque acting along the shaft. The IG stator voltage can be varied up to a precautionary safety limit of its armature winding current of 8 A, allowing a maximum torque achievable during operation of 16 Nm. The main shaft is instrumented at each end with a barcode featuring eight equal black–white segments, with a 5.5 mm stripe width, fitting exactly around the shaft. The barcode stripe pair number was selected as a trade-off between measurement uncertainty and computational cost. In correspondence to each bar code, an Optek reflective line reader sensor is mounted on a stationary rigid support, placed at the optimum distance of 0.76 mm from the target. The distance between the two optical sensors is 45.8 cm. An in-line Magtrol TMB 313/431 torque transducer is mounted on the test bench and, being a well-established state-of-the-art technique, it has been assumed as the reference measurement system during the experimental campaign. The in-line transducer is also used as a reference tachometer as it outputs 60 ppr for speed measurements. Signals from the optical probes and the reference torque transducer are acquired by a PicoScope 4824 oscilloscope, with a sampling frequency, f_s, of 100 kHz.

4 Data processing

A LabVIEW programme (VI) has been implemented to automatically process the optical probe pulse signals and obtain the shaft angular shift by direct timing of their rising edges.

The main steps of the optical system data processing are:

(1) signals are first initialised to overcome any problems associated with initial probe and barcode mounting offset;
(2) the time at which the rising edges of the two initialised signals occur is captured by applying an edge trigger with a threshold level equal to half the peak-to-peak signal amplitude;
(3) a flicker filter is applied to remove any possible timing errors from signal flickering around the trigger level;
(4) the shaft rotational speed, n, is calculated from the pulse train period by applying conventional rotary encoder techniques, as detailed by (2);
(5) an eight-point moving average filter, with seven-point overlap over time, is implemented to calculate the pulse time shift. This is to reduce inherent periodic noise in pulse timing due to tangential and radial displacements between the shaft and optical probes, typically caused by vibrations or shaft deformation; and
(6) the shaft absolute angular shift is then calculated according to (1).

Table 1 summarises the main features of the contactless torque meter mounted on the test bench.

5 System calibration

The contactless torque meter calibration curve has been obtained by comparison with the reference measurements of the in-line torque transducer. The calibration process is schematically shown in Fig. 3. Steady-state tests were performed on the test rig at four different shaft speeds. For each case, no-load and different torque

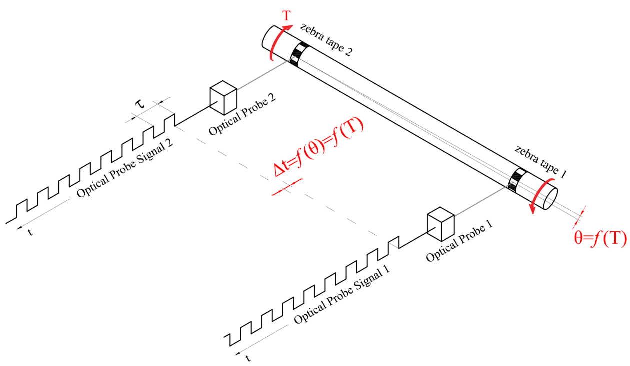

Fig. 1 *Operating principle of the contactless torque meter [14]*

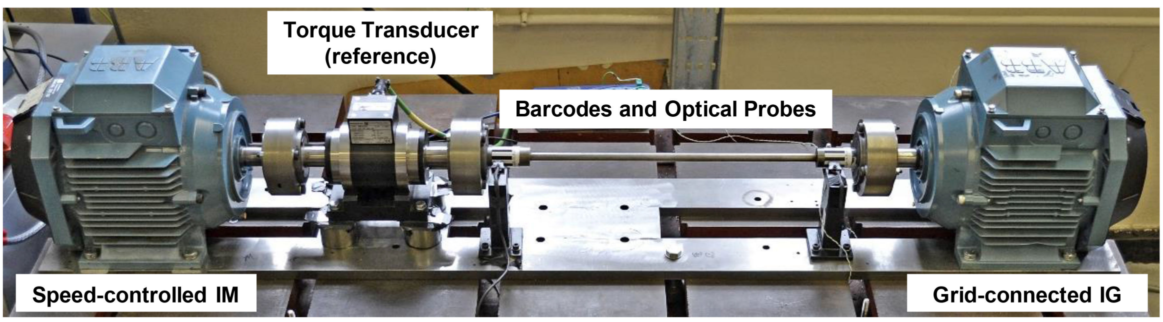

Fig. 2 *Experimental test rig*

Table 1 Main parameters of the experimental optical torque meter

pulses per revolution (ppr)	8
barcode period	11 mm
measurable angular range	$\left[-\frac{\pi}{\text{ppr}}, \frac{\pi}{\text{ppr}}\right]$
angular resolution ($\delta\theta$)	$\frac{2\pi n}{60 f_s}$
angular twist sampling frequency	$\frac{n\ \text{ppr}}{60}$

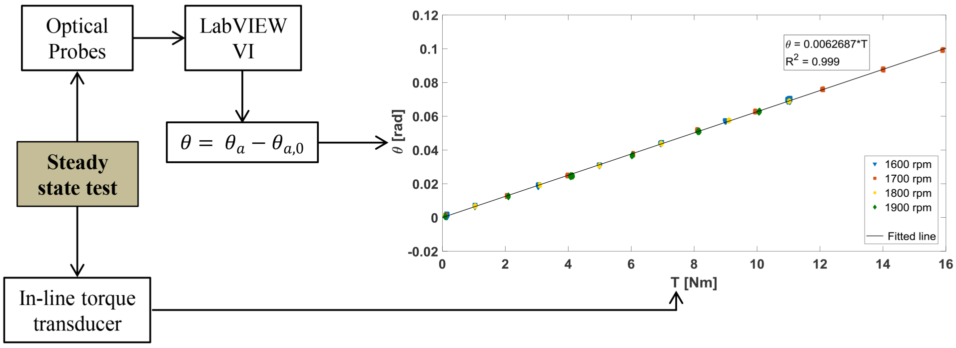

Fig. 3 *Schematic representation of the calibration process*

Table 2 Summary of the experimental work performed on the torque test rig

Test	Torque range, Nm	Speed range, rpm	Test duration, s	WT operation	RMSE	
					Torque, Nm	Speed, rpm
turbulent torque oscillations (Fig. 4)	−0.8 to 17	1671 to 1706	30	normal running, turbulent conditions	0.53	0.31
drastic shaft torque increase (Fig. 5)	−1.2 to 7.3	1681 to 1702	5	starting event	0.48	0.35
drastic shaft torque reduction (Fig. 6)	−2 to 13.2	1704 to 1756	5	stopping event	0.53	0.45
variable frequency torque fluctuation (Fig. 7)	4.3 to 10.2	1686 to 1697	28	rapid torque fluctuations	0.54	0.31
variable shaft speed (Fig. 8)	2.9 to 13	1547 to 1853	9	variable speed	0.59	0.33

levels, up to 16 Nm, were applied for around 10 s and corresponding signals were recorded and processed.

The linear regression between the shaft relative twist and the corresponding reference torque, measured by the in-line transducer, has provided the system calibration curve. As predicted by (4), the torque-twist trend is linear under steady-state conditions. The calibration curve shows an R^2 value of 0.999, indicating a good fit of the experimental data by the regression line. The statistical analysis of the residuals of the calibration data has provided an expanded measurement uncertainty, with respect to the system full-scale torque, of ±0.3% [14].

6 Results

Experiments have been performed to emulate shaft dynamic transient loads experienced by a WT drive train, during anomalous wind speed fluctuations and control actions. Table 2 shows the details of each experiment including the torque and speed range the duration and the WT operating condition emulated on the test bench. In each case, the contactless torque meter torque and speed measurements, and dynamic response have been compared with those of the reference in-line torque transducer. The performance of the contactless torque meter against the reference system has been estimated by calculating the signal root-mean-square error (RMSE), as detailed in Table 2. Both signals have been resampled at the same frequency of 200 Hz to allow RMSE calculation.

Results shown in Figs. 4–7 have been obtained by varying the IG stator voltage through the variable transformer. The corresponding changes in speed are the result of the applied torque that was not countered by the variable speed drive connected to the IM. Fig. 4 shows results for the case of turbulent torque oscillations, similarly to those encountered in WT normal running under turbulent conditions. Both the contactless metre torque and speed measurements allow tracking the turbulent shaft oscillations, during the whole transient without any time delay. Figs. 5 and 6 show the effects of torque reversal due to a drastic increase and reduction of the shaft torque, as typically occurring in WT starting and stopping events, respectively. In both cases, the torque meter measurements show good agreement with reference measurements.

Fig. 7 shows the good performance of the optical torque meter during torque harmonic fluctuations, with frequency varying between 0.28 and 0.76 Hz, imposed on the shaft. Results shown in Fig. 8 have been obtained by applying rapid and significant variations to the shaft speed via the ABB drive at a fixed generator stator voltage. The optical measurements, though giving, in the case of the torque, a slightly higher RMSE value than in previous experiments, correlate closely with the reference measurements, showing a good dynamic response to shaft speed and load changes.

The RMSE values of the performed tests, shown in Table 2, are consistent and indicate good accuracy of the proposed contactless torque meter, with the closeness of agreement between its measurements and the reference torque and speed values measured by the in-line torque transducer. Overall, the investigated shaft transient load conditions show average RMSE values of 0.53 Nm and 0.35 rpm for the torque and speed, respectively, corresponding to 3.3 and 0.02% of the maximum operating conditions tested during the experiments.

7 Discussion

Long-term mechanical torque measurements are important for fully understanding the WT dynamics and for CM purposes. In the wind

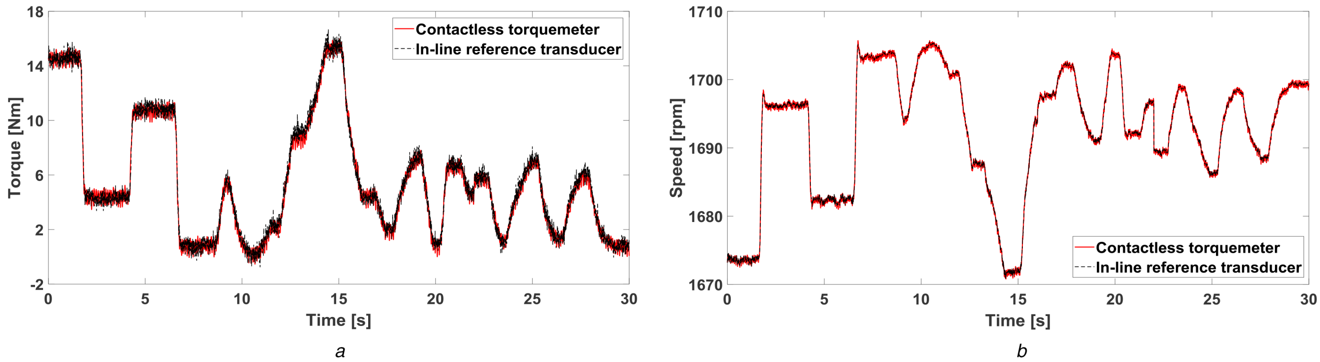

Fig. 4 *Turbulent torque oscillations*
(a) Torque, ***(b)*** Speed measurements

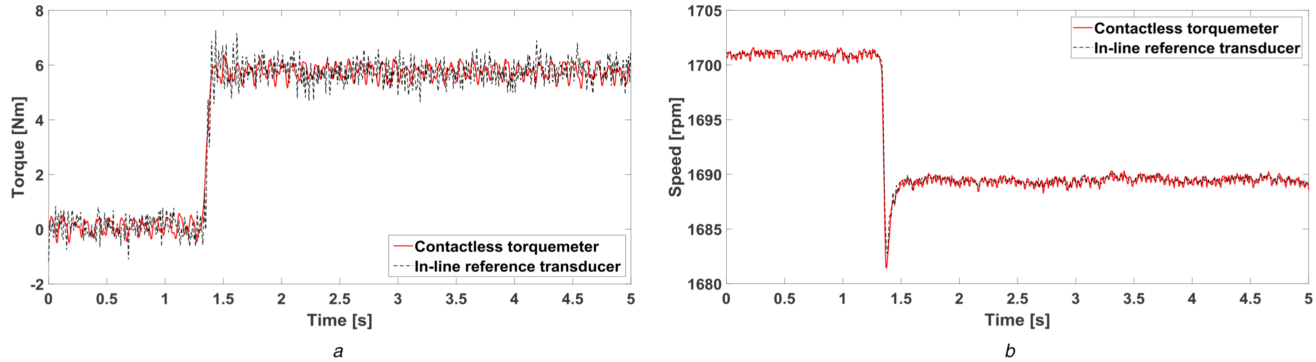

Fig. 5 *Drastic shaft torque increase*
(a) Torque, ***(b)*** Speed measurements

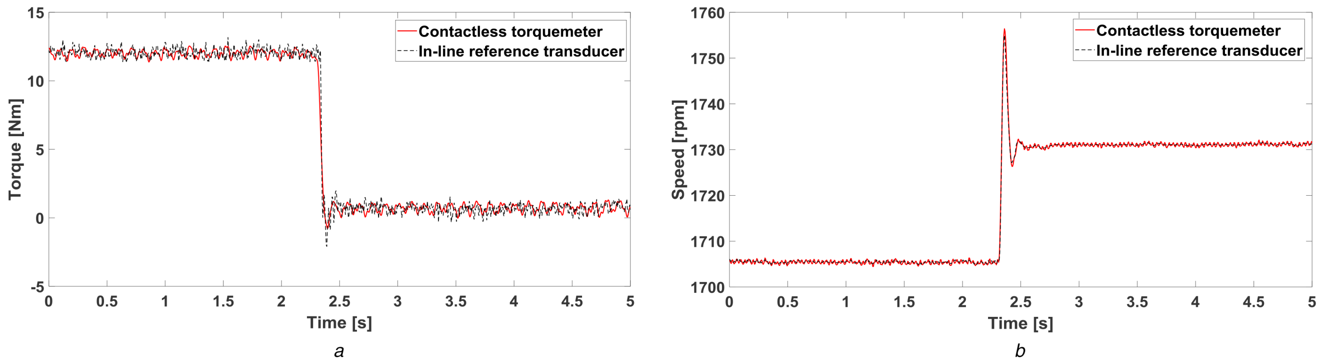

Fig. 6 *Drastic shaft torque reduction*
(a) Torque, ***(b)*** Speed measurements

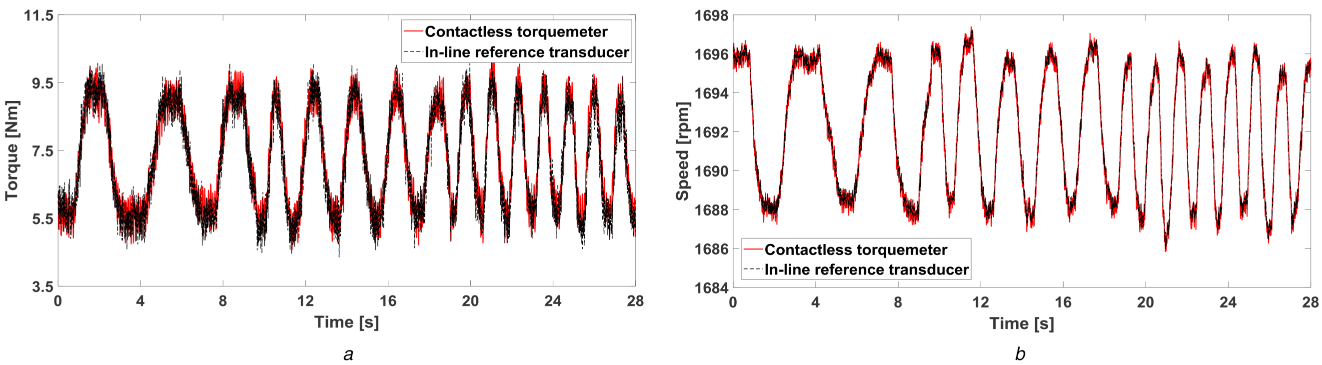

Fig. 7 *Variable frequency torque fluctuations*
(a) Torque, ***(b)*** Speed measurements

industry, there is increasing awareness and growing interest in measuring the machine loads by direct, cheap and non-intrusive techniques.

In this work, the use of a contactless torque meter to measure WT drive train shaft torque and speed is experimentally investigated. Unlike conventional in-line torque transducers and conventional strain gauge techniques, this torque meter does not require costly embedded sensors, electronics or wires on the rotating shaft. It is relatively simple and cheap to implement into a commercial WT CMSs for non-intrusive torque monitoring. Also,

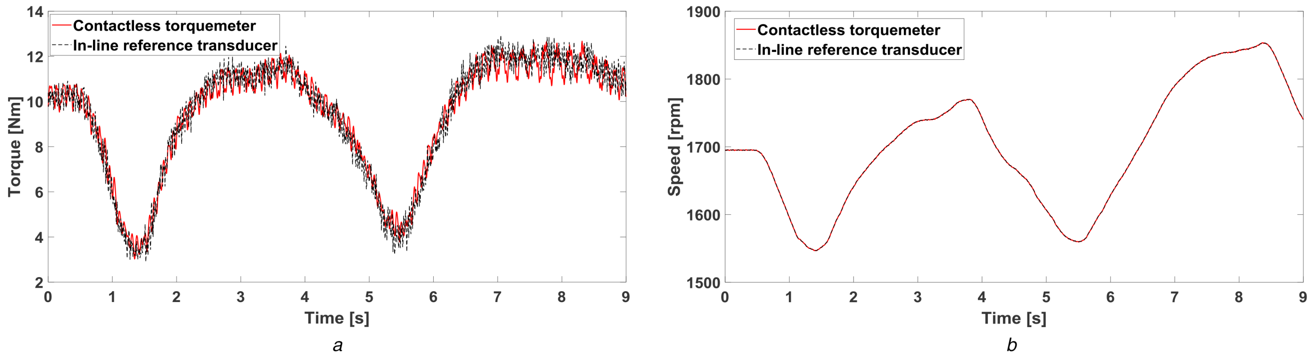

Fig. 8 *Variable shaft speed*
(a) Torque, ***(b)*** Speed measurements

the accuracies of strain gauges often do not meet engineering requirements due to crosstalk phenomena, which can significantly increase the measurement uncertainty [17]. The proposed system allows direct measurement of the shaft dynamic behaviour at relatively high frequency, under transient conditions that have been shown to be the most critical for the WT drive train components. Such a measurement is more advantageous compared with deriving the electromagnetic torque from the measure of the machine electrical power, which does not provide direct and realistic information about the WT drive train dynamics, due to internal frictional, electric and magnetic losses affecting the measurements.

Although still at the small-scale stage implementation, the economic benefits of the proposed technique over conventional in-line torque transducers are evident. The contactless torque meter installed on the experimental test bench costs overall €100. It compares well with the cost of the corresponding reference in-line sensor, which goes well beyond €5000. The difference in costs will be, of course, even larger in a commercial WT application, due to the much larger shaft sizes.

8 Conclusions

This paper presents a novel, contactless torque meter for direct real-time measurement of WT drive train load and speed. The performance and accuracy of the proposed optical torque system during dynamic transient load conditions have been experimentally demonstrated through comparison with reference measurements from an in-line torque transducer. Results indicate good accuracy of the proposed contactless torque meter, with average RMSE values of 0.53 Nm and 0.35 rpm for the torque and speed, respectively. Unlike conventional measurement methods, the proposed barcode torque meter does not require costly embedded sensors or shaft-mounted electronics. It can also be designed to be fitted, or retrofitted, on any WT shaft diameter and material without mechanical interference. This overcomes the majority of problems currently limiting the industrial direct real-time measurements of WT drive train loads for performance monitoring, control and CM purposes.

9 Acknowledgment

This work was funded as part of the UK EPSRC SUPERGEN Wind Hub, EP/L014106/1.

10 References

[1] Crabtree, C.J., Zappalá, D., Hogg, S.I.: 'Wind energy: UK experiences and offshore operational challenges', *Proc. Inst. Mech. Eng. A, J. Power Energy*, 2015, **229**, (7), pp. 727–746
[2] BVG Associates: 'Offshore wind cost reduction pathways: technology work stream', 2012. https://bvgassociates.com/Publications/ accessed on April 2018
[3] Herr, D.: 'Transient wind events and their effect on drivetrain loads', *Windtech Int.*, 2015, **11**, (3), https://www.aerotorque.com/sites/default/files/2-Windtech%20with%20cover.pdf accessed on April 2018
[4] Guo, Y., Keller, J., Moan, T., *et al.*: 'Model fidelity study of dynamic transient loads in a wind turbine gearbox'. Proc. 2103 WINDPOWER Conf., Chicago, IL, 2013
[5] Al-Hamadani, H., An, T., King, M., *et al.*: 'System dynamic modelling of three different wind turbine gearbox designs under transient loading conditions', *Int. J. Prec. Eng. Manuf.*, 2017, **18**, (11), pp. 1659–1668
[6] Qiao, W., Lu, D.: 'A survey on wind turbine condition monitoring and fault diagnosis – part II: signals and signal processing methods', *IEEE Trans. Ind. Electron.*, 2015, **62**, (10), pp. 6546–6557
[7] Yang, W., Tavner, P.J., Crabtree, C.J., *et al.*: 'Cost-effective condition monitoring for wind turbines', *IEEE Trans. Ind. Electron.*, 2010, **57**, (1), pp. 263–271
[8] Abdusamad, K.B., Gao, D.W., Li, Y.: 'Condition monitoring system based on effects of electrical torque pulsations of wind turbine generators'. 2014 IEEE PES General Meeting, Conf. Exposition, National Harbor, MD, 2014, pp. 1–5
[9] Djurović, S., Vilchis-Rodriguez, D.S., Smith, A.C.: 'Vibration monitoring for wound rotor induction machine winding fault detection'. 2012 XXth Int. Conf. Electrical Machines, Marseille, 2012, pp. 1906–1912
[10] Wilkinson, M.R., Spinato, F., Tavner, P.J.: 'Condition monitoring of generators & other subassemblies in wind turbine drive trains'. 2007 IEEE Int. Symp. Diagnostics for Electric Machines, Power Electronics and Drives, Cracow, 2007, pp. 388–392
[11] Soker, H., Kieselhorst, S., Royo, R.: 'Load monitoring on a mainshaft. A case study'. German Wind Energy Conf. DEWEK, Wilhelmshaven, 2004
[12] Perišić, N., Kirkegaard, P.H., Pedersen, B.J.: 'Cost-effective shaft torque observer for condition monitoring of wind turbines', *Wind Energy*, 2015, **18**, (1), pp. 1–19
[13] Yang, W., Tavner, P.J., Crabtree, C.J., *et al.*: 'Wind turbine condition monitoring: technical and commercial challenges', *Wind Energy*, 2014, **17**, (5), pp. 673–693
[14] Zappalá, D., Bezziccheri, M., Crabtree, C.J., *et al.*: 'Non-intrusive torque measurement for rotating shafts using optical sensing of zebra-tapes', *Meas. Sci. Technol.*, 2018, **29**, (6), pp. 1–18, https://doi.org/10.1088/1361-6501/aab74a
[15] Sue, P., Wilson, D.D., Farr, L., *et al.*: 'High precision torque measurement on a rotating load coupling for power generation operations'. Proc. 2012 IEEE Int. Instrumentation and Measurement Technology Conf., Graz, Austria, 2012, pp. 518–523
[16] Friswel, V.M.I., Penny, J.E.T., Garvey, S.D., *et al.*: '*Dynamics of rotating machines*' (Cambridge University Press, Cambridge, UK, 2010)
[17] de Silva, C.W.: '*Sensors and actuators: engineering system instrumentation*' (CRC Press, Boca Raton, FL, USA, 2015)

The Journal of Engineering

The 9th International Conference on Power Electronics, Machines and Drives (PEMD 2018)

Power converter junction temperature measurement using infra-red sensors

eISSN 2051-3305
Received on 22nd June 2018
Accepted on 2nd August 2018
E-First on 4th April 2019
doi: 10.1049/joe.2018.8098
www.ietdl.org

Christopher J. Smith[1], Donatella Zappalá[1], Christopher J. Crabtree[1] ✉, Justo Lapiedra[2], Brian Mulholland[2]
[1]*Durham University, UK*
[2]*Anecto, Ireland*
✉ *E-mail: c.j.crabtree@durham.ac.uk*

Abstract: Studies demonstrate that the power converter has one of the highest failure rates in a wind turbine, with a key failure driver being the power module junction temperature (T_j). This paper details an experimental setup for simplified emulation of wind turbine conditions on a power converter with infra-red sensing of IGBT T_j. Results are compared to previous simulation work for a PMSG wind turbine, with the same trend of increasing mean T_j with wind speed found, and the need to use an equivalent generator reactance in highlighted. A commercial-scale prototype for more accurate wind turbine converter emulation is also detailed.

1 Introduction

Studies have shown that the power converter has one of the highest failure rates in a wind turbine [1]. Furthermore, the converter failure rate increases with turbine power rating and wind speed due to higher stressing and a higher number of components [2]: the current trend in offshore wind farms. Therefore, the converter, particularly in permanent-magnet synchronous generator turbines [3], is reliability-critical and must be understood in order to maximise the impact of improving reliability on the levelised cost of energy from wind.

Power module failure is the failure mode for nearly all major converter repairs [2]. Traditionally, power module failure has been linked to power module thermal loading, where the variation of temperature in the insulated gate bipolar transistors (IGBT) and diode cases causes fatigue through expansion and contraction between package layers [4]. The reference temperature is the virtual junction temperature (T_j), which is a virtual representation of the chip p-n junction temperature [4]. T_j variation is deemed the most important aspect to measure for physics-of-failure reliability analysis.

Present converter lifetime estimations and simulation models are validated using only static operating conditions with fixed currents and frequencies [5]. In reality, wind turbines have constantly varying frequency, voltage, and current throughputs due to the stochastic nature of the wind and the reactionary turbine controllers. There is, therefore, uncertainty over the applicability of present approaches for determining the suitability of converter designs to surviving electrical loading characteristics offshore.

In response, a holistic approach to wind turbine power converter reliability is proposed. This includes a combination of effective drive train modelling, simulation, and physical emulation of the power converter and its junction temperature (T_j) response under realistic wind turbine operating conditions. This will allow for developments in either computational or experimental fields to inform the formulation of results of the other.

Previous research by the authors has provided drive train modelling and thermal loading simulation [4]. This paper outlines the wind turbine power converter physical emulation and surrounding drive train to answer the following research questions (RQ):

(i) How should the device temperature be monitored to provide high-frequency, high-accuracy T_j measurements without affecting the control or operation of the device under test? (Section 2)
(ii) How can wind turbine operating conditions be emulated in a scaled down test bench? (Section 3, 4)
(iii) How do the results of simulation and physical testing compare? (Section 5)
(iv) How can this experimental rig be implemented for commercial scale device testing and certification? (Section 6)

2 Junction temperature measurement

To answer RQ1, this section reviews current methods for temperature measurement, determines the most suitable approach, and describes the realised thermal measurement experimental set up.

2.1 Measurement approach selection

There are three main approaches to temperature monitoring: direct contact, proxy using temperature-sensitive electrical parameters, or infra-red (IR) measurement.

Direct contact can be carried out using a thermocouple or thermistor. As thermocouples rely on conduction, they require direct adhesion to the device under test (DUT), and typically have slow response times of hundreds of ms [6] making them unsuitable for high-frequency temperature measurements as required by this research.

Temperature sensitive electrical parameters use measurable device voltages and currents to estimate the temperature of the power module. Some examples include the measurement of collector-emitter saturation voltage (V_{ces}), gate-emitter voltage (V_{ge}), and saturation current (I_{css}) [7]. In all cases, a small measurement signal is needed that is independent of normal operating conditions. Therefore, to be used in a functional environment, the converter control requires complex changes and the measured signals are susceptible to the noisy converter electromagnetic environment. This makes the approach impractical and it is not considered further.

IR measurement relies on capturing the IR radiation emitted by a body. The spectral content is determined by the temperature of the body and the emissivity of the body's surface. This relationship is well documented and can be calculated using Planck's law for a black body (emissivity (e) of 1). Therefore, by measuring the spectral radiance from a body over a specified wavelength range using a photoconductive sensor and correcting for output by the emissivity of the body (as a percentage of the radiance from a

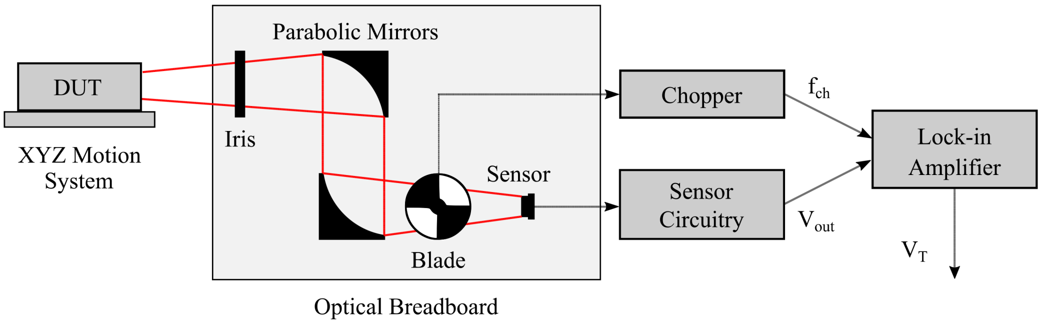

Fig. 1 *Experimental optical set-up. V_T is the temperature dependent voltage output and f_{ch} is the chopping frequency*

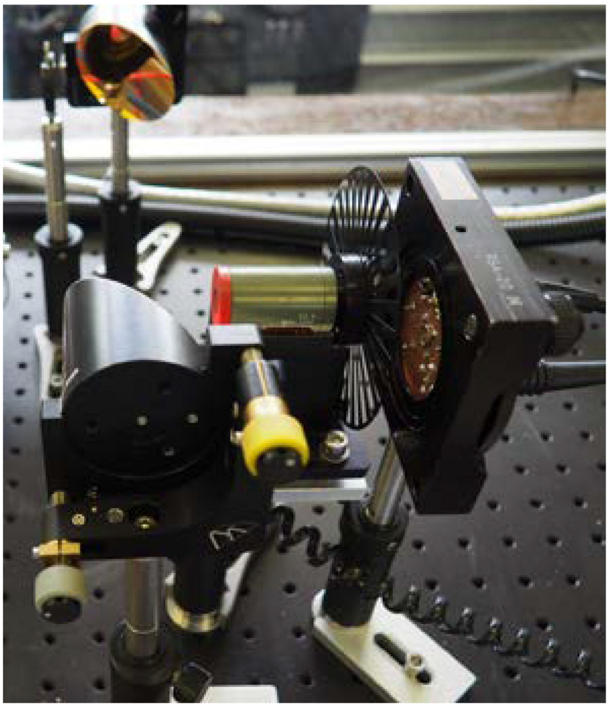

Fig. 2 *Photograph of optical set-up*

black body), the temperature can be measured without physical contact with the body.

IR measurement comes in two main forms; IR cameras and IR sensors. The outputs of an IR camera are recognisable by their multi-coloured images, providing an array of temperature measurements across a surface. Unfortunately, IR cameras are very expensive, particularly when fast response times and accurate temperature measurements are required, making them unsuitable for this experimental work. In contrast, IR sensors are essentially single pixel IR cameras and are subsequently less expensive. They are also able to measure spot temperatures more accurately, making them ideal for use in T_j monitoring in the power module.

IR approaches have some disadvantages. Although requiring no physical contact with the measured device, line of sight is required. This requires modification of the measured device through removal of its protective casing, as discussed in Section 3.2.

2.2 Experimental set-up

With an IR sensor approach chosen, the temperature measurement setup was developed to enhance the output of the IR sensor. The schematic of this setup is shown in Fig. 1. The key aspects of the optical set up are:

- *The IR sensor* is a Thor Labs PbSe photoconductive IR sensor [8] with a spectral measurement range of 1–4.8 µm and a response time of 10 µs.
- *The mirrors*. For rig flexibility, parabolic mirrors were used to focus the IR radiation from the DUT.
- *The XYZ position system* allows for precise positioning of the DUT to ensure repeatable testing and accuracy.
- *The chopper and lock-in amplifier*. As IR sensors are supplied with a high DC voltage (100 V), they have inherent DC bias on their output that can interfere with the measurement. To remove this bias, and to reduce background noise, an optical chopper is used to shift the temperature signal to 3.5 kHz. A lock-in amplifier is used as a band-pass filter linked to the chopper.

Fig. 2 presents a photograph of the optical set up.

The lock-in amplifier voltage output V_T in Fig. 1 is converted to a temperature measurement using a parabolic calibration curve derived from a range of temperature measurements taken by a FLIR C2 camera.

3 Drive train set-up

With the temperature measurement ready, wind turbine emulation was required. This included selecting an appropriately scaled DUT, preparing the DUT for measurement, scaling the DC link to emulate the larger wind turbine DC link, controlling the DUT, and mitigating noise issues. The schematic diagram of the experimental rig is provided in Fig. 3.

3.1 DUT selection

In [4], two parallel SEMIKRON SKSB2100GD69/11-MAPB stacks were used containing SKiiP2013GB172-4DWV3 half-bridge SKiiP modules. Ideally, these modules would be the DUT but this was impractical due to the cost and experimental impracticality of current and voltage ratings (1000 A_{nom} and 1700 V_{ces}).

A lower rated power module was required to operate within the available laboratory infrastructure. The power module selected was the SEMIKRON 01NAC066V3 MiniSKiiP module [9], which has lower current and voltage ratings (6 A_{nom} and 600 V_{ces}) and lower unit cost while still using the Trench3 IGBT technology found in the larger device, allowing for practical but realistic laboratory testing.

The key limitation of the 01NAC066V3 module is the packaging technology; the SKiiP2013 uses SKiNTER technology which replaces solder with cold-welded silver chip, and has the gate drivers incorporated into the package [10]. However, according to expert advice, this increases the lifetime of the device but does not change the fundamental failure modes, meaning that the 01NAC066V3 module was suitable for emulation of the large modules found in MW-scale turbines.

3.2 Device preparation

The device comes with a plastic case that uses sprung metallic legs to connect to the device and it is coated in an insulating silicon gel to avoid flash over. One of the main challenges with the chosen temperature measurement approach is the need to have line-of-sight to the IGBTs. To achieve this, the case was removed and the sprung metallic legs were replaced with direct solder joints. This direct soldering required the silicon gel to be removed by placing the whole device in a dodecylbenzenesulfonic acid bath for 24–48

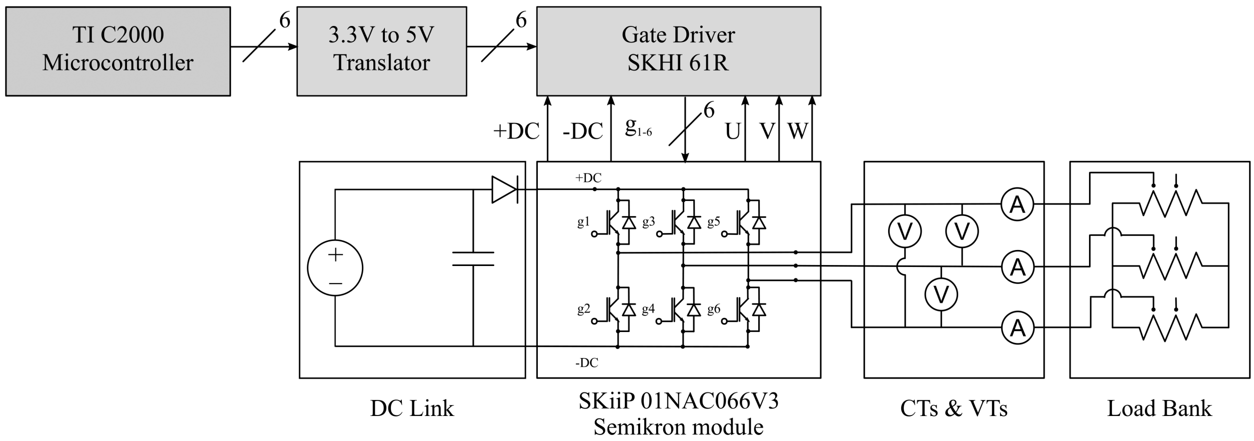

Fig. 3 *Electrical circuit diagram of the experimental rig*

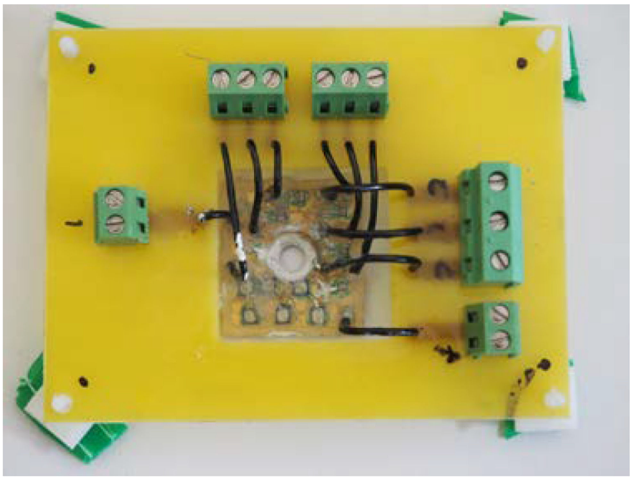

Fig. 4 *SEMIKRON 01NAC066V3 MiniSKiiP module modified for testing*

Table 1 Power module voltage parameters

Parameter	Value
$V_{ces,e}$	600 V
$V_{ces,f}$	1700V
$V_{DC,e}$	406 V
$V_{DC,f}$	1150V

h. The connections were then soldered to the device, the silicon gel reapplied, and the device secured to a heat-sink with a nylon screw and thermal paste (Fig. 4).

3.3 DC link

As the DUT collector-emitter saturation voltage ($V_{\rm ces}$) is lower than that of the MW-scale power modules, the DC link voltage must be scaled accordingly. Then, (1) can be applied to determine the equivalent DC-link voltage.

$$V_{\rm DC,e} = V_{\rm ces,e}(V_{\rm ces,f})^{-1}V_{\rm DC,f} \tag{1}$$

where $V_{{\rm ces},e}$ and $V_{{\rm ces},f}$ are the experimental and full-scale power module collector-emitter saturation voltages, respectively, and $V_{{\rm DC},e}$ and $V_{{\rm DC},f}$ are the experimental and full-scale DC-link voltages, respectively. The values are given in Table 1.

A switch mode power supply with an output capacitor was used to emulate the DC link (Fig. 3). Due to equipment limitations, the DC-link voltage could only be set to a maximum of 300 V but this was deemed reasonable as it was assumed that the current throughput would have the greater impact on thermal loading.

3.4 Control circuitry

To invert the DC-link voltage, the six IGBTs were switched using sine wave pulse width modulation (SPWM) at 2 kHz. The SPWM was generated using a Texas Instruments micro-controller interfaced with MATLAB/Simulink to allow the use of in-built function blocks. The voltage was controlled in an open-loop configuration with the required voltage set in software and uploaded to the micro-controller.

3.5 Noise

Due to the high-frequency noise generated by switching, there were a number of issues with interference on both the gate driver and the temperature measurement output. To mitigate this, the following steps were taken:

- Isolated grounding and braiding for power circuitry, control circuitry, and measurement circuitry.
- Metallic shielding for control circuitry.
- Load bank placed away from the experiment.
- Power and gate driver cables kept perpendicular.

4 Wind turbine condition emulation

To replicate the fixed wind speeds in [4], the operating conditions have to be scaled to match the experimental constraints. The constant 12.7 m/s wind speed conditions simulated in [4] could not be replicated as the DC source did not have the current or voltage capacity required (5 A instead of 6 A, and 300 V instead of 406 V). The load bank's discrete resistances also meant that independent control of voltage and current was impossible, and the modulation index, m, would have to change to accommodate the different maximum voltages available. Current was given priority, and the voltage was varied as required as the losses are driven by the collector current.

The simulation parameters and their physical test equivalents are given in Table 2. m_f is the full-scale modulation index, m_e is the experimental modulation index, $I_{c,f}$ is the full-scale IGBT collector current, $I_{c,e}$ is the experimental IGBT collector current, and R_L is the load resistance. $I_{c,e}$ was calculated by using the ratio between rated $I_{c,e}$ and rated $I_{c,f}$ (6/2800) [6], and m_e was set so that the scaled equivalent AC voltage matched the full-scale AC voltage output.

5 Results and discussion

With the experimental rig constructed, the first stage was to verify the experimental rig outputs. Following this, to answer RQ3, the results from [4] are compared with the experimental results.

Table 2 Experimental test parameters and values for four wind speeds

Wind speed, m/s	Frequency, Hz	$V_{DC,f}$ (V)	$V_{DC,e}$ (V)	m_f	m_e	$I_{c,f}$ (A)	$I_{c,e}$(A)	R_L, Ω
4	3.1	1150 V	300 V	0.28	0.57	323A	0.56	150
6	4.6	1150 V	300 V	0.42	0.67	483A	1.26	80
8	6.1	1150 V	300 V	0.55	0.79	633A	2.24	52
10	7.7	1150 V	300 V	0.72	0.93	828A	3.50	40

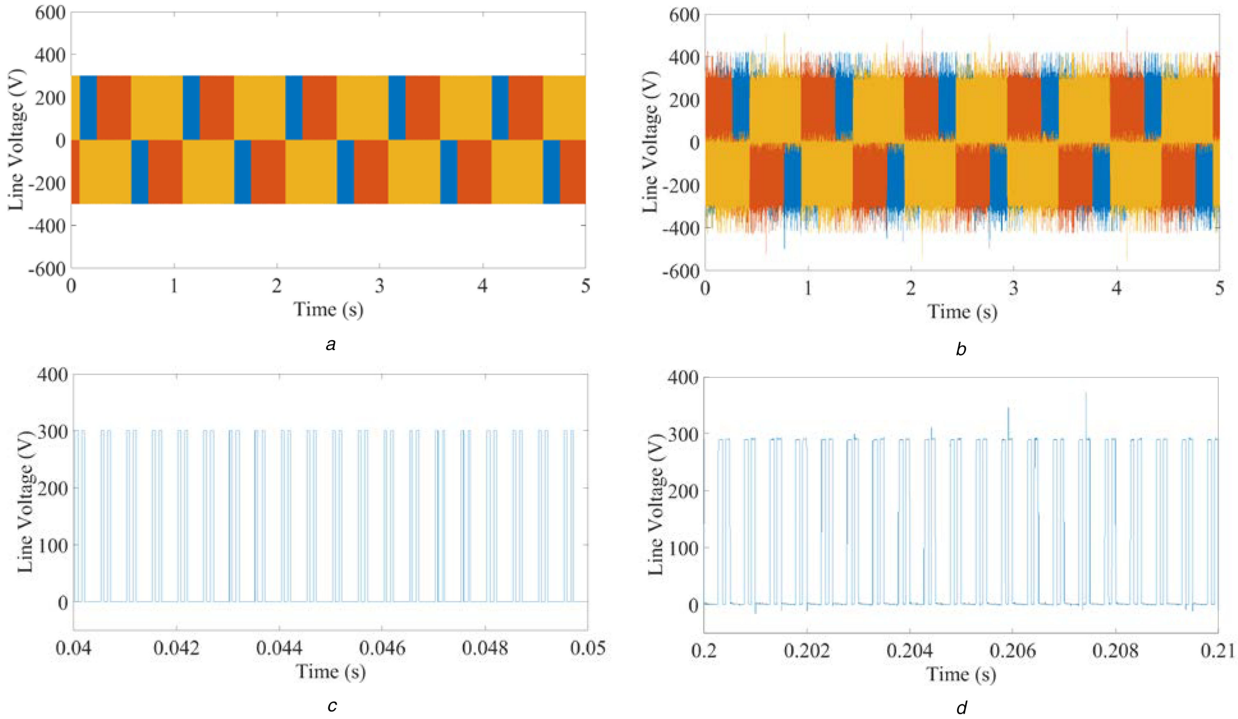

Fig. 5 *Verification of 3-phase voltage output*
(a) Simulated voltage, ***(b)*** Measured voltage, ***(c)*** Zoomed-in simulated voltage, ***(d)*** Zoomed-in experimental voltage

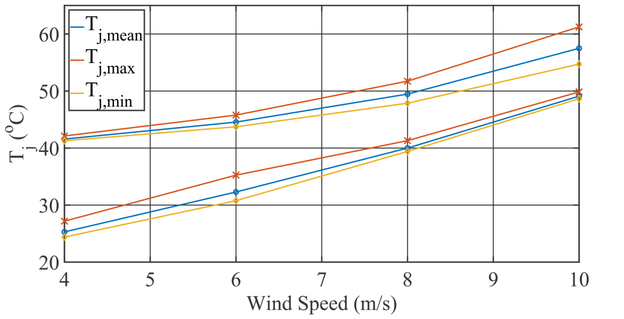

Fig. 6 *T_j results for equivalent wind speed tests. Dashed lines are simulated results and solid lines and experimental results*

5.1 Experimental verification

To verify that the experimental rig was producing expected voltage and current profiles, the experimental rig (Fig. 3) was modelled and simulated in Simulink. The same conditions were then applied to both model and rig and the voltage and current waveforms compared.

The simulated and experimental voltage waveforms were compared at 300 V with a 32 Ω star-connected resistive load with an output frequency of 1 Hz (Fig. 5). Unsurprisingly, the simulated three-phase voltage output is cleaner (Fig. 5*a*) than that of the experimental rig (Fig. 5*b*) as the simulation assumes that the IGBTs are perfect switches. In contrast, the real IGBTs are imperfect and produce short voltage transients when switching. However, both produce very similar magnitude waveforms and Figs. 5*c* and *d* reveal that individual voltage changes are consistent between simulation and experiment, validating the experimental rig output.

5.2 Comparison with simulation results

Experimental IGBT mean, maximum and minimum T_j resulting from the conditions in Table 2 are summarised in Fig. 6 alongside equivalent simulation results. The rise in mean temperature with wind speed confirms the increase found in [4]. This is because the overall device power losses increase with increased power throughput of the device.

However, unlike the simulation where the ΔT_j increased with increasing wind speed, in this case ΔT_j actually reduced. At first glance, this seemingly disproves the results in [4]. However, this result can be explained by the use of a resistive load in the experimental rig. The average I_c increased with increasing wind speed, increasing the total power losses experienced by the device and, therefore, raising the mean T_j. However, the instantaneous I_c when the device is switching is still 5 A regardless of the average I_c, causing the instantaneous switching power losses to remain relatively constant.

Therefore, as m increases with increasing wind speed, there are fewer switching events occurring per cycle, causing lower overall switching power losses. This in turn creates a lower ΔT_j with increasing wind speed.

In contrast, the inductive load in the simulations acts as a low-pass filter, smoothing the current throughput, reducing the instantaneous I_c experienced at switching events, particularly at lower wind speeds, and, therefore, reducing the switching losses at lower wind speed.

These results validate that the mean temperature will increase with increasing wind speed in a PMSG power module, and highlight the importance of providing an equivalent reactive load to emulate the power module conditions in future testing.

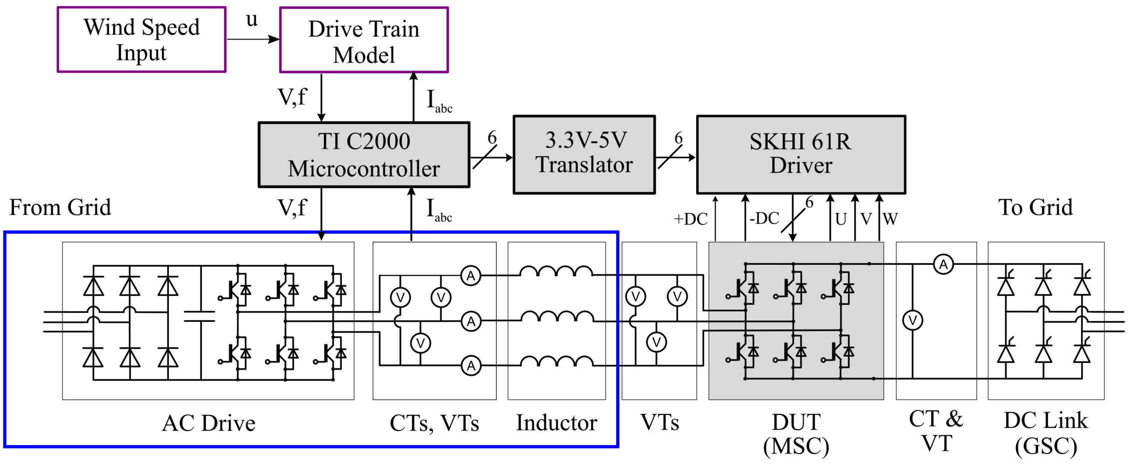

Fig. 7 *Test bench to allow variable wind condition testing*

6 Ongoing research: commercial test bench

This paper has provided a starting point for power converter reliability testing, but has highlighted a need for more advanced, larger scale testing of devices. In response, Anecto have supported an ongoing research project to construct a larger rig to emulate more realistic variable wind turbine operating conditions applied to a power converter in a laboratory environment.

This rig is based on the test bench described here, with several changes implemented to extend the operational range for more realistic, industrial-scale testing. Fig. 7 details the configuration of the larger wind turbine emulation rig. There are a number of enhancements over the current setup to the rig planned and under construction:

- The current has been reversed so that the DUT is configured as a rectifier as it is in simulation.
- To emulate a wind turbine drive train and generator (a requirement from Section 5.2), an AC–AC converter and inductor bank have been added that act as the generator armature and reactance, respectively.
- The load bank in Fig. 3 has been replaced with a DC link for regeneration.
- The control has been significantly expanded to allow for closed-loop control of the AC–AC converter and DUT to emulate wind turbine conditions more closely by allowing varying conditions. Much of this control is based on the model constructed in [4].

The test bench is designed to test a 600 V_{ces}, 30 A MiniSKiiP 15AC066V1 power module [11] to examine the impact of scaling factors on the temperature results as compared to the 6 A device. There is also scope to test at wind turbine drive train currents at ANECTO's industrial facilities once the intermediate rig has been constructed and validated.

7 Conclusions

A holistic approach to wind turbine power converter reliability is proposed. This includes a combination of effective drive train modelling, simulation, and physical emulation of the power converter and its junction temperature (T_j) response under realistic wind turbine operating conditions. This paper provides details of the experimental rig construction and validation.

Power module failure has been linked to power module thermal loading. As such, a unique approach of using high-frequency, low-cost PbSe photoconductive IR sensors has been used to capture the fundamental frequency temperature variations on a simplified drive train rig in the laboratory.

The results were compared to simulations in previous work. The increase in mean T_j of the IGBT in the simulations was validated experimentally, and the results highlighted the need to incorporate the reactive component of the PMSG. This led to a proposed commercial test bench being constructed in collaboration with Anecto to bring more realistic testing regimes to the wind industry.

8 Acknowledgments

This work was in part supported by the EPSRC SUPERGEN Wind Hub [grant number EP/L014106/1] and Impact Acceleration Account funding from Durham University.

9 References

[1] Spinato, F., Tavner, P.J., van Bussel, G.J.W., *et al.*: 'Reliability of wind turbine subassemblies', *IET Renew. Power Gener.*, 2009, **3**, pp. 387–401

[2] Carroll, J., McDonald, A., McMillan, D.: 'Reliability comparison of wind turbines with DFIG and PMG drive trains', *IEEE Trans. Energy Convers.*, 2015, **30**, (2), pp. 663–670

[3] Xie, K., Jiang, Z., Li, W.: 'Effect of wind speed on wind turbine power converter reliability', *IEEE Trans. Energy Convers.*, 2012, **27**, pp. 96–104

[4] Smith, C.J., Crabtree, C.J., Matthews, P.C.: 'Impact of wind conditions on thermal loading of PMSG wind turbine power converters', *IET Power Electron.*, Accepted Manuscript, 2017, **10**, 11, pp. 1268–1278

[5] Wintrich, A., Nicolai, U., Tursky, W., *et al.*: '*Application manual power semiconductors*' (SEMIKRON International GmbH, Nuremberg, Germany, 2015)

[6] RS: 'RS pro k type thermocouple glass fibre 2 m 0.3 mm diameter −50°C + 750°C', 2017. Available at http://uk.rs-online.com/web/p/products/6212170/

[7] Avenas, Y., Dupont, L.: 'Evaluation of IGBT thermo- sensitive electrical parameters under different dissipation conditions-comparison with infrared measurements', *Microelectron. Reliab.*, 2012, **52**, (11), pp. 2617–2626

[8] Thorlabs: 'Fdpse2 × 2 lead selenide photoconductor user guide', 2017. Available at https://www.thorlabs.com/drawings/c7b0c7db2ebcb5c-75C9AC04-5056-2306-D929B1EBB3AF0DB5/FDPSE2X2-Manual.pdf

[9] SEMIKRON: 'Skiip 01nac066v3', 2017. Available at https://www.semikron.com/dl/service-support/downloads/download/semikron-datasheet-skiip-01nac066v3-25232340/

[10] SEMIKRON: 'Skinter technology', 2015. Available at http://www.semikron.com/innovation-technology/construction-and-connectiontechnology/skinter-technology.html

[11] SEMIKRON: 'Skiip 15nac066v1', 2017. Available at https://www.semikron.com/dl/service-support/downloads/download/semikron-datasheet-skiip-15ac066v1-25230700/

This article has been accepted for publication in a future issue of this journal, but has not been fully edited. Content may change prior to final publication. Citation information: DOI 10.1109/TSTE.2019.2904113, IEEE Transactions on Sustainable Energy

Modeling, Analysis and Validation of Controller Signal Interharmonic Effects in DFIG Drives

Nur Sarma, *Member, IEEE*, Paul M. Tuohy, Siniša Djurović, *Member, IEEE*

***Abstract*—This paper presents the development of a doubly fed induction machine (DFIG) harmonic model in MATLAB/Simulink, which is used to examine the spectral content of DFIG controller signals and improve the understanding of their behavior and spectral nature. The reported DFIG harmonic model has the capability of representing the effects of higher order time and space harmonics and thus, allows detailed analysis of the controller signals embedded spectral effects. The model consists of a wound rotor induction machine (WRIM) harmonic model coupled with a stator flux oriented controller (SFOC) model. The WRIM space harmonic effects are represented using the conductor distribution function approach to enable the calculation of winding inductances as harmonic series. In addition, analytical expressions are derived to define the possible spectral content in the controller signals of DFIGs. Both the reported DFIG harmonic model and the analytical equations are validated by comparison with measurements taken from a purpose built vector controlled DFIG laboratory test-rig. The findings confirm the capability of the developed DFIG harmonic model in representing the controller signals embedded spectral effects, as well as the accuracy of the reported analytical expressions, and enable a much improved understanding of the spectral nature of the DFIG controller signals.**

***Index Terms*—Doubly fed induction generator, harmonics, interharmonics, stator flux oriented control, wind turbines.**

I. Introduction

COMPREHENSIVE electric machine and drive modeling, which allows for detailed analysis of spectral effects in operational parameters is increasingly required in a number of areas such as condition monitoring and fault detection [1], renewable power generation [2], harmonic control in electrical power systems for power quality studies [3] and harmonic torque analysis [4]. As the doubly fed induction generator (DFIG) topology is presently one of the most commonly used in power generator applications [5, 6], DFIGs have received a high level of research interest. A DFIG comprises a wound rotor induction machine (WRIM) whose rotor is interfaced to the grid via a back-to-back converter whilst the stator is directly connected to the grid.

Interharmonics are frequency components that are not integer multiples of the fundamental frequency of the supply system/grid. Like harmonics, interharmonics can also cause overheating, component life reduction, torque oscillations and voltage fluctuations, etc., [7]. Several studies have been presented in the literature investigating interharmonic effects in DFIG terminal quantities and mechanical signals [8, 9, 10]. For example, the interharmonic effects created by higher order stator and rotor supply harmonics in grid connected DFIG systems were investigated using stator and rotor currents, electromagnetic torque and frame acceleration signals measurements [8, 10]. In addition, a number of papers have examined the general spectral content of various electrical and mechanical signals from DFIGs such as the stator currents [11], rotor currents [12], stator active power [13] and stator reactive power [14]. Switching harmonics effects were studied in [9] using electromagnetic torque measurements and the stator and rotor currents for stand-alone DFIG systems. [15] reported a study of the spectral contents of voltage and current signals at the generator terminals and the high voltage points of interconnections of MW size commercial DFIG's, and emphasized that the interharmonics caused by the nonsinuosidal winding distribution were an important contributor to wind generator interharmonic emissions.

There have been limited studies investigating the spectral contents of DFIG controller signals and in particular, the interharmonics effects in these due to the nonsinusoidal distribution of the generator windings. Some research has been conducted on the *dq*-axis rotor currents [16], *dq*-axis rotor currents controller error [17] and rotor modulating signals [18]. These were driven by diagnostic purposes and constrained to investigating the fundamental harmonic related effects only and therefore did not cater for higher order components in the controller signals' spectra, nor provide the general wide band spectral contents definition of the examined signals. Better understanding of the wide band spectral nature of the controller signals, and their interharmonic contents arising from generator nonsinusoidal windings distribution in particular, could enable research on improved mitigation of associated DFIG electro-mechanical interharmonic effects leading to enhanced utilization of existing DFIG systems through: establishment of dedicated controllers for harmonic emissions and thus, power quality improvements through dedicated current injection at target frequency (or frequencies) to reduce or eliminate undesirable terminal quantity spectral components. The development of such solutions would dispense of the need for usage of costly filter banks that seems prevalent in current practice [19]. This is not only constrained to power quality and electrical stress issues mitigation but could be extended to the mitigation of undesirable mechanical stress in the drivetrain. Furthermore, enabling better understanding of the control loop signals general spectral nature can also enable their improved spectral interpretation and its correlation with operating conditions and therefore, create opportunities for more effective use of readily available controller signals for advanced condition monitoring. For this to be achieved, suitable dynamic models are required that can represent the relevant controller embedded spectral effects. This paper aims to progress this area by reporting an experimentally validated modeling study of DFIG controller embedded interharmonic effects arising from nonsinusoidal

N. Sarma is with Duzce University, Konuralp/Merkez, Duzce, Turkey, 81620 (e-mail: nursarma@duzce.edu.tr).

P. M. Tuohy and S. Djurović are with The University of Manchester, Manchester, UK, M13 9PL (e-mail: sinisa.durovic@manchester.ac.uk).

This article has been accepted for publication in a future issue of this journal, but has not been fully edited. Content may change prior to final publication. Citation information: DOI 10.1109/TSTE.2019.2904113, IEEE Transactions on Sustainable Energy

distribution of the windings and their analytical definitions.

A DFIG model required to underpin the controller signals interharmonic analysis has to be capable of considering a given electric machine design's relevant electromagnetic phenomena that gives rise to air-gap field harmonic effects such as the non-sinusoidal distribution of the windings. Furthermore, the simulation time must be sufficiently rapid to allow implementation of the complex controller system architecture in a DFIG [20]. A two-axes (*dq*) [21] or a three-axes (*abc*) [22] modeling approach is conventionally used for DFIG control studies due to their simplicity and fast simulation speed. However, these modeling techniques do not represent the higher order air-gap magnetic field effects and are therefore not capable of facilitating complete DFIG interharmonic studies. Proprietary commercial models aimed at power system studies exist that represent DFIG terminal quantity harmonic emissions; these are however not designed for high fidelity drive behavior analysis and ignore MMF harmonics and their associated interharmonic effects [23].

As a numerical modeling technique, the finite element method (FEM) can be used to model DFIGs [14]. FEM uses the magnetic vector potential method, the geometry of an electric machine and layout of the stator and rotor windings, along with material properties to produce a detailed machine model. As a result, FEM models are capable of credible representations of higher order field effects. However, they are also highly computationally intensive and their accuracy is dependent on mesh density: fine meshing causes a longer model execution time [13] but is nevertheless typically required to obtain good quality results. Extended calculation time is not a desirable feature of an electric machine model that needs to interface with a control algorithm and thus, FEM models are not a practical optimal choice for facilitating effective stator flux oriented control (SFOC) scheme DFIG model based interharmonic studies.

The magnetic equivalent circuit (MEC) method is another technique used for modeling DFIGs [20]. MEC uses a permeances network model comprising MMF sources and reluctances [24] to provide a high level representation of electro-magnetic effects, similar to that of FEM. However, MEC modeling complexity and long calculation times pose challenges in optimal use of this method where a control algorithm is included.

A DFIG harmonic model can also be modeled using the winding function approach (WFA) [25] and the conductor distribution function approach (CDFA) [26]. Both these techniques can cater for the non-sinusoidal distribution of the windings and their associated magnetic field effects. Furthermore, both techniques have a relatively fast computational time compared to numerical modeling techniques such as FEM. CDFA was previously used in [10, 27] to model an open-loop DFIG system in MATLAB. However, these works did not include the control system in the DFIG model and therefore cannot facilitate the investigation of the controller embedded signals.

This paper utilizes CDFA modeling principles to build a harmonic model of the WRIM that is then coupled to a full SFOC scheme model to establish a novel DFIG harmonic model architecture capable of representation and analysis of the wide band spectral effects of SFOC scheme signals and their dynamic behavior. The developed model is capable of mapping the variations in the wide band spectrum of both the outer and inner controller signals due to the nonsinuosidal distribution of the stator and rotor windings. Its implementation procedure in the widely used SIMULINK software platform, to enable straightforward adoption and utilization of the proposed modeling principles, is provided. The model is developed to perform a study of the wide band spectral content of DFIG controller signals with a focus on interharmonic effects. In addition, this work undertakes an analytical study of the possible frequency (or frequencies) contents of the SFOC scheme inner and outer control loop signals, and derives a set of closed form equations that relate wide band spectral frequencies of individual controller signals with DFIG operating conditions. These equations are generalized and enable effective prediction and analysis of the controller signals spectral signatures of interest. The reported results and analytical analysis from the DFIG harmonic model are validated via a range of laboratory tests on a purpose built grid connected 30 kW SFOC scheme DFIG test system that facilitates access to the controller signals.

II. DFIG Harmonic Model

The DFIG harmonic model is developed by integrating a WRIM harmonic coupled-circuit model with an SFOC model.

A. Harmonic Coupled-circuit Model of a WRIM

The WRIM model uses the coupled-circuit approach based on the principles of complex conductor distribution theory to calculate the electric machine inductances for any distribution of windings conductors [16, 28]. In addition, higher order air-gap MMF harmonics are considered during the inductance calculations. The model enables representation of an arbitrary number of phases and windings. The WRIM behavior in Simulink is defined by conventional equations as:

$$[V]=[R][I]+\frac{d}{dt}\{[L][I]\} \tag{1}$$

$$T_e=\frac{1}{2}[I]^T\frac{d[L]}{d\theta}[I] \tag{2}$$

$$T_e-T_{load}=J\frac{d}{dt}\omega_m \tag{3}$$

$$\omega=\frac{d\theta_m}{dt} \tag{4}$$

where: [V] is the voltage vector [V]; [R] is the resistance matrix [Ω]; [I] is the current vector [A]; [L] is the inductance matrix [H]; T_e is the electromagnetic torque [N.m]; T_{load} is the load torque [N.m]; J is the rotor inertia [kg.m^2]; ω_m is the rotor mechanical speed [rad/s]; and, θ_m is the rotor mechanical angle [rad]. The stator voltages, windings parameters, rotor inertia and load torque are assumed to be known in the simulations.

The coupled-circuit model includes the space harmonic effects by employing CDFA principles to evaluate the coupling between windings as a harmonic summation [16, 17]. For any layout of windings, this allows the effective evaluation of the self-inductances and mutual-inductances, as illustrated in Fig. 1, by integrating the contributions of individual air-gap magnetic field harmonics.

The total harmonic coupling between an arbitrary stator/rotor winding x and an arbitrary stator/rotor winding y is calculated as [27]:

$$L_{xy}=\frac{\mu_0 w\pi d^3}{2g}\sum_{v=-\infty}^{v=\infty}k_{sk}^{v}\frac{\overline{C_x^k}\,\overline{C_y^k}}{v^2}e^{-j\left(\frac{2v\beta(t)}{d}\right)} \tag{5}$$

This article has been accepted for publication in a future issue of this journal, but has not been fully edited. Content may change prior to final publication. Citation information: DOI 10.1109/TSTE.2019.2904113, IEEE Transactions on Sustainable Energy

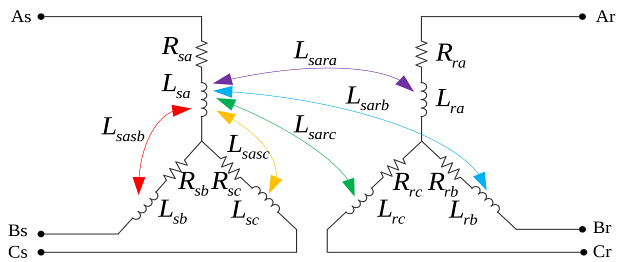

Fig. 1. Illustration of the harmonic coupling between the stator a-phase winding of the WRIM with all other machine windings.

where: μ_0 is the permeability of free space [H.m^{-1}]; w is the stack length [m]; d is the mean air-gap diameter [m]; g is the air-gap length [m]; k_{sk} is the ν^{th} harmonic skew factor; $\overline{C_x^k}$ is the ν^{th} harmonic complex conductor distribution of an arbitrary winding x [turns/m]; $\overline{C_y^k}$ is the ν^{th} harmonic complex conductor distribution of an arbitrary winding y [turns/m]; and, $\beta(t)$ is the rotor displacement [m]. When evaluating the coupling between any stator-to-stator or rotor-to-rotor windings, $\beta(t)$ is set to zero whereas it is variable when performing stator-to-rotor or rotor-to-stator coupling calculations.

The WRIM harmonic model is formed by the system of equations given in (1)-(5). The model is solved using an appropriate time-stepping iterative procedure in Simulink, as shown in Fig. 2. The procedure ensures that at any given rotor step, the harmonic coupling is evaluated and superimposed in the calculations to enable the representation of space harmonic effects in the time and frequency domains [29]. The general Simulink block representation of the model is shown in Fig. 2.

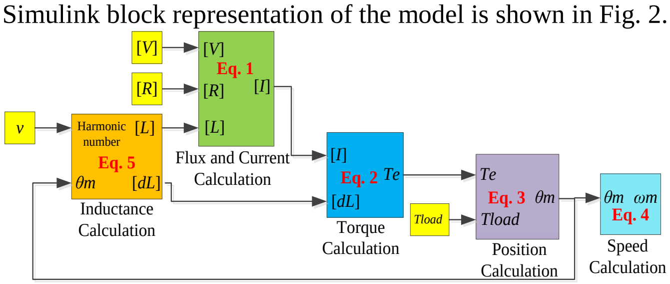

Fig. 2. WRIM harmonic coupled-circuit model block diagram.

B. Controller System of a DFIG

The SFOC scheme is one of the most common DFIG control schemes [30] and is thus used in this work. SFOC enables the independent control of DFIG stator active (P_s) and reactive (Q_s) powers by manipulating the two-axis rotor currents in a synchronously rotating reference frame (dq). Therefore, three-phase (abc) variables of the DFIG must be first converted into their dq-axis equivalents before executing the SFOC. The transformation of abc-axis variables is achieved via the orientation angle (θ_s), i.e. the angle between the d-axis of the synchronously rotating reference frame and the d_s-axis of the stationary reference frame.

The SFOC scheme comprises two cascade control loops for both the d- and q-axis, i.e. outer (power) loops and inner (current) loops, respectively, as illustrated in Fig. 3.

In Fig. 3: Q_s* is the reference reactive power [var]; P_s* is the reference active power [W]; I_{rd}* and I_{rq}* are the d-axis and q-axis rotor currents [A], respectively; V_{rd}* and V_{rq}* are the d-axis and q-axis reference rotor voltages [V], respectively; reference V_{ra}*, V_{rb}* and V_{rc}* are the abc-axes

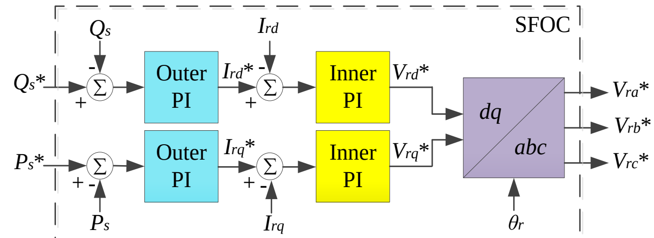

Fig. 3. Block diagram representation of the SFOC scheme.

reference rotor voltages [V], respectively; and, θ_r is the rotor angle [rad] used for transformation of the rotor variables from dq- to abc-axes (i.e. the angle between the synchronous and rotor reference frame). The outer loops calculate the values of the reference dq-axes rotor currents for the inner control loops, and are defined as [31]:

$$P_s = -V_{sq}\frac{L_m}{L_s}I_{rq} \tag{6}$$

$$Q_s = V_{sq}\frac{\psi_{sd}}{L_s} - V_{sq}\frac{L_m}{L_s}I_{rd} \tag{7}$$

where: V_{sq} is the q-axis component of the stator voltage vector [V]; L_m is the magnetizing inductance [H]; L_s is the stator self-inductance [H]; I_{rq} and I_{rd} are the rotor currents vectors q-axis and d-axis components, respectively [A]; and, ψ_{sd} is the stator flux linkage vector d-axis component [Wb].

The SFOC scheme inner loops calculate the reference dq-axes rotor voltages, which can be written as [32]:

$$V_{rd} = R_r I_{rd} + L_c\frac{dI_{rd}}{dt} - \omega_{slip}L_c I_{rq} \tag{8}$$

$$V_{rq} = R_r I_{rq} + L_c\frac{dI_{rq}}{dt} + \omega_{slip}L_c I_{rd} + \omega_{slip}\frac{L_m}{L_s}\psi_{sd} \tag{9}$$

where: V_{rd} and V_{rq} are the d-axis and q-axis components of the rotor voltage vector, respectively [V]; R_r is the stator referred rotor phase resistance [Ω]; L_c is the leakage coefficient [H]; and, ω_{slip} is the angular slip speed [rad/s].

The outer and inner PI controllers were tuned using a conventional transfer function approach [33]. In this tuning approach, the inner controllers are tuned via (8) and (9) whilst the outer controllers are tuned via (6) and (7). The parameters of the outer and inner control loops were calculated from their closed-loop transfer functions [34]. The outer and inner PI controllers' parameters must be chosen carefully to provide satisfactory performance, since they can affect the quality of the generated power [35]. It is important to choose appropriate time constants for both the outer and inner control loops, to ensure adequate controller performance during the calculations. Choosing different time constants generates separation of the outer and inner control loops, which is ideal for implementation of the cascade control loops. The time constant of the inner control loops was set to be at least five times smaller than that of the outer control loops in this work.

C. Simulink Implementation of a DFIG Harmonic Model

A DFIG harmonic model was developed by integrating the WRIM harmonic model, shown in Fig. 2, with the SFOC model. The block diagram representation of the DFIG harmonic model in the Simulink environment is provided in Fig 4.

This article has been accepted for publication in a future issue of this journal, but has not been fully edited. Content may change prior to final publication. Citation information: DOI 10.1109/TSTE.2019.2904113, IEEE Transactions on Sustainable Energy

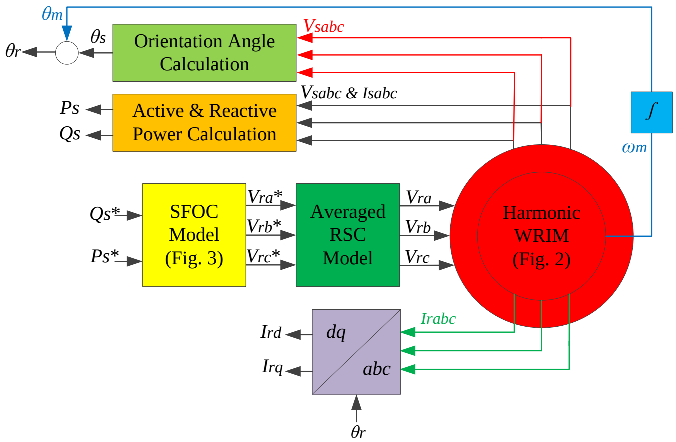

Fig. 4. Block diagram representation of the DFIG harmonic model.

A single frequency voltage source was used in the averaged Rotor Side Converter (RSC) Model, as represented in Fig. 4, since the representation of switching harmonics is beyond the focus of this study, but could easily be achieved by replacing the averaged RSC model with a switched one. The WRIM operational speed, ω_m, was emulated in Simulink by pre-setting the desired speed point. The *Orientation Angle Calculation* block (Fig. 4) calculates the orientation angle (θs) using the three-phase stator voltages [36]. During this calculation, the *d*-axis of the synchronously rotating reference frame is aligned with the stator flux linkage vector and its *q*-axis with the stator voltage vector, since the stator resistance can typically be neglected [37]. The reference three-phase rotor voltages, shown in Fig. 4, are the stator referred values. Therefore, before supplying the rotor windings of the WRIM, the rotor voltages must be transformed back into their natural values using the turns ratio for accurate execution of the developed simulation model.

The WRIM model equations (1-4), the non-linear time-varying inductance equation (5), and the SFOC scheme controller system equations (6-9) form the DFIG harmonic mathematical model and are solved in Simulink at each integration step for a given rotor position in an appropriate time-stepping numerical procedure. It is important to choose a suitable integration step for accurate calculation of the orientation angle, as well as other model variables. The step choice is principally driven by control loop dynamics, and not by the significantly slower electric machine (i.e. WRIM) dynamics. The proprietary Simulink Runga-Kutta integration method with a (1/15) ms step size was used in this work due to its relative accuracy.

The SFOC requires accurate information of WRIM parameters. Therefore, performance of the simulations can be degraded if the actual electric machine parameters differ from those used in the control system. In addition, the current controllers need to be carefully tuned to ensure system stability and adequate response within the whole operating range, as well as to obtain sufficient simulation performance. Finally, in order to optimize model execution time, the WRIM self and leakage inductances were pre-calculated and stored in look-up tables, which were read at each simulation integration step. The pre-calculated inductance values were also used to calculate the PI controllers' parameters at the beginning of each simulation.

III. Analysis of DFIG Controller Signals Spectra

This section reports an analytical study of the possible spectral content of DFIG SFOC signals, with a focus on interharmonic effects arising from WRIM space harmonics. The DFIG supply is assumed to be a balanced fundamental frequency three-phase system and the WRIM is assumed to be electrically balanced. Furthermore, the rotor converter switching effects are neglected. The derivations are performed for a general case of a three-phase, *p* pole-pair, DFIG system. The general equations defining the time/frequency domain nature of the DFIG currents and voltages signals under these assumed constraints can be written as [9 - 11, 23]:

$$V_{sabc}(t) = V_M \cos(\omega_s t + \varphi_v) \tag{10}$$

$$I_{sabc}(t) = \sum_k I_{sM}^k \cos([1 \mp 6k(1-s)]\omega_s t + \varphi_{Is}) \tag{11}$$

$$V_{rabc}(t) = \sum_k V_{rM}^k \cos([s \mp 6k(1-s)]\omega_s t + \varphi_{Vr}) \tag{12}$$

$$I_{rabc}(t) = \sum_k I_{rM}^k \cos([s \mp 6k(1-s)]\omega_s t + \varphi_{Ir}) \tag{13}$$

where: V_M is the peak value of the stator voltage [V]; φ_v is the phase shift between the three-phase stator voltages [rad]; I^k_{sM} is the peak value of the k^{th} harmonic stator current [A]; φ_{Is} is the phase shift between the three-phase stator currents [rad]; *s* is the slip; *k* is the air-gap magnetic field pole number (*k* = 0, 1, 2,...); V^k_{rM} is the peak value of the k^{th} harmonic rotor voltage [V]; φ_{Vr} is the phase shift between the three-phase rotor voltages [rad]; I^k_{rM} is the peak value of the k^{th} harmonic rotor current [A]; and, φ_{Ir} is the phase shift between the three-phase rotor currents [rad]. The phase shift between the three-phase fundamental values is accounted for as $2\pi/3$.

Equations (10) and (11) allow for the derivation of the equation defining the nature of the DFIG stator active power signal by multiplying the corresponding voltage and current terms [38] as:

$$P_s(t) = V_{sa} I_{sa} + V_{sb} I_{sb} + V_{sc} I_{sc} \tag{14}$$

Hence, the resultant total instantaneous active power equation can be written as:

$$P_s(t) = \frac{3}{2} \sum_k V_M I_{sM}^k \cos([6k(1-s)]\omega_s t) \tag{15}$$

The stator total instantaneous reactive power is calculated using (10) and (11) as [39]:

$$Q_s(t) = \frac{1}{\sqrt{3}} [(V_{sb} - V_{sc}) I_{sa} + (V_{sc} - V_{sa}) I_{sb} + (V_{sa} - V_{sb}) I_{sc}] \tag{16}$$

giving the total instantaneous reactive power equation:

$$Q_s(t) = \frac{3}{2} \sum_k V_M I_{sM}^k \sin([6k(1-s)]\omega_s t) \tag{17}$$

The analytical equations describing the time/frequency domain nature of the DFIG rotor *dq*-axis currents in the stator flux aligned reference frame can be derived after applying the standard Park transformation to the instantaneous three-phase rotor currents, as defined in (13), as:

$$I_{rd}(t) = \sqrt{\frac{3}{2}} \sum_k I_{rM}^k \cos([6k(1-s)]\omega_s t) \tag{18}$$

$$I_{rq}(t) = \sqrt{\frac{3}{2}} \sum_k I_{rM}^k \sin([6k(1-s)]\omega_s t) \tag{19}$$

This article has been accepted for publication in a future issue of this journal, but has not been fully edited. Content may change prior to final publication. Citation information: DOI 10.1109/TSTE.2019.2904113, IEEE Transactions on Sustainable Energy

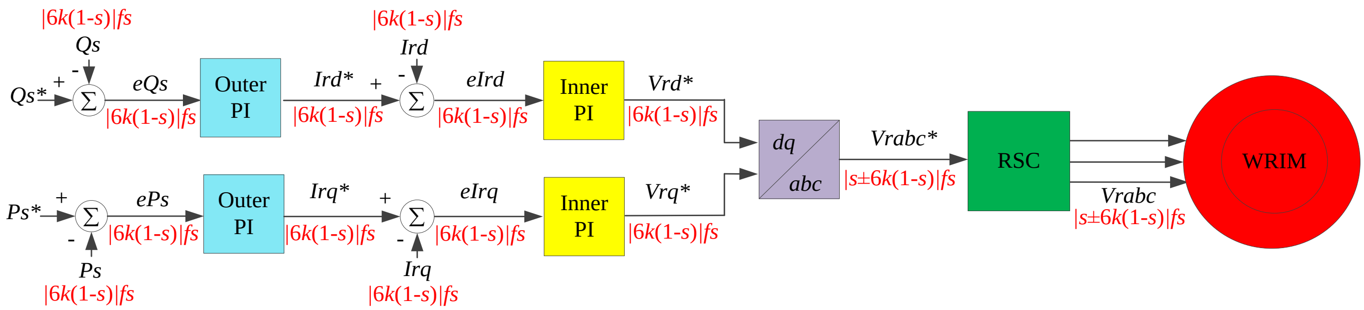

Fig. 5. Flowchart of the DFIG SFOC strategy showing individual signals possible spectral content definition.

The stator active and reactive power signals, and the stator flux oriented rotor *dq*-axis current signals, are the inputs to the SFOC. Therefore, their spectral nature will largely define the spectral nature of the remaining SFOC signals, depending on the controller loops bandwidths. The closed form analytical expressions that define the possible frequency components of electromagnetic origin of SFOC controller signals can therefore be obtained from the presented derivations and are summarized in Table I. These show that the controller signals spectral contents are predominantly dependent on the operating speed, stator supply frequency and possible air-gap magnetic field pole-numbers. The fundamental harmonic or DC component frequency is obtained for $k = 0$ in the corresponding expressions, while the speed-dependent frequencies are obtained for k = 1, 2, 3...

The DFIG SFOC is implemented on two separate magnetic axes (*d* and *q*). Assuming equally tuned controllers in both axes, as is conventional, the *d*- and *q*-axis frequency components behavior is expected to be identical and their spectral content the same. Furthermore, the expressions provided in Table I enable the evaluation of this content on each magnetic axis.

TABLE I
Signal Spectral Contents Closed Form Expressions.

V_{ra}, I_{ra}	P_s, Q_s, I_{rd}, I_{rq}
$\lvert s\pm6k(1-s)\rvert f_s$	$\lvert 6k(1-s)\rvert f_s$

The derived definitions of the DFIG SFOC signals embedded interharmonic effect are illustrated in the flowchart presented in Fig. 5. The figure shows that the error signals of the outer (*ePs* and *eQs*) and inner (*eIrd* and *eIrq*) controllers have the same frequency content as the inputs of the outer (*Ps* and *Qs*) and inner (*Ird* and *Irq*) controllers. This is caused by the DC nature of the controllers reference input signals.

IV. Test-Rig Description

An experimental investigation of the DFIG controller signals embedded interharmonic effects and validation of the reported DFIG harmonic model were achieved using a purpose built closed-loop controlled DFIG test-rig facility utilizing standard industrial converters.

The laboratory DFIG test-rig contains an industrial four-pole, three-phase, 50 Hz, 30 kW WRIM (machine parameters presented in Appendix A), which is mechanically coupled to a DC machine. The DC machine is operated as a prime mover in the test-rig and is used to provide a desired DFIG load point via a commercial DC machine drive. The reported experiments are undertaken for steady-state conditions to enable the analysis required for the purposes of this study.

The WRIM stator windings were directly connected to the grid, whereas the rotor windings were interfaced to the grid via a commercial back-to-back converter system. The back-to-back converter comprises a Control Techniques Unidrive SP-4401 grid side converter (GSC) and a Control Techniques Unidrive SP-4401 rotor side converter (RSC), coupled via a DC link. The SFOC scheme was implemented on the commercial converters through a dSPACE 1103 real-time controller platform via a purpose developed routine, which has previously been reported in [34, 40].

The real time control platform was also used for capturing relevant signal measurements during the experiments. This included the input signals to the inner and outer controller loops, i.e. the rotor currents and stator power signals, along with the controller embedded signals such as the PI controller inputs and finally the rotor voltage signals. The test rig was fully instrumented for monitoring the relevant DFIG electrical signals (i.e. stator currents and voltages) using LEM LA 55-P current and LEM LV25-600 voltage Hall effect transducers. The rotor mechanical speed was measured by a 1024ppr incremental encoder. The simplified layout of the laboratory test-rig is shown in Fig. 6.

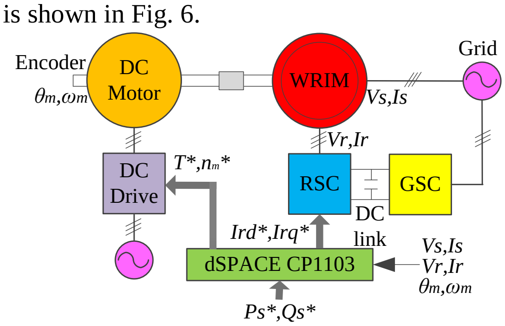

Fig. 6. DFIG experimental test-rig layout.

V. Experimental Study and Validation

The validation of the DFIG harmonic model and the derived expressions to represent both the fundamental and higher order MMF harmonic effects in the spectra of the controller signals, and the stator and rotor signals, as well as the experimental investigation of the DFIG controller signals embedded interharmonic effects, will be presented in this section. The underlying purpose of the presented analysis is not only to validate the proposed DFIG harmonic model and presented expressions, but to also facilitate an improved understanding of the wide band interharmonic spectral content of the SFOC signals. For brevity, the rotor variables from a single phase (phase-*a*) were chosen for the presentation of results. However, it is to be noted that practically the same

This article has been accepted for publication in a future issue of this journal, but has not been fully edited. Content may change prior to final publication. Citation information: DOI 10.1109/TSTE.2019.2904113, IEEE Transactions on Sustainable Energy

results were observed in the other phases.

The DFIG harmonic model time domain results were processed using a Fast Fourier transform (FFT) function with a 2^{17} point rectangular window length. The measured experimental results were imported into MATLAB, where they were also processed using FFT analysis. A 2^{19} point FFT routine was implemented on the recorded experimental time-domain signals due to the sampling time limitations of the real time dSPACE platform. This phenomenon has been previously discussed in greater detail in [34]. Although a different number of data points for the Simulink DFIG harmonic model and the experimental data were used, both of their spectral analyses gave the same resolution (< 0.1 Hz) for consistency.

A. Validation Study

The validation of the DFIG harmonic model and the derived expressions is presented in this sub-section. The model and experimental results are for a typical super-synchronous operating speed of 1,620 rpm. Closely similar spectral patterns to those observed for the presented operating point were identified throughout the operating range, but are not shown for the sake of brevity. The DFIG harmonic model and the laboratory test-rig were operated with active and reactive power demands of -6.5 kW and 0 var, respectively.

The predicted (blue, (a)) and measured (red, (b)) SFOC scheme signal spectra are shown in Figs. 7 to 20. The spectra are explored in a bandwidth of 0-700 Hz, as this is where the most pronounced spectral effects of interest were identified. In this spectral bandwidth, the air-gap magnetic field pole number values for k = 0, 1 and 2 are applied in the equations given in Table I, and the calculated results are presented in Table II for the examined operating speed.

TABLE II
Calculated Frequency Components for an Operating Speed of 1,620 rpm.

V_{ra}, I_{ra}			P_s, Q_s, I_{rd}, I_{rd}		
k = 0 (f_0)	k = 1 (f_1)	k = 2 (f_2)	k = 0 (f_0)	k = 1 (f_1)	k = 2 (f_2)
4 Hz	320 Hz 328 Hz	644 Hz 652 Hz	0 Hz	324 Hz	658 Hz

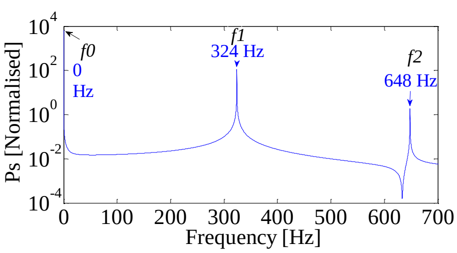

a. Simulation results

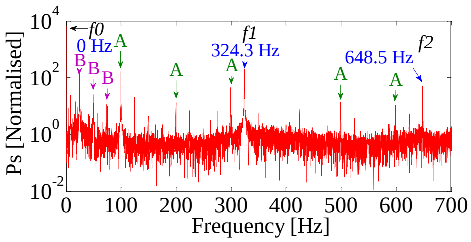

b. Experimental results

Fig. 7. FFT spectrum of the stator acive power signal for 1,620 rpm operation.

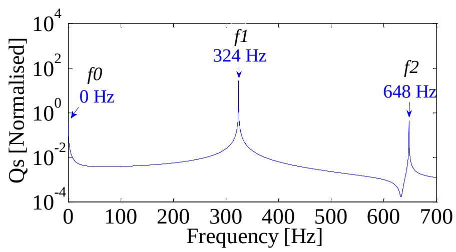

a. Simulation results

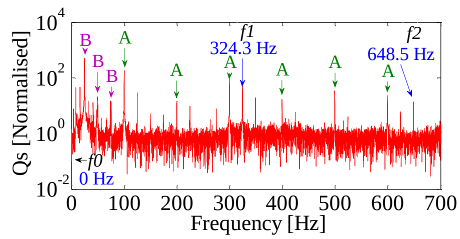

b. Experimental results

Fig. 8. FFT spectrum of the stator reactive power signal for 1,620 rpm operation.

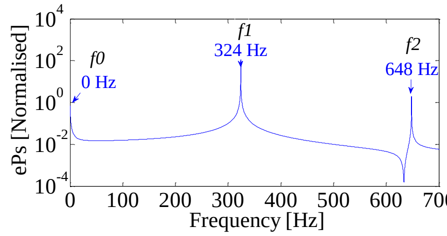

a. Simulation results

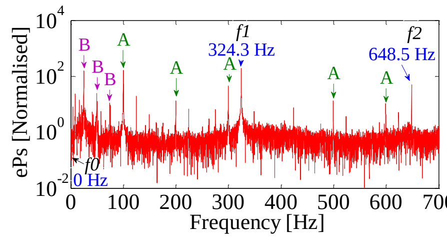

b. Experimental results

Fig. 9. FFT spectrum of the stator active power error signal for 1,620 rpm operation.

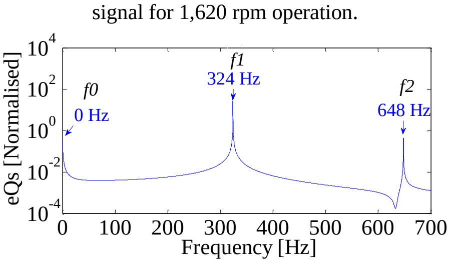

a. Simulation results

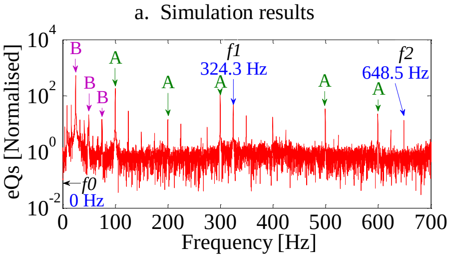

b. Experimental results

Fig. 10. FFT spectrum of the stator reactive power error signal for 1,620 rpm operation.

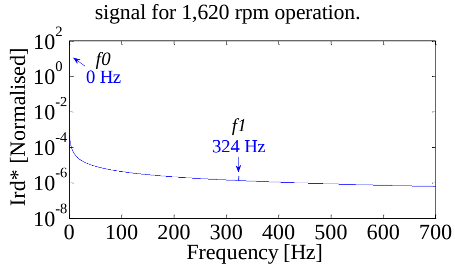

a. Simulation results

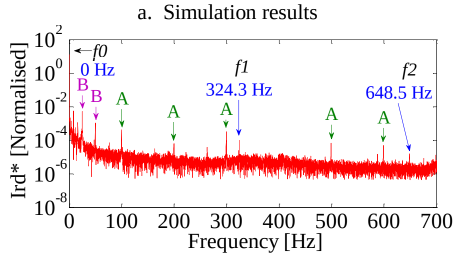

b. Experimental results

Fig. 11. FFT spectrum of the reference d-axis rotor current signal for 1,620 rpm operation.

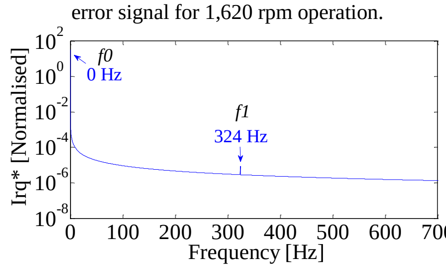

a. Simulation results

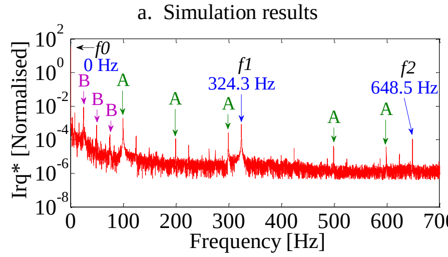

b. Experimental results

Fig. 12. FFT spectrum of the reference q-axis rotor current signal for 1,620 rpm operation.

This article has been accepted for publication in a future issue of this journal, but has not been fully edited. Content may change prior to final publication. Citation information: DOI 10.1109/TSTE.2019.2904113, IEEE Transactions on Sustainable Energy

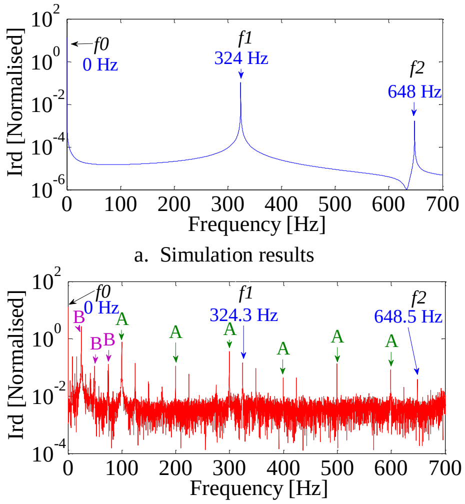

a. Simulation results

b. Experimental results

Fig. 13. FFT spectrum of the d-axis rotor current signal for 1,620 rpm operation.

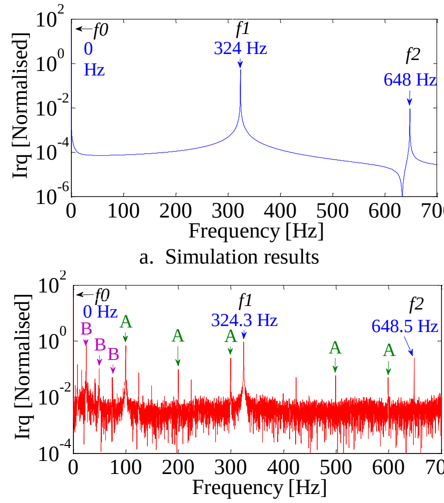

a. Simulation results

b. Experimental results

Fig. 14. FFT spectrum of the q-axis rotor current signal for 1,620 rpm operation.

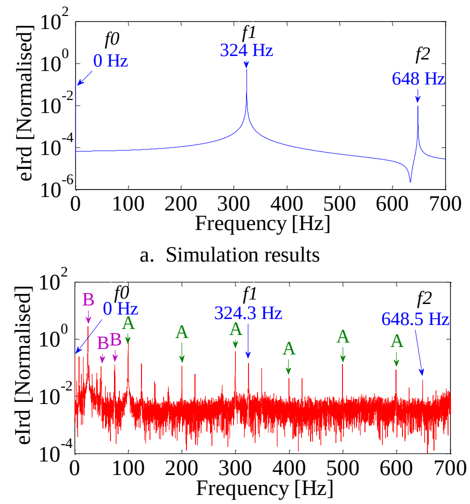

a. Simulation results

b. Experimental results

Fig. 15. FFT spectrum of the d-axis rotor current error signal for 1,620 rpm operation.

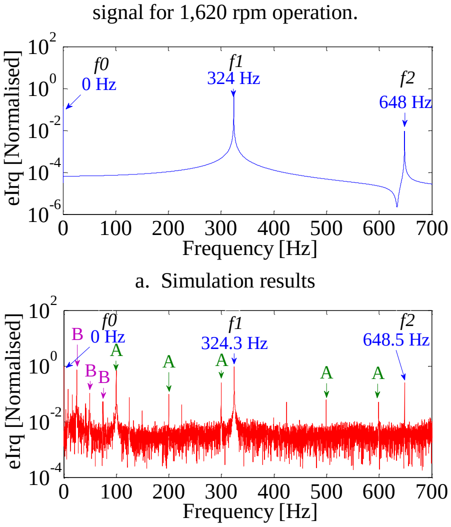

a. Simulation results

. Experimental results

Fig. 16. FFT spectrum of the q-axis rotor current error signal for 1,620 rpm operation.

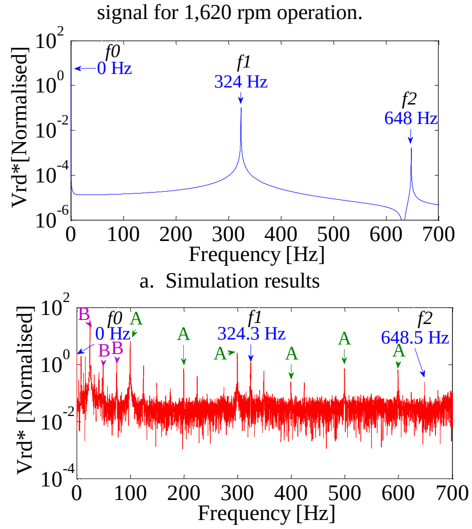

a. Simulation results

b. Experimental results

Fig. 17. FFT spectrum of the reference d-axis rotor voltage for 1,620 rpm operation

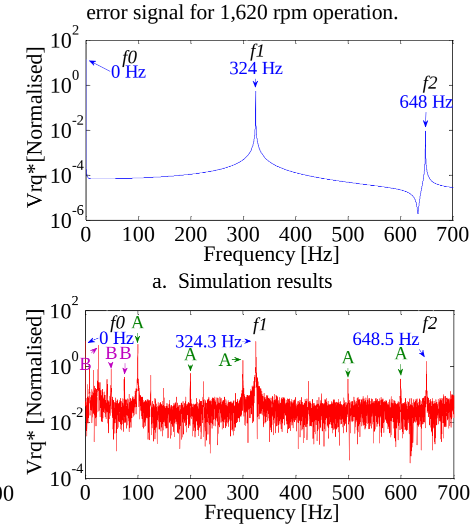

a. Simulation results

b. Experimental results

Fig. 18. FFT spectrum of the reference q-axis rotor voltage signal for 1,620 rpm operation

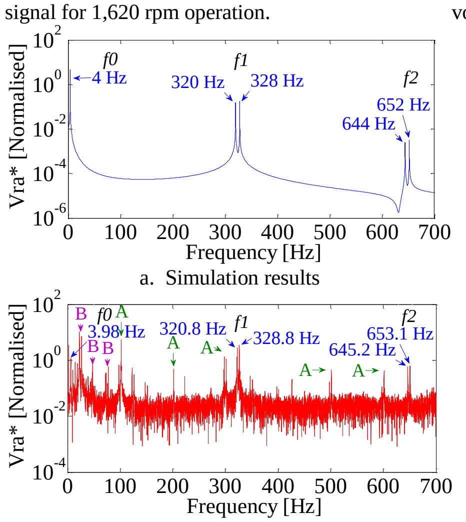

a. Simulation results

b. Experimental results

Fig. 19. FFT spectrum of the reference a-axis rotor voltage signal for 1,620 rpm operation.

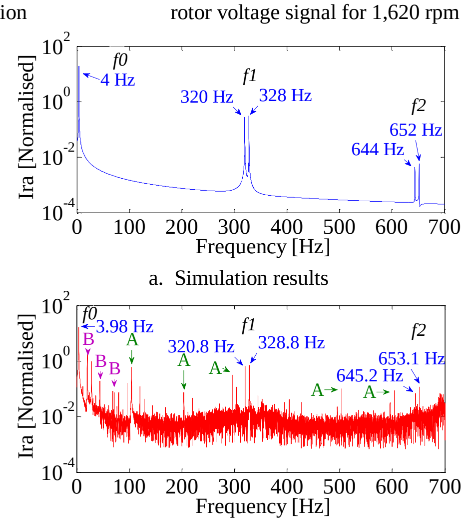

a. Simulation results

b. Experimental results

Fig. 20. FFT spectrum of the a-axis rotor current signal for 1,620 rpm operation.

Figs. 7-20 show the wide band interharmonic effects of the predicted and experimentally measured controller signals. The investigated frequency components are labeled in the figures using the nomenclature given in Table II, in order to enable straightforward comparison and validation of the calculated, predicted and experimental results. Figs. 7-20 show that f_0 is generally the dominant component for the controller signals (0 Hz) and the reference a-axis rotor voltage and current (~4 Hz). However, the dominant component for the outer and inner control loops error signals is f_1, as seen Figs. 9, 10, 15 and 16.

The presented data show good agreement between the predicted and measured results, both of which follow the spectral content patterns defined by the closed form equations derived from first principles in Table I. In addition to the expected fundamental supply and MMF harmonic induced spectral content, the examined electrical signals are seen to contain a number of additional interharmonic components, whose frequencies are accurately predicted by the proposed DFIG harmonic model and analytical expressions, and match those observed in the corresponding experimental spectra.

The labeled frequency components in Figs. 7-20 may appear in the spectra of the controller signals irrespective of what condition the DFIG operates, since these frequency components originate from the design of the WRIM. Therefore, it is important to fully understand their manifestation. For the examined operating point, the wide band interharmonics are calculated as 324 Hz and 658 Hz using the derived expressions. These are provided in Table II and are identified in Figs. 7-20 as f_1 and f_2, respectively. It can be seen from Figs. 7-20 that f_1 and f_2 are generally more pronounced in the q-axis signals spectra, since the reference reactive power was 0 var.

It is to be noted that the experimentally measured data contains additional frequency components to those predicted by the developed DFIG harmonic model. Some of these additional components are due to the effects of the higher order supply harmonics mapped at integer multiples of the supply frequency. These have been identified and labeled as 'A' in Figs. 7-20. Furthermore, the RSC switching harmonics, exhibited at *6ksf* frequencies, in the controller signals have also been identified and labeled as 'B' in Figs. 7-20 [10]. Additional effects are also expected to be present due to inherent electrical and mechanical unbalances but are not investigated or identified in this study for brevity. None of these additional frequency components are seen in the simulation results, since the sources of these effects were not modeled or considered during the simulations. The effects of these phenomena in the controller signals of DFIGs are presently being investigated and will be presented in future publications.

Figs. 11 and 12 show that, as expected, the outer PI controllers act as low-pass filters and suppress the magnitudes of the wide band interharmonic components coming from the error signals of the outer controllers seen in Figs. 9 and 10. This is also the case for the inner loops (Figs. 17 and 18). This attenuation effect is however more pronounced in the outer loops, since their bandwidth is significantly smaller than that of the inner loops.

B. Representation of Higher Order Space Harmonic Effects

The ability of (5) and thus, the DFIG harmonic model to represent the MMF fundamental, as well as the higher order space harmonic effects in the spectra of the controller signals, is presented in this sub-section using Figs. 21 and 22. For brevity, only the d- and q-axis rotor currents are chosen for the analysis of the presented results, as practically identical effects were observed in other controller signals.

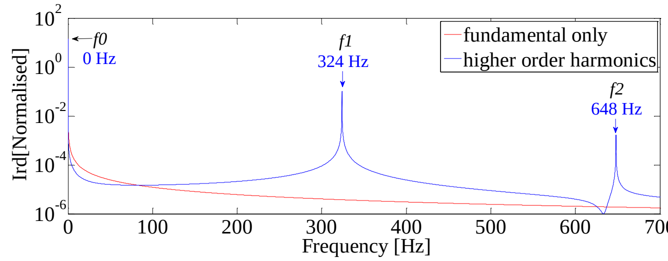

Fig. 21. FFT spectra of the predicted d-axis rotor current from the DFIG harmonic model for 1,620 rpm

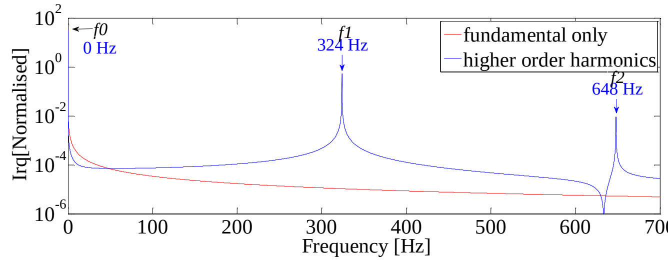

Fig. 22. FFT spectra of the predicted q-axis rotor current from the DFIG harmonic model for 1,620 rpm

Figs. 21 and 22 show the spectrum of the d- and q-axis rotor currents, respectively, by comparing the calculated signals when only the fundamental frequency (red) and also when the higher order MMF (i.e. coupling inductance) harmonics (blue) are considered. As Figs. 21 and 22 show, there is a significant difference when more than just the fundamental frequency is considered for the coupling inductance calculation presented in (5). However, the higher order MMF harmonic effects in the spectra are not represented when only the fundamental frequency MMF (i.e. harmonic inductance) is considered, and are identical to what would be obtained by application of a conventional two-axis dynamic (dq) electric machine model. The inclusion of the higher order harmonic effects is seen to provide a more accurate insight into the spectral signatures of the controller signals from DFIGs.

C. P_s and Q_s Demand Levels Influence Study on Interharmonic Magnitudes

The effects of changes in the active and reactive power demands on the examined controller signals interharmonics magnitudes are experimentally investigated in this sub-section. To understand these effects, two experiments were conducted.

In the first experiment, three step load levels were applied to the active power demand: 33.3%, 66% and 100%, whilst the reactive power demand was kept constant at 0 Var. The results of this experiment are presented in Figs. 23 and 25. In the second experiment, three step load levels were applied to the reactive power demand: 33.3%, 66% and 100% whilst the active power demand was kept constant at 0 W. The results of the second experiment are presented in Figs. 24 and 26. The test-rig was operated at 1,340 rpm during both experiments.

The dq-axis rotor currents, as well as the dq-axis rotor currents error signals are presented here for the sake of brevity, as closely similar behavior was observed in other controller signals but is not shown due to space restrictions.

Furthermore, the frequency components that were investigated in Section V.A are presented in this sub-section for consistency.

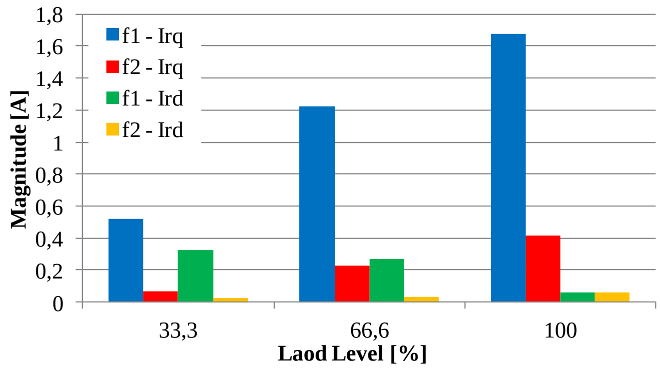

Fig. 23. Measured *dq*-axis rotor current interharmonic components magnitude in P_s change tests at 1,340 rpm

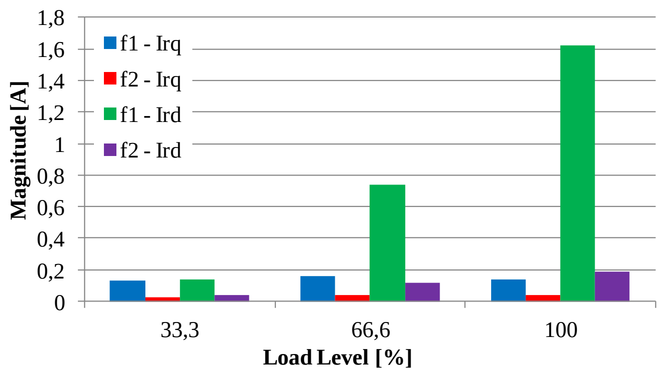

Fig. 24. Measured *dq*-axis rotor current interharmonic components magnitude in Q_s change tests at 1,340 rpm

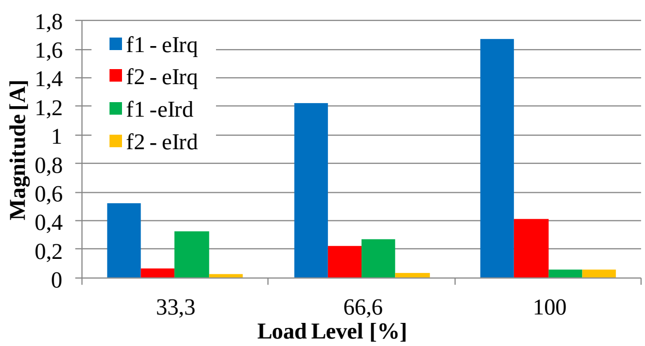

Fig. 25. Measured *dq*-axis rotor current error signal interharmonic components magnitude in P_s change tests

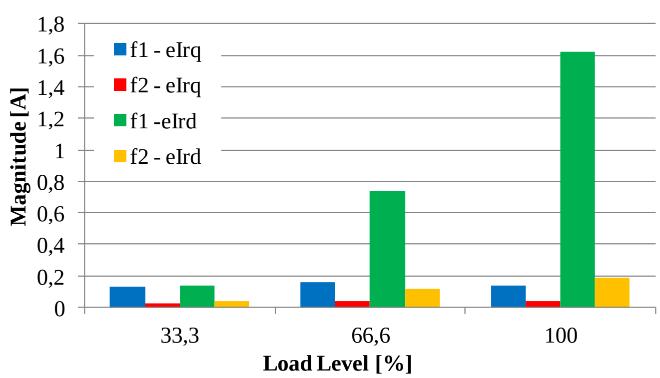

Fig. 26. Measured *dq*-axis rotor current error signal interharmonic components magnitude in Q_s change tests

Figs. 23 - 26 show that the magnitudes of the interharmonic components of the inner controller signals generally increase with increasing active and reactive power load levels. This is caused by an increase in the air-gap magnetic field strength with increasing load. Therefore, the highest magnitudes for each of the investigated interharmonic components are generally identified for 100% of active and reactive power load levels. However, the magnitude can sometimes decrease such as f1-Ird in Fig. 23 with increasing active power load levels. This may be caused by inherent supply and machine winding unbalances, which could cause suppressions of the magnetic fields.

VI. Conclusion

This paper investigates the DFIG controller embedded signals wide band spectral nature with a focus on interharmonic effects. The paper first presents the development of a novel, computationally efficient, DFIG harmonic model and its implementation procedure in the widely used Simulink environment. This work also reports closed form analytical expressions, derived from first principles, which define the possible wide band spectral content of the SFOC signals as a function of DFIG operating point parameters.

The performance of the developed DFIG harmonic model and the derived expressions were evaluated and validated using a purpose built grid connected DFIG experimental test-rig facility. To this end the controller signals spectra were examined and cross correlated using the derived expressions, model predicted and test-rig experimentally measured results. The influence of the generator air-gap MMF harmonic effects on the wide band spectral frequency content of the controller signals was investigated in detail, and their associated interharmonic spectral nature clarified. In general the WRIM MMF harmonics effects in the controller variables were observed at frequencies that are orders of $6(1\text{-}s)f_s$. The presented data shows that there is good agreement between the calculated, simulation and experimental results and thus, confirming the validity of the proposed model and closed from expressions.

The developed DFIG harmonic model and the derived expressions enable a clear representation and understanding of the spectral nature of DFIG controller signals, and can be used to underpin studies of controller embedded and other related spectral effects in DFIG drives to further the understanding of their behavior. Furthermore the reported model presents a versatile tool for analysis of harmonic effects in DFIG drives that can be expanded to cater for other spectral phenomena of interest such as inverter switching harmonics or grid imposed time harmonics. The presented conclusions are obtained from analysis undertaken on a typical academic scale DFIG system and would be expected to be applicable on a wide range of general DFIG designs. However, further research studies encompassing different commercial designs would be needed to confirm the generality of the observed phenomena.

This article has been accepted for publication in a future issue of this journal, but has not been fully edited. Content may change prior to final publication. Citation information: DOI 10.1109/TSTE.2019.2904113, IEEE Transactions on Sustainable Energy

VII. Appendix A

Wound Rotor Induction Machine Parameters.

PARAMETERS	VALUE	UNITS
Stator voltage	120	Vrms
Stator current	56	A
Full-load power	30	kW
Full-load speed	1470	rpm
Stator / Rotor resistance	0.09 / 0.066	Ω/phase
Stator leakage inductance	0.911	mH/phase
Rotor leakage inductance	0.459	mH/phase
Magnetizing inductance	44.6	mH/phase
Effective turns ratio	1.33	-

VIII. Appendix B

The electric machine geometry and the number of conductors in the slots are important variables for the calculation of electric machine inductances using the CDFA, since this method is based on the spatial distribution of winding conductors [11]. The CDFA for an arbitrary n^{th} stator or rotor coil is defined as [28]:

$$c_n(y) = \sum_{v=-\infty}^{v=\infty} \bar{C}_n^k e^{-jk_v y} \tag{20}$$

where:

$$\bar{C}_n^k = -j\frac{2N_n}{\pi d} k_b^v k_p^v e^{jk_v y_n} \tag{21}$$

In (21): v is the space harmonic order number (v = 1, 2, 3,...), y_n is the position of the center of the n^{th} coil [m], k_v is winding conductor distribution wave number of the v^{th} harmonic, N_n is the number of conductors in a slot, d is the mean air-gap diameter [m], k_b^v is the v^{th} harmonic slot mouth width factor, and, k_p^v is the v^{th} harmonic pitch factor of the n^{th} coil of a winding.

k_v is calculated as:

$$k_v = 2v / d \tag{22}$$

k_b^v is calculated as:

$$k_b^v = \sin\left(\frac{k_v b}{2}\right) / \left(\frac{k_v b}{2}\right) \tag{23}$$

and, k_p^v is calculated as:

$$k_p^v = \sin\left(\frac{k_v \alpha_n}{2}\right) \tag{24}$$

where: b is slot mouth width [m], and, α_n is coil pitch of the n^{th} coil.

IX. Acknowledgments

This work was funded as part of the UK EPSRC SUPERGEN Wind Hub, EP/L014106/1.

X. References

[1] S. Nandi, H. Toliyat and X. Li, "Condition monitoring and fault diagnosis of electrical motors-a review," *IEEE Transactions on Energy Conversion,* vol. 20, no. 4, pp. 719-729, 2005.

[2] Y. Wang, Q. Wu, W. Gong, et al. "H∞ robust current control for DFIG-based wind turbine subject to grid voltage distortions," *IEEE Transactions on Sustainable Energy,* vol. 8/2, pp. 816-825, 2017.

[3] L. Trilla, O. Gomis-Bellmunt, A. Junyent-Ferré, et al. "Modeling and validation of DFIG 3-MW wind turbine using field test data of balanced and unbalanced voltage sags," *IEEE Transactions on Sustainable Energy,* vol. 2/no.4, pp.509-19, 2011.

[4] S. Djurović, D. Vilchis-Rodriguez and A. C. Smith, "Vibration monitoring for wound rotor induction machine winding fault detection," in *XXth Int. Conference on Electrical Machines*, Marseille, 2012.

[5] M. Edrah, K. L. Lo and O. Anaya-Lara, "Impacts of High Penetration of DFIG Wind Turbines on Rotor Angle Stability of Power Systems," *IEEE Trans. on Sustainable Energy,* vol. 6, no. 3, pp. 759-766, 2015.

[6] L. G. Meegahapola, T. Littler and D. Flynn, "Decoupled-DFIG fault ride-through strategy for enhanced stability performance during grid faults," *IEEE Trans.Sustainable Energy,* vol. 1/no. 3, pp.152-62, 2010.

[7] A. Testa, M. F. Akram and R. Burch, "Interharmonics: Theory and Modeling," *IEEE Trans.Power Del.,* vol. 22, no. 4, pp. 2335-2348, 2007.

[8] E. Hernández and M. Madrigal, "A Step Forward in the Modeling of the Doubly-fed Induction Machine for Harmonic Analysis," *IEEE Transactions on Energy Conversion,* vol. 29, no. 1, pp. 149-157, 2014.

[9] L. Fan, S. Yuvarajan and R. Kavasseri, "Harmonic Analysis of a DFIG for a Wind Energy Conversion System," *IEEE Transactions on Energy Conversion,* vol. 25, no. 1, pp. 181-190, 2010.

[10] S. Djurović, D. S. Vilchis-Rodriguez and A. C. Smith, "Supply Induced Interharmonic Effects in Wound Rotor and Doubly-Fed Induction Generators," *IEEE Trans. Energy Convers.,* vol. 30, no. 4, pp. 1397-1408, 2015.

[11] S. Williamson and S. Djurovic, "Origins of stator current spectra in DFIGs with winding faults and excitation asymmetries," in *2009 IEEE International Electric Machines and Drives Conference*, Miami, 2009.

[12] D. Shah, S. Nandi and P. Neti, "Stator-Interturn-Fault Detection of Doubly Fed Induction Generators Using Rotor-Current and Search-Coil-Voltage Signature Analysis," *IEEE Transactions on Industry Applications,* vol. 45, no. 5, pp. 1831-1842, 2009.

[13] S. Djurovic, C. J. Crabtree, P. J. Tavner, et al. "Condition monitoring of wind turbine induction generators with rotor electrical asymmetry," *IET Renewable Power Generation,* vol. 6, pp.207-16, 2012.

[14] J. Faiz and S. M. M. Moosavi, "Detection of mixed eccentricity fault in doubly-fed induction generator based on reactive power spectrum," *IET Electric Power Applications,* vol. 11, no. 6, pp. 1076-1084, 2017.

[15] C. Larose, R. Gagnon, P. Prud'Homme, et al. "Type-III wind power plant harmonic emissions: field measurements and aggregation," *IEEE Trans.on Sustainable Energy,* vol. 4, pp.797-04,2013

[16] A. Bellini, F. Flippetti, G. Franceschini, et al. "Closed-loop control impact on the diagnosis of induction motors faults," *IEEE Transactions on Industry Applications,* vol. 36, no. 5, pp. 1318-29, 2000.

[17] M. Zaggout, P. Tavner, C. Crabtree, et al. "Detection of rotor electrical asymmetry in wind turbine doubly-fed induction generators," *IET Renewable Power Generation,* vol. 8, no. 8, pp. 878-886, 2014.

[18] A. Stefani, A. Yazidi, C. Rossi, et al. "Doubly Fed Induction Machines Diagnosis Based on Signature Analysis of Rotor Modulating Signals," *IEEE Trans. Ind. Appl.,* vol. 44, no. 6, pp. 1711-1721, 208.

[19] K. N. B. M. Hasan, K. Rauma, A. Luna, J. I. Candela and P. Rodríguez, "Harmonic Compensation Analysis in Offshore Wind Power Plants Using Hybrid Filters," in *IEEE Transactions on Industry Applications*, vol. 50, no. 3, pp. 2050-2060, May-June 2014.

[20] J. Faiz, S. M. Moosavi, M. B. Abadi, et al. "Magnetic equivalent circuit modelling of doubly-fed induction generator with assessment of rotor inter-turn short-circuit fault indices," *IET Renewable Power Generation,* vol. 9, no. 10, pp. 1431-1440, 2016.

[21] M. Wu and L. Xie, "Calculating steady-state operating conditions for DFIG-based wind turbines," *IEEE Transactions on Sustainable Energy,* vol. 9, no. 1, pp. 293-301, 2018.

[22] Y. Liao, L. Ran, G. A. Putrus, et al. "Evaluation of the Effects of Rotor Harmonics in a Doubly-Fed Induction Generator With HarmonicInduced Speed Ripple," *IEEE Trans. Energy Conver.,* vol. 18/4, pp. 508-515, 2003.

[23] R. Gagnon, M. Fecteau, P. Prud'Homme, et al. "Hydro-québec strategy to evaluate electrical transients following wind power plant integration in the gaspésie transmission system," *IEEE Transactions on Sustainable Energy,* vol. 3, no. 4, pp. 880 - 889, 2012.

[24] M. Yilmaz and P. T. Krein, "Capabilities of finite element analysis and magnetic equivalent circuits for electrical machine analysis and design," in *2008 IEEE Power Electronics Specialists Conference*, Rhodes, 2008.

[25] Q. F. Lu, Z. T. Cao and E. Ritchie, "Model of stator inter-turn short circuit fault in doubly-fed induction generators for wind turbine," in *IEEE Annual Power Electronics Specialists Conference*, Aachen, 2004.

[26] S. Djurovic and S. Williamson, "A coupled-circuit model for a DFIG operating under unbalanced condition," in *2008 18th International Conference on Electrical Machines*, Vilamoura, 2008.

[27] S. Djurovic, S. Williamson and A. Renfrew, "Dynamic model for doubly-fed induction generators with unbalanced excitation, both with and without winding faults," *IET Electric Power Applications,* vol. 3, no. 3, pp. 171-177, 2009.

[28] S. Williamson and E. R. Laithwaite, "Generalised harmonic analysis for the steady-state performance of sinusoidally-excited cage induction motors," *IEE Proceedings B - Electric Power Applications,* vol. 132, no. 3, pp. 157-163, 1985.

[29] N. Sarma, K. Tshiloz, S. Vilchis-Rodriguez, et al. "Modelling of induction machine time and space harmonic effects in the SIMULINK environment," in *2015 IEEE International Electric Machines & Drives Conference (IEMDC),* Coeur d'Alene, ID, 2015.

[30] W. Qiao, W. Zhou, J. M. Aller, et al. "Wind Speed Estimation Based Sensorless Output Maximization Control for a Wind Turbine Driving a DFIG," *IEEE Trans. Power Electron.,* vol. 23/3, pp. 1156-1169, 2008.

This article has been accepted for publication in a future issue of this journal, but has not been fully edited. Content may change prior to final publication. Citation information: DOI 10.1109/TSTE.2019.2904113, IEEE Transactions on Sustainable Energy

[31] H. M. Jabr, D. Lu and N. C. Kar, "Design and Implementation of Neuro-Fuzzy Vector Control for Wind-Driven Doubly-Fed Induction Generator," *IEEE Trans.on Sust. Energy*, vol. 2/4, pp. 404-13, 2011.

[32] H. Xu, J. Hu and Y. He, "Operation of Wind-Turbine-Driven-DFIG Systems Under Distorted Grid Voltage Conditios: Analysis and Experimental Validations," *IEEE Transactions on Power Electronics*, vol. 27, no. 5, pp. 2354-2366, 2012.

[33] Atkinson, D., Lakin, R. and Jones, R.: "A Vector-Controlled Doubly-fed Induction Generator for a Variable-Speed Wind Turbine Application", Transactions of the Institute of Measurement and Control, 1997, vol. 19, pp. 2-12.

[34] N. Sarma, P. M. Tuohy, J. M. Apsley, S. Djurović, Y. Wang "DFIG Stator Flux Oriented Control Scheme Execution for Test Facilities Utilising Commercial Converters," *IET Renewable Power Generation (RPG) Journal*, Volume 12, Issue 12, Pages 1366-1374, October 2018.

[35] G. Tapia, A. Tapia and J. X. Ostolaza, "Two Alternative Modeling Approaches for the Evaluation of Wind Farm Active and Reactive Power Performances," *IEEE Transactions on Energy Conversion*, vol. 21, no. 4, pp. 909-920, 2006.

[36] G. Abad, J. Lopez, M. A. Rodriguez, et al. Doubly Fed Induction Machine: Modeling and Control for Wind Energy Generation, Hoboken: Wiley, 2011.

[37] Hopfensperger, D. J. Atkinson and R. A. Lakin, "Stator-flux-oriented control of a doubly-fed induction machine with and without position encoder," *IEE Proceedings - Electric Power Applications*, vol. 147, no. 4, pp. 241-250, 2000.

[38] K. Tshiloz, D. Vilchis-Rodriguez, S. Djukanović, et al. "Sensorless speed estimation in wound rotor induction machines by spectral search of the stator phase power signal," *IET Electric Power Applications*, vol. 10, no. 6, pp. 581-592, 2016.

[39] P. Fang, G. W. Ott and D. J. Adams, "Harmonic and reactive power compensation based on generalized instantaneous reactive power theory for three-phase four-wire systems," *IEEE Transaction on Power Electronics*, vol. 13, no. 6, pp. 1174-1181, 1998.

[40] N. Sarma, J. M. Apsley and S. Djurovic, "Implementation of a conventional DFIG stator flux oriented control scheme using industrial converters," in *2016 IEEE International Conference on Renewable Energy Research and Applications (ICRERA)*, Birmingham, UK, 2016.

BIOGRAPHIES

Nur Sarma (M'15) received her BSc and MSc degrees in Electrical and Electronic Engineering (EEE) from Sakarya University, Turkey. She subsequently received her Ph.D. degree in EEE from The University of Manchester, UK, in 2017.

She is currently working in Düzce University, Turkey, as an Assistant Professor. Her research interests are in fault diagnosis and condition monitoring of electric machines, renewable power generation and power conversion.

Paul M. Tuohy received the BEng. (Hons.) degree in Mechatronics with Industrial Experience and the Ph.D. degree in Electrical Engineering from The University of Manchester, Manchester, UK, in 2006 and 2011, respectfully,

He is currently a Research Fellow at the Rolls-Royce University Technology Centre (Electrical Systems for Extreme Environments) at The University of Manchester, Manchester, UK. His research interests include the design, finite element analysis, and testing of electric machines, actuators and drives for aerospace, vehicle, marine and renewable energy applications.

Dr. Tuohy was the recipient of the Siemens Medal in 2006. He was elected Whitworth Scholar in 2007 and Whitworth Senior Scholar in 2012. He is also the holder of two patents.

Siniša Djurovic (M'09) received the Dipl. Ing. degree in Electrical Engineering from University of Montenegro in 2002 and the Ph.D. degree from University of Manchester in 2007.

He is currently a Senior Lecturer with the Power Conversion Group at Manchester. His research interests are in the area of operation, design, monitoring and diagnostics of electric machines and drives.

Renewable Energy 131 (2019) 14–24

Contents lists available at ScienceDirect

Renewable Energy

journal homepage: www.elsevier.com/locate/renene

Electrical & mechanical diagnostic indicators of wind turbine induction generator rotor faults

D. Zappalá [a, *], N. Sarma [b, c], S. Djurović [b], C.J. Crabtree [a], A. Mohammad [b], P.J. Tavner [a]

[a] Department of Engineering, Durham University, South Road, Durham, UK
[b] School of Electrical and Electronic Engineering, Power Conversion Group, The University of Manchester, Manchester, UK
[c] Department of Electrical & Electronics Engineering, Duzce University, Duzce, Turkey

ARTICLE INFO

Article history:
Received 4 April 2018
Received in revised form
22 June 2018
Accepted 24 June 2018
Available online 28 June 2018

Keywords:
Wind turbine
Condition monitoring
Doubly-fed induction generator (DFIG)
Electrical & mechanical signature analysis
Rotor electrical unbalance
Fault indicator

ABSTRACT

In MW-sized wind turbines, the most widely-used generator is the wound rotor induction machine, with a partially-rated voltage source converter connected to the rotor. This generator is a significant cause of wind turbine fault modes. In this paper, a harmonic time-stepped generator model is applied to derive wound rotor induction generator electrical & mechanical signals for fault measurement, and propose simple closed-form analytical expressions to describe them. Predictions are then validated with tests on a 30 kW induction generator test rig. Results show that generator rotor unbalance produces substantial increases in the side-bands of supply frequency and slotting harmonic frequencies in the spectra of current, power, speed, mechanical torque and vibration measurements. It is believed that this is the first occasion in which such comprehensive approach has been presented for this type of machine, with healthy & faulty conditions at varying loads and rotor faults. Clear recommendations of the relative merits of various electrical & mechanical signals for detecting rotor faults are given, and reliable fault indicators are identified for incorporation into wind turbine condition monitoring systems. Finally, the paper proposes that fault detectability and reliability could be improved by data fusion of some of these electrical & mechanical signals.

1. Introduction

Wind energy has a crucial role in providing sustainable energy. By the end of 2017, the world-wide wind power installed capacity has risen to 540 GW [1], of which 169 GW are in the EU, approximately 153 GW onshore and 16 GW offshore [2]. Offshore wind has significant generation potential in Europe, especially in the UK, thanks to beneficial wind resources and sea-bed conditions. Optimising operations and maintenance (O&M) strategy through the adoption of cost-effective and reliable condition monitoring (CM) techniques is a clear target for competitive offshore wind development [3–5]. One of the main challenges currently facing the wind CM industry is to improve the reliability of diagnostic decisions, including component fault severity assessment [6]. Wound Rotor Induction Generators (WRIG), using a partially-rated Voltage Source Converter (VSC) to supply the rotor, known as Doubly-Fed Induction Generators (DFIG), are identified as the most widely-used generator in wind industry for MW-size variable speed applications [7,8], where Induction Generators in general are dominant, although Permanent Magnet Generators are gaining acceptance. Reliability surveys have highlighted that generator faults make a significant contribution to onshore wind turbine (WT) down-time [9–11]. With reduced accessibility offshore, any down-time is significantly extended. References [12–14] have also shown that rotor winding unbalance, caused by brush-gear or slip-ring wear/fault or winding electrical faults, are major contributors to WT generator failure rate. Monitoring generator electrical faults has not yet become standard practice in the wind industry where the majority of CM systems (CMS) are based on monitoring high-frequency vibration in gearbox and generator bearings [15]. Increasing concern about WT electrical component reliability [11], particularly offshore, could be overcome by expanding current CMS capabilities.

Steady-state DFIGs winding fault detection based on analysis of readily available current, power or even vibration signals has been widely researched and several diagnostic methods, based on time- or frequency-domain techniques, have been proposed to detect rotor failures. The first paper to consider current, speed and

* Corresponding author.
E-mail address: donatella.zappala@durham.ac.uk (D. Zappalá).

https://doi.org/10.1016/j.renene.2018.06.098

vibration measurement for detecting induction machine faults was [16] in 1982, in particular the presence of slip-dependant components in various induction machine electrical & mechanical signals has been reported in papers since 1978. However, more recent references [17–23] provide much greater analytical detail, at least for electrical signals. The feasibility of using mechanical signal spectra, vibration, torque or speed, as generator electrical unbalance fault indicators were investigated in Refs. [24–28]. However, all these papers relied on the analysis of single signals only, rather than considering the possibility of reducing effects of signal noise and improving detectability by combining multiple signals. The adoption of a data fusion approach, based on the comparison of independent single signals, could contribute to increasing confidence and reduce false alarms, as already demonstrated for WT gearboxes in Refs. [29–31]. Despite interest in recognising generator fault signatures in multiple signals, there is a lack of literature explaining how to improve reliability by combining relevant diagnostic signals. Furthermore in WTs, the use of a VSC-connected machine monitored by a CMS now means that both electrical & mechanical signals are readily available to the operator.

This paper, therefore, sets out comprehensive generator signal prediction and measurement under rotor electrical unbalance (REU), at varying load and fault levels, with the aim of measuring wide-band, fault-related, electrical & mechanical harmonic side-bands, comparing and amalgamating them to improve fault recognition and raise reliability. The work builds on previous research [17], [18], [22], [28], [32], providing a comprehensive investigation of rotor electrical fault effects on DFIG stator current, I_s, power, P_e, shaft speed, N_s, mechanical torque, T_m & frame vibration, A_v.

First, the paper provides closed-form analytical expressions, arising from author's previous published work, linking fault-related signal frequencies to generator operating conditions. A harmonic model of a laboratory DFIG is then used to investigate REU wide-band spectral signatures. The extent to which fault-related frequencies, predicted by theory, are manifested in DFIG electrical & mechanical signals is then investigated experimentally. Finally, the correlation between the identified electrical & mechanical signal spectral components and their ability to demonstrate rotor fault severity progression within the generator operating range is explored with the aim of identifying reliable fault indicators for potential incorporation in commercial WT CMSs.

2. Generator rotor electrical unbalance: model study

Closed-form analytical expressions defining the spectral characteristics of I_s & P_e, for a DFIG with an electrically balanced rotor were previously presented by the Authors in Refs. [17], [28], [32] and are summarised in Table 1. These equations account for unbalanced stator supply and higher order field harmonics, typical of practical applications. According to [16], [33], [34], a spectral content of electro-magnetic origin is also detectable in the speed signal, N_s. Machine electrical & mechanical spectra under balanced conditions, described by equations in Table 1, are defined by a set of characteristic frequencies, referred to as carrier frequencies (CF). These frequencies are an artefact of generator design and supply harmonic content, and depend on: rotor slip (s), supply frequency (f), supply harmonic order (i and l, where $i, l = 1,2,3 \ldots$) and air-gap magnetic field pole pair number (k, where $k = 1,2,3 \ldots$). The CF expressions in Table 1 contain two distinct subgroups:

i. Supply frequency harmonic carriers (H), rotor speed invariant artefacts of supply harmonics, corresponding to $k = 0$ and $i \neq 0$ for current or $l \pm i \neq 0$ for other signals;
ii. Slot harmonic carriers (S), rotor speed dependant inter-harmonic frequencies due to slotting, corresponding to $k \neq 0$ and $i \neq 0$ for current or $l \pm i \neq 0$ for other signals.

REU gives rise to additional $\pm 2nsf$ side-bands around existing CF components in I_s spectra, which are consequently reflected into counter-part $\pm 2nsf$ components of the CFs identified in the P_e & N_s spectra [22], [28], [33], [34], [35], where n can take any positive integer value, i.e. $n = 0, 1, 2, 3 \ldots$ The third column in Table 1 summarises analytical expressions describing possible DFIG signal spectral content under REU operation, derived by taking account of CFs $2nsf$ side-bands, i.e. CF$\pm 2nsf$. As side-bands generally decay with order [22], only fundamental (i.e. first order side-band) components are examined further in this work. REU-induced side-band equations can be resolved into two distinct sub-groups depending on whether they correspond to supply harmonic side-bands (H_L and H_U) or slot harmonic side-bands (S_L and S_U), where subscripts L and U denote lower and upper $2sf$ CF side-bands, respectively.

To understand REU-induced electrical & mechanical spectra, a time-stepped DFIG harmonic model was developed [18], [36]. A 4-pole laboratory generator has been used in this research; the model emulated its design and operational data as model inputs. The model enables the analysis of higher order harmonic effects and was used to study the steady-state spectral content of I_s, P_e & N_s signals. Generator operation was simulated for illustration purposes at the loaded operating speed of 1590 rpm, 90 rpm above synchronous speed and speed-ripple effects were incorporated in model calculations [33,34]. The three-phase supply was modelled with 3% magnitude unbalance to match typical laboratory levels. The stator windings were modelled as balanced for the purposes of this study. To study the spectral effects of interest predicted spectra were investigated over 0–450 Hz band-width for I_s & P_e, and 0–150 Hz band-width for N_s. The harmonic model was used to evaluate the influence of supply harmonics on signal spectra for the generator operating with an electrically balanced rotor using wide-band modelling of dominant 3rd, 5th, 7th, 11th and 13th supply harmonics, $H_{1+3+5+7+11+13}$, with mean rms value limits, in terms of fundamental percentage, of 5%, 6%, 5%, 3.5% and 3%, respectively, as specified in the relevant grid code [40].

Predictions were obtained from the model to evaluate wide-band REU spectral signatures by increasing one rotor phase winding resistance by 300% of its rated value.

The predicted stator phase current, I_s, total power, P_e and

Table 1
I_s, P_e & N_s, Carrier Frequencies (CF) and their $\pm 2nsf$ side-bands.

Generator Signal	Closed-Form Analytical Expressions	
	Balanced Rotor (CF)	Unbalanced Rotor (CF $\pm$ $2nsf$)
Stator Current, I_s	$\lvert i \pm 6k(1-s) \rvert f$	$\lvert (i \pm 2ns) \pm 6k(1-s) \rvert f$
Stator Active Power, Rotational Speed, P_e & N_s	$\lvert (l \pm i) \pm 6k(1-s) \rvert f$	$\lvert [(l \pm i) \pm 2ns] \pm 6k(1-s) \rvert f$

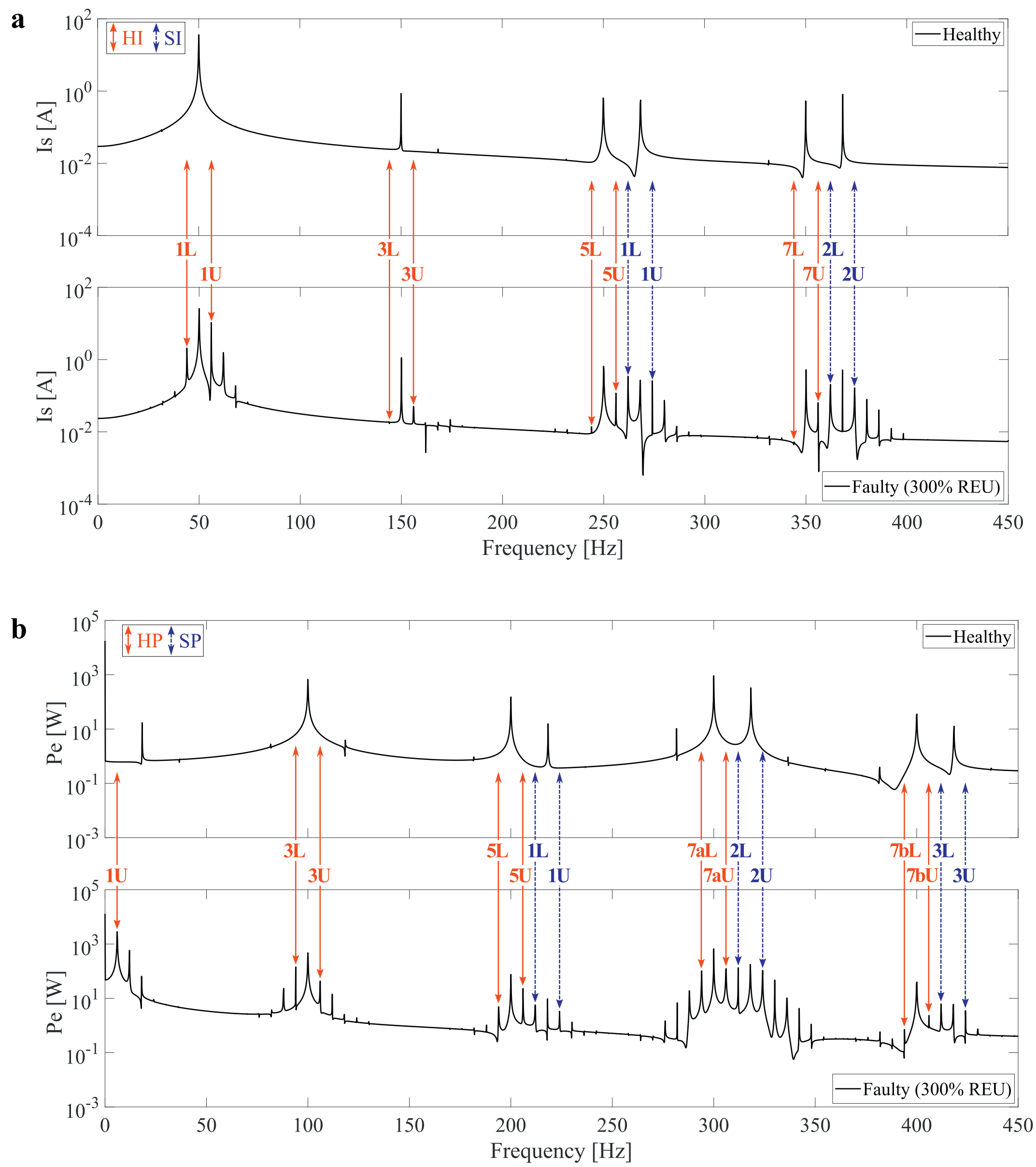

Fig. 1. Predicted I_s (a) & P_e (b) spectra at 1590 rpm, balanced rotor winding & 300% REU.

generator speed, N_s, under balanced and unbalanced, 300% REU, conditions are shown in Figs. 1 and 2. For each signal direct comparison of healthy and faulty spectra enables a clear understanding of REU wide-band spectra.

Supply harmonic carriers derived from I_s and P_e & N_s have been denoted by HI and HP, respectively; while slotting harmonic carriers have been denoted by SI and SP, respectively. For clarity, only REU first order side-band frequencies are labelled in Figs. 1 and 2, where the subscripts L and U denote CF *2sf* lower and upper side-bands, respectively, identified by the red solid lines for H harmonic side-bands and by the blue dotted lines for S slot harmonic side-bands.

Spectral frequencies labelled in the graphs can be calculated for corresponding operating conditions by appropriate expressions in Table 1. This confirms the validity of the proposed closed-form equations for analysis of REU induced spectral signature. Tables 2–5 list equation parameters and corresponding spectral frequency numeric values observed in model results.

3. Generator rotor electrical unbalance: experimental validation

3.1. Experimental test rig

Model results were experimentally validated and quantified in a series of experiments on a laboratory test rig, illustrated in Fig. 3, comprising an industrial 4-pole, three phase, 240 V, 50 Hz, 30 kW, star-connected WRIG. The generator rotor rated phase resistance was 0.066Ω. The WRIG was mechanically coupled with a 40 kW DC generator, used to drive the WRIG at a pre-chosen constant speed during experiments. The generator stator windings were connected to the grid via a three phase variable transformer, whilst the rotor

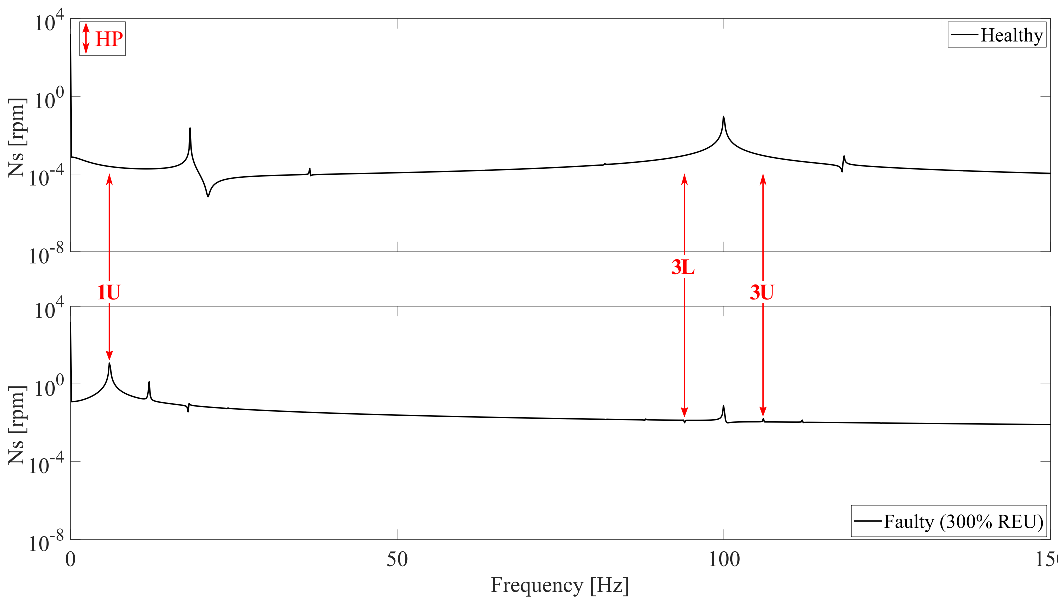

Fig. 2. Predicted N_s spectra at 1590 rpm, balanced rotor winding & 300% REU.

Table 2
Predicted I_s supply frequency harmonics and their side-bands.

i	*k*	Supply Harmonic Carrier Frequencies (CF) HI		Supply Harmonic CF Side-bands			
		CF	Hz	CF+2*sf*	Hz	CF-2*sf*	Hz
1	0	HI_1	50	HI_{1L}	44	HI_{1U}	56
3	0	HI_3	150	HI_{3L}	144	HI_{3U}	156
5	0	HI_5	250	HI_{5L}	244	HI_{5U}	256
7	0	HI_7	350	HI_{7L}	344	HI_{7U}	356

Table 3
Predicted I_s slotting harmonics and their side-bands.

i	*k*	Slotting Harmonic Carrier Frequencies (CF) SI		Slotting Harmonic CF Side-bands			
		CF	Hz	CF+2*sf*	Hz	CF-2*sf*	Hz
1	1	SI_1	268	SI_{1L}	262	SI_{1U}	274
1	1	SI_2	368	SI_{2L}	362	SI_{2U}	374

Table 4
Predicted P_e & N_s supply frequency harmonics and their side-bands.

i	*l*	*k*	Supply Harmonic Carrier Frequencies (CF) HP		Supply Harmonic CF Side-bands			
			CF	Hz	CF+2*sf*	Hz	CF-2*sf*	Hz
1	1	0	HP_1	0			HP_{1U}	6
3	1	0	HP_3	100	HP_{3L}	94	HP_{3U}	106
5	1	0	HP_5	200	HP_{5L}	194	HP_{5U}	206
7	1	0	HP_{7a}	300	HP_{7aL}	294	HP_{7aU}	306
7	1	0	HP_{7b}	400	HP_{7bL}	394	HP_{7bU}	406

Table 5
Predicted P_e & N_s slotting harmonics and their side-bands.

i	*l*	*k*	Slotting Harmonic Carrier Frequencies (CF) SP		Slotting Harmonic CF Side-bands			
			CF	Hz	CF+2*sf*	Hz	CF-2*sf*	Hz
1	1	1	SP_1	218	SP_{1L}	212	SP_{1U}	224
1	1	1	SP_2	318	SP_{2L}	312	SP_{2U}	324
1	1	1	SP_3	418	SP_{3L}	412	SP_{3U}	424

windings were short-circuited. REU conditions were emulated by introducing additional resistance into one rotor phase winding.

The DC generator speed and torque were controlled by a commercial DC controller. A shaft mounted 1024 ppr incremental encoder was used for speed measurement and its output signals processed in real-time using a dSPACE 1103 platform to extract the value of N_s. WRIG instantaneous stator currents, I_s, and voltages, V, were measured using Hall effect sensors and synchronously recorded by a LeCroy WaveSurfer digital oscilloscope sampling at a rate of 10 kHz. Recorded currents and voltages were used to calculate the total instantaneous stator power, P_e, using the two wattmeter method. The WRIG was mounted on a Kistler 9281B force platform, containing three-axis piezoelectric transducers, to measure the dynamic shaft torque [37]. The piezoelectric sensor signals were acquired by a NI DAQ-6351 card and then processed to calculate the shaft torque, T_m. The WRIG frame vibration, A_v, was measured on the horizontal axis with a Brüel&Kjaer (B&K) DT4394 piezoelectric accelerometer, which was fitted to the generator load-side end-plate. The vibration spectrum was recorded with 0–1 kHz band-width at 6400 lines of resolution using a B&K PULSE vibration analysis platform. Other signals were processed using the MATLAB FFT routine with 2^{17} data points to achieve a frequency resolution of 0.0763 Hz/line. Monitored signals were recorded during generator steady-state operation and their spectra examined for this study over a 0–450 Hz band-width for I_s, P_e, T_m & A_v signals, and over a 0–150 Hz band-width for N_s.

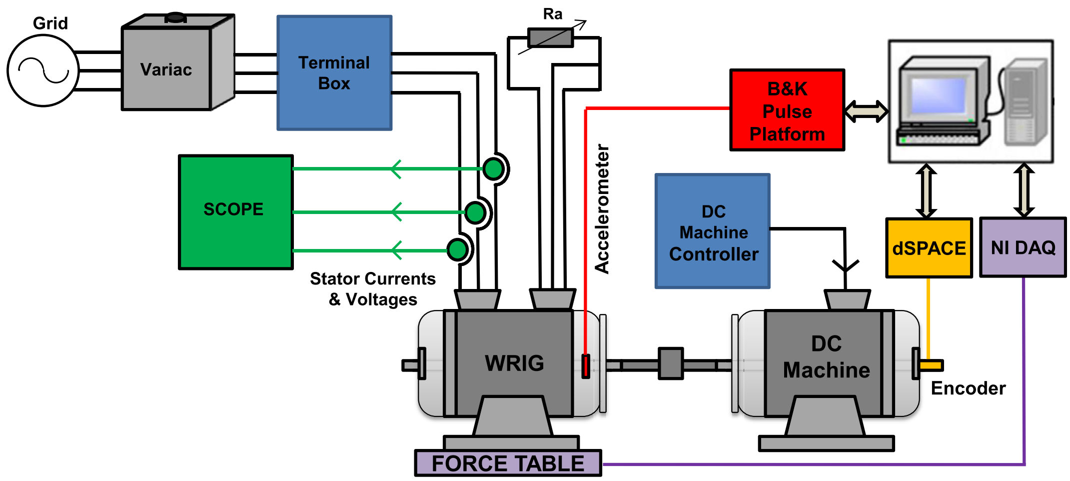

Fig. 3. Schematic diagram of the experimental test rig and its instrumentation.

3.2. Electrical & mechanical signal analysis

To allow direct comparison with model predictions presented in Section 2, tests were first performed at 1590 rpm. An external additional resistance of ≈0.198Ω was introduced into one rotor phase to give up to 300% REU. I_s, P_e & N_s spectra measured for healthy and faulty conditions are shown in Figs. 4 and 5. Detectable frequencies of interest, corresponding to $\pm 2sf$ side-bands tabulated in Tables 2–5, are labelled in the measurements. Measured spectra are in good agreement with predictions, where contents originating from supply-induced inter-harmonic effects, slotting side-bands and REU side-bands are shown. As predicted by analysis reported in section 2, the presented measurements confirm that REU causes additional, slip-dependant side-bands at calculable frequencies, confirming this research.

Small discrepancies between numerical and experimental results are due to inherent supply frequency variations and velocity measurement accuracy limitations. Some REU-related side-bands are present in the healthy generator spectra, at low magnitude, as an artefact of inherent rotor unbalance, unavoidable in any practical generator, arising from manufacturing imperfections [17]. Measurements are also much noisier than model predictions due to inevitable geometrical inaccuracies in machine construction and the full air-gap electro-magnetic effects, as well as supply secondary noise effects not represented in the model for the sake of clarity. However, most predicted REU-specific components are clearly visible above measurement noise. Comparison between healthy and faulty spectra indicates that REU induces considerable change in many components, with I_s & P_e side-bands giving clearer fault indication than N_s.

4. Discussion

4.1. Model study

Model predictions in Figs. 1 and 2 and Tables 2–5 show the presence of significant wide-band signatures in all I_s, P_e & N_s generator signals. For operation under REU conditions additional $\pm 2nsf$ side-band components clearly arise in supply and slot harmonic spectral components that can be correlated across different signals. Previous work [25], [26], [28], [32], [38] has shown that effects associated with attractive rotor-stator radial magnetic forces can also give rise to oscillations at identical frequencies in T_m & A_v as in P_e & N_s spectra. In summary, models identified the following components to be looked for in experimental signals:

- SI, HI lower and upper $2sf$ side-bands in I_s;
- SP & HP lower and upper $2sf$ side-bands in P_e, N_s, T_m & A_v, respectively.

These side-bands correspond to those disparately described in previous literature, presented comprehensively in this model study.

4.2. Experimental study

I_s, P_e & N_s model predictions are confirmed by the experimental results presented in Section 3.2 and shown in Fig. 4 for I_s & P_e and Fig. 5 for N_s. Fig. 6 shows the experimental results for T_m & A_v. Note that, in this case, the same side-band labelling system as for P_e & N_s has been adopted to indicate the detectable $\pm 2sf$ frequencies.

Inherent rotor unbalance artefacts, due to manufacturing imperfections in practical generators [17], give rise to low magnitude $\pm 2sf$ side-bands in T_m & A_v even under healthy operation; this is expected and clearly seen in Fig. 6. T_m & A_v spectra are noisier than corresponding electrical signals, partly due to the mechanical instrumentation but also because A_v is affected by both air-gap excitation and frame response [26], [38], [39]. The majority of REU-related supply frequency harmonic and slotting component $\pm 2sf$ side-bands, predicted by the model, are clearly visible in measured T_m spectra but because of the dependency of the vibrations on the generator frame mechanical response, not all frequencies observed in T_m are manifested in A_v. A_v shows similar but non-identical characteristics, compared to I_s, P_e, T_m & N_s because, whilst the air-gap flux density is modulated by the fault harmonics, vibration signals are also attenuated by the resonant vibration response of the machine stator core and frame, as described in Refs. [16] and [28]. Slotting harmonic (SP) side-bands together with HP_{1U}, in the case of T_m, and with HP_{3U}, in the case of A_v, are most prominent and, in most cases, exhibit clear increases under generator fault conditions. The upper $2sf$ side-band of the fundamental harmonic at zero Hz, HP_{1U}, traditionally used as an REU indicator [41], is invisible in A_v spectra because of the limited frequency response of the piezoelectric accelerometer, i.e. 5 Hz-10 kHz; a similar constraint will exist in commercial CMS sensors [15].

Table 6 summarises the detectable supply and slotting harmonic side-bands in I_s, P_e, N_s, T_m & A_v measured signals, present in REU faults, derived directly from the generator air-gap flux density,

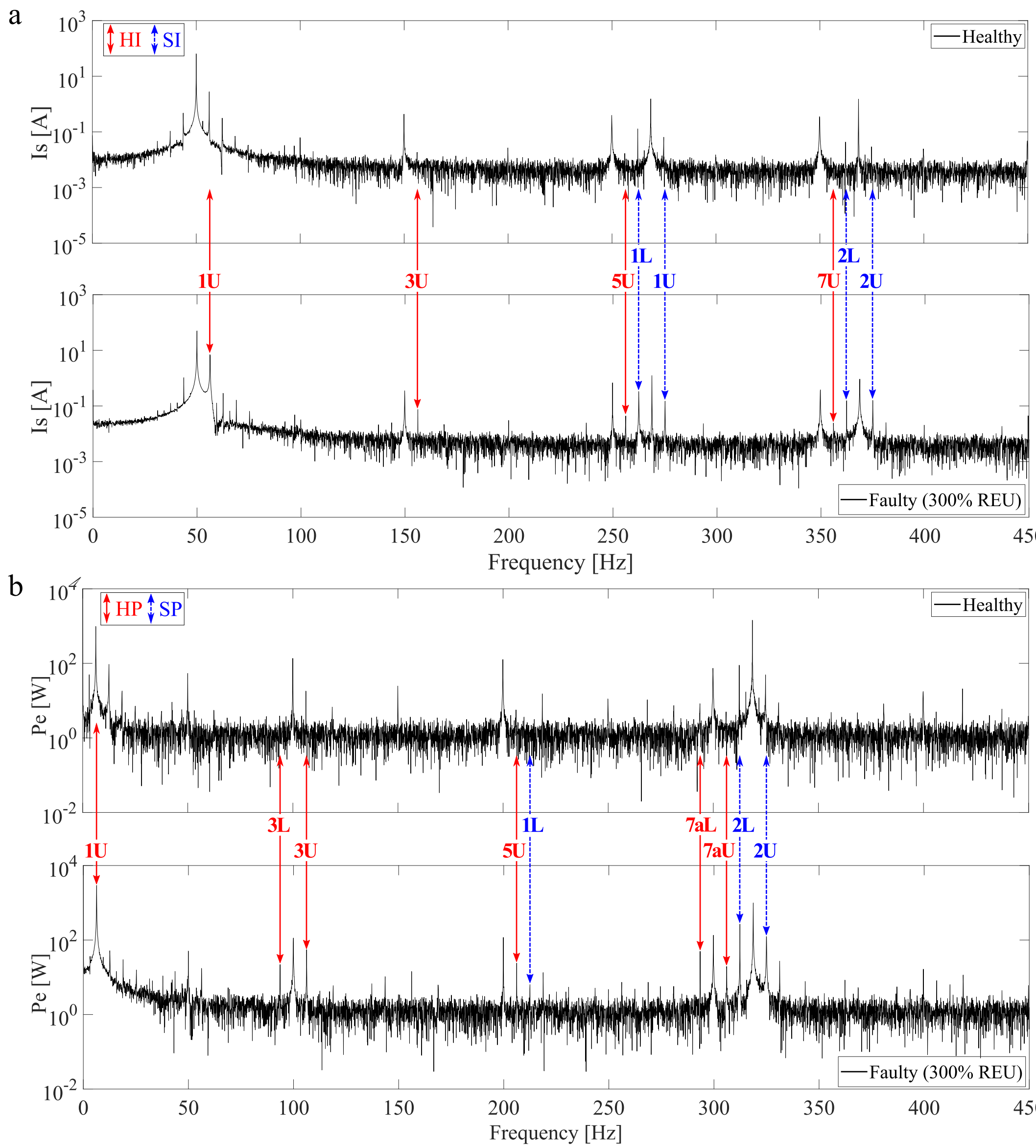

Fig. 4. Measured I_s (a) & P_e (b) spectra at 1590 rpm, balanced rotor winding & 300% REU.

modulated by rotor fault harmonics, and in A_v affected by frame response.

4.3. Fault detection

The influence of REU severity and generator load on the fault recognition capability of identified $\pm 2sf$ side-bands has been investigated by performing a series of tests under steady-state conditions over the full generator operating range. The WRIG speed was increased in steps of 30 rpm, from no-load, 1500 rpm, up to full-load, 1590 rpm. At each steady-state load, the generator was first tested under balanced rotor conditions and then under three increasing severity REU levels, shown in Table 7. The REU level was estimated as a percentage of balanced phase resistance, comparable to those used in previous studies [19], [21], [24].

For each fault and load condition, five separate $I_{s,}$ V, N_s & A_v measurements and four separate *Tm* measurements were recorded. The fault signal spectra examined in steady-state agreed with the predicted and experimental results described in Sections 2 & 3. The magnitudes of $\pm 2sf$ fault-related side-bands, identified in Table 6, were extracted from each signal and averaged to minimise sensitivity to supply variations. A normalised detectability algorithm, *D*, applied to the measured data has been defined as:

$$D = \frac{\sum_i F_i^2}{\sum_i H_i^2} \quad (1)$$

where:

- $\sum F_i^2$ is the sum of amplitudes squared of selected fault condition CF harmonic side-bands;
- $\sum H_i^2$ is the sum of amplitudes squared of selected unfaulted condition CF harmonic side-bands.

Results were then compared, in Fig. 7, to investigate the ability of each identified component to discriminate fault severity over the

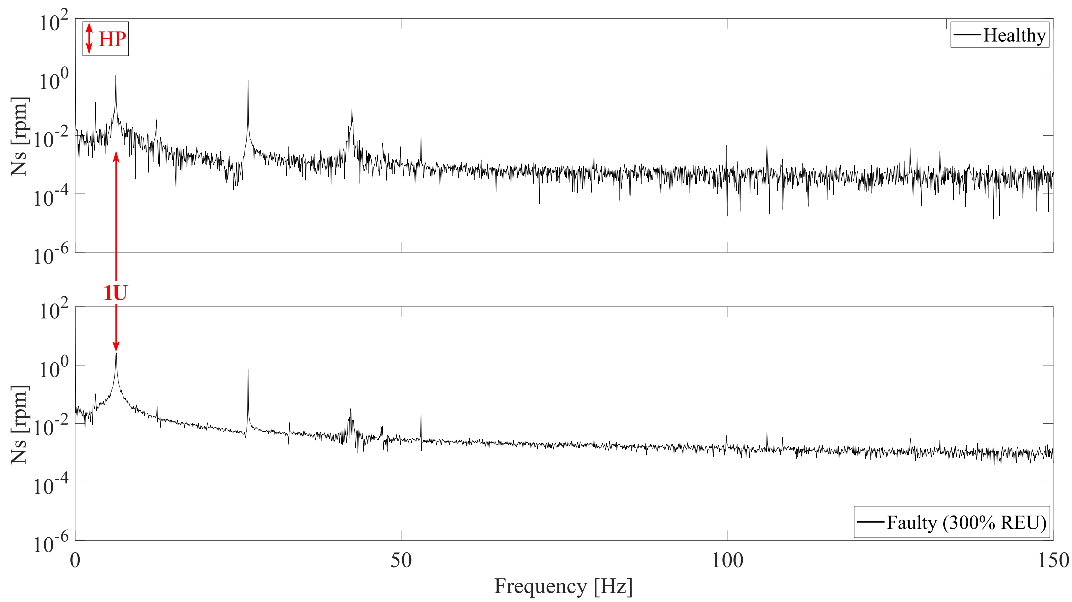

Fig. 5. Measured N_s spectra at 1590 rpm, balanced rotor winding & 300% REU.

full generator operating range, based on the harmonics listed in Table 6. Note that D has a floor level of 1 when $\sum_i F_i^2 = \sum_i H_i^2$, as indicated in Fig. 7 graphs by the grey base to ordinate D.

In Fig. 7 I_s & P_e show the most distinct responses to REU changes, even for small fault magnitudes; T_m also exhibits clear rising trends, with an exception at 1530 rpm, while N_s also provides a reliable fault indicator, although with lower sensitivity as unbalance increases. Fig. 7.e shows that vibration, A_v, did not exhibit side-bands giving consistent fault recognition within the generator operating range, due to the A_v-REU signature being attenuated by generator frame mechanical response, which, in this case, varies significantly with operating speed [28]. In addition the accelerometer frequency response in these experiments could not identify HP_{1U} vibration components. Fault recognition using this side-band could be possible if low frequency resolution accelerometers, such as fibre optics, were employed.

4.4. Improving fault detectability by data fusion

Various authors have advocated data fusion to improve fault detectability, notably for wind turbine gearboxes [30] and electrical machines [41]. The principal of data fusion is to increase detectability and detection confidence for the condition monitor and maintainer by combining signals from different sources. The suitability of combining REU-specific frequencies in generator signals as CMS fault indicators for data fusion can be assessed using the experimental load-dependency discussed in Section 4.3. The signals considered for data fusion from this paper, are with justification:

- Electrical, I_s or P_e, attractive as these signals are strong, closely related to the air-gap magnetic field and hence to REU;
- Mechanical, T_m, N_s or A_v, attractive as these signals come from reliable sources, trusted by generator operators, but less closely related to the air-gap magnetic field and hence REU.

The combination of I_s & A_v, P_e & N_s and I_s & T_m has been investigated. In each case, the combined normalised detectability, D_f, has been calculated by applying simplistic additive data fusion as:

$$D_f = \left(\frac{\sum_i F_i^2}{\sum_i H_i^2}\right)_e + \left(\frac{\sum_i F_i^2}{\sum_i H_i^2}\right)_m \quad (2)$$

where $\left(\frac{\sum_i F_i^2}{\sum_i H_i^2}\right)_e$ and $\left(\frac{\sum_i F_i^2}{\sum_i H_i^2}\right)_m$ are the normalised detectability of the electrical and mechanical signal, respectively, calculated using equation (1). The results of this simplistic additive data fusion are shown in Fig. 8, to the same scale as Fig. 7.

Fig. 8 demonstrates that each considered simple additive data fusion of electrical & mechanical signals delivers increased detectability with consistent behaviour over a range of REU fault sizes and WRIG loads, plus increased robustness and confidence for the operator. More complex data fusion algorithms could be developed, dependant on experience and the response features of a given system being monitored.

5. Conclusions

This paper presents an investigation of electrical & mechanical signatures for DFIG rotor electrical unbalance (REU), identifying the best diagnostic reliability condition monitoring indicators. It is shown that by simple additive data fusion of specific electrical & mechanical signatures fault detectability can be enhanced with the following specific conclusions:

- Closed-form analytic expressions defining electrical & mechanical signal spectral content for healthy and faulty operating conditions have been derived and validated, by comparison between model predictions and tests on a fully instrumented 30 kW WRIG laboratory test rig. A comprehensive study of DFIG REU electrical & mechanical spectral signatures has been made using this high fidelity laboratory test system.
- It has been shown that the magnitude of slip-dependant side-bands of a wide range of both supply frequency and slotting harmonics show significant experimental increases under faulty REU conditions.
- Specific side-bands, of current, power, torque and speed, giving clear fault recognition, have been identified and give consistent

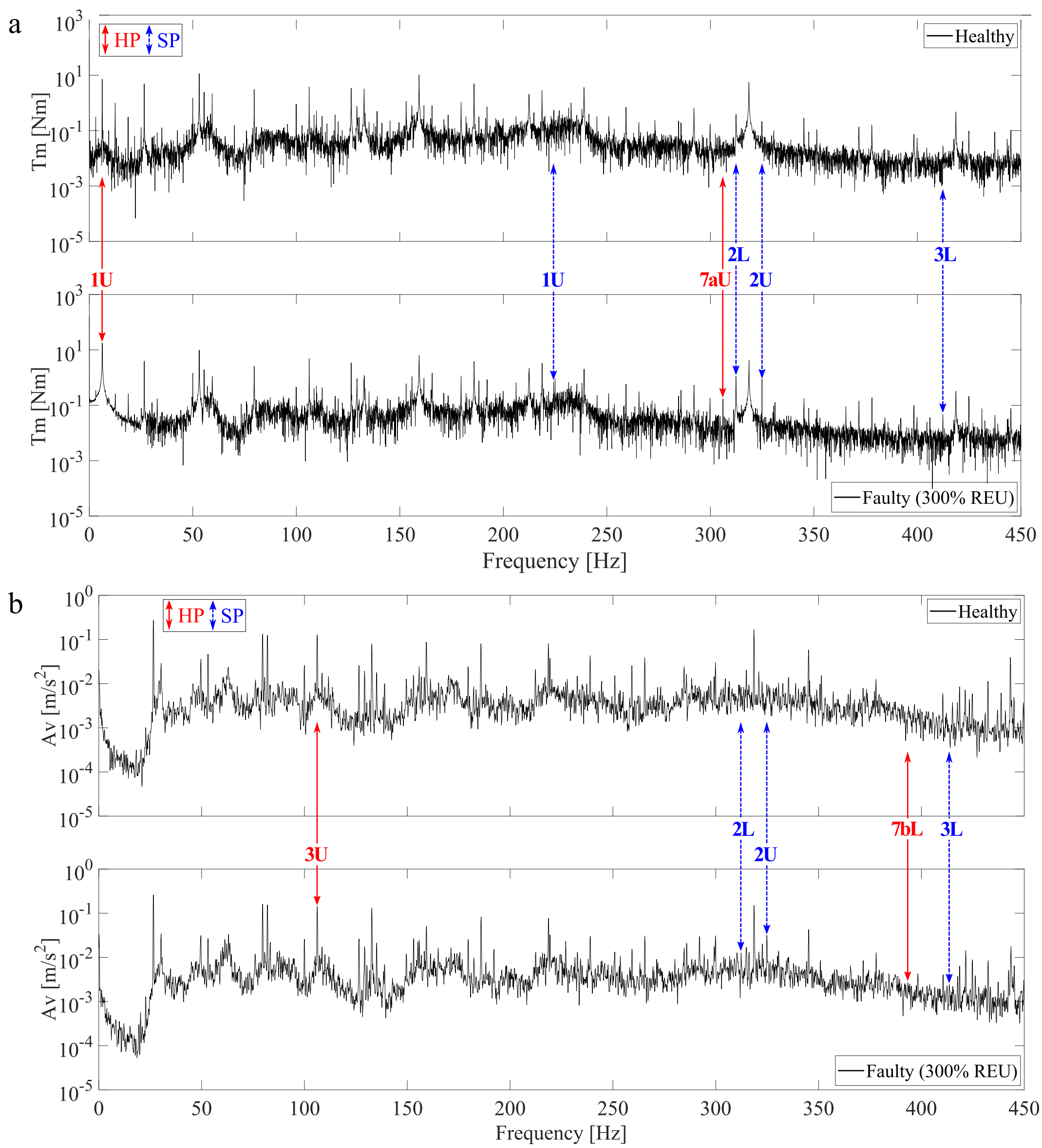

Fig. 6. Measured T_m (a) & A_v (b) spectra at 1590 rpm, balanced rotor winding & 300% REU.

Table 6
Measured P_e, I_s, T_m, N_s & A_v supply, H, and slotting, S, harmonic side-bands showing presence of REU faults, taken from Figs. 4–6, based on faults predicted in Tables 2–5.

		I_s	P_e	–
Electrical Signals	Supply harmonic side-bands	HI_{1U} HI_{3U} HI_{5U} HI_{7U}	HP_{1U} HP_{3L}, HP_{3U} HP_{5U} HP_{7aL}, HP_{7aU}	–
	Slotting side-bands	SI_{1L}, SI_{1U} SI_{2L}, SI_{2U}	SP_{1L} SP_{2L}, SP_{2U}	–
		N_s	T_m	A_v
Mechanical Signals	Supply harmonic side-bands	HP_{1U}	HP_{1U}	
				HP_{3U}
			HP_{7aU}	HP_{7bL}
	Slotting side-bands		SP_{1U} SP_{2L}, SP_{2U} SP_{3L}	 SP_{2L}, SP_{2U} SP_{3L}

behaviour across the generator operating range. They will be high diagnostic reliability indicators of REU.

- Experimental results show that REU produces consistent, high fault and load sensitivity current $\pm 2sf$ side-band spectral

Table 7
REU progressively introduced into one rotor phase circuit.

Additional Phase Resistance [Ω]	REU Level [%]
0.099	150
0.1485	225
0.198	300

increases around slotting harmonic components, in addition to traditionally used upper *2sf* side-band of the fundamental supply harmonic component.

- In the case of P_e, T_m & N_s signals DC component *2sf* side-bands have been shown to be the most sensitive and reliable REU fault indicators. However, in the case of P_e & T_m, other side-bands of supply frequency and slotting related spectral components are also responsive to REU.
- Vibration signals, A_v, also exhibit the presence of REU as *2sf* side-bands, clearly detectable in the vibration spectra. However those side-bands show less consistent fault level recognition across the generator operating range, because of the effect of frame response. This suggests that, in addition to conventional electrical signals, mechanical A_v, T_m & N_s signals could be monitored to diagnose generator electrical fault severity or progression over time.
- Simplistic additive data fusion of simultaneous electrical & mechanical signals real-time side-bands has demonstrated enhanced REU fault recognition sensitivity and could be used in a CMS to allow assessment of damage severity. This has been confirmed experimentally in this paper for electrical & mechanical signal combinations of I_s & A_v, P_e & N_s or I_s & T_m. Confirmatory fault data from disparate sources increases robustness and confidence and would be a crucial step for successfully implementing condition-based maintenance.

Further work would be required to investigate how to apply the information in this paper to a practical wind turbine generator CMS system and propose more developed methods of data fusion than presented here to improve damage severity assessment.

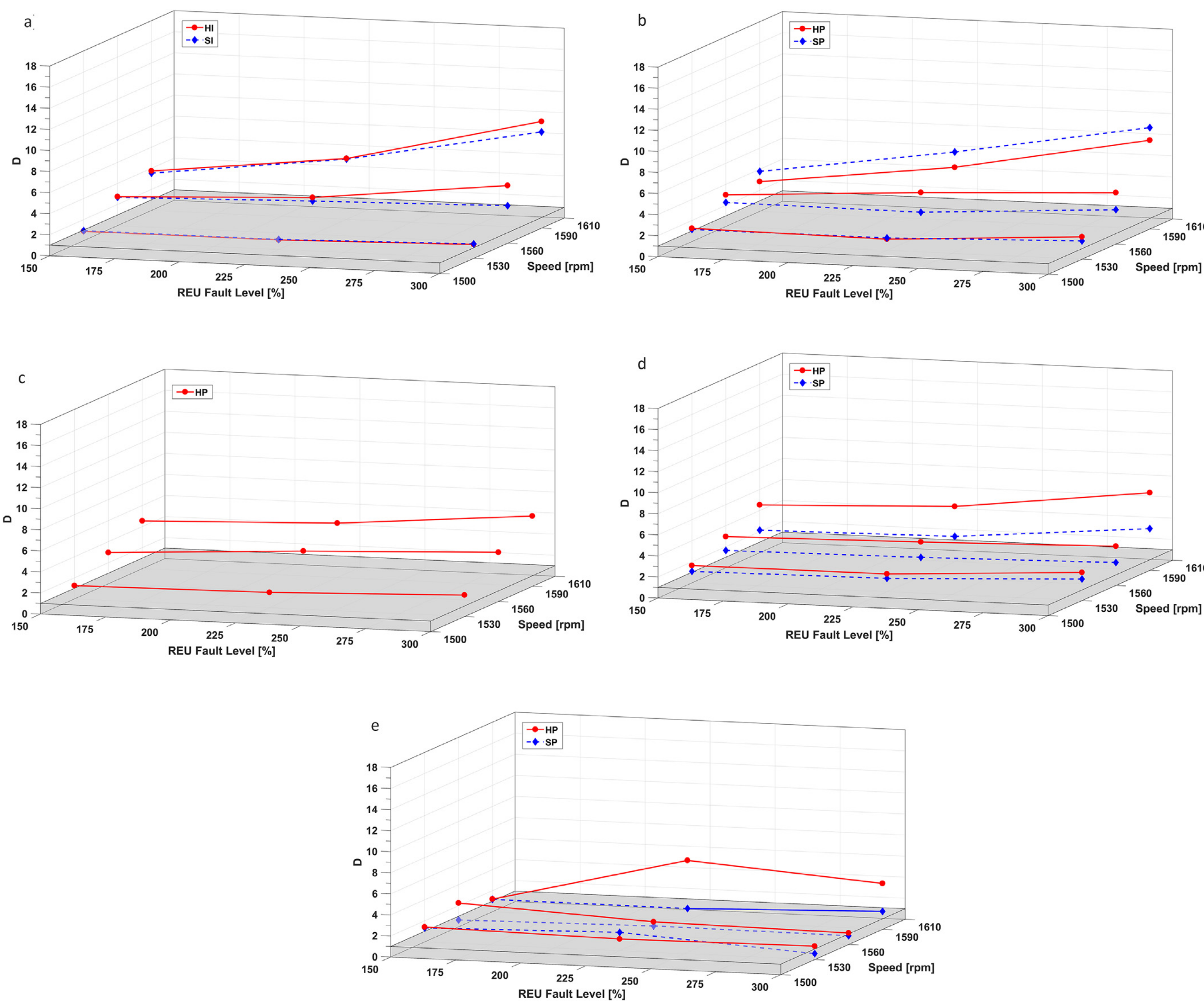

Fig. 7. Normalised Detectability, *D*, from various separate electrical & mechanical signals, I_s (a), P_e (b), N_s (c), T_m (d) and A_v (e), from Table 6, for varying load and rotor fault severity.

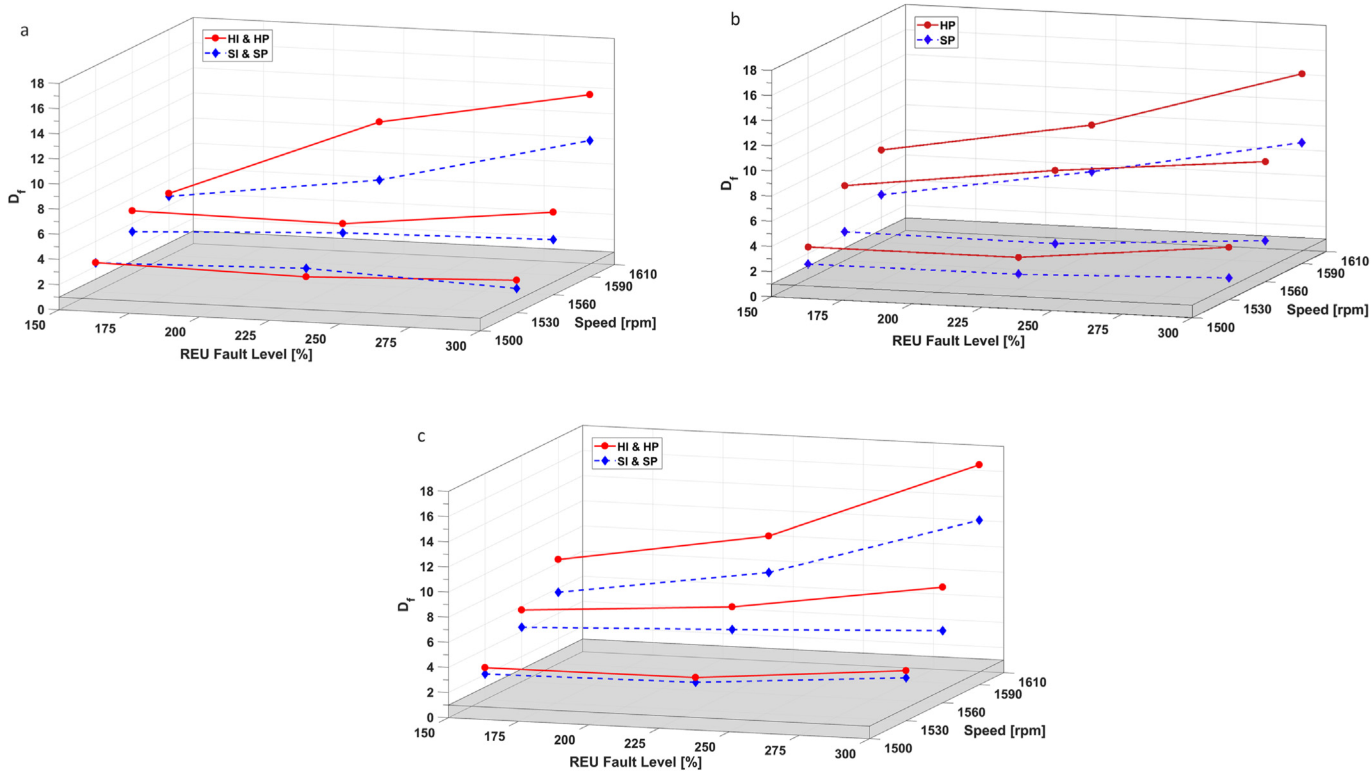

Fig. 8. Normalised Detectability, D_f, from data fusion of selected electrical & mechanical signals, I_s & A_v (a), P_e & N_s (b) and I_s & T_m (c), for varying load and rotor fault severity.

Declarations of interest

None.

Acknowledgments

This work was funded as part of the UK EPSRC SUPERGEN Wind Hub, EP/L014106/1. The data presented in this paper are available from the Durham Research Online Data Depository at https://doi.org/10.15128/r28049g5063.

References

[1] GWEC, 'Global wind statistics, Global Wind Energy Council, 2018, 2017, pp. 1–4.
[2] EWEA, 'Wind in power, European Statistics' (European Wind Energy Association, 2018), 2017, pp. 1–26.
[3] F.P. Garcia Marquez, A.M. Tobias, J.M. Pinar Perez, et al., Condition monitoring of wind turbines: techniques and methods, Renew. Energy 46 (2012) 169–178.
[4] BVG Associates, Pathways to Cost Reduction in Offshore Wind Technology: Technology Workstream, The Crown Estate, 2012, pp. 1–232.
[5] D. Coronado, K. Fischer, Condition Monitoring of Wind Turbines: State of the Art, User Experience and Recommendations, Fraunhofer Institute for Wind Energy and Energy System Technology IWES, 2015, pp. 1–83.
[6] C.J. Crabtree, D. Zappalá, S.I. Hogg, Wind energy: UK experiences and offshore operational challenges, Proc. Inst. Mech. Eng. Part A J. Power Energy 229 (7) (2015) 727–746.
[7] P.J. Tavner, Offshore Wind Turbines: Reliability, Availability & Maintenance, first ed., Institution of Engineering and Technology, 2012.
[8] R.L. Arántegui, 2013 JRC Wind Status Report - Technology, Market and Economic Aspects of Wind Energy in Europe,' EC, 2014.
[9] J. Ribrant, L.M. Bertling, Survey of failures in wind power systems with focus on Swedish wind power plants during 1997-2005, IEEE Trans. Energy Convers. 22 (1) (2007), 167-73.
[10] P.J. Tavner, S. Faulstich, B. Hahn, et al., Reliability & availability of wind turbine electrical & electronic components, EPE J. 20 (4) (2010) 45–50.
[11] M. Wilkinson, B. Hendriks, F. Spinato, et al., Methodology and results of the ReliaWind reliability field study, in: Proc. Scientific Track of the European Wind Energy Association Conference, Warsaw, Poland, 2010.
[12] K. Alewine, W. Chen, Wind turbine generator failure modes analysis and occurrence, in: Proc. Windpower, Dallas, Texas, May 2010, pp. 1–6.
[13] K. Alewine, W. Chen, A review of electrical winding failures in wind turbine generators, in: Proc. IEEE Electrical Insulation Conference (EIC), Annapolis, MD, USA, June 2011, pp. 392–397.
[14] J. Carroll, A. McDonald, D. McMillian, Reliability comparison of wind turbines with DFIG and PMG drive trains, IEEE Trans. Energy Convers. 30 (2) (2015) 663–670.
[15] C.J. Crabtree, D. Zappalá, P.J. Tavner, Survey of Commercially Available Condition Monitoring Systems for Wind Turbines, Durham University and the SUPERGEN Wind Energy Technologies Consortium, 2014, pp. 1–22.
[16] C. Hargis, B.G. Gaydon, K. Kamash, The detection of rotor defects in induction motors, IEE Conf. Publ. 213 (1982) 216–220.
[17] S. Williamson, S. Djurović, Origins of stator current spectra in DFIGs with winding faults and excitation asymmetries, in: Proc. IEEE International Electric Machines and Drives Conference, IEMDC '09, Miami, USA, 2009, pp. 563–570.
[18] S. Djurović, S. Williamson, A. Renfrew, Dynamic model for doubly-fed induction machines with unbalanced excitation, both with and without winding faults, IET Electr. Power Appl. 3 (3) (2009) 171–177.
[19] A. Yazidi, G.A. Capolino, F. Filippetti, et al., A new monitoring system for wind turbines with doubly-fed induction generators, in: Proc. MELECON 2006-2006 IEEE Mediterranean Electrotechnical Conference, Malaga, 2006, pp. 1142–1145.
[20] M. Riera-Guasp, J.A. Antonino-Daviu, G.A. Capolino, Advances in electrical machine, power electronic, and drive condition monitoring and fault detection: state of the art, IEEE Trans. Ind. Electron. 62 (3) (2015) 1746–1759.
[21] Y. Gritli, C. Rossi, D. Casadei, et al., Square current space–vector signature analysis for rotor fault detection in wound-rotor induction generator, in: Proc. IEEE XXII International Conference on Electrical Machines, ICEM 2016. Lausanne, Switzerland, September 2016, pp. 2896–2900.
[22] S. Djurović, C.J. Crabtree, P.J. Tavner, et al., 'Condition monitoring of wind turbine induction generators with rotor electrical asymmetry', IET Renew. Power Gener. 6 (4) (2012) 207–216.
[23] E. Artigao, A. Honrubia-Escribano, E. Gomez-Lazaro, Current signature analysis to monitor DFIG wind turbine generators: a case study', Renew. Energy 116 (B) (2018) 5–14.
[24] J.S. Hsu, Monitoring of defects in induction motors through air-gap torque observation, IEEE Trans. Ind. Appl. 31 (5) (1995) 1016–1021.
[25] F. Ding, F.C. Trutt, Calculation of frequency spectra of electromagnetic vibration for wound-rotor induction generators with winding faults, Electr. Gener. Power Syst. 14 (3–4) (1988) 137–150.

[26] F.C. Trutt, J. Sottile, J.L. Kohler, Detection of AC machine winding deterioration using electrically excited vibrations, IEEE Trans. Ind. Appl. 37 (1) (2001) 10–14.
[27] P.J. Rodriguez, A. Belahcen, A. Arkkio, Signatures of electrical faults in the force distribution and vibration pattern of induction motors, Proc. Inst. Electr. Eng. – Electr. Power Appl. 153 (2006) 523.
[28] S. Djurović, D.S. Vilchis-Rodriguez, A.C. Smith, Investigation of wound rotor induction generator vibration signal under stator electrical fault conditions, IET J. Eng. 4 (2014) 719–729.
[29] Y. Feng, Y. Qiu, C.J. Crabtree, et al., Monitoring wind turbine gearboxes, Wind Energy 16 (5) (2013) 728–740.
[30] P.J. Dempsey, S. Sheng, Investigation of data fusion applied to health monitoring of wind turbine drive train components, Wind Energy 16 (4) (2013) 479–489.
[31] S. Soua, P. Van Lieshout, A. Perera, et al., Determination of the combined vibrational and acoustic emission signature of a wind turbine gearbox and generator shaft in service as a pre-requisite for effective condition monitoring, Renew. Energy 51 (2013) 175–181.
[32] S. Djurović, D.S. Vilchis-Rodriguez, A.C. Smith, Supply induced inter-harmonic effects in wound rotor and doubly-fed induction generators, IEEE Trans. Energy Convers. 30 (4) (2015) 1397–1408.
[33] F. Filippetti, G. Franceschini, C. Tassoni, et al., AI techniques in induction machines diagnosis including the speed ripple effect, IEEE Trans. Ind. Appl. 34 (1) (1998) 98–108.
[34] S. Djurović, S. Williamson, Investigation of the impact of speed-ripple and inertia on the steady-state current spectrum of a DFIG with unbalanced rotor, in: Proc. 5th IET International Conference on Power Electronics, Machines and Drives (PEMD), Brighton, UK, April 2010.
[35] C. Kral, F. Pirker, G. Pascoli, The impact of inertia on rotor fault effects - theoretical aspects of the Vienna monitoring method, IEEE Trans. Power Electron. 23 (4) (2008) 2136–2142.
[36] N. Sarma, K. Tshiloz, D.S. Vilchis-Rodriguez, et al., Modelling of induction generator time and space harmonic effects in the SIMULINK environment, in: Proc. 2015 IEEE International Electric Machines and Drives Conference (IEMDC), Coeur d'Alene, ID, USA, May 2015, pp. 1279–1285.
[37] R.C. Healey, S. Lesley, S. Williamson, et al., The measurement of transient electromagnetic torque in high performance electrical drives, in: Proc. Sixth Int. Conf. Power Electronics and Variable Speed Drives, Nottingham, UK, 1996, pp. 226–229.
[38] W.R. Finley, M.M. Hodowanec, W.G. Holter, An analytical approach to solving motor vibration problems, in: Proc. Industry Applications Society 46th Annual Petroleum and Chemical Technical Conference (Cat.No. 99CH37000), San Diego, CA, 1999, pp. 217–232.
[39] S. Djurović, D.S. Vilchis-Rodriguez, A.C. Smith, Vibration monitoring for wound rotor induction generator winding fault detection, in: Proc. XXth International Conference on Electrical Machines (ICEM), Marseille, France, September 2012, pp. 1–6.
[40] EN 50160, Voltage Characteristics of Electricity Supplied by Public Distribution Systems, 2010.
[41] P.J. Tavner, L. Ran, J. Penman, H. Sedding, Condition Monitoring of Rotating Electrical Machines, second ed., Institution of Engineering and Technology, 2008.

IET Renewable Power Generation

Research Article

DFIG stator flux-oriented control scheme execution for test facilities utilising commercial converters

ISSN 1752-1416
Received on 20th October 2017
Revised 2nd May 2018
Accepted on 18th June 2018
E-First on 20th August 2018
doi: 10.1049/iet-rpg.2018.5195
www.ietdl.org

Nur Sarma[1], Paul M. Tuohy[1], Judith M. Apsley[1], Yingzhao Wang[1], Siniša Djurović[1] ✉
[1]Department of Electrical and Electronic Engineering, The University of Manchester, Manchester, UK
✉ *E-mail: Sinisa.Durovic@manchester.ac.uk*

Abstract: The utilisation of conventional industrial converters for development of doubly-fed induction generator (DFIG) test facilities poses an attractive prospect as it would provide proprietary commercial protection and functionality. However, standard commercial converters present significant challenges in attainable DFIG operational capability. This is due to the fact that they are designed for execution of a limited set of pre-programmed common control modes. They typically do not cater for execution of complicated stator flux-oriented vector control (SFOC) schemes required for DFIG drive control. The research work presented in this study reports a methodology that enables effective implementation of SFOC on industrial converters through a dedicated external real-time platform and a velocity/position communication module. The reported scheme is validated in laboratory experiments on an experimental DFIG test-rig facility. The presented principles are general and are therefore applicable to conventional DFIG drive architectures utilising standard industrial converters.

1 Introduction

The penetration of large-scale wind turbines (WTs) into power networks is increasing worldwide, with ambitious capacity expansion plans driven by national targets for carbon reduction of the electricity supply. The on-going expansion of wind power generation has given rise to an increased research interest in the process of WT electro-mechanical energy conversion; how this process, enabled by the electric generator/drive system at the core of the turbine, interfaces with the power network is of particular interest [1–3]. To avoid complicated and potentially damaging full-scale tests on sensitive and costly commercial WT units, the practical aspects of WT energy conversion research are typically underpinned by utilisation of laboratory facilities capable of emulating WT electric drive behaviour. The development of real-scale laboratory facilities for this purpose [4] can, however, pose prohibitive limitations in the academic research community where there is a need for lower cost yet representative test facilities to enable proof of concept research of various aspects of WT operations: these can range from model and control method verification to examination of power quality, fault effects and grid support capability [2–11].

Variable-speed constant-frequency electric drive topologies remain attractive for WT applications due to the variability of the mechanical power extracted from the wind. While alternatives have emerged, the most prevalent utility-scale WT electric drive architecture in use today remains that of the doubly-fed induction generator (DFIG) [3], which has become a standard component for the industry. The DFIG drive topology comprises a wound rotor induction machine (WRIM) whose rotor is interfaced to the grid through a back-to-back (alternating current (AC)/direct current (DC)/AC) converter. The back-to-back converter comprises two three-phase bidirectional voltage source converters: a rotor side converter (RSC) and a grid side converter (GSC), sharing a common DC link.

A DFIG drive provides controllability of the generated active and reactive powers with the benefit of a reduced power electronic converter rating [1]. DFIG drive operation in WT applications is generally facilitated through a specialised vector control scheme [12]. The type of control scheme used in DFIGs is defined by the choice of reference frame. Whilst alternative control algorithms continue to receive attention [13–15], the three synchronously rotating schemes: stator flux-oriented control (SFOC), stator voltage-oriented control and the air-gap flux-oriented control schemes remain commonly used [16].

Due to the prevalence of DFIG use in existing installations and its rapidly changing exploitation requirements, there is a continuous need for better understanding and improvement of operational aspects of these drives [17–19]. Credible emulation of realistic WT vector-controlled DFIG conditions on test-rig facilities is thus of significant interest for research purposes. The majority of published practical research employs proprietary converter system designs that allow direct access to switching signals and thus the implementation of appropriately specialised DFIG control schemes [2, 12, 20]. While such designs generally enable real-time implementation of DFIG control utilising digital signal processor (DSP)-based controllers, this approach is challenging and complex for practical implementation. The use of commercial off-the-shelf power electronics equipment in DFIG research test facilities would be considerably more cost-effective, provide a significant advantage in simpler to manage switching signals in the real-time application, and also safer operation due to the availability of proprietary commercial protection [21, 22]. Commercial converter systems application, however, poses considerable challenges, as they are not designed to allow direct access to switching signals control nor the application of non-standard control routines, such as those required for DFIG operation.

The literature treating DFIG control utilising commercial off-the-shelf power electronics equipment is limited [19, 21, 22]. In [21, 22], the RSC operates in open loop mode, since the standard power electronics equipment is generally not designed to facilitate straightforward application of DFIG vector control schemes. In [19], achieving practical SFOC DFIG control required additional computing and specialised software which imposed limitations in switching synchronisation and therefore a requirement for system de-rating, yielding a costly yet operationally constrained practical SFOC DFIG facility.

This research proposes a straightforward and operational method for establishment of closed loop control on grid-connected DFIG test-rig facilities utilising commercial converter systems. The presented solution for implementation of a conventional SFOC routine requires a WRIM coupled to a commercial back-to-back converter system operated through an external control platform. The magnitude, frequency, and position of the DFIG rotor current vector are calculated using an external real-time platform (dSPACE) and supplied to the RSC through a dedicated communications module (SM-Resolver module). In comparison with reported methods utilising off-the-shelf commercial converters [19, 21, 22], the proposed methodology enables effective implementation of SFOC: here, the RSC is operated in a conventional closed-loop servo control mode employing the external references provided by the dSPACE platform; the real-time platform is operated to execute a proposed routine providing the RSC real-time demand that is evaluated to ensure the implementation of rotor current control following the principles of SFOC. Furthermore, the GSC requires no modification and uses commercial off-the-shelf filters and protection components. The proposed solution was validated on an experimental DFIG test-rig and enables the establishment of the SFOC scheme on DFIG test facilities utilising off-the-shelf commercial converters. The reported study significantly expands on the initial work reported by the authors in [23], including full details of the complete controller architecture implementation, its tuning, feedback provision, experimental validation and an assessment of decoupling effects representation.

2 Test-rig facility

The DFIG test-rig facility contains a 30 kW WRIM with an industrial back-to-back converter interfacing its rotor circuit to the mains. The converter comprises two commercial three-phase, four-quadrant, AC drives (CT UNIDRIVE SP-4401) [24] coupled by a DC link. The AC drives are manufactured to enable operation in a variety of open-loop or closed-loop control modes by executing standard vector control algorithms for conventional induction and servo machines.

The challenge in implementing a practical SFOC scheme on the commercial RSC is that its proprietary design limits the available operating modes to only standard pre-programmed control strategies [24]. To overcome this limitation, a dSPACE 1103 real-time control platform and a commercial speed and position feedback interface device (CT SM-Resolver module [25]) were used. The general layout of the DFIG test-rig facility is illustrated in Fig. 1. A more detailed connection schematic of the DFIG test-rig facility is shown in Fig. 2. The WRIM is a four-pole, three-phase, 50 Hz, 415 V, 225 frame size design and was mechanically coupled to a 40 kW DC machine. The stator windings of the WRIM were connected to the grid whilst its rotor windings were supplied through the back-to-back converter. The separately excited DC machine was used as a prime mover during the experiments. The DC machine was controlled by a commercial, variable-speed, DC drive (CT MENTOR II, M75R [26]) working in speed control mode. It operated at a predefined constant speed (n^*_m in Fig. 2) or torque (T^*_{DC} in Fig. 2) during the experiments. The speed or torque was controlled through the dSPACE platform, which transmitted the desired speed and torque reference values from its digital-to-analogue channels (DACs) to the analogue-to-digital channels of the DC drive. These values were appropriately scaled in a dSPACE-executed Simulink real-time algorithm to match the ratings of the DC drive and motor.

The DC motor shaft speed and position were measured by a 1024 ppr incremental encoder. The encoder outputs were fed to the DC drive, to enable speed control of the motor, and also to the dSPACE platform, to enable real-time implementation of the DFIG SFOC scheme, as illustrated in Fig. 2. The dSPACE platform controlled the behaviour of the RSC by manipulating the magnitude, frequency and phase of the DFIG rotor currents through an appropriate Simulink implementation of the SFOC scheme. This was achieved by setting the RSC to operate in servo control mode with rotor speed and position feedback for closed-loop control of the DFIG rotor currents. The GSC was set to operate in regenerative control (Regen) mode. Furthermore, the GSC maintained the DC link voltage at a constant pre-set value of 700 V_{DC} during the experiments.

The DFIG stator and rotor currents were measured using LEM LA 55-P current sensors, and the stator voltages were measured using LEM LV25-600 voltage Hall effect transducers. The stator active and reactive powers were calculated in the dSPACE platform from the measured stator currents and voltages. The dSPACE platform was also used for recording the investigated electrical signals of interest from the DFIG test-rig facility such as the stator currents, rotor currents, stator active and reactive powers etc. The WRIM parameters were obtained from the standard characterisation tests, and are presented in the Appendix [11, 27].

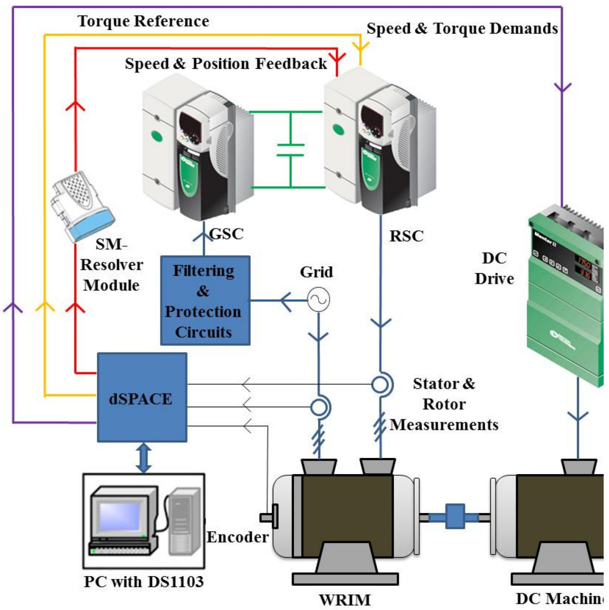

Fig. 1 *Experimental DFIG test-rig facility layout*

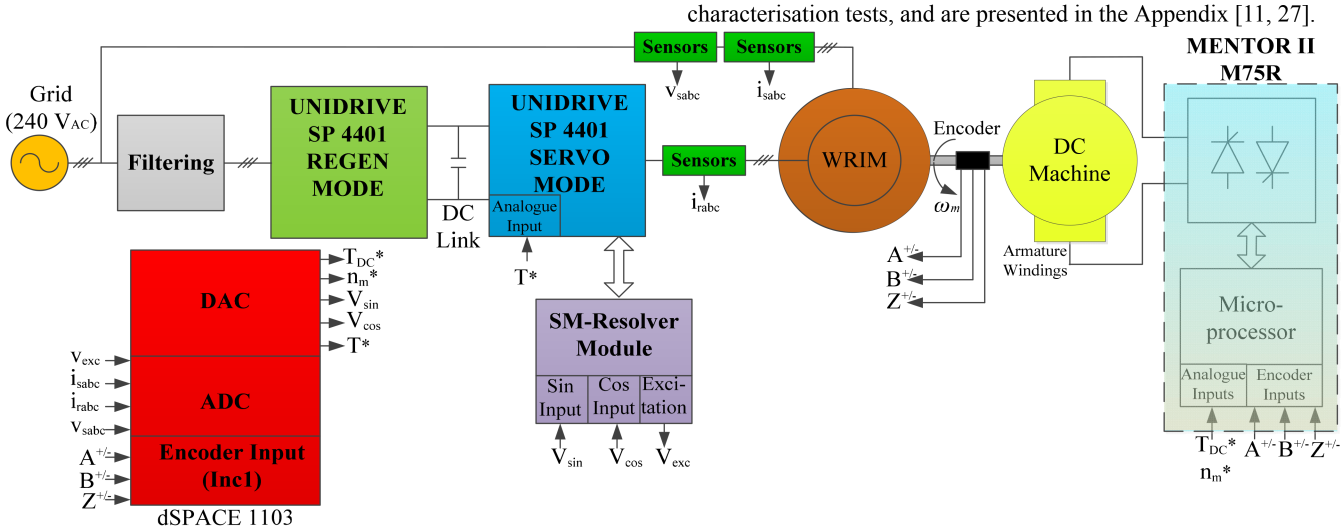

Fig. 2 *Connections schematic of the experimental DFIG test-rig facility*

3 SFOC using commercial converters

3.1 Conventional SFOC scheme

This section describes the conventional SFOC scheme. SFOC provides independent control of the DFIG stator active and reactive powers by means of regulation of the two-axis rotor currents (I^*_{rd} and I^*_{rq}) in a synchronously rotating reference frame (dq). The variables of the synchronously rotating reference frame are DC quantities in the steady state. The d-axis of the reference frame is conventionally aligned with the stator flux linkage vector in the SFOC scheme [19]. The general phasor diagram of the DFIG variables relevant for SFOC implementation is illustrated in Fig. 3, where: $\alpha_s\beta_s$ is the stationary (stator) reference frame; $\alpha_r\beta_r$ is the rotor reference frame; dq is the synchronously rotating reference frame; $\boldsymbol{V}_s$ is the stator voltage vector; $\boldsymbol{\psi}_s$ is the stator flux linkage vector; $\boldsymbol{I}^*_r$ is the reference rotor current vector; $I_{rd}*$ and $I_{rq}*$ are the d- and q-axis components of the reference rotor current vector, respectively; ω_s is the angular frequency of the synchronously rotating reference frame; ω_m is the electrical frequency of the rotor; θ_i is the position of the reference rotor current vector with respect to the d-axis of the synchronously rotating reference frame; θ_s is the orientation angle; θ_r is the electrical rotor angle; and, θ_{slip} is the electrical slip angle.

The separate regulation of the DFIG stator active and reactive powers is facilitated through the independent control of the DFIG rotor currents by utilising the direct relationship between the stator active and reactive powers and their corresponding rotor current components in the stator flux-oriented synchronous reference frame, which can be calculated as [8]

$$P_s = -V_{sq}\frac{L_m}{L_s}I_{rq}, \tag{1}$$

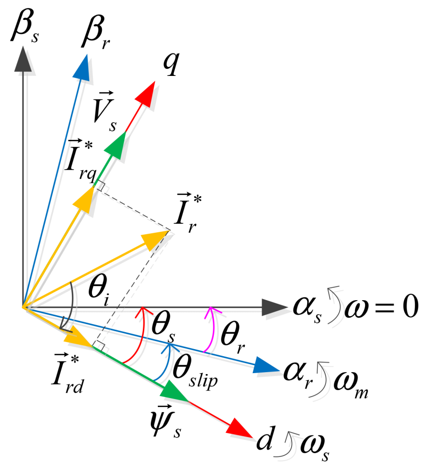

Fig. 3 *General phasor diagram of the DFIG variables*

$$Q_s = V_{sq}\frac{\psi_{sd}}{L_s} - V_{sq}\frac{L_m}{L_s}I_{rd}, \tag{2}$$

where V_{sq} is the q-axis component of the stator voltage vector; L_m is the magnetising inductance; L_s is the stator self-inductance of the DFIG; I_{rq} is the q-axis component of the rotor current vector; ψ_{sd} is d-axis component of the stator flux linkage vector; and, I_{rd} is the d-axis component of the rotor current vector. Equation (1) shows that the stator active power is a function of the q-axis rotor current whereas (2) shows that the stator reactive power depends on the d-axis rotor current. In addition, the stator active and reactive powers are only dependent on the q-axis stator voltage term if the stator phase resistances are neglected since the stator voltage vector is assumed to align with the q-axis of the synchronously rotating reference frame, as shown in Fig. 3.

Typically, the structure of the conventional SFOC comprises two cascaded control loops for the d- and q-axis: an outer (power) control loop and an inner (current) control loop [28]. The structure of the conventional SFOC is shown in Fig. 4 [29].

The outer control loops are used to calculate the reference dq-axes rotor current values for the inner control loops. Although (1) and (2) can be implemented in open-loop, each loop generally employs a closed-loop proportional–integral (PI) controller, which reduces sensitivity to parameter errors. The inner control loops establish the reference dq-axes rotor voltages and thus, the reference rotor voltage vector for the desired DFIG power output. The relationship between the rotor voltages and currents is [30]

$$V_{rd} = R_r I_{rd} + L_c\frac{dI_{rd}}{dt} - \omega_{slip}L_c I_{rq}, \tag{3}$$

$$V_{rq} = R_r I_{rq} + L_c\frac{dI_{rq}}{dt} + \omega_{slip}L_c I_{rd} + \omega_{slip}\frac{L_m}{L_s}\psi_{sd}, \tag{4}$$

where V_{rd} is the d-axis component of the rotor voltage vector; R_r is the stator referred rotor resistance per-phase; L_c is the leakage coefficient; ω_{slip} is the angular slip speed; and, V_{rq} is the q-axis component of the rotor voltage vector.

The SFOC inner (current) controllers are generally tuned through (3) and (4). The third term in (3) and (4) is known as the cross-coupling term whereas the fourth term in (4) is the perturbation term. The decoupling and feed-forward terms (as illustrated in Fig. 4) are generally applied to the outputs of the inner controllers, in order to eliminate the rotor currents' cross-coupling and speed dependency, respectively [20]. The implementation of decoupling provides an improvement in the tracking performance of the inner controllers, as well as an easier tuning procedure [20].

In general, the SFOC outer (power) controllers are tuned through (1) and (2). The first term in (2) is dependent on the stator flux and is considered as a constant disturbance effect [28]. Therefore, this term is removed from the d-axis outer control loop using compensation, as illustrated in Fig. 4. Furthermore, removing

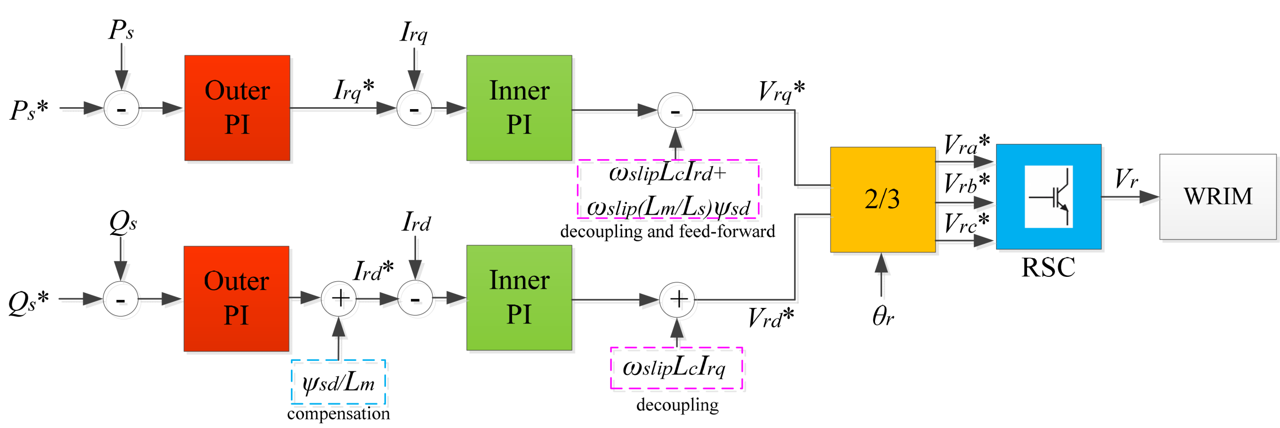

Fig. 4 *Conventional SFOC structure*

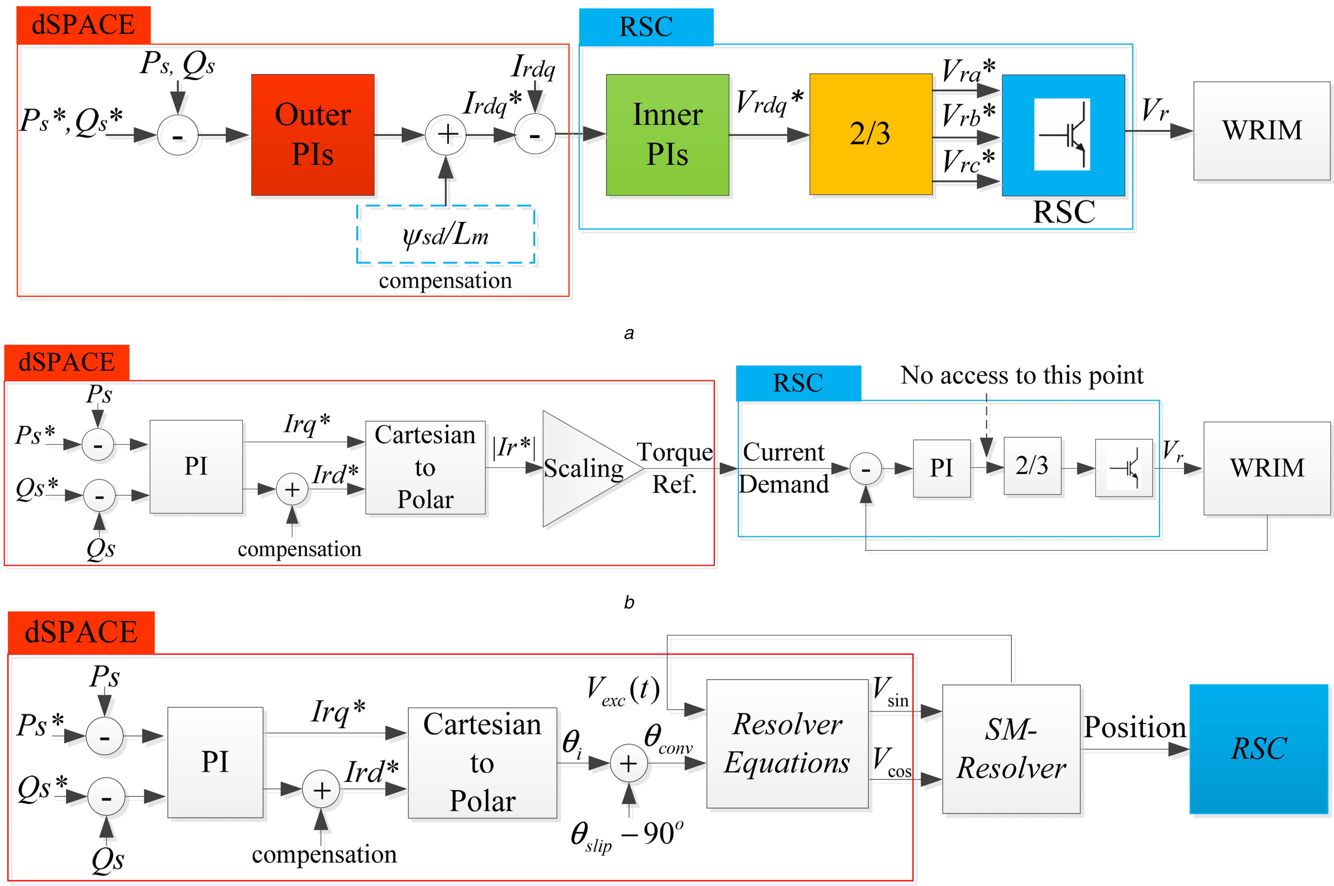

a

b

c

Fig. 5 *Real-time implementation of the SFOC scheme*
(a) General architecture of the SFOC implementation, ***(b)*** Magnitude control of the SFOC scheme, ***(c)*** Real-time speed and position control of the SFOC scheme

the disturbance term also enables the same transfer function to be used for tuning the *dq*-axes outer control loops.

3.2 SFOC implementation on commercial converters

The implementation of the SFOC scheme (which utilises cascaded control loops) using commercial converters is complicated by the fact that the inner control loops must reside in the commercial RSC. To protect the power switches, there is no direct control of the RSC voltages, so the inner controllers must be executed through one of the commercial converters pre-defined control mode options. For this reason, the SFOC scheme was realised in this work by implementing the outer control loops on the dSPACE platform (as outlined in Section 1) and linking their outputs with the inputs of the inner control loops embedded within the RSC operating in servo mode, as illustrated in Fig. 5*a*. In servo mode, reference torque and angle values were used to generate the internal reference *dq*-axes currents.

The RSC included the inner control loops. However, the RSC imposed a limitation, as it did not allow access to the outputs of its PI controllers (see Fig. 5*a*), where the SFOC decoupling terms (shown in Fig. 4) should be included. The effect of omitting decoupling is analysed in the Appendix and is found acceptable for: changes in the outer control loop such as demanded power flow; slowly varying disturbances, for example, wind speed; any operation at close to synchronous speed. However, with decoupling omitted, the controller is not able to reject rapid disturbances in the inner loop, especially at high slip, which means that the system would not be suitable for network fault studies. Under these conditions, conventional stator active power/stator reactive power (PQ) control would not be used anyway. For low-voltage ride-through additional hardware or control is required, since the field-oriented assumptions are invalid if the stator flux varies [31]. Furthermore, in principle, assuming the commercial converter system manufacturer's proprietary knowledge on the design features of the servo control mode decoupling routine is available, it could be modified to be adapted to the execution of an SFOC characteristic decoupling scheme. This knowledge, however, is generally seen as commercially sensitive and was not available in this study, and thus, in addition to the points raised previously in this paragraph, decoupling has been omitted from the proposed SFOC practical implementation routine.

The magnitude control of the rotor currents was achieved by using the external torque reference parameter of the RSC, as shown in Fig. 5*b*. The reference rotor currents provided by the outer control loops were used to define the torque reference value in the dSPACE platform, which was then passed to the RSC. The calculated torque reference value must be appropriately scaled for the voltage range of the analogue input of the RSC. The scaling shown in the diagram in Fig. 5*b* is calculated as

$$\text{Scaling} = \frac{\text{analogueinputfullscalevoltage}}{\text{RSCMAXcurrentrating}}. \qquad (5)$$

The scaled torque reference value was generated by a DAC of the dSPACE platform (shown in a red box, Fig. 5*b*) and then passed to the RSC analogue input and converted back to the corresponding current value internally. Depending on the relationship between the desired and measured rotor currents, the pre-programmed servo control routine of the RSC created the appropriate excitation voltages for the DFIG rotor windings (shown in the blue box, Fig. 5*b*).

The frequency and phase control of the rotor currents were achieved using an SM-Resolver module, as shown in Fig. 5*c*. For the servo control mode of operation, the RSC controller assumes that the output current vector is aligned with the *q*-axis of the servo reference frame [32]. A servo reference frame, therefore, had to be introduced to the general phasor diagram of Fig. 3, to illustrate the appropriate orientation that is needed to be provided to the RSC servo controller to ensure correct implementation of the SFOC scheme. The resultant phasor diagram is shown in Fig. 6, where:

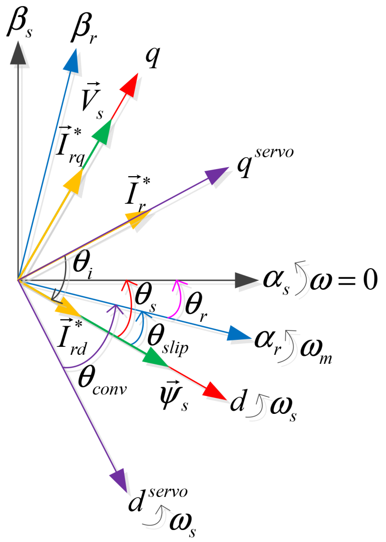

Fig. 6 *Resultant phasor diagram*

d^{servo} and q^{servo} are the servo reference frame d- and q-axis, respectively, and, θ_{conv} is the appropriate reference position angle for the RSC servo controller. The servo controller reference position, θ_{conv}, was chosen to align q^{servo} with the SFOC defined reference rotor current vector, $\boldsymbol{I}_{\text{r}}^*$, and thus, ensured appropriate implementation of the SFOC scheme. θ_{conv} was obtained using the instantaneous angle between the known servo d^{servo}-axis and the rotor α_{r}-axis positions, as illustrated in Fig. 6, which can be calculated from

$$\theta_{\text{conv}} = \theta_i + \theta_{\text{slip}} - 90^{\circ}. \tag{6}$$

The dSPACE platform was used to emulate the resolver real-time feedback signals matching the established servo controller orientation angle (shown in the red box, Fig. 5*c*). The emulated resolver output signals were connected to the corresponding inputs of the SM-Resolver module (shown in Fig. 2), to ensure the appropriate orientation of the RSC controller.

Reliable determination of the orientation angles shown in Fig. 6 is therefore essential for successful implementation of SFOC. The correct estimation of the position of the stator flux linkage space vector is particularly important. A common approach to estimating the flux vector position is based on neglecting the stator resistive voltage drop and assuming the flux linkage vector lags the stator voltage vector by 90 electrical degrees [20]. Hence, the position of the flux linkage vector with respect to the stator reference frame (θ_{s}) can readily be obtained from the three-phase stator voltages measurements using a phase-lock-loop [27]. The rotor reference frame position with respect to the stationary reference frame (θ_{r}) was obtained from the shaft-mounted encoder output signals, multiplied by the pole-pairs of the WRIM. θ_{r} was then used in combination with θ_{s} to determine the real-time value of the rotor slip angle ($\theta_{\text{slip}} = \theta_{\text{s}} - \theta_{\text{r}}$) in dSPACE. The real-time slip angle value was used to transform the relevant three-phase rotor variables to the synchronously rotating reference frame.

3.3 Controller tuning procedure

The tuning procedure of the proposed SFOC scheme is summarised in this section. The SFOC was tuned using a conventional transfer function approach [29], whilst taking care to ensure the parameters of the inner controllers, residing within the RSC, were appropriately identified and set. Choosing appropriate time constants for both the outer and inner control loops was key to ensuring adequate controller performance. The separation of the outer and inner control loops was enabled by choosing different time constants and noting that the time constant of the inner control loops should ideally be at least five times smaller than the outer control loops [28]. Therefore, the outer control loops would not react to the faster inner control loops and thus, the inputs of the inner control loops can be accurately calculated. In addition, choosing a smaller time constant for the inner loops enables their representation as a constant gain for the outer control loops' analysis.

The control parameters of the outer and inner control loops were calculated from their closed-loop transfer functions. These are the proportional gain (K_{po} is the outer control loops and K_{pi} is the inner control loops) and the integral gain (K_{io} is the outer control loops and K_{ii} is the inner control loops). The closed-loop transfer function of the outer control loops can be expressed as

$$\frac{P_{\text{s}}}{P_{\text{s}}^*} = \frac{Q_{\text{s}}}{Q_{\text{s}}^*} = \frac{1 + s\left(K_{\text{po}}/K_{\text{io}}\right)}{1 + s\left(\dfrac{1 + K_{\text{po}}\left(-V_{sq}L_{\text{m}}/L_{\text{s}}\right)}{K_{\text{io}}\left(-V_{sq}L_{\text{m}}/L_{\text{s}}\right)}\right)} \tag{7}$$

and, the transfer function of the inner loops as

$$\frac{I_{\text{r}d}}{I_{\text{r}d}^*} = \frac{I_{\text{r}q}}{I_{\text{r}q}^*} = \frac{\left(K_{\text{ii}}/L_{\text{c}}\right) + s\left(K_{\text{pi}}/L_{\text{c}}\right)}{\left(K_{\text{ii}}/L_{\text{c}}\right) + s\left(\left(R_{\text{r}} + K_{\text{pi}}\right)/L_{\text{c}}\right) + s^2}. \tag{8}$$

Assuming $K_{\text{po}} \ll K_{\text{io}}$ and $K_{\text{pi}} \ll K_{\text{ii}}$, (7) and (8) can be approximated as first-order and second-order transfer functions, respectively [28]. This assumption simplifies the calculation of the control parameters of the outer and inner control loops. In this work, K_{po} was chosen to be zero. Therefore, the only control parameter required for the outer control loops was K_{io}, which is calculated by

$$K_{\text{io}} = \frac{1}{\tau_{\text{o}}\left(-V_{sq}L_{\text{m}}/L_{\text{s}}\right)}, \tag{9}$$

where τ_{o} is the time constant of the outer control loops. The grid voltages were assumed to be stiff and the stator inductances were considered constant for the purpose of this calculation. K_{io} was calculated for the WRIM installed in the experimental DFIG test-rig facility as $-0.009\ \text{V}^{-1}\ \text{s}^{-1}$ with a time constant of 0.54 s.

The inner controllers needed to be tuned appropriately to reflect the proposed SFOC scheme. In conventional applications, the RSC control loop parameters are recommended to be determined using the proprietary auto-tuning routine [24], which automatically measures the WRIM parameters and adjusts the parameters of the inner controllers [33]. However, the auto-tuning routine was not capable of obtaining the parameters of the RSC controllers for the proposed SFOC scheme, since the RSC assumes it is operating with a synchronous machine in servo control mode. The parameters of the inner controllers are therefore first determined using the second-order transfer function given in (8). The bandwidth and damping factor of the inner controllers were set to 18 Hz and 1.8 in this study, respectively. This provided a time constant of 0.005 s and a K_{ii} and K_{pi} of $34\text{VA}^{-1}\ \text{s}^{-1}$ and $1\ \text{V A}^{-1}$, respectively. Once determined, the gains were programmed into the RSC controllers using their proprietary software interface.

3.4 Resolver feedback emulation

The accuracy of the emulated real-time resolver feedback for the reference frame orientation of the RSC controllers is vital for ensuring good performance of the proposed SFOC scheme. The calculation of the emulated resolver output signals required the excitation signal, $V_{\text{exc}}(t)$, provided by the commercial SM-Resolver module, as shown in Fig. 7. The output sine and cosine signals of the real-time resolver were then emulated in dSPACE from the calculated real-time reference position angle for the RSC controllers, θ_{conv}, using the following equations [34]:

$$V_{\sin} = gV_{\text{exc}}\sin(\theta_{\text{conv}}(t))\sin(\omega_{\text{c}}t), \tag{10}$$

$$V_{\cos} = gV_{\text{exc}}\cos(\theta_{\text{conv}}(t))\sin(\omega_{\text{c}}t), \tag{11}$$

where g is the resolver turns ratio; and V_{exc} and ω_c are the magnitude and angular frequency of the excitation signal, respectively.

The SM-Resolver module parameters had to be appropriately set through the RSC proprietary settings menu to obtain the correct position feedback. The excitation signal frequency was fixed at 6 kHz in this work whilst the resolver turns ratio and the magnitude of the excitation signal was set to 2:1 and $4V_{rms}$, respectively. The dSPACE emulated resolver output signals were sent to the SM-Resolver module, which provided the orientation feedback for the RSC controllers to generate the desired frequency and phase of the rotor current through the 'position' signal, as shown in Fig. 5*c*. This signal provided the absolute position of the rotor current vector with respect to the *d*-axis of the servo reference frame [32].

The synchronously measured position and emulated resolver output signals for a rotor current frequency of ⊄3.3 Hz, corresponding to a slip of (⊄100 rpm), are illustrated in Fig. 7. The emulated resolver output is seen to be at twice the frequency of the corresponding position signal due to the SM-Resolver module design, which operates to provide mechanical position information [25].

To obtain a good trade-off between achieving more sinusoidal-emulated resolver outputs and maintaining a sufficient execution speed of the SFOC scheme on the dSPACE platform, it was important to select an appropriate sampling rate in dSPACE. The effect of the dSPACE sampling rate choice on the emulated resolver outputs is illustrated in Fig. 8. Fig. 8 shows the corresponding signals measured at the DAC outputs of the dSPACE platform (identified in Fig. 2). Fig. 8 shows the emulated resolver output signals for the applied sampling frequencies of 55, 25, and 10 kHz, respectively.

The recorded data show that the emulated resolver outputs become distorted when the dSPACE sampling rate comes close to the resolver excitation frequency of 6 kHz. This can cause potential errors in the calculation of the frequency and position of the rotor current vector. In addition, for sampling frequencies >70 kHz, the controller performance can also degrade, as dSPACE is unable to complete the required control algorithm calculations within the set sample period. In this work, the optimal operating range of the dSPACE platform was found to be between 55 and 65 kHz in the experiments.

4 Results

The implemented SFOC scheme is experimentally evaluated in this section using the laboratory DFIG test-rig facility described in Section 2. A typical step change in the time-domain of the stator active and reactive power demands was applied for validation of the proposed SFOC scheme. This is a conventional method of assessing DFIG controller performance [12, 20, 28] since the separate implementation of active and reactive power step changes provides different behaviour and thus, operational analysis of the executed SFOC scheme. The results of step changes in the stator active and reactive power demands are presented in Figs. 9 and 10.

The DFIG test-rig facility was operated at an arbitrary super-synchronous operating point of 1560 rpm (0.04 slip) during the experiments. In the active power demand step change test, the stator active power demand was controlled to change from −3 to −6 kW (power is negative when generating since the motoring convention was used) at 3 s, whilst the stator reactive power demand was kept at a constant value of 0 VAr. In the reactive power demand step change test, the stator reactive power demand was set to change from 0 VAr to 2 kVAr at 5 s, whilst maintaining the stator active power demand at a constant value of −5 kW.

The effects of the stator active power step change on the measured DFIG electrical signals during the experiments are shown in Fig. 9, whilst Fig. 10 shows the effects of the stator reactive power step changes on the measured DFIG electrical.

The alignment of the stator voltage and flux vectors during the SFOC control reference frame orientation angle calculation (as discussed in Section 3) enables the regulation of the *d*- and *q*-axis rotor current components in relation with the stator reactive and active powers, respectively. This means that the active power step change caused a major effect on the *q*-axis rotor current component, whereas the *d*-axis rotor current remained principally affected by a change in the stator reactive power, as can be observed from the experimental data presented in Figs. 9*c* and 10*c*, respectively. These figures also show that the *d*- and *q*-axis rotor currents exhibited a very minor variation as a result of the implemented active and reactive powers step change, respectively. This arises due to an amalgamation of effects related to inherent inaccuracy in orientation angle calculation such as neglecting stator resistance [20], and the previously discussed omission of the decoupling effects on the RSC embedded inner controller; the magnitude of the observed variation in the experimental results is, however, seen to be negligible and these effects, therefore, deemed acceptable for the purpose of this study.

The response time of the outer and inner controllers to the step changes recorded in Figs. 9*a* to 10*b* matched the design parameters calculated in Section 3. The calculated time constant of the outer control loops (≈0.54 s) shows good agreement with the measured responses of the outer control loops. The inner control loops are seen to effectively follow the references set by the outer control loops, due to their time constants, which are chosen to be faster than those of the outer controller. The response of the controllers used in this study is considered representative of WT applications, characterised by relatively slow dynamics of wind speed and therefore generator rotational speed change [10, 35, 36].

A small percentage of ripples is generally seen to be present in the measured data. This was found in the experiments to be largely dominated by the shaft rotational frequency components arising from the small inherent mechanical unbalances in the test-rig, as well as the prominent space harmonic effects inherent to the examined WRIM design [11]. Similar effects have been observed in previous publications [20]. In addition, the effects of the speed ripple caused by the inevitable inherent electrical asymmetry of the test-rig were also found to contribute to the observed SFOC signal ripple [37]. Figs. 9*c* and 10*c* also show that the ripple in the *d*-axis reference rotor current was higher than that observed in the *q*-axis reference rotor current. This difference is largely caused by the compensation term in the *d*-axis outer control loop, as stated in (2) and shown in Fig. 4.

In general, the measured rotor currents are seen to appropriately change to follow the set demand in the DFIG stator active and reactive powers imposed through the SFOC scheme. Rotor current control is enabled by the demanded rotor current position implemented on the RSC through the SM-Resolver module and the external dSPACE platform. Figs. 9 and 10 show that the presented SFOC scheme implementation procedure for DFIGs enables effective practical control of the rotor currents and thus, the generated stator active and reactive powers using standard commercial converters. Consistent results have also been observed at other operating speeds on the test-rig facility but are not included in this study for brevity.

5 Conclusions

This study reports an experimentally validated procedure for implementing an SFOC scheme on a DFIG practical facility utilising standard off-the-shelf converters. The presented solution provides a competent means of establishing SFOC capability in DFIG drive topologies utilising commercial converters, which do not inherently possess the facility of the SFOC and do not allow the end-user to define switching device control modes. Furthermore, the presented solution provides an advantage of retaining the full protection of the system as it utilises off-the-shelf commercial equipment, and imposes no requirement for the development of proprietary converter design and protection to allow SFOC execution.

The proposed procedure was evaluated in real-time experiments on a laboratory DFIG test-rig facility involving step changes in the power demand of the stator active and reactive powers. Standard active and reactive power step change tests were separately implemented on the DFIG test-rig to evaluate the performance of the SOFC implemented by the proposed method. The measured step change response of the control loops shows good agreement

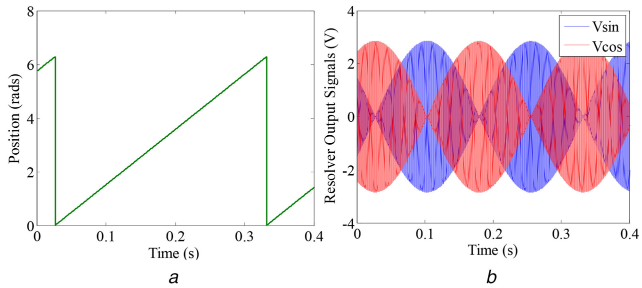

Fig. 7 *Synchronously measured position angle for the RSC servo controller and emulated resolver output signals*
(a) Position signal, ***(b)*** Emulated resolver output signals

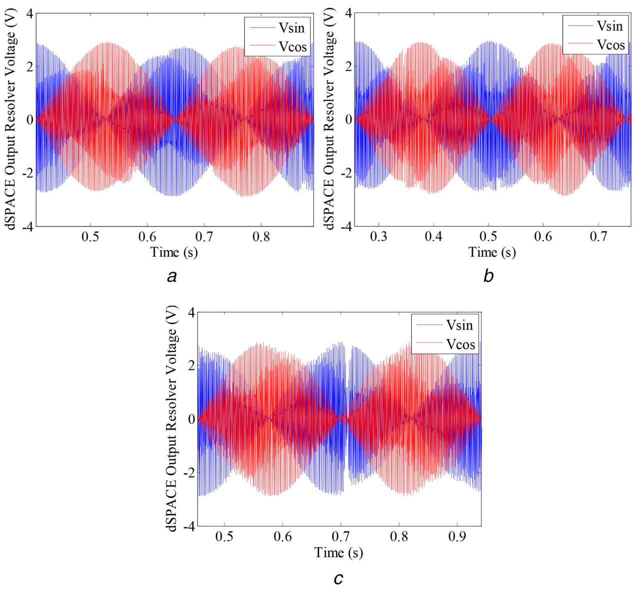

Fig. 8 *Emulated resolver outputs measured at the dSPACE DACs*
(a) Sampling frequency at 55 kHz, ***(b)*** Sampling frequency at 25 kHz, ***(c)*** Sampling frequency at 10 kHz

with the calculated settling times. The minor coupling during transients, as well as a small percentage of ripple, was identified in the measured data and found to be an amalgamation of the effects inherent of the examined WRIM design and the proposed SFOC implementation method, but more importantly, manifested at a low level which was deemed acceptable for this research. The experimental results showed that the presented work enables the practical establishment of an operative SFOC scheme allowing the DFIG rotor currents and thus the generated stator active and reactive powers to be effectively controlled in the steady state. The reported test results are for a typical super synchronous operating speed of 1560 rpm, however, consistent performance has been observed in the test system throughout the operating speed range. In addition, a study of the effects of the proposed scheme's limitations in representation of decoupling effects is reported, suggesting that these do not adversely affect its operation for changes in the outer control loop such as demanded power flow; slowly varying disturbances, for example, wind speed; or any operation at close to synchronous speed.

The details of the practical implementation of the SFOC scheme on the commercial converter, the tuning of the controller parameters and the appropriate controller orientation feedback requirements were presented, to enable full understanding of the reported solution. Whilst the proposed SFOC practical implementation procedure has been applied and validated on a specific commercial converter in this study, the proposed principles are generally applicable to other modern commercial converters and could, therefore, be utilised in alternative DFIG architectures, including multi-level topologies since most converters support a torque reference input and resolver interface.

6 Acknowledgments

Dr Nur Sarma's Ph.D. study at The University of Manchester was funded by the Turkish Ministry of Education. This work was supported in part by the UK EPSRC Supergen Wind Hub Consortium under grant EP/L014106/1.

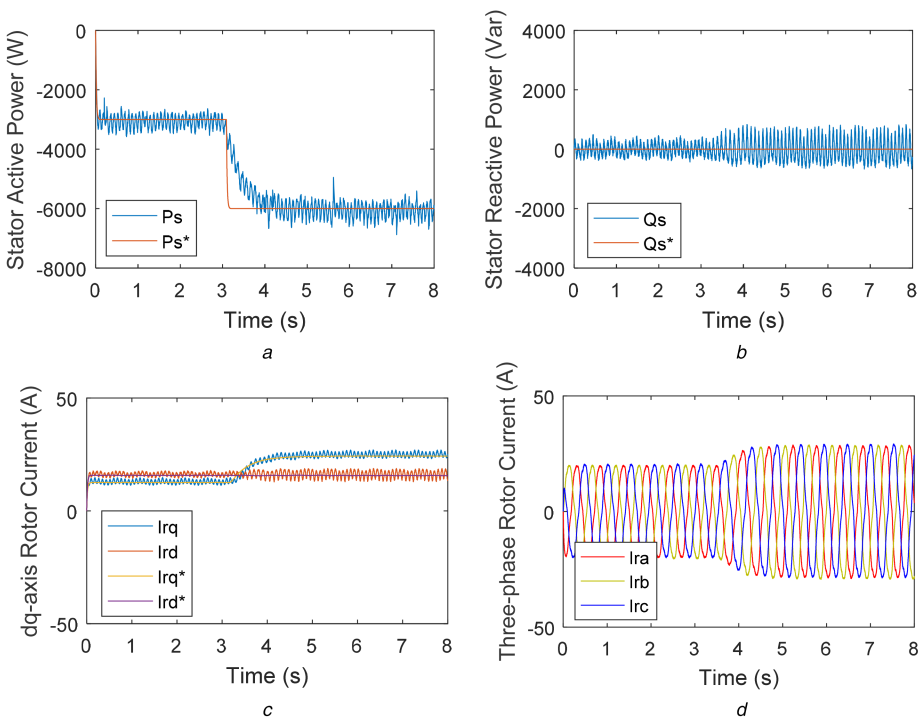

Fig. 9 *Stator active power step change implementation, 1560 rpm*
(a) Measured and reference stator active powers, ***(b)*** Measured and reference stator reactive powers, ***(c)*** Measured and reference *dq*-axis rotor currents, ***(d)*** Measured three-phase rotor currents

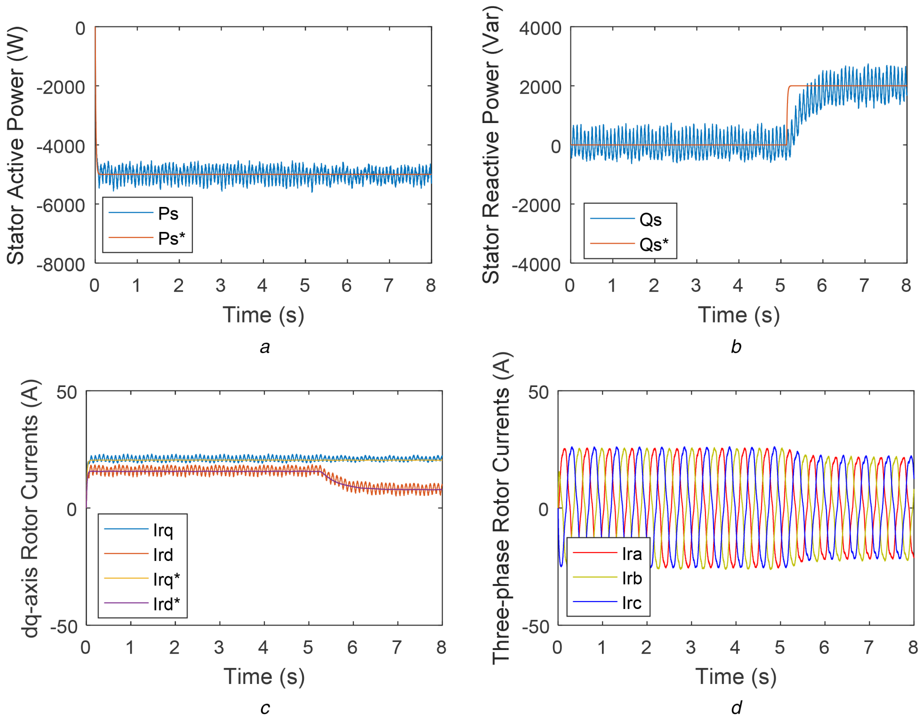

Fig. 10 *Stator reactive power step change implementation, 1560 rpm*
(a) Measured and reference stator active powers, ***(b)*** Measured and reference stator reactive powers, ***(c)*** Measured and reference *dq*-axis rotor currents, ***(d)*** Measured three-phase rotor currents

7 References

[1] Muller, S., Deicke, M., Doncker, R.W.D.: 'Doubly fed induction generator systems for wind turbines', *IEEE Ind. Appl. Mag.*, 2002, **8**, pp. 26–33

[2] Morfin, O.A., Ruiz-Cruz, R., Loukianov, A.G., *et al.*: 'Torque controller of a doubly-fed induction generator impelled by a DC motor for wind system applications', *IET Renew. Power Gener.*, 2014, **8**, (5), pp. 484–497

[3] Edrah, M., Lo, K.L., Anaya-Lara, O.: 'Impacts of high penetration of DFIG wind turbines on rotor angle stability of power systems', *IEEE Trans. Sustain. Energy*, 2015, **6**, pp. 759–766

[4] Zeni, L., Gevorgian, V., Wallen, R., *et al.*: 'Utilisation of real-scale renewable energy test facility for validation of generic wind turbine and wind power plant controller models', *IET Renew. Power Gener.*, 2016, **10**, (8), pp. 1123–1131

[5] Hansen, A.D., Michalke, G.: 'Multi-pole permanent magnet synchronous generator wind turbines' grid support capability in uninterrupted operation during grid faults', *IET Renew. Power Gener.*, 2009, **3**, (3), pp. 333–348

[6] Chondrogiannis, S., Barnes, M.: 'Specification of rotor side voltage source inverter of a doubly-fed induction generator for achieving ride-through capability', *IET Renew. Power Gener.*, 2008, **2**, (3), pp. 139–150

[7] Djurovic, S., Williamson, S., Renfrew, A.: 'Dynamic model for doubly-fed induction generators with unbalanced excitation, both with and without winding faults', *IET Electr. Power Appl.*, 2009, **3**, (3), pp. 171–177

[8] Zhu, R., Chen, Z., Wu, X.: 'Dynamic performance of doubly-fed induction generator stator flux during consecutive grid voltage variations', *IET Renew. Power Gener.*, 2015, **9**, (7), pp. 720–728

[9] Ma, Z., Teng, W., Liu, Y., *et al.*: 'Application of the multi-scale enveloping spectrogram to detect weak faults in a wind turbine gearbox', *IET Renew. Power Gener.*, 2017, **11**, (5), pp. 578–584

[10] Djurovic, S., Crabtree, C.J., Tavner, P.J., *et al.*: 'Condition monitoring of wind turbine induction generators with rotor electrical asymmetry', *IET Renew. Power Gener.*, 2012, **6**, (4), pp. 207–216

[11] Djurović, S., Vilchis-Rodriguez, D.S., Smith, A.C.: 'Supply induced interharmonic effects in wound rotor and doubly-fed induction generators', *IEEE Trans. Energy Convers.*, 2015, **30**, (4), pp. 1397–1408

[12] Pena, P., Clare, J.C., Asher, G.M.: 'Doubly fed induction generator using back-to-back PWM converters and its application to variable-speed wind-energy generation', *IEE Proc., Electr. Power Appl.*, 1996, **143**, pp. 231–241

[13] Arnalte, S., Burgos, J.C., Rodriguez-Amenedo, J.L.: 'Direct torque control of a doubly-fed induction generator for variable speed wind turbines', *Electr. Power Compon. Syst.*, 2002, **30**, pp. 199–216

[14] Mahmodicherati, S., Elbuluk, M., Sozer, Y.: 'An improved direct power control of a doubly fed induction generator wind power system'. IEEE Industry Applications Society Annual Meeting, Lake Buena Vista, FL, 2013, pp. 1–8

[15] Datta, R., Ranganathan, V.T.: 'Direct power control of grid-connected wound rotor induction machine without rotor position sensors', *IEEE Trans. Power Electron.*, 2001, **16**, pp. 390–399

[16] Petersson, A., Harnefors, L., Thiringer, T.: 'Evaluation of current control methods for wind turbines using doubly-fed induction machines', *IEEE Trans. Power Electron.*, 2005, **20**, pp. 227–235

[17] Faiz, J., Moosavi, S.M.M.: 'Detection of mixed eccentricity fault in doubly-fed induction generator based on reactive power spectrum', *IET Electr. Power Appl.*, 2017, **11**, (6), pp. 1076–1084

[18] Bu, S.Q., Du, W., Wang, H.F., *et al.*: 'Power angle control of grid-connected doubly fed induction generator wind turbines for fault ride-through', *IET Renew. Power Gener.*, 2013, **7**, (1), pp. 18–27

[19] Zaggout, M., Tavner, P., Crabtree, C., *et al.*: 'Detection of rotor electrical asymmetry in wind turbine doubly-fed induction generators', *IET Renew. Power Gener.*, 2014, **8**, (8), pp. 878–886

[20] Hopfensperger, B., Atkinson, D.J., Lakin, R.A.: 'Stator-flux-oriented control of a doubly-fed induction machine with and without position encoder', *IEE Proc., Electr. Power Appl.*, 2000, **147**, pp. 241–250

[21] Wegener, R., Soter, S., Rosmann, T.: 'Facility employing standard converters for testing DFIG wind generators up to 30 kW'. 2006 IEEE Int. Symp. on Industrial Electronics, Montreal, Canada, 2006, pp. 1025–1029

[22] Wegener, R., Soter, S., Rosmann, T.: 'Operation of double Fed induction generators with unmodified Low cost standard converters'. 37th IEEE Power Electronics Specialists Conf., Jeju, Korea, 2006, pp. 1–5

[23] Sarma, N., Apsley, J.M., Djurovic, S.: 'Implementation of a conventional DFIG stator flux oriented control scheme using industrial converters'. 2016 IEEE Int. Conf. on Renewable Energy Research and Applications, Birmingham, 2016, pp. 236–241

[24] Control Techniques: 'User guide unidrive SP model sizes 1 to 9'. Control Techniques, October 2005

[25] Control Techniques: 'User guide SM-resolver' (C.T.D. Ltd, Telford, September 2004)

[26] Control Techniques: 'User guide mentor II DC drives 25 A to 1850 A output', (C.T.D. Ltd., Telford, January 2006)

[27] Cashman, D.P., Hayes, J.G., Egan, M.G., *et al.*: 'Comparison of test methods for characterization of doubly fed induction machines', *IEEE Trans. Ind. Appl.*, 2010, **46**, pp. 1936–1949

[28] Tapia, G., Tapia, A., Ostolaza, J.X.: 'Two alternative modeling approaches for the evaluation of wind farm active and reactive power performances', *IEEE Trans. Energy Convers.*, 2006, **21**, pp. 909–920

[29] Atkinson, D., Lakin, R., Jones, R.: 'A vector-controlled doubly-fed induction generator for a variable-speed wind turbine application', *Trans. Inst. Meas. Control*, 1997, **19**, pp. 2–12

[30] Wang, Z., Sun, Y., Li, G., *et al.*: 'Magnitude and frequency control of grid-connected doubly fed induction generator based on synchronised model for wind power generation', *IET Renew. Power Gener.*, 2010, **4**, (3), pp. 232–241

[31] Justo, J.J., Mwasilu, F., Jung, J.W.: 'Doubly-fed induction generator based wind turbines: a comprehensive review of fault ride-through strategies', *Renew. Sustainable Energy Rev.*, 2015, **45**, pp. 447–467

[32] Control Techniques: 'Advanced user guide unidrive SP', June 2009

[33] Drury, B.: '*Control techniques drives and controls handbook*' (IET, London, 2001)

[34] Aung, N.L.H., Bi, C., Mamun, A.A., *et al.*: 'A demodulation technique for spindle rotor position detection with resolver', *IEEE Trans. Magn.*, 2013, **49**, pp. 2614–2619

[35] Ibrahim, R., Watson, S., Djurović, S., *et al.*: 'An effective approach for rotor electrical asymmetry detection in wind turbine DFIGs', *IEEE Trans. Ind. Electron.*, 2018, **65**, (11), pp. 8872–8881

[36] Breslan, D.J., Apsley, J.M., Smith, A.C.*, et al.*: 'Control of a vertical axis wind turbine in gusty conditions'. Eighth IET Int. Conf. on Power Electronics, Machines and Drives (PEMD 2016), Glasgow, 2016, pp. 1–6

[37] Filippetti, F., Franceschini, G., Tassoni, C.*, et al.*: 'AI techniques in induction machines diagnosis including the speed ripple effect', *IEEE Trans. Ind. Appl.*, 1998, **34**, (1), pp. 98–108

[38] Liang, J., Howard, D.F., Restrepo, J.A.*, et al.*: 'Feed-forward transient compensation control for DFIG wind turbines during both balanced and unbalanced grid disturbances', *IEEE Trans. Ind. Appl.*, 2011, **49**, (3), pp. 1452–1463

8 Appendix

The parameters of the WRIM parameters are presented in Table 1.

8.1 Omission of decoupling

Assuming that the controller orientation is correct and that the converter is ideal and the stator dynamics is not excited, the combined controller and WRIM can be represented in the synchronous reference frame, as shown in Fig. 11 (where coupling within the WRIM model is included). To simplify the analysis, the magnetising term in the reactive power and the associated compensation in the controller have been omitted, since they are assumed to cancel.

Full analytical expressions can be derived for the transfer functions between the steps in the reference inputs (P_s* and Q_s*, or I_{rd}* and I_{rq}*) and the outputs (P_s, Q_s, I_{rd}, and I_{rq}), respectively. Fig. 12 shows the magnitudes of these transfer functions as a function of frequency at 4% slip, i.e. the operating point used in the presented tests, and 30% slip, i.e. the typical speed range of a DFIG. The direct trace shows the response in the direct axis, I_{rq}/I_{rq}* (top) and P_s/P_s* (bottom), which is independent of the slip. The coupled traces show the disturbance in the opposite channel, I_{rd}/I_{rq}*, Q_s/P_s*, at 4 and 30% slip, respectively. Since the coupling terms depend on the slip, there is no coupling at a synchronous speed. It can be seen that at the operating point of 1560 rpm (i.e. 4% slip), the attenuation is >100 (40 dB); there is a less good rejection of disturbances directly injected into the current loop where the attenuation is a factor of 10 (20 dB). At 30% slip, there is still a good rejection of disturbances in P_s and Q_s, but steps injected directly into the current loop show a similar magnitude in the coupled channel compared with the direct channel.

The use of the servo controller means that the *q*-axis of the RSC is aligned with the desired rotor current rather than the *d*-axis alignment with the stator flux. The PI controller can be written in the RSC frame (denoted $_1$) as

$$\frac{\mathrm{d}V^*_{r1dq}}{\mathrm{d}t} = K_{pi}\frac{\mathrm{d}}{\mathrm{d}t}\left(I^*_{r1dq} - I_{r1dq}\right) + K_{ii}\left(I^*_{r1dq} - I_{r1dq}\right). \quad (12)$$

Mapping values to the synchronous reference frame using the angle transformation: $\mathrm{e}^{-\mathrm{j}(\theta_i - \pi/2)}$, gives

$$\begin{aligned}\frac{\mathrm{d}V^*_{rdq}}{\mathrm{d}t} &= K_{pi}\frac{\mathrm{d}}{\mathrm{d}t}\left(I^*_{rdq} - I_{rdq}\right) + K_{ii}\left(I^*_{rdq} - I_{rdq}\right)\\ &\quad - \mathrm{j}\omega_i\left[V^*_{rdq} - K_{pi}\left(I^*_{rdq} - I_{rdq}\right)\right].\end{aligned} \quad (13)$$

Hence, the RSC introduces further coupling into the inner current loop that depends on the rate of change of the current angle with time, ω_i. This term is zero in the steady state and because of the low bandwidth of the outer loop, it is small during transients. The experimental results in Figs. 9 and 10 show a negligible effect from this coupling.

The analysis presented above neglects the dynamics of the stator circuit. A full state-space analysis shows poles from the stator circuit at a frequency close to 50 Hz. The rotor current loop is usually tuned to avoid exciting the stator dynamics. Where this is not possible, a more advanced controller would be required [38], and the commercial drive used in this work would not be suitable.

Table 1 WRIM parameters

Parameters	Value
stator current	56 A
full-load power	30 kW
full-load speed	1470 rpm
stator resistance	0.09 Ω/phase
rotor resistance	0.066 Ω/phase
stator leakage inductance	0.911×10^{-3} H/phase
rotor leakage inductance	0.459×10^{-3} H/phase
magnetising inductance	44.6×10^{-3} H/phase
effective turns ratio	1.33

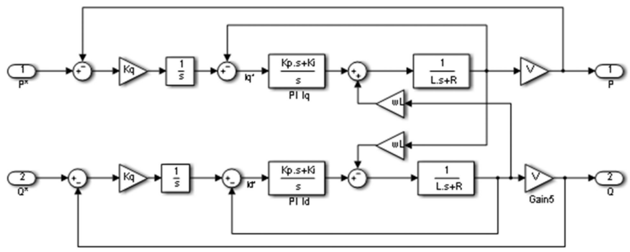

Fig. 11 *Control structure for coupled system analysis*

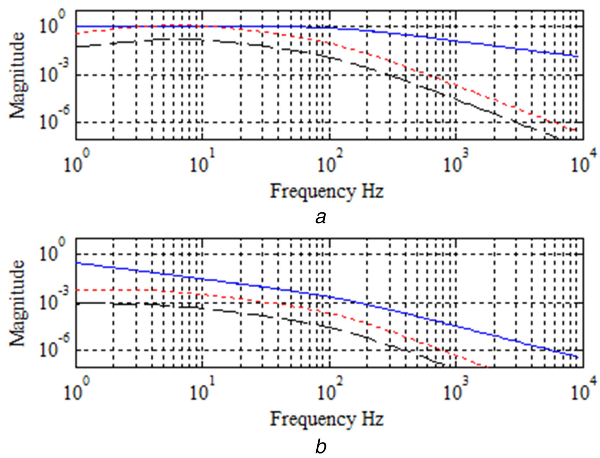

Fig. 12 *Coupling rejection: direct axis (blue solid line); coupled axis @ 4% slip (black dashed line); coupled axis @ 30% slip (red dotted line)*
(a) Current loop, ***(b)*** Power loop

An Effective Approach for Rotor Electrical Asymmetry Detection in Wind Turbine DFIGs

Raed Khalaf Ibrahim, Simon J. Watson, *Member, IEEE*, Siniša Djurović, and Christopher J. Crabtree

***Abstract*—Determining the magnitude of particular fault signature components (FSCs) generated by wind turbine (WT) faults from current signals has been used as an effective way to detect early abnormalities. However, the WT current signals are time varying due to the constantly varying generator speed. The WT frequently operates with the generator close to the synchronous speed, resulting in FSCs manifesting themselves in the vicinity of the supply frequency and its harmonics, making their detection more challenging. To address this challenge, the detection of rotor electrical asymmetry in WT doubly fed induction generators, indicative of common winding, brush gear, or high resistance connection faults, has been investigated using a test rig under three different driving conditions, and then an effective extended Kalman filter (EKF) based method is proposed to iteratively estimate the FSCs and track their magnitudes. The proposed approach has been compared with a continuous wavelet transform (CWT) and an iterative localized discrete Fourier-transform (IDFT). The experimental results demonstrate that the CWT and IDFT algorithms fail to track the FSCs at low load operation near-synchronous speed. In contrast, the EKF was more successful in tracking the FSCs magnitude in all operating conditions, unambiguously determining the severity of the faults over time and providing significant gains in both computational efficiency and accuracy of fault diagnosis.**

***Index Terms*—Condition monitoring (CM), continuous wavelet transform (CWT), doubly fed induction generators (DFIGs), extended Kalman filter (EKF), fault diagnosis, Fourier transform, induction generators, signal processing, time-frequency analysis, wavelet transforms, wind power generation, wind turbines (WTs).**

Manuscript received September 5, 2017; revised November 29, 2017 and January 17, 2018; accepted February 13, 2018. Date of publication March 19, 2018; date of current version June 26, 2018. This work was supported by the SUPERGEN Wind Hub under Grant EP/L014106/1. The work of R. K. Ibrahim was supported by the Higher Committee for Education Development in Iraq. *(Corresponding author: Raed Khalaf Ibrahim.)*

R. K. Ibrahim is with the Wolfson School of Mechanical, Electrical and Manufacturing Engineering, Centre for Renewable Energy Systems Technology, Loughborough University, Loughborough LE11 3TU, U.K. (e-mail: r.ibrahim@lboro.ac.uk).

S. J. Watson is with the TU Delft Wind Energy Institute, Delft University of Technology, Delft 2629 HS, The Netherlands (e-mail: s.j.watson@tudelft.nl).

S. Djurović is with the School of Electrical and Electronic Engineering, Manchester University, Manchester M13 9PL, U.K. (e-mail: sinisa.durovic@manchester.ac.uk).

C. J. Crabtree is with the School of Engineering, Durham University, Durham DH1 3HP, U.K. (e-mail: c.j.crabtree@durham.ac.uk).

Color versions of one or more of the figures in this paper are available online at http://ieeexplore.ieee.org.

Digital Object Identifier 10.1109/TIE.2018.2811373

I. Introduction

In recent years, wind energy has experienced substantial growth compared to other forms of power generation. While alternatives are emerging, a large proportion of currently installed and manufactured wind turbines (WTs) continue to use induction generators. The doubly fed induction generator (DFIG) in particular remains an attractive generator technology with a strong market position [1] due to its unique wide-range variable-speed-constant-frequency operating capability coupled with low-power electronic inverter rating requirements and effective power flow control.

Undetected generator faults in DFIGs have been associated with high failure rates, replacement of major components, and subsequent significant downtime [2]. The primary cause of this higher downtime in the offshore environment is the increased need for heavy-lifting vessels [3]. Usually, faults evolve from an incipient stage to a progressively more severe condition and eventually turn to failure. Early fault detection can hence avoid catastrophic failures and downtime reduction through enabling careful condition-based maintenance planning [4]. An analysis of failure statistics showed that 20% to 70% of the generator faults were related to bearings, 3% to 38% to the stator, 7% to 50% to the rotor, and the rest were categorized as "other" [5]. Another study, which reviewed 80 journal papers published by the IEEE and IEE/IET on the subject of induction machine failure statistics over the past 26 years, reported that 21% of generator faults were bearing problems, 35% stator related, and 44% rotor related [6]. Rotor electrical unbalance is identified as an indicator of some of the major contributors to WT generator failure rate [7], [8]. This condition is representative of a number of recognized rotor electrical fault modes in DFIG systems such as brush gear degradation, rotor winding fault, and/or improper connection between the slip ring unit and the rotor cable leads and its analysis and detection have been the topic of a number of studies conducted on representative academic scale test rig systems and MW-size DFIG field applications [4]–[12]. Undetected electric faults may gradually develop to a major short circuit, and can cause severe damage to the machine and the system to which it is connected [13]. Therefore, early detection of rotor electrical unbalance faults of in-service generators is essential to eliminate consequential damage.

Previous works [14], [15] showed that faults in electrical machines can be detected in a noninvasive manner by either current or power signal analysis. The use of current and power signals analysis has consequently been proposed as a general tool for

WT fault detection [16]–[20]. In particular, the diagnostic application of stator current signature analysis to detect DFIG rotor asymmetry conditions has been studied on laboratory test rigs, simulation studies [5], [8], [9], [21], [22], or analytical formulations of fault frequencies [10], [11]. Rotor electrical unbalance has been emulated by connecting external resistances to machine windings [4]–[11], [23], [24].

The available literature indicates that rotor asymmetries generate particular spectral signatures (called fault signatures) in the frequency spectra of WT current signals. Theoretical and analytical formulations of fault signature frequencies and their generation were attempted in [8], [10], and [25] to define the signal spectral component that can be monitored for diagnostic purposes. To date, various WT condition monitoring (CM) techniques that aim to utilize these and similar diagnostic signals have been developed [17], [19], [26], [27]. However, a fully satisfactory method to detect the full range of WT faults in their early stages has not been achieved yet, and false alarms are still frequently reported from sites with the generator being a significant contributor [2], demonstrating the need to optimize these alarms. The root cause of generator false alarms can be related to the following problems.

1) The lack of clear understanding of the diagnostic information embedded in the DFIG stator current spectral content.
2) The lack of signal processing tools with sufficient sensitivity and reasonable computational efficiency to extract the instantaneous amplitude (IA) of fault signature components (FSCs) from the WT current signals.

The first problem has largely been addressed in [9], [10], [21], and [28] with a comprehensive theoretical analysis of the DFIG stator current spectrum content for the machine operating in steady state, both with and without supply and/or winding asymmetries. The research reported in this paper will focus on a potential solution to address the second problem where the FSCs in the WT current signals have nonlinear and nonstationary characteristics due to the constantly varying shaft rotating speeds caused by turbine variable loads [29]. Furthermore, a wide range of CM technique performance assessment under relevant transient conditions has not been widely reported in the literature, particularly when the machine operates at low load near to synchronous speed. As a result, in these conditions, the FSCs are particularly difficult to detect or differentiate using existing methods, which may lead to an increase in the false alarms for these conditions. This problem has not received attention in reported literature despite the fact that actual WTs frequently operate at low load conditions where the generator rotational speed is close to the synchronous speed, motivating the research in this study to propose potential solutions.

In this paper, we introduce an effective approach to enhance the detection of rotor electrical asymmetry in WT DFIGs by analyzing the generator current signals. First, the analytical expressions defining rotor electrical asymmetry fault signature in DFIG stator current described in [9] and [28] have been used to enable FSCs to be recalculated over time as a function of machine speed. Second, an adaptive extended Kalman filter (EKF) tracker has been proposed to extract the IAs of the FSCs based on the corresponding machine speed signal and the estimated error covariance. At each time step, the calculated FSCs along with those extracted from the measured current signal are processed by the EKF to predict the future state of the FSCs, and continuously update the IAs of FSCs as real-time monitored signal data samples become available. The proposed technique has been validated experimentally on a WT drive train test rig with two fault levels of rotor electrical asymmetries at three different driving conditions whose variability is representative of WT generator field operation. The performance of the proposed approach is compared with some of the leading WT generator CM techniques [9], [30]. The reported experimental findings demonstrate clear and significant gains in both the computational efficiency and the diagnosis accuracy using the proposed technique.

This paper is organized as follows. Section II describes the signature of rotor electrical asymmetry in the DFIG current signals and the use of continuous wavelet transform (CWT) and iterative localized discrete Fourier-transform (IDFT) for frequency tracking. Section III describes the methodology used in the present work using an EKF for diagnosing rotor electrical asymmetry. Section IV describes the data available and employed in this paper. In Section V, the results obtained for three test cases are presented using the EKF, CWT, and IDFT tracking algorithms. Finally, conclusions are drawn and final remarks are made in Section VI.

II. Frequency Tracking and Fault Detection

The rotor electrical asymmetry condition in DFIGs is manifested through a range of additional sideband components in the stator current signal spectrum; it was experimentally proven in [9] and [28] that the rotor electrical imbalance faults in a WT-based DFIG can give rise to additional frequency components in the stator current at frequencies given by

$$f_f = \left(I \pm \frac{k(1-s)}{p}\right).f_s \tag{1}$$

where f_f are the series of the calculated FSCs related to the fault, f_s is the fundamental supply frequency, k is the component order ($k = 1, 2, 3, ...$), s is the slip, I is a constant that relates to air-gap field space harmonics, and p is the number of pole pairs.

Rotor electrical imbalance faults could be detected by monitoring the magnitudes of the components in (1) over time, taking into account variable operating conditions. Efforts have been made to extract the magnitude of the FSCs using a CWT [31]–[33]. However, the CWT cannot achieve fine resolution in both the time and frequency domains simultaneously. In addition, high computational time (CT) is needed to obtain good results with the CWT, making it unsuitable for large size data analysis. To overcome this, another frequency tracking methodology was proposed in [9] using the IDFT algorithm to extract the energy of the FSCs, defined in (1), over time. The IDFT has good computational efficiency and applies a discrete Fourier analysis over a narrow band around the frequency of interest to extract a peak amplitude, which is assumed to be the amplitude of the FSC within the predefined window. However, the challenge with this assumption is that the FSC can be difficult to isolate accurately as it can be merged with other frequency components irrelevant to the fault or it can be hidden in other components such as the supply frequency and its harmonics due to the variable operating conditions. This makes the use of the IDFT difficult to implement when monitoring actual WTs. One of the purposes of this paper is to demonstrate an approach, which is better able to isolate an FSC under variable loading conditions. Section III will illustrate the theory behind this approach.

III. EKF for Frequency Tracking

The EKF is an efficient recursive algorithm widely applied in the fields of radar tracking [34] and adaptive control [35]. The conventional Kalman filter assumes a linear system dynamics model with Gaussian noise in the measurements, which is not always realistic in many applications. The EKF on the other hand is an extension of the conventional Kalman filter to nonlinear system dynamics and has been used for state estimations of induction motors and WT DFIGs [36], [37]. In this section, the observed FSC at time k is first modeled. The mathematical formulation of the EKF used to iteratively estimate the FSCs is then briefly presented. Theoretically, the stator current waveform in one phase (e.g., phase A) of DFIG can be expressed as follows:

$$z_k(t) = \sum_i A_i \cos(2\pi f_i t_k + \theta_i) \tag{2}$$

where A_i and f_i are the amplitude with initial phase θ_i and the frequency of the ith sinusoid, respectively. We used a Fourier transform to convert the time description of the stator current waveform into an equivalent function in the frequency domain thus

$$z_k(f) = \sum_i A_i[\delta(f_k + f_i) + \delta(f_k - f_i)]. \tag{3}$$

The one-sided Fourier transform of (3) at (f_s) the main supply frequency can be written as follows:

$$z_k(f) = A\delta(f_k - f_s). \tag{4}$$

By substituting (1) into (4), we obtain the representation of the FSCs in the frequency domain

$$\begin{aligned} z_k(f) &= A\delta\left(f_k - \left(\frac{p}{pI \pm k(1-s)}\right) f_f\right) \\ &= A\delta(f_k - \alpha f_f) \end{aligned} \tag{5}$$

where

$$\alpha = \left(\frac{p}{pI \pm k(1-s)}\right). \tag{6}$$

The dynamics of the state variables can be represented by the state variable equation as follows:

$$\boldsymbol{x}_k = \mathbf{f}(\boldsymbol{x}_{k-1}, \mathbf{u}_k) + \mathbf{w}_k \tag{7}$$

where $\mathbf{f}$ is a nonlinear function of states, $\mathbf{u}_k$ is the control vector, and $\mathbf{w}_k$ is a white noise driving function to account for the dynamic variation of the state variables. The observed FSC $\boldsymbol{y}_k$ at time k with the additive noise $\boldsymbol{v}_k$ can be described as follows:

$$\boldsymbol{y}_k = \mathbf{z}_k + \mathbf{v}_k \tag{8}$$

and can be represented by the following linear stochastic system:

$$\boldsymbol{y}_k = \begin{bmatrix} 1 & 1 \end{bmatrix} \begin{bmatrix} A \\ \alpha f_f \end{bmatrix} + \mathbf{v}_k. \tag{9}$$

The above-mentioned linear representation is also equivalent to the following nonlinear stochastic system:

$$\text{State equation } \boldsymbol{x}_{k+1} = \mathbf{f}(x_k) + \mathbf{w}_k \tag{10}$$

$$\text{Measurement equation } \boldsymbol{y}_k = \mathbf{H}\boldsymbol{x}_k + \mathbf{v}_k \tag{11}$$

where

$$\boldsymbol{x}_k = \begin{bmatrix} x_k(1) & x_k(2) \end{bmatrix}^T = \begin{bmatrix} A & \alpha f_f \end{bmatrix}^T \tag{12}$$

$$\mathbf{f}(x_k) = \begin{bmatrix} x_k(1) & x_k(1)x_k(2) \end{bmatrix}^T = \begin{bmatrix} A & A\alpha f_f \end{bmatrix}^T \tag{13}$$

$$\boldsymbol{H} = \begin{bmatrix} 1 & 1 \end{bmatrix}. \tag{14}$$

This formulation leads to the EKF algorithm in order to linearize the above-mentioned system, which is slightly different from a standard linear Kalman filter model. The recursive tracking process of a series of fault frequencies at any time step from k equal to zero is outlined as follows.

Step 1: Predict the estimates of the state variables $\hat{\boldsymbol{x}}_{k+1|k}$ and the error covariance $\mathbf{M}_{k+1|k}$

$$\hat{\boldsymbol{x}}_{k+1|k} = \mathbf{f}\hat{\boldsymbol{x}}_{k|k} \tag{15}$$

$$\mathbf{M}_{k+1|k} = \mathbf{F}\mathbf{P}_{k|k}\mathbf{F}^T + \mathbf{Q}_k. \tag{16}$$

Step 2: Update the Kalman gain $\mathbf{K}_k$

$$r_k = |\boldsymbol{z}_k - \hat{\boldsymbol{z}}_k| \tag{17}$$

$$\mathbf{S}_k = \mathbf{H}_k\mathbf{P}_{k|k-1}\mathbf{H}_k^T + r_k \tag{18}$$

$$\mathbf{K}_k = \mathbf{P}_{k|k-1}\mathbf{H}_k^T\mathbf{S}_k^{-1} \tag{19}$$

where

$$\begin{aligned} \mathbf{F}_k &= \frac{\partial \mathbf{f}(x_k)}{\partial x_k}\bigg|_{x_k = \hat{x}_{k|k}} = \begin{bmatrix} 1 & 0 \\ \hat{x}_{k|k}(2) & \hat{x}_{k|k}(1) \end{bmatrix} \\ &= \begin{bmatrix} 1 & 0 \\ (1-\varepsilon)(\alpha \hat{f}_f)_{k|k} & \hat{A}_{k|k} \end{bmatrix}. \end{aligned} \tag{20}$$

Step 3: Update the state variables $\hat{\boldsymbol{x}}_{k|k}$

$$\hat{\boldsymbol{x}}_{k|k} = \bar{\boldsymbol{x}}_{k|k-1} + \mathbf{K}_k[\boldsymbol{y}_k - \mathbf{H}_k(\bar{\boldsymbol{x}}_{k|k-1})]. \tag{21}$$

Step 4: Update the error covariance

$$\begin{aligned} \mathbf{P}_{k|k} &= (\mathbf{I} - \mathbf{K}_k\mathbf{H})\mathbf{P}_{k|k-1} + q\mathbf{B} \\ \mathbf{B} &= \begin{bmatrix} 0 & 0 \\ 0 & 1 \end{bmatrix} \end{aligned} \tag{22}$$

where the symbols $^-$ and $\hat{}$ stand for the predicted and updated values, respectively. $\mathbf{I}$ is the identity matrix. The vector $\boldsymbol{z}_k$ is the observed FSCs, which is obtained by applying the fast Fourier transform (FFT) algorithm for each interval of interest from the current signal in the time domain, and $\hat{\boldsymbol{z}}_k$ is the expected normal state, which represents the calculated FSCs in (1). r_k denotes the measurement innovation.

The design of a stable EKF was largely addressed in [38] and [39], which reports theoretically supported design guidelines to characterize the EKF design by a vector of three parameters (r, ε, q). An easier and more transparent tuning of EKFs is introduced in [40] where the results showed that ε must be set to zero to achieve the basic property of unbiasedness, and that the performance of the EKF tracker then only depends on the ratio $\lambda = r/q$; Bittanti and Savaresi [40] proceed to suggest that $q = 1$ (and hence $\lambda = r$) for a further significant simplification of the tuning procedure. Hence, the task of tuning the design parameters of the EKF tracker (parameterized with r, ε, q) is reduced to the fact that only a single parameter ($\lambda = r$) has to be chosen [40]. This EKF tuning approach was followed in this paper, where r is set to be the difference between the observed FSCs and the calculated FSCs in order to limit the variation of the innovation vector, cope with spurious measured values, enhance the estimated accuracy, and help the EKF to provide proper weighting.

In the implementation of the EKF, we assume that at time k an initial estimate of the state variable is known and is denoted by $\boldsymbol{x}_{k-1|k-1}$ and that its associated covariance matrix is also known and denoted by $\mathbf{M}_{k-1|k-1}$. The estimated variables are not affected by this assumption because the EKF is not sensitive to moderate changes in the initial covariance [41].

The principal stages of the tracking method based on the EKF to iteratively estimate the FSCs in the stator current signal are as follows.

1) Input the initial measured generator rotational speed and the stator current data points, the initial value of the state variables $\boldsymbol{x}_0$ and its associated covariance matrix $\mathbf{M}_0$, and covariance of the measured error r_0 at a sampling interval Δt_k.
2) Calculate the mean speed for the sample and the slip.
3) Calculate the stator current spectrum using an FFT.
4) Calculate discrete constants from frequencies of interest, k.
5) Calculate amplitudes for each constant, k.
6) Extract maximum amplitude and its frequency $\boldsymbol{z}_k$.
7) Calculate the FSCs of interest using (1) $\hat{\boldsymbol{z}}_k$.
8) Predict the estimates of the state variables and the error covariance using (15) and (16).
9) Calculate covariance of the measured error r_k using (17).
10) Compute the Kalman filter gain $\mathbf{K}_k$ using (19).
11) Update the estimates of the state variables and the error covariance with the measurement $\boldsymbol{z}_k$ using (21) and (22).
12) Project ahead using (15) and (16).
13) Repeat the process starting with next sampling interval Δt_{k+1}.

IV. Case Study

The proposed approach has been applied to the generator current signals collected from a purpose built WT drive train test rig. As shown in Fig. 1, the test rig comprises a 54-kW dc variable-speed drive connected via a two-stage gearbox to a four-pole DFIG that was rated for the experiment at 30 kW. The rotational speed of the dc motor is controlled by an external model incorporating the properties of a 2-MW WT operating under closed-loop conditions, driven by realistic wind conditions at a variety of wind speeds and turbulence intensities. The rotor circuit of the generator is coupled via slip rings to an external three-phase resistive load bank so that electrical imbalance can be applied to the generator rotor. The test rig was instrumented and controlled using LabVIEW, see [42] for more details. In the experiments, a rotor unbalance fault was implemented on the test rig by adding two additional external resistances to one phase of the rotor circuit through an external load bank. In the healthy state, the rotor resistance was 1.3 Ω per phase and additional resistances of 0.3 and 0.6 Ω were successively added to one phase to create two fault levels. These correspond to two levels of rotor unbalance of 23% and 46%, respectively, given as a percentage of the rotor balanced phase resistance. The test rig enables the generator to be driven at a desired preprogramed wind speed profile that emulates realistic WT transient behavior and is achieved by providing a predefined speed reference profile to the controller. The relevant signals for CM were collected from the terminals of the generator at a sampling frequency of 5 kHz. An example of the measured current signal under faulty conditions is shown in Fig. 2.

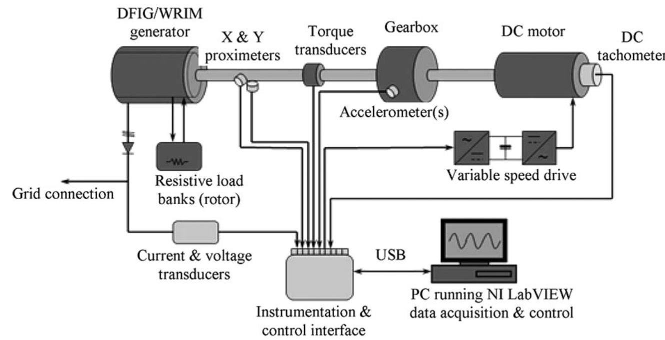

Fig. 1. Schematic representation of the test rig.

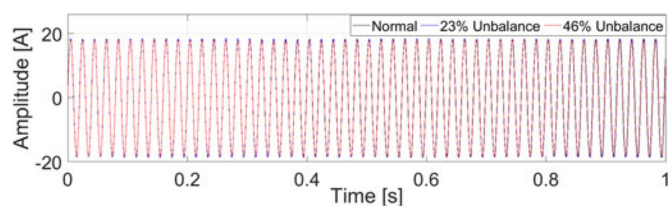

Fig. 2. Current–time waveform.

It can be seen that the amplitude of the current–time waveform gave no indication of abnormal conditions. Consequently, an FFT algorithm is used to convert the generator current signal from the time domain into the frequency domain in a healthy condition (no unbalance) and with a rotor unbalance, as shown in Fig. 3. As is generally expected for any grid connected machine the supply frequency (50 Hz) and its harmonics are clearly seen in the spectra. There are also spectral components present

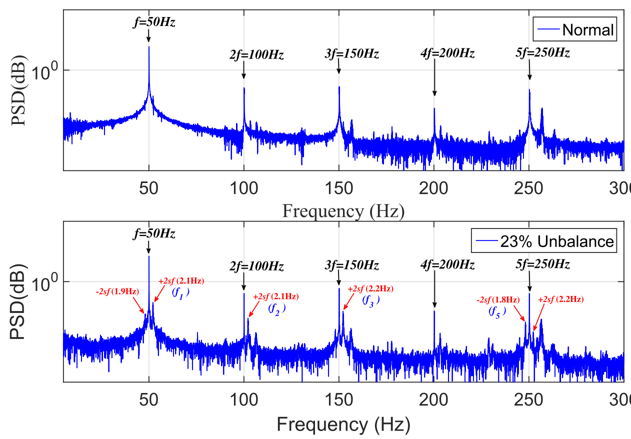

Fig. 3. Comparison of the current spectra for healthy case and rotor unbalance case.

around the even and odd harmonics even when operating in a healthy state. This is believed to be caused by pre-existing low-level rotor excitation imbalance commonly induced by inherent manufacturing imperfections [9], [21]. However, the comparison of healthy and faulty data indicates a significant rise in the magnitude of a number of twice slip frequency 2sf sideband components on the current harmonics, which can be clearly observed when the 23% unbalance is applied to the generator rotor. In Fig. 3, the FFT algorithm cannot reveal the time information of any frequency changes, i.e., no time-domain information is available regarding fault occurrence and progression. Thus, an EKF has been proposed to detect faults by monitoring the magnitudes of the FSCs over time, taking into account variable operating conditions. The rotor unbalance fault gave rise to a number of side-band components in the current spectra. Monitoring all components would be impractical in an operating environment, so we have selected a series of FSCs that exhibit the highest magnitude. The FSCs of interest to be tracked using the EKF algorithm are labeled as f_1, f_2, f_3, f_5 in Fig. 3.

V. Performance Comparison

In order to show the effectiveness of the proposed approach based on an EKF, we have selected the CWT and IDFT, used in [9] and [30] for WT generator CM, for comparison. The algorithms are tested under varying rotational speed conditions representative of the operating regimes seen by a hypothetical WT out in the field. At each test, the test rig was run for a period of 150 s after which the 23% and 46% unbalance fault conditions were applied at 150 s and 300 s, respectively. The driving conditions selected for testing are shown in Fig. 4, corresponding to the following WT operating conditions.

Test case 1. Supersynchronous speed with high turbulence intensity: In this test, a high mean wind speed (15 m/s) with high turbulence intensity (20%) was applied to the test rig via a dc motor, the speed of which was controlled by an external model incorporating the properties of a 2-MW exemplar turbine model developed by the University of Strathclyde as part of the Supergen Wind Energy Technologies Consortium [9]. The CWT, IDFT, and EKF methods have been applied to the current spectra in Fig. 3 to extract the IAs of the four defined

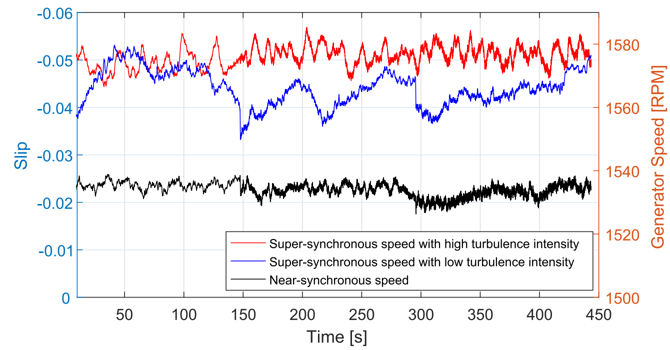

Fig. 4. Generator speed test conditions.

frequencies of interest (f_1, f_2, f_3, f_5) for the detection of rotor unbalance. The results under supersynchronous speed with high turbulence intensity are shown in Fig. 5. Note, if the tracked FSC of each method shows a step change in magnitude when the fault condition was present or has changed, then the method has successfully captured the component frequency related to the fault.

In Fig. 5(a), the conventional CWT is able to capture fault components f_1 and f_2 where their IAs did show a marked change when the fault condition was applied or has changed. The CWT failed to capture other components due to the influence of the window function on the results, where the window size is well matched with the oscillation of component f_1 and f_2 but as the fault frequency increases the window is no longer able to capture the variation of the fault components. A more robust window design is necessary in order to improve simultaneously high time resolution and high frequency resolution. But, this is not an easy task as the difference between the f_1, f_2, and f_3 components is about 50 Hz and increases to 100 Hz for component f_5. In addition, these components overlap with the main supply frequencies and other dominant frequency components of the current signal that are irrelevant to the fault. To overcome these shortcomings, the IDFT algorithm was applied to extract the magnitude of the FSCs. The results are shown in Fig. 5(b).

In Fig. 5(b), it is seen that the IDFT method has successfully tracked the magnitude of the four fault-related frequencies with increasing fault severity (i.e., from 300 to 450 s) despite the fact that the shaft speed was varying continuously throughout the experiments. Similar to the IDFT results, the EKF algorithm has successfully picked up the four FSCs that are changing proportionally to the rotational speed, as shown in Fig. 5(c). The results show that the EKF is able to track the fault frequencies, giving quantitative information about the fault progression.

However, the tracking results of each algorithm in Fig. 5 follow different variation tendencies due to the fact that the current signals from an operational WT are not stationary but are time varying in nature because of the constantly varying generator speed, making the detection of FSCs by the tracking algorithms more challenging. In order to demonstrate the best achieved performance for detecting the rotor unbalance fault and revealing the actual fault degree, the performance of all diagnostic methods during the fault event is evaluated using root-mean-squared error (RMSE) values. Since the increase in the degree of rotor unbalance can be calculated from the IA

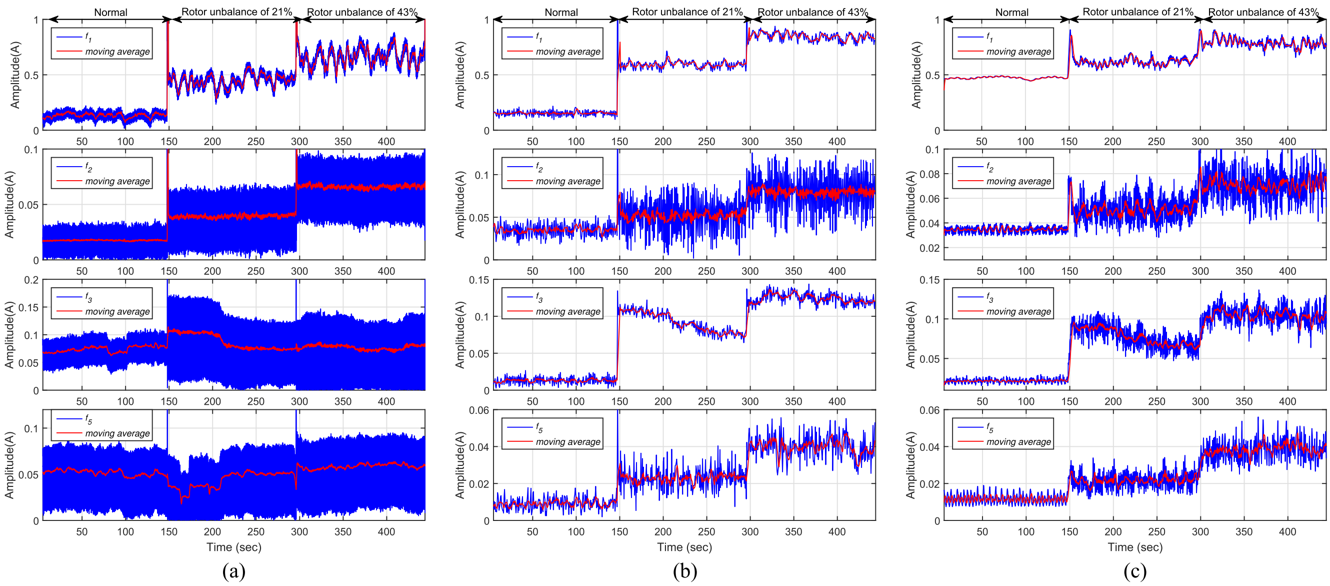

Fig. 5. Tracking the magnitude of fault frequencies of interest using (a) CWT, (b) IDFT, and (c) EKF for test case 1.

TABLE I
RMSE OF THE TRACKING METHODS FOR TEST CASE 1

FSCs	RMSE values (%)		
	CWT	IDFT	EKF
f_1	1.967	2.135	0.325
f_2	1.134	1.301	0.258
f_3	N/A	2.115	0.441
f_5	N/A	0.420	0.236

TABLE II
RMSE OF THE TRACKING METHODS FOR TEST CASE 2

FSCs	RMSE Values (%)		
	CWT	IDFT	EKF
f_1	2.757	2.413	0.318
f_2	2.213	0.608	0.276
f_3	N/A	2.067	0.382
f_5	N/A	0.388	0.234

variations of the FSCs extracted by the diagnostic methods, a general expression is derived for machine operation with rotor unbalance degree $\hat{\boldsymbol{\eta}}_k$ by calculating the difference between the IA for each component under healthy and faulty conditions divided by the order of the component order times the average under healthy conditions as follows:

$$\hat{\boldsymbol{\eta}}_k = \frac{\mathbf{IA}_f - \mathbf{IA}_h}{\mathbf{k}.\mathbf{IA}_h} \times 100\% \tag{23}$$

where $\mathbf{IA}_h$ and $\mathbf{IA}_f$ are the IA at any time step k for each component under healthy and faulty conditions, respectively, and $\mathbf{k}$ is the component order ($\mathbf{k} = 1, 2, 3, ...$). The RMSE is given by

$$\mathbf{RMSE} = \frac{1}{N}\sum_{i=1}^{N}(\boldsymbol{\eta}_i - \hat{\boldsymbol{\eta}}_i) \tag{24}$$

where $\boldsymbol{\eta}_i$ is the degree of the fault during the experiment, corresponding to the two levels of rotor unbalance of 23% and 46%. Table I summarizes the results of the performance evaluation. It is clear from the table that the IDFT and EKF methods perform best in terms of the RMSE for all FSCs. The CWT is incapable of detecting the fault by tracking the components f_3 and f_5, but the RMSE values for components f_1 and f_2 are lower than the same components for the IDFT. The comparison between the three methods shows that the RMSE for all FSCs is much lower when using the EKF method.

Test case 2. Supersynchronous speed with low turbulence intensity: This test represents 7.5 m/s mean wind speed with low turbulence intensity 6%. The slip for this state differs significantly from case 1 with a wide range as seen in Fig. 4. Similar results to the previous test case are observed in Fig. 6, where the CWT is only able to track the fault component f_1 and f_2. This explains why in [30] and [43] only the fault component f_1, which is the twice slip frequency was tracked using the CWT. In contrast, both the IDFT and EKF methods can successfully show the presence of the fault. It is also clear that the variation tendencies of the IAs at the four characteristic frequencies have been correctly extracted despite the time-varying features due to the variable-speed operation and the disturbance of the components unrelated to the fault.

The performances of the three methods are summarized in Table II. Again, the performance of the IDFT and EKF is better in terms of the RMSE values for all FSCs. Compared to the CWT and IDFT, the EKF proved capable of dealing with different variable-speed driving conditions with lower RMSE values. In addition, the components f_1 and f_2 for the CWT show higher RMSE values compared to the results in case 1 as larger variation

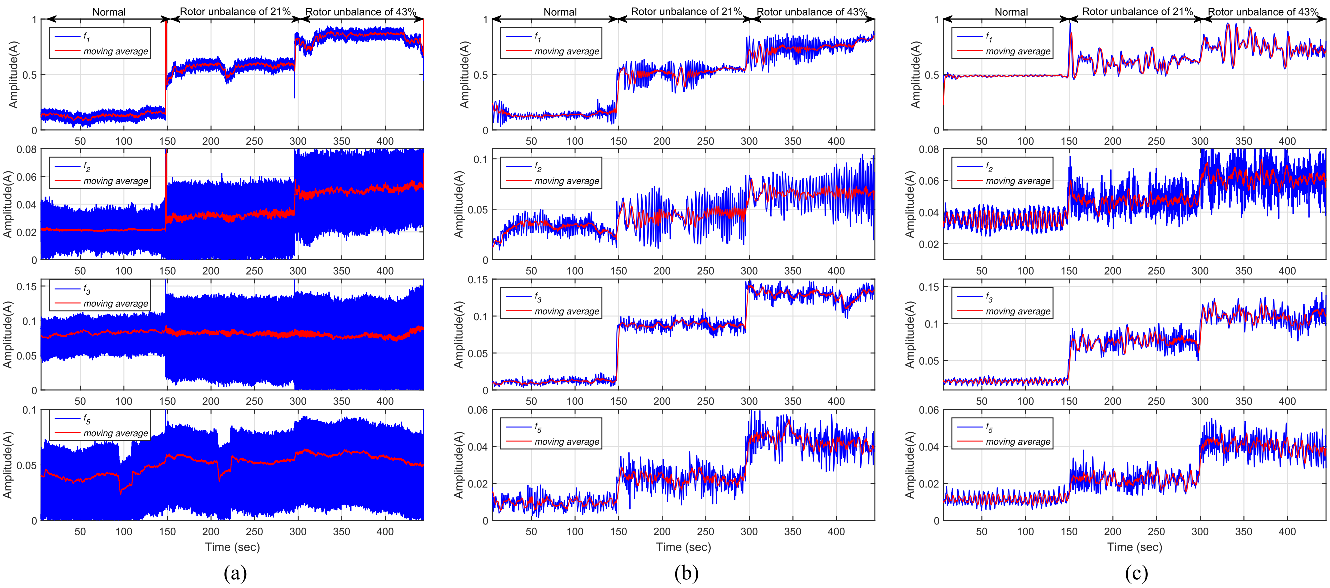

Fig. 6. Tracking the magnitude of fault frequencies of interest using (a) CWT, (b) IDFT, and (c) EKF for test case 2.

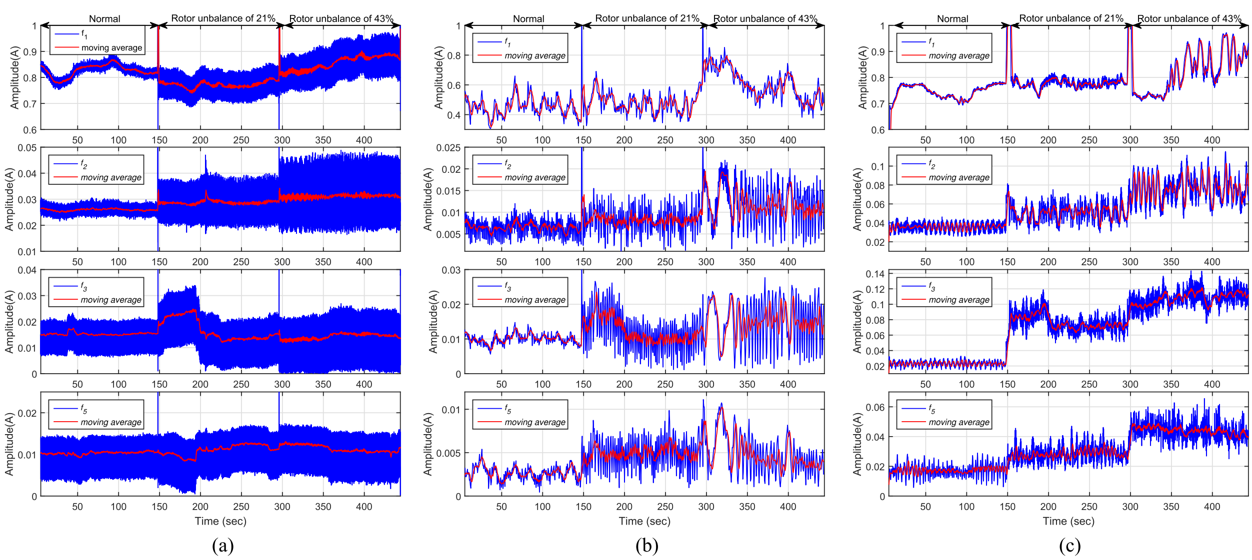

Fig. 7. Tracking the magnitude of fault frequencies of interest using (a) CWT, (b) IDFT, and (c) EKF for test case 3.

in rotational speed for test case 2 makes it more challenging to track the FSCs. It can be concluded that the EKF not only showed the best performance overall in terms of RMSE metric, but also in terms of the rotor unbalance fault detection at different driving conditions, whereas the CWT method performed worst. One explanation for the poor performance of the CWT method can be the windowing technique, which has been influenced by the speed variations.

Test case 3. Near-synchronous speed: Following the successful detection of the fault conditions at supersynchronous speed, it is important now to verify the CM capability of the algorithms when the machine operates near to the synchronous speed. In this case, the slip will be near to zero so the FSCs in (1) will be very close to the supply frequency (50 Hz) and its harmonics (both odd and even), making CM and fault detection more challenging even though this condition occurs frequently for an operational WT. The results of such a scenario are shown in Fig. 7.

Both the CWT and IDFT algorithms, shown in Fig. 7(a) and (b), have failed to effectively track the FSCs; the shortcoming of the CWT and IDFT methods is that both use windowing technique, and do not have an observer to avoid tracking the FSCs when they are so close as to be effectively merged with the supply frequency and its harmonics.

On the other hand, the EKF shows much better resolution of the varying fault conditions, as shown in Fig. 7(c). The results clearly show that the amplitude of the fault-related frequencies jumps sharply when the 23% unbalance fault is introduced at

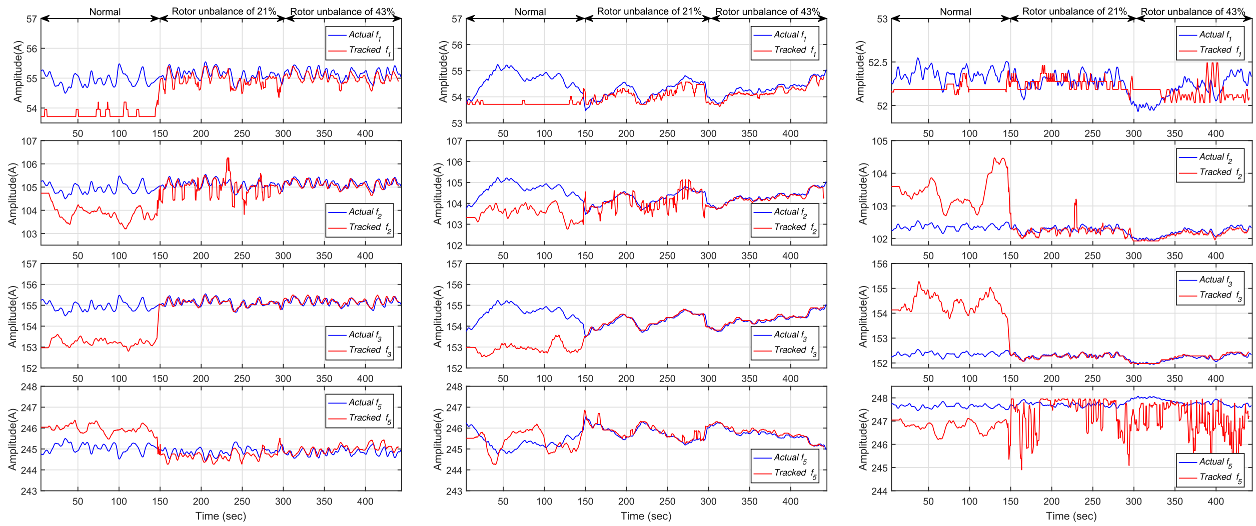

(a) (b) (c)

Fig. 8. Tracking the fault frequencies of interest using EKF for (a) test case 1, (b) test case 2, and (c) test case 3.

150 s. A similar jump occurs for the 46% unbalance condition introduced at 300 s that shows clear differences between healthy and faulty conditions particularly for components f_2, f_3, and f_5. The performances of the FSCs tracked by the EKF in terms of the percentage RMSE values are found to be 0.378, 0.244, 0.386, and 0.352 for f_1, f_2, f_3, and f_5, respectively. It can be seen that the EKF shows more accurate fault tracking across all the driving conditions and the RMSE values for all FSCs are very close. Over the three cases, the EKF shows better fault resolution compared to the CWT and IDFT as it does not use any windowing technique, rather it uses the Kalman gain($\mathbf{K}_k$). The Kalman gain acts as a relative weight given to the current extracted and measurement values, and its value is continuously tuned to get the correct estimation value of the FSCs and their magnitude from the nonstationary current signal. At each time step, $\mathbf{K}_k$ is calculated from the covariance. The constantly varying generator speeds and nonlinear operation lead to an increase or decrease of the Kalman gain, so with a high gain the filter places more weight on the most recent measurements, and thus follows them more responsively to avoid tracking the noise (i.e., the supply frequency and its harmonics or other dominant frequency components of the current signal), which are irrelevant to the fault. With a low gain, the filter follows the model predictions more closely to track the fault signatures and smooth out the noise.

To show the effectiveness of the proposed EKF, we compare in Fig. 8 the tracking results of the EKF associated with the spectral component frequencies against the actual frequencies, described by equation (1), across all driving conditions. As it can be seen from Fig. 8, that the tracking frequencies are different from the actual frequencies in normal operation when there is no fault because the magnitude of the actual frequencies is very small and merged with the noise so they are difficult to detect or differentiate. Once, the fault has been applied, the EKF immediately captured the frequencies related to the fault and continued to track them over time despite the fact that the actual frequencies are more affected by the speed variations and follow exactly the same speed variation tendencies, as shown in Fig. 4. It can also be seen for case 3 that the f_1 and f_5 FSCs are particularly difficult to capture compared to the others cases due to the operation at low load near to synchronous speed, resulting in FSCs manifesting themselves in the vicinity of the supply frequency and its harmonics with extraneous noise, as shown in Fig. 3. This led to an increase in the variation of the innovation vector r_k for these conditions. However, the magnitude of the tracked f_1 and f_5 FSCs is still useful for fault detection, and did show a step change in magnitude when the fault condition was present or was changed as discussed previously.

In summary, the results for the three cases show that the rotor electrical unbalance fault can be accurately detected by tracking any component using the EKF, but overall the second component f_2 showed the lowest RMSE in revealing the fault degree. The results using the IDFT in Tables I and II show that the fifth component f_5 provides the lowest RMSE (0.404 as an average percentage), whereas the results obtained from other components are not effective in revealing the degree of rotor unbalance. If we only consider component f_5 for fault diagnosis, our proposed approach demonstrates a significant improvement over the IDFT method in imbalance diagnosis accuracy by reducing the percentage RMSE from 0.404 to 0.235. Since the results show that the second component f_2 has the best accuracy in the case of the EKF, whereas the fifth component f_5 provides the best accuracy in the case of the IDFT, this indicates we have successfully reduced the volume of data required for analysis and storage. To clarify, based on the Nyquist–Shannon sampling theorem, the data requirements to monitor component f_5 for a period of one year would enable the monitoring of component f_2 for a period of approximately two years and four months, due to the fundamental fact that f_5 is greater than f_2 and requires a higher sampling rate to capture. Hence, our approach shows success in tracking the magnitude of the FSCs and revealing the severity of the faults over time with significant

TABLE III
COMPUTATIONAL COMPLEXITY OF THE TRACKING METHODS

FSCs	CT (s)		
	CWT	IDFT	EKF
f_1	35.65	0.98	1.2
f_2	20.05	1.01	1.1
f_3	14.79	1.05	1.16
f_5	4.32	1.09	1.1

gains in both the computational efficiency and the diagnosis accuracy.

A. Computational Time

To further highlight the improvement offered by an EKF, we perform CT analysis comparing the EKF method against the CWT and IDFT methods. The calculations were performed on a computer with an Intel i7 core processor and 32.0-GB RAM. Table III shows the plot of the averaged CT for the results obtained in Figs. 5–7 for the series of FSCs. It is seen that the CWT method requires a higher CT for the FSCs with lower frequencies because these tend to have much longer wavelengths with a high signal-to-noise ratio, whereas the higher FSCs have much shorter wavelengths with low signal-to-noise ratio. Accordingly, this affects the width of the window function in time to capture the frequencies of interest; therefore, it requires more computational resources. In contrast, the IDFT and EKF require far less computational resource compared to the CWT. This is due to the fact that the IDFT and EKF methods apply a discrete Fourier analysis over a narrow band around the frequency of interest. The IDFT and EKF have very similar CT requirements making them more suitable for online monitoring than the CWT.

VI. CONCLUSION

This paper proposed the use of an EKF in the detection of rotor electrical unbalance fault, indicative of common winding, brush gear, or high resistance connection faults, in a WT DFIG. The EKF performance was compared with that of a CWT and an IDFT in terms of its ability to track a series of fault frequencies associated with three different unbalance condition levels and for three different simulated transient operating regimes using data generated by a test rig. The EKF demonstrated better overall resolution of fault frequencies particularly where those frequencies are close to the synchronous frequencies and their harmonics; a condition that can occur frequently when a turbine is operating with the generator close to synchronous speed. Due to the parsimonious nature of the EKF and the fact that it does not employ windowing, it is able to accurately detect fault frequencies with minimal computational requirements when compared with a CWT. The EKF was shown to be capable of detecting the degree of rotor unbalance with greater accuracy than an IDFT or CWT. The results presented show that the EKF algorithm shows promise as a low cost, efficient method for condition monitoring the output of a WT generator particular with regard to the detection of electrical faults such as rotor unbalance.

Future work is required to apply this approach to real operating WTs, which may be suffering from rotor electrical asymmetries, and to use the detection of the fault degree to potentially predict the fault progression some time in advance. Work is also necessary to assess the potential of the reported technique to be used for the detection of a wider range of WT faults such as generator bearing, gearbox-bearing, and rotor eccentricity faults.

REFERENCES

[1] Y. Zhou, P. Bauer, J. A. Ferreira, and J. Pierik, “Operation of grid-connected DFIG under unbalanced grid voltage condition,” *IEEE Trans. Energy Conversion*, vol. 24, no. 1, pp. 240–246, Mar. 2009.

[2] Y. Qiu, Y. Feng, P. Tavner, P. Richardson, G. Erdos, and B. Chen, “Wind turbine SCADA alarm analysis for improving reliability,” *Wind Energy*, vol. 15, no. 8, pp. 951–966, 2012.

[3] J. Carroll, A. McDonald, I. Dinwoodie, D. McMillan, M. Revie, and I. Lazakis, “Availability, operation and maintenance costs of offshore wind turbines with different drive train configurations,” *Wind Energy*, vol. 20, no. 2, pp. 361–378, 2017.

[4] Y. Gritli, L. Zarri, C. Rossi, F. Filippetti, G. A. Capolino, and D. Casadei, “Advanced diagnosis of electrical faults in wound-rotor induction machines,” *IEEE Trans. Ind. Electron.*, vol. 60, no. 9, pp. 4012–4024, Sep. 2013.

[5] M. Zaggout, P. Tavner, C. Crabtree, and L. Ran, “Detection of rotor electrical asymmetry in wind turbine doubly-fed induction generators,” *IET Renewable Power Gener.*, vol. 8, no. 8, pp. 878–886, 2014.

[6] P. Tavner, “Review of condition monitoring of rotating electrical machines,” *IET Elect. Power Appl.*, vol. 2, no. 4, pp. 215–247, 2008.

[7] M. Mengoni *et al.*, “Online detection of high-resistance connections in multiphase induction machines,” *IEEE Trans. Power Electron.*, vol. 30, no. 8, pp. 4505–4513, Aug. 2015.

[8] Y. Gritli, C. Rossi, D. Casadei, F. Filippetti, and G. A. Capolino, “A diagnostic space vector-based index for rotor electrical fault detection in wound-rotor induction machines under speed transient,” *IEEE Trans. Ind. Electron.*, vol. 64, no. 5, pp. 3892–3902, May 2017.

[9] S. Djurovic, C. J. Crabtree, P. J. Tavner, and A. Smith, “Condition monitoring of wind turbine induction generators with rotor electrical asymmetry,” *IET Renewable Power Gener.*, vol. 6, no. 4, pp. 207–216, 2012.

[10] S. Williamson and S. Djurovic, “Origins of stator current spectra in DFIGs with winding faults and excitation asymmetries,” in *Proc. IEEE Int. Elect. Mach. Drives Conf.*, May 2009, pp. 563–570.

[11] Y. Gritli, A. Stefani, A. Chatti, C. Rossi, and F. Filippetti, “The combined use of the instantaneous fault frequency evolution and frequency sliding for advanced rotor fault diagnosis in DFIM under time-varying condition,” in *Proc. 35th Annu. Conf. IEEE Ind. Electron.*, Nov. 2009, pp. 3471–3476.

[12] G. A. Skrimpas *et al.*, “Analysis of generator bearing vibration data for diagnosing rotor circuit malfunction in DFIGs,” in *Proc. Int. Conf. Elect. Mach.*, 2014, pp. 1746–1751.

[13] H. A. Toliyat, S. Choi, and S. Nandi, *Electric Machines: Modeling, Condition Monitoring, and Fault Diagnosis*. Boca Raton, FL, USA: CRC Press, 2012.

[14] M. E. H. Benbouzid, “A review of induction motors signature analysis as a medium for faults detection,” *IEEE Trans. Ind. Electron.*, vol. 47, no. 5, pp. 984–993, Oct. 2000.

[15] B. Lu, Y. Li, X. Wu, and Z. Yang, “A review of recent advances in wind turbine condition monitoring and fault diagnosis,” in *Proc. IEEE Power Electron. Mach. Wind Appl.*, Jun. 2009, pp. 1–7.

[16] R. K. Ibrahim and S. Watson, “Effect of power converter on condition monitoring and fault detection for wind turbine,” in *Proc. 8th IET Int. Conf. Power Electron., Mach. Drives*, 2016, pp. 1–5.

[17] Z. Hameed, Y. Hong, Y. Cho, S. Ahn, and C. Song, “Condition monitoring and fault detection of wind turbines and related algorithms: A review,” *Renewable Sustain. Energy Rev.*, vol. 13, no. 1, pp. 1–39, 2009.

[18] R. Ibrahim and S. Watson, “Stator winding fault diagnosis in synchronous generators for wind turbine applications,” in *Proc. 5th IET Int. Conf. Renewable Power Gener.*, Sep. 2016, pp. 1–6.

[19] W. Qiao and D. Lu, “A survey on wind turbine condition monitoring and fault diagnosis—Part II: Signals and signal processing methods,” *IEEE Trans. Ind. Electron.*, vol. 62, no. 10, pp. 6546–6557, Oct. 2015.

[20] R. K. Ibrahim and S. J. Watson, "Condition monitoring of permanent magnet synchronous generator for wind turbine applications," in *Proc. 3rd Conf. Control Fault-Tolerant Syst.*, Sep. 2016, pp. 648–653.
[21] S. Djurovic, S. Williamson, and A. Renfrew, "Dynamic model for doubly-fed induction generators with unbalanced excitation, both with and without winding faults," *IET Elect. Power Appl.*, vol. 3, no. 3, pp. 171–177, 2009.
[22] M. Riera-Guasp, J. A. Antonino-Daviu, and G. A. Capolino, "Advances in electrical machine, power electronic, and drive condition monitoring and fault detection: State of the art," *IEEE Trans. Ind. Electron.*, vol. 62, no. 3, pp. 1746–1759, Mar. 2015.
[23] W. Yang, P. J. Tavner, and W. Tian, "Wind turbine condition monitoring based on an improved spline-kernelled chirplet transform," *IEEE Trans. Ind. Electron.*, vol. 62, no. 10, pp. 6565–6574, Oct. 2015.
[24] P. M. de la Barrera, G. R. Bossio, and J. A. Solsona, "High-resistance connection detection in induction motor drives using signal injection," *IEEE Trans. Ind. Electron.*, vol. 61, no. 7, pp. 3563–3573, Jul. 2014.
[25] E. Artigao, A. Honrubia-Escribano, and E. Gomez-Lazaro, "Current signature analysis to monitor DFIG wind turbine generators: A case study," *Renewable Energy*, vol. 116, pt. B, pp. 5–14, Feb. 2018.
[26] R. K. Ibrahim and S. J. Watson, "Advanced algorithms for wind turbine condition monitoring and fault diagnosis," in *Proc. WindEur. Summit Conf.*, Hamburg, Germany, Sep. 2016, pp. 1–5.
[27] R. K. Ibrahim, J. Tautz-Weinert, and S. J. Watson, "Neural networks for wind turbine fault detection via current signature analysis," in *Proc. WindEur. Summit Conf.*, Hamburg, Germany, Sep. 2016, pp. 1–7.
[28] C. Crabtree, S. Djurovic, P. Tavner, and A. Smith, "Condition monitoring of a wind turbine DFIG by current or power analysis," in *Proc. 5th IET Int. Conf. Power Electron., Mach. Drives*, Apr. 2010, pp. 1–6.
[29] W. Yang, C. Little, P. J. Tavner, and R. Court, "Data-driven technique for interpreting wind turbine condition monitoring signals," *IET Renewable Power Gener.*, vol. 8, pp. 151–159, Mar. 2014.
[30] W. Yang, P. J. Tavner, C. J. Crabtree, and M. Wilkinson, "Cost-effective condition monitoring for wind turbines," *IEEE Trans. Ind. Electron.*, vol. 57, no. 1, pp. 263–271, Jan. 2010.
[31] C.-S. Tsai, C.-T. Hsieh, and S.-J. Huang, "Enhancement of damage-detection of wind turbine blades via CWT-based approaches," *IEEE Trans. Energy Convers.*, vol. 21, no. 3, pp. 776–781, Sep. 2006.
[32] C. Kar and A. Mohanty, "Monitoring gear vibrations through motor current signature analysis and wavelet transform," *Mech. Syst. Signal Process.*, vol. 20, no. 1, pp. 158–187, 2006.
[33] H. Douglas, P. Pillay, and A. K. Ziarani, "A new algorithm for transient motor current signature analysis using wavelets," *IEEE Trans. Ind. Appl.*, vol. 40, no. 5, pp. 1361–1368, Sep./Oct. 2004.
[34] G. Y. Kulikov and M. V. Kulikova, "The accurate continuous-discrete extended Kalman filter for radar tracking," *IEEE Trans. Signal Process.*, vol. 64, no. 4, pp. 948–958, Feb. 2016.
[35] F. Auger, M. Hilairet, J. M. Guerrero, E. Monmasson, T. Orlowska-Kowalska, and S. Katsura, "Industrial applications of the Kalman filter: A review," *IEEE Trans. Ind. Electron.*, vol. 60, no. 12, pp. 5458–5471, Dec. 2013.
[36] E. Zerdali and M. Barut, "The comparisons of optimized extended Kalman filters for speed-sensorless control of induction motors," *IEEE Trans. Ind. Electron.*, vol. 64, no. 6, pp. 4340–4351, Jun. 2017.
[37] S. Yu, K. Emami, T. Fernando, H. H. C. Iu, and K. P. Wong, "State estimation of doubly fed induction generator wind turbine in complex power systems," *IEEE Trans. Power Syst.*, vol. 31, no. 6, pp. 4935–4944, Nov. 2016.
[38] B. F. La Scala, R. R. Bitmead, and M. R. James, "Conditions for stability of the extended Kalman filter and their application to the frequency tracking problem," *Math. Control, Signals, Syst.*, vol. 8, no. 1, pp. 1–26, 1995.
[39] B. F. La Scala and R. R. Bitmead, "Design of an extended Kalman filter frequency tracker," *IEEE Trans. Signal Process.*, vol. 44, no. 3, pp. 739–742, Mar. 1996.
[40] S. Bittanti and S. M. Savaresi, "On the parametrization and design of an extended Kalman filter frequency tracker," *IEEE Trans. Automat. Control*, vol. 45, no. 9, pp. 1718–1724, Sep. 2000.
[41] M. Saha, R. Ghosh, and B. Goswami, "Robustness and sensitivity metrics for tuning the extended Kalman filter," *IEEE Trans. Instrum. Meas.*, vol. 63, no. 4, pp. 964–971, Apr. 2014.
[42] C. Crabtree, "Condition monitoring techniques for wind turbines," Ph.D. dissertation, Durham Univ., Durham, U.K., 2011.
[43] S. J. Watson, B. J. Xiang, W. Yang, P. J. Tavner, and C. J. Crabtree, "Condition monitoring of the power output of wind turbine generators using wavelets," *IEEE Trans. Energy Convers.*, vol. 25, no. 3, pp. 715–721, Sep. 2010.

Raed Khalaf Ibrahim received the B.Sc. degree in electrical and electronic engineering from Tikrit University, Tikrit, Iraq, in 2009, and the M.Sc. degree in electrical and electronic engineering from Mosul University, Mosul, Iraq, in 2011.

He was an Electrical Engineer with the North Oil Company and then he was selected by the Ministry of Oil to be seconded to the prestigious Baiji Oil Institute as an Industrial Teacher and a Trainer. He is currently a Ph.D. Researcher with the Centre for Renewable Energy Systems Technology, Loughborough University, Loughborough, U.K. His research interests include wind turbine condition monitoring and fault diagnosis, advanced signal processing, machine learning, artificial intelligence, and data analysis.

Simon J. Watson (M'05) received the B.Sc. degree in physics from Imperial College London, London, U.K., in 1987, and the Ph.D. degree in nuclear physics from Edinburgh University, Edinburgh, U.K., in 1990.

He has been working in the field of wind energy since 1990 and began his career with the Energy Research Unit of the Rutherford Appleton Laboratory. In 1999, he joined Good Energy, a supplier of green electricity to domestic and small commercial customers. In 2001, he was appointed as a Senior Lecturer with the Centre for Renewable Energy Systems Technology, Loughborough University, Loughborough, U.K., and in 2010, he became a Professor in Wind Energy. In 2017, he joined TU Delft as a Professor in wind energy systems and the Director of DUWIND (the TU Delft Wind Energy Institute), Delft, the Netherlands. His research interests include wind climate, wind resource assessment, wind turbine wakes and wind turbine reliability, and condition monitoring.

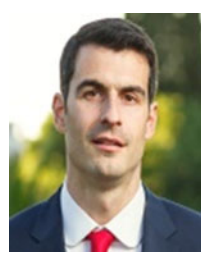

Siniša Djurović (M'09) received the Dipl.Ing. degree in electrical engineering from the University of Montenegro, Podgorica, Montenegro, in 2002, and the Ph.D. degree in electrical engineering from the University of Manchester, Manchester, U.K., in 2007.

He is a Senior Lecturer with the Power Conversion Group, Manchester, U.K. His research interests include electric machines and drive operation, design, monitoring and diagnostics, and their use in renewables and automotive applications.

Christopher J. Crabtree received the M.Eng. degree in engineering from Durham University, Durham, U.K., in 2007, and the Ph.D. degree in electrical engineering from Durham University, in 2011, with a thesis on condition monitoring techniques for wind turbines.

He is an Assistant Professor in Wind Energy Systems with Durham University. His research interests include reliability, condition monitoring, and operations and maintenance of offshore wind farms.

Mr. Crabtree is leading Durham's contribution to the EPSRC HOME Offshore project on wind farm reliability and operations. Much of his research has been undertaken as part of the U.K. EPSRC SUPERGEN Wind Energy Technologies Consortium.

Measurement Science and Technology

PAPER • OPEN ACCESS

Non-intrusive torque measurement for rotating shafts using optical sensing of zebra-tapes

To cite this article: D Zappalá *et al* 2018 *Meas. Sci. Technol.* **29** 065207

OPEN ACCESS
IOP Publishing
Measurement Science and Technology
Meas. Sci. Technol. 29 (2018) 065207 (18pp)
https://doi.org/10.1088/1361-6501/aab74a

Non-intrusive torque measurement for rotating shafts using optical sensing of zebra-tapes

D Zappalá[1], M Bezziccheri[2], C J Crabtree[1] and N Paone[2]

[1] Department of Engineering, Durham University, Durham, United Kingdom
[2] Università Politecnica delle Marche, DIISM, Ancona, Italy

E-mail: donatella.zappala@durham.ac.uk

Received 22 May 2017, revised 13 March 2018
Accepted for publication 16 March 2018
Published 10 May 2018

Abstract
Non-intrusive, reliable and precise torque measurement is critical to dynamic performance monitoring, control and condition monitoring of rotating mechanical systems. This paper presents a novel, contactless torque measurement system consisting of two shaft-mounted zebra tapes and two optical sensors mounted on stationary rigid supports. Unlike conventional torque measurement methods, the proposed system does not require costly embedded sensors or shaft-mounted electronics. Moreover, its non-intrusive nature, adaptable design, simple installation and low cost make it suitable for a large variety of advanced engineering applications. Torque measurement is achieved by estimating the shaft twist angle through analysis of zebra tape pulse train time shifts. This paper presents and compares two signal processing methods for torque measurement: rising edge detection and cross-correlation. The performance of the proposed system has been proven experimentally under both static and variable conditions and both processing approaches show good agreement with reference measurements from an in-line, invasive torque transducer. Measurement uncertainty has been estimated according to the ISO GUM (Guide to the expression of uncertainty in measurement). Type A analysis of experimental data has provided an expanded uncertainty relative to the system full-scale torque of $\pm 0.30\%$ and $\pm 0.86\%$ for the rising edge and cross-correlation approaches, respectively. Statistical simulations performed by the Monte Carlo method have provided, in the worst case, an expanded uncertainty of $\pm 1.19\%$.

Keywords: non-intrusive torque measurement, zebra tape, pulse train time shift, shaft twist angle, pulse train rising edge, cross-correlation, uncertainty

(Some figures may appear in colour only in the online journal)

1. Introduction

Torque is a fundamental operating parameter of rotating mechanical systems. Some of the most common industrial applications of torque measurement include both conventional [1, 2] and emerging [3, 4] power generation, electric motor testing [5], robot arms [6], marine [7] and automotive [8] industry. Power and efficiency optimisation based on highly accurate and reliable torque measurement, besides enabling significant energy savings, fits to the steadily increasing requirements of the international regulation, especially for large mechanical drives with high nominal torque [9], such as marine engines [10]. Despite torque measurement and control being critical to dynamic performance monitoring, condition monitoring for predictive maintenance and control of mechanical systems, reliable measurements can be difficult to obtain in a cost-effective and non-intrusive manner.

The methods used to measure torque can be divided into two categories, either direct or indirect.

Direct methods use in-line torque transducers, already calibrated by the manufacturer, which are integrated into the drive shaft. These sensors have some susceptibility to noise and require bearings for support, which also implies maintenance. The major obstacle to the industrial application of direct measurement systems is the costly and intrusive nature of the required equipment, which is impractical for short-term use, particularly on large systems. The act of mounting the in-line transducer may also change system dynamics and, consequently, torque values. Moreover, direct measurements cannot be implemented when the rotating mechanical system design does not allow adapting the shaft design or lengthening the drivetrain to accommodate the in-line transducer.

Indirect methods are based on the measurement of torque-related parameters and subsequent torque calculation. These methods have the advantage of avoiding modifications to the original shaft, therefore minimising the impact on mechanical design and not modifying the static and dynamic behaviour of the shaft. The conventional indirect systems are based on measurement of surface strain or angle of twist [11]. Surface strain measurement systems typically use either strain gauges, directly bonded on the shaft body in a Wheatstone bridge configuration, or magnetostrictive methods. These methods rely on the change of resistance [12] or magnetization properties of the material [13], respectively, when torque is applied. Strain gauges are the most commonly used in industrial applications thanks to their low cost and high sensitivity. However, the main limitations of this method are the complexity of installation of the sensors on cylindrical surfaces, the need to install electronics on the rotating shaft, the requirement for specialised personnel required for installation, usability, resolution, noise susceptibility and the requirement for regular calibration. Moreover, unwanted forces can create unintended directional disturbance, such as crosstalk phenomena, that can increase the uncertainty in the measured loads and reduce accuracy [13]. Angle of twist measurement methods are based on the measurement of the phase between two points on the shaft, separated by a suitable distance, through magnetic or optical angular position sensing [7]. The first use toothed gears which are angularly displaced with respect to each other as the shaft shift twist angle increases, thereby increasing the electrical phase difference between the signals measured by magnetic pickups [13]. Conventional optical methods use slotted discs which move with respect to each other as torque is applied, thereby changing the on-times of light pulses created by the shutter actions of the rotating discs [14, 15]. Both systems can be retrofitted to existing systems and do not have the inherent complexity of strain gauge installations. However, they require the installation of quite large rings and plates around the shaft which can be impractical in some industrial applications, such as in-vehicle and mobile measurements, due to space constraints. They also suffer from environmental factors such as dust, humidity, temperature, vibration, electromagnetic interference and aging. In addition to performance limitations, these methods usually suffer from low range-to-resolution ratio [11]. A laser torque meter was first presented in [16] and later analysed in [17–19]. This instrument is based on the cross-correlation of the periodic speckle patterns generated by two axially separated laser beams on a rotating shaft, having known mechanical proprieties. Even if this is a smart non-contact approach, it suffers from decorrelation of speckle patterns due to shaft displacement and tilt, making its practical application difficult. Several advanced contactless torque measurements techniques have been researched recently, such as the photo-elastic torque sensor based on the birefringence effect of optically anisotropic materials [20] and the non-contact Hall effect design sensor [21]. However, most of these sensors have significant limitations such as requiring torque sensitive materials to be attached on the shaft surface, such as ferromagnetic and piezoelectric materials, and limited speed range and resolution. Moreover, very few solutions can provide both shaft torque and speed measurement from the same sensor, which is useful whenever one desires to measure mechanical power.

This paper presents a novel and simple contactless torque and speed measurement system consisting of two zebra tape codes directly glued around the shaft with two optical sensors mounted on non-rotating supports. This technique operates entirely contact-free and allows torque measurement on standard installations, across their operational life, avoiding the use of permanently installed in-line intrusive torque meters, by simply instrumenting the existing shaft with the two zebra tapes located as far as possible from each other. The use of optical sensors and zebra tapes on rotating shafts is not new; however, literature reports only application for torsional vibration measurement [22, 23], while this research proposes their use for torque measurement. This paper introduces the operating principle of the proposed non-intrusive torque measurement system and its experimental implementation and validation. Two different approaches for processing the optical probe (OP) pulse train signals and estimating the shaft twist, and hence the applied torque, are then presented. After calibrating the system under stationary conditions, its response and performance under both static and time-varying torque conditions is demonstrated by comparing the results of the two proposed signal processing approaches against the reference measurements from an in-line torque transducer mounted on the test bench shaft.

2. Methodological approach

A torque acting on a shaft causes the shaft itself to twist, with one end rotating with respect to the other by an angle displacement θ. Assuming a uniform circular cross-section and linear homogenous elastic material, the relationship between the torque applied to a rotating shaft, T (N m), and the relative rotation of the ends of the shaft section, θ (rad), is described [24] by:

$$T = I\ddot{\theta} + C\dot{\theta} + K\theta \quad (1)$$

where I is the rotating system moment of inertia (kg m^2), C is the shaft damping coefficient (kg m^2 s^{-1} rad^{-1}) and K is the shaft torsional stiffness (N m rad^{-1}).

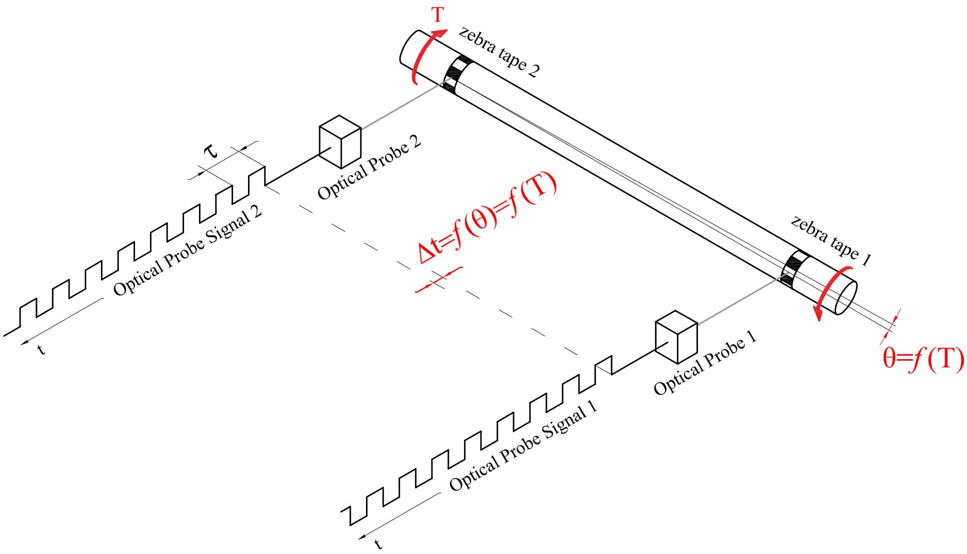

Figure 1. Operating principle of the non-intrusive torque measurement system.

The non-intrusive torque measurement system proposed in this paper employs a set of two zebra tapes and two OPs, one at each end of the shaft, as shown in figure 1.

The zebra tapes feature an equal number of equidistant black and white stripes and are glued around the shaft. As the shaft rotates, each optical sensor, mounted on a non-rotating component, generates a pulse train signal proportional to the light intensity reflected by the zebra tape stripes. When a torque, T, is applied to the shaft, the relative rotation of the ends of the shaft section, θ, results in a time shift, Δt, between the two pulse train signals. The principle of the proposed method is to quantify the shaft relative twist angle by measuring the phase difference between the two pulse signals and thence deriving the applied torque, from a known torque-twist relationship. This is achieved according to the following procedure:

(1) Estimation of the time shift, Δt (s), between the pulse trains measured by the two OPs;
(2) Measurement of the pulse trains period, τ (s), and calculation of the shaft rotational speed, n (rpm):

$$n = \frac{60}{\tau\, ppr} \tag{2}$$

where *ppr* is the number of pulses per shaft revolution;
(3) Conversion of time shift to absolute angular shift, θ_a, according to [25]:

$$\theta_a = \frac{2\pi}{60} n \Delta t. \tag{3}$$

The shaft absolute twist angle, θ_a, could be different to the shaft relative twist angle, θ, due to the mounting misalignment between the two OPs and/or the two zebra tapes. This error manifests itself as an apparent angular shift, $\theta_{a,0}$, at the no load condition;

(4) Calculation of the shaft relative twist angle, θ, according to the following equation:

$$\theta = \theta_a - \theta_{a,0}. \tag{4}$$

(5) Estimation of the shaft torque based on the known calibration curve, that is the relationship between the shaft relative twist angle θ and torque T for a given shaft and material.

One of the main advantages of this approach is that it allows the measurement of a wide torque range by carefully designing the zebra tapes and their distance along the shaft. This makes it suitable for a large variety of engineering applications.

3. Experimental set-up

Experiments were performed to calibrate and validate the proposed non-intrusive torque measurement system. The calibration was performed by comparing the zebra tape torque meter with a reference state-of-the-art measurement technique; in particular, an industrial in-line torque meter, based on the principle of a variable, torque-proportional transformer coupling, was used. This technology is robust against electromagnetic interference and temperature effects; therefore, the system can be effectively used as a reference for calibration. Figure 2 provides a schematic of the torque test rig developed at Durham University, in collaboration with Università Politecnica delle Marche. Figure 3 shows the implemented test stand with its main components and instrumentation.

The test rig comprises a 4-pole 4 kW grid-connected induction generator driven by a 4-pole 4 kW induction motor controlling the speed profile. Both machines are manufactured by ABB Motors. The motor shaft speed is varied via an inverter drive up to 2100 rpm. The generator is connected to a variable transformer to vary its stator voltage and hence the shaft torque in the range from 0 to 16 N m.

The main rig solid shaft, shown schematically in figure 4, features a reduced diameter cross-section in its central part for experimental purposes in order to enhance sensitivity

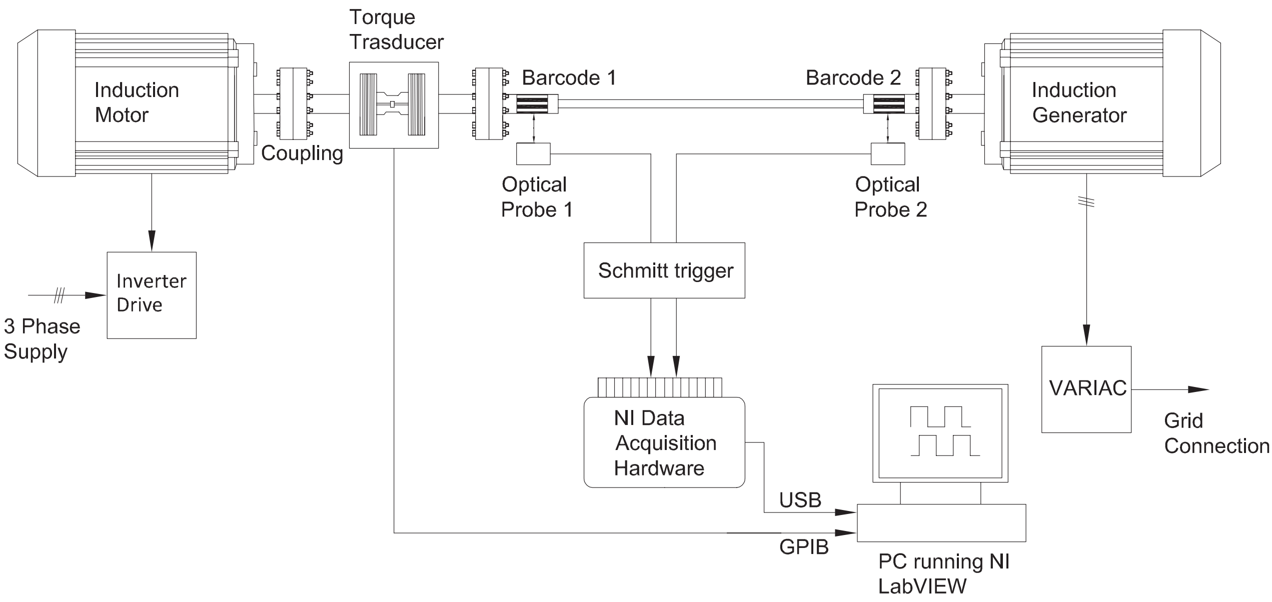

Figure 2. Schematic diagram of the torque test rig.

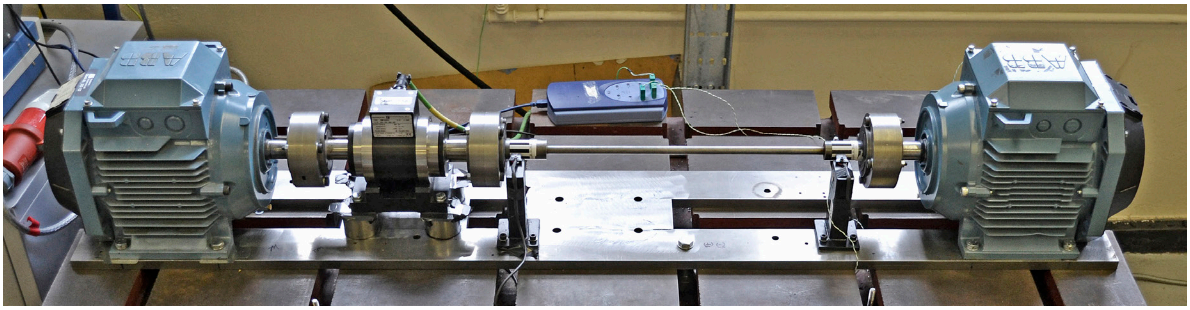

Figure 3. Main components and instrumentation of the torque test rig.

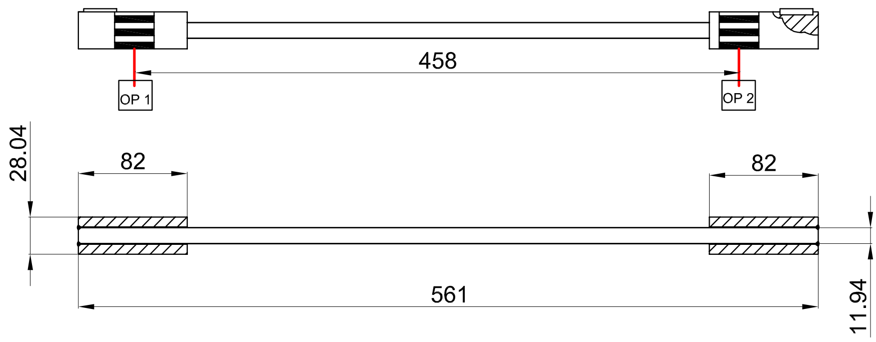

Figure 4. Solid shaft layout and location of the two zebra tapes.

with respect to the test rig torque range and hence achieve a higher twist angle θ for the same applied torque. Indeed, this allows angular shifts of the same order of magnitude as would be observed in the case of larger torques applied to larger diameter shafts in industrial applications, despite the limitations of the maximum torque possible using this test rig.

A high-quality, laser-printed zebra tape is glued around each end of the shaft. The passage of the alternating light and dark stripes is measured by two Optek OPB739RWZ reflective line reader sensors placed at the optimum distance of 0.76 mm from the target, as shown in figure 5.

First, the output from the two OPs is transformed into a series of square pulses through a Schmitt trigger. The pulses are then acquired by a National Instruments (NI) 16-bit data acquisition system (USB-6211 DAQ) driven by the LabVIEW data acquisition environment. The sampling frequency, f_{OP}, is set at 125 kHz, the maximum possible for the NI USB-6211 DAQ hardware.

An in-line Magtrol TMB 313/431 torque transducer, with a rated torque of 500 N m and a combined error of linearity and hysteresis less than ±0.15% of the rated torque, acts as a reference for calibration and comparison with the optical non-intrusive system output. The transducer is capable of

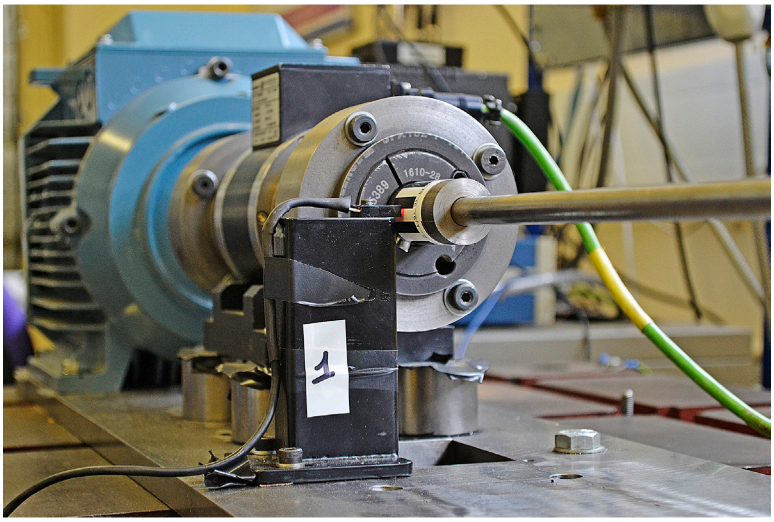

Figure 5. Detail of the contactless shaft torque measurement system.

outputting 60 pulses per revolution for speed measurement so is also used as a reference tachometer. The torque transducer output is collected through a Magtrol 6400 torque display which is connected by a GPIB/IEEE-488 interface to the LabVIEW data acquisition environment. The time synchronisation between the torque transducer and the OPs' readings is obtained by comparing the Unix timestamp of the two system acquisitions.

3.1. Zebra tape design

The design of the zebra tape, particularly the number of pulses per revolution, has a significant impact on the precision of the torque measurements [26]. For a given shaft and zebra tape design, the maximum measurable phase difference between two pulse signals is given by half the zebra tape period, that is half the length of each of its black–white segments, corresponding to 180° phase shift. Indeed, any twist larger than half the period of the zebra tape would be confused with a lower one, as always happens in periodic signals.

When designing the zebra tapes, the minimum zebra tape period, $P_{\min}$ (m), can be calculated as a function of the maximum torsion angle of the shaft expected during operation, $\theta_{\max}$:

$$P_{\min} > 2\theta_{\max} r \tag{5}$$

where $\theta_{\max}$, (rad) is given by:

$$\theta_{\max} = \frac{T_{\max} L}{JG} \tag{6}$$

where $T_{\max}$ is the maximum torque expected during operation (N m), L is the distance between the two OPs (m), J is the shaft polar moment of inertia (m^4) and G is the shear modulus of elasticity for the shaft material (Pa). The corresponding zebra tape maximum allowable number of pulses per revolution, $ppr_{\max}$, can then be calculated as:

$$ppr_{\max} = \mathrm{int}\left(\frac{2\pi r}{P_{\min}}\right) < \frac{2\pi r}{2\theta_{\max}\, r} \tag{7}$$

where r (m) is the shaft radius and int the integer part function.

Table 1. Features of the experimental zebra tape.

Symbol	Description	Value
P	Zebra tape period (length of each black–white segment)	11.0 mm
ppr	Number of pulses per revolution	8
$\theta_{\mathrm{full\_scale}}$	Maximum measurable shaft torsion angle	$\frac{\pi}{8}$

In the case of the experimental test bench described in this work, given the shaft geometry and the maximum torque achievable during operation (16 N m) equation (7) provides a maximum allowable number of pulses per revolution of 45. Within this constraint, the choice of the zebra tape design is a key factor influencing the performance of the proposed torque measurement system. The larger the number of pulses per revolution, the larger the samples required per revolution, that is the larger the sample frequency of the proposed torque transducer, but the more the computational cost needed to implement the data processing. For the purpose of this work, the test bench shaft was instrumented with two bar codes featuring 8 equal stripe pairs, with a stripe width of 5.5 mm, fitting exactly around the shaft. The selection of 8 pulses per revolution represents a trade-off between uncertainty and computational cost. The zebra tape design was selected so that the resulting pulses have a 50% duty cycle which makes phase shift measurement processing easier.

Table 1 summarises the features of the zebra tapes used in the test bench.

3.2. Optical sensor output

Figure 6(a) shows how the zebra tape passage determines the sensor output. The OP emits an unfocussed beam which lights the zebra tape surface. An unfocussed OP has been chosen because it allows for variations of sensor to shaft distance over a larger depth of field with respect to focused probes. However, it produces pulses with lower rising and falling edge gradients, with respect to focused probes. Scattered

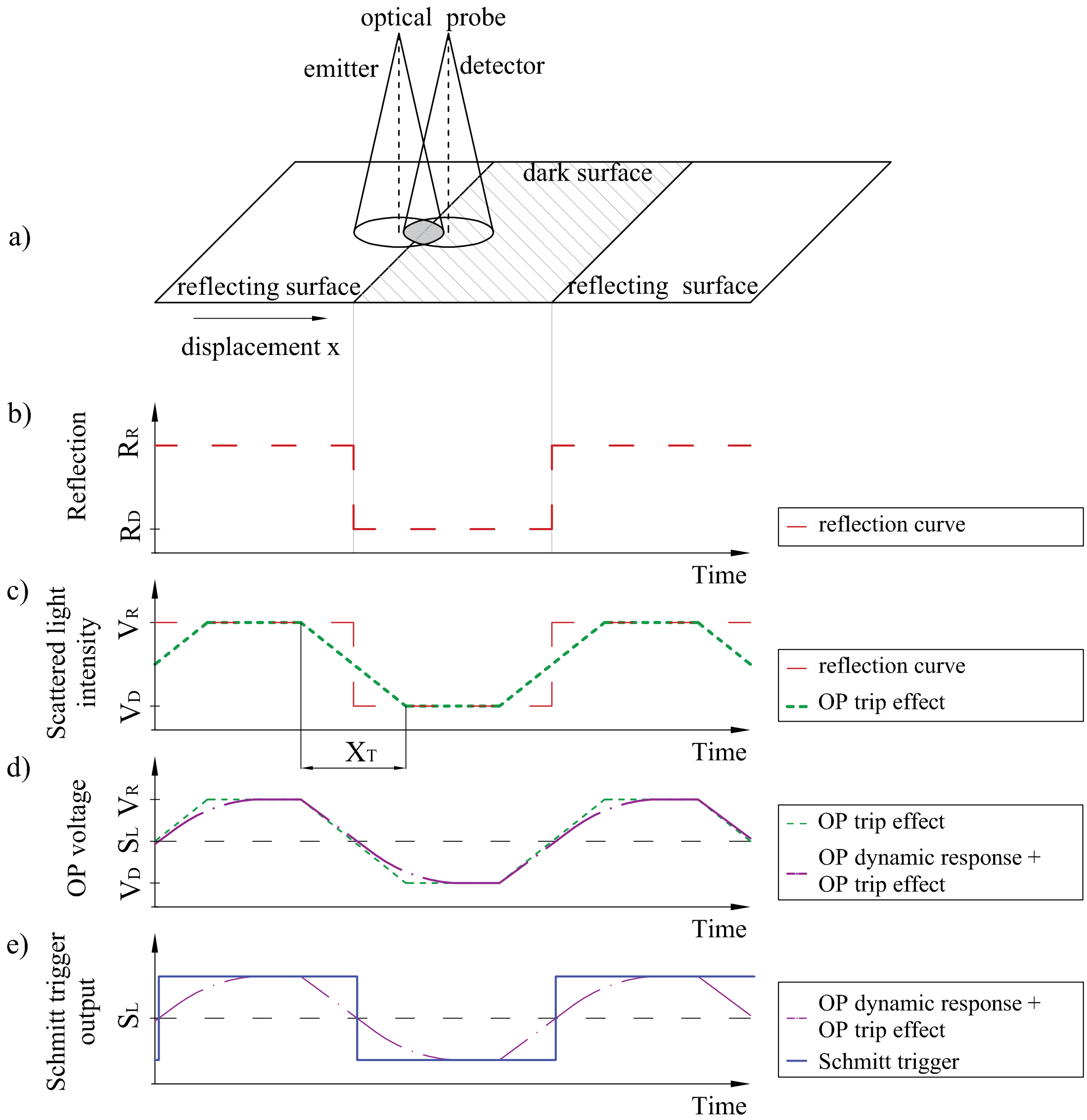

Figure 6. OP response to zebra tape. (a) Passage of the alternating reflecting and dark stripes measured by the OP sensor; (b) zebra tape step profile reflection; (c) scattered light intensity; (d) OP voltage output; (e) Schmitt trigger output.

light is collected back through a detector with a certain angle of aperture. Light scattering intensity from the white surface is significantly larger than that from the black surface. Therefore, even if the zebra tape surface has a step profile (figure 6(b)), the scattered light intensity changes continuously from low to high during the passage of the white stripe. The change in the radiation reflected to the detector is not abrupt, but undergoes a gradual transition along a switching distance X_T (figure 6(c)) [27]. The OP voltage output results from this gradual change in scattered light intensity due to the motion of the black–white stripe through the illuminated area (called trip effect) and the first order dynamic response of the photodetector (figure 6(d)). A Schmitt trigger is implemented to square the probe output voltage when it crosses a pre-set threshold, S_L (figure 6(e)), and to convert it into a train of constant amplitude pulses. The photodetector signal is squared to produce pulses with almost vertical rising and falling edges, easing timing and analysis.

This train of square pulses will be phase shifted by torque variations, as described earlier. In case of variation of the distance between the shaft and the OPs, the amplitude of the output voltage from the photodetectors will vary, resulting in an amplitude modulated signal. This would affect the train of pulses from the Schmidt trigger, which operates on a fixed threshold. The effects of this source of uncertainty will be discussed later in the paper.

3.3. Data processing

3.3.1. Signal pre-processing. In order to automatically extract the values of the shaft angular shifts from the two zebra tape optical signals, dedicated programmes, known as virtual instruments (VIs), were developed and built in the LabVIEW environment. Figure 7 shows the data processing flow chart of the VIs implemented for pulse train analysis.

The data processing consists of two steps:

(1) The shaft rotational speed is calculated by estimating the time per shaft revolution from the rising edges of the two pulse trains;

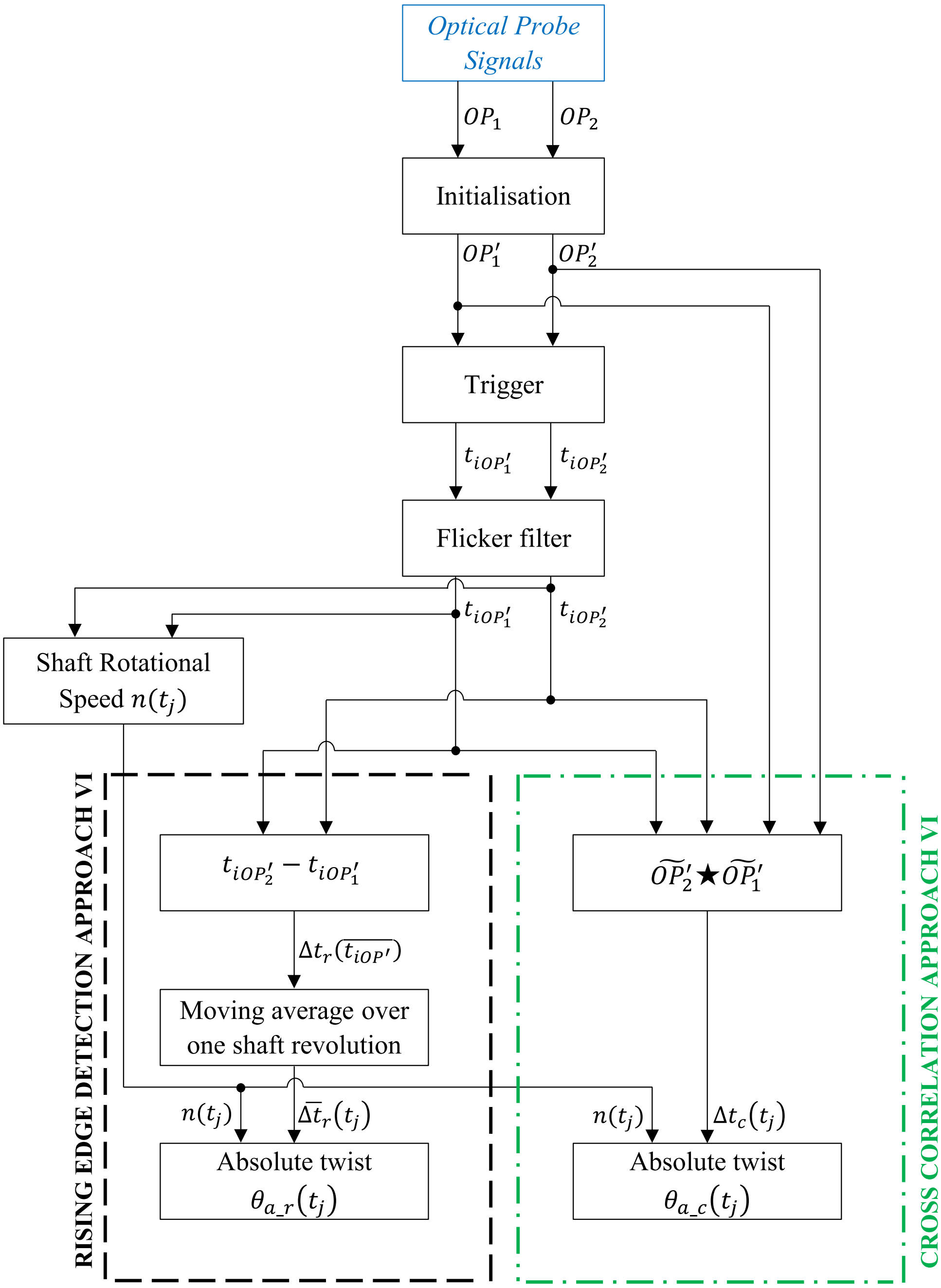

Figure 7. Data processing flow diagram.

(2) The shaft absolute twist is calculated by adopting the rising edge detection and the cross-correlation approaches.

OP installation and zebra tape mounting offset could cause initial misalignment of the pulse trains at the start of recording with a consequent erroneous estimation of the initial time shift, and hence angular shift. To overcome this problem, the signals recorded by the OPs are first initialised when the data system acquisition is started. Figures 8(a) and (b) shows an example of two pairs of similar pulse trains; they feature the same time shift, Δt_r, however their recording starts at two different positions with respect to the pulses. The time shift measured between their first two rising edges will be different, Δt_{r_a} and Δt_{r_b}, respectively. In order to avoid this error in the measurements, the OP signals, OP_1 and OP_2, are initialised by forcing the recording to start only when both signals are in the high or low state, i.e. at the instant t_p in figures 8(c) and (d). Now, the same time shift, Δt_r, is measured based on the time between the first rising edges of the initialised signals, OP'_1 and OP'_2.

The time at which the rising edges of the two initialized signals occur is defined as $t_{iOP'_k}$, where $i = 1,2, \ldots m$, with m equal to the number of rising edges in the initialized signals, and $k = 1,2$ is the index that identifies the two OPs. The rising edge time instants $t_{iOP'_k}$ are captured by triggered acquisition where the threshold level is set equal to half of the peak-to-peak signal amplitude. A flicker filter is also applied to remove rising edge timing errors resulting from possible signal flickering around the trigger level. Flickering would result in more

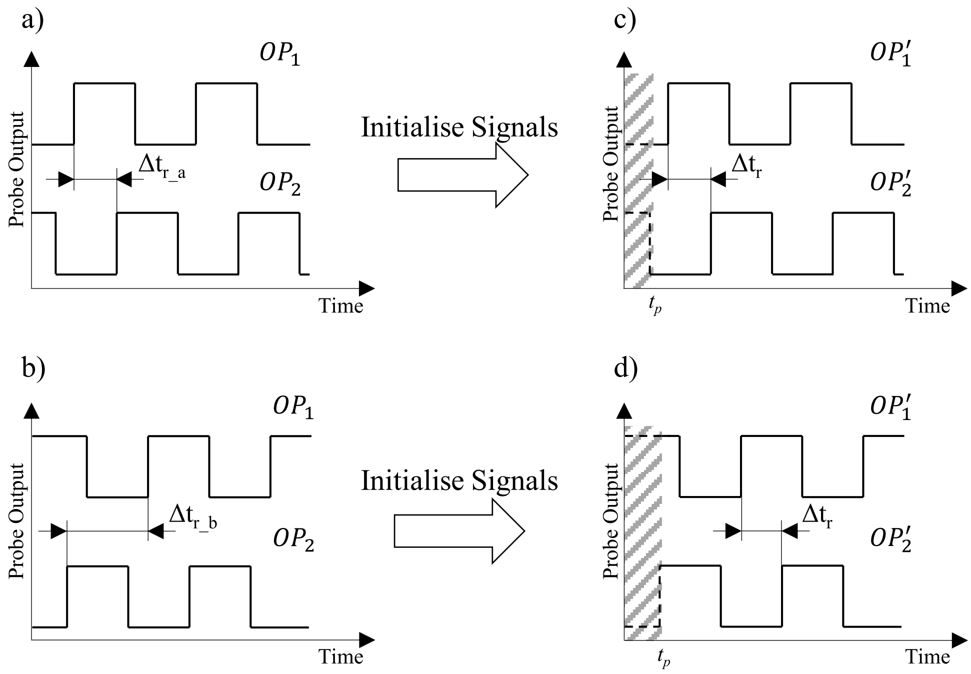

Figure 8. Signal initialisation (a) and (b) similar pulse trains recorded at two different start positions with respect to the pulse state; (c) and (d) OP initialisation with signals both in the high or low state.

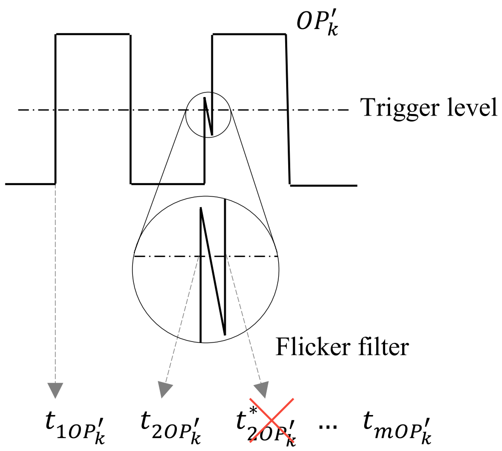

Figure 9. Flicker filter.

than one output from the trigger block for each signal rising edge, i.e. $t_{2\text{OP}'_k}$ and $t^*_{2\text{OP}'_k}$ in figure 9. For each pulse train, the filter compares the time interval between two consecutive rising edges against that estimated from the expected shaft rotational speed, 1500–1900 rpm, and the number of pulses per revolution, 8. When the two values do not match, the filter acts on the signal to keep only the first output from the trigger block and remove all other unwanted outputs, that is $t^*_{2\text{OP}'_k}$ in figure 9. For each signal, the output of the flicker filter is a 1D array containing m elements representing the rising edge times of the train of pulses.

3.3.2. Shaft rotational speed. For each zebra tape, the identified rising edge times, $t_{i\text{OP}'_k}$, where $k = 1,2$, are then used to estimate the corresponding shaft speed, $n_k\left(t_{k,j}\right)$ (rpm), by applying conventional speed encoder techniques, according to equation (3), as follows:

$$n_k\left(t_{k,j}\right) = \frac{60}{t_{(ppr+l-1)\text{OP}'_k} - t_{l\text{OP}'_k}} \tag{8}$$

where $l = 1,2,.., (m\text{-}ppr)$ and $t_{k,j}$ is the mean time of the windows $t_{(ppr+l-1)\text{OP}'_k} - t_{l\text{OP}'_k}$, calculated as:

$$t_{k,j} = \frac{\sum_{n=j+1-\left|\frac{ppr}{2}\right|_{\text{up}}}^{j+\left|\frac{ppr}{2}\right|_{\text{down}}} t_{n\text{OP}'_k}}{ppr} \tag{9}$$

where $j = \left(\left|\frac{ppr}{2}\right|_{\text{up}}\right), \ldots, \left(m - \left|\frac{ppr}{2}\right|_{\text{down}}\right)$, with $\left|\frac{ppr}{2}\right|_{\text{up}}$ and $\left|\frac{ppr}{2}\right|_{\text{down}}$ equal to half of ppr rounded up and down, respectively.

The shaft rotational speed, $n\left(t_j\right)$, is then calculated as the average of those two speeds to minimise the error:

$$n\left(t_j\right) = \frac{n_1\left(t_{1,j}\right) + n_2\left(t_{2,j}\right)}{2} \tag{10}$$

where t_j is given by:

$$t_j = \frac{t_{1,j} + t_{2,j}}{2}. \tag{11}$$

3.3.3. Shaft absolute twist.

3.3.3.1. Time shift measurement by direct timing of rising edges. The rising edge detection approach is the most straightforward method for determining the time delay between the pulses. It is based on the measurement of the times at which the rising edges of the two pulse trains occur and on the calculation of their relative phase shift, as shown in figure 10. In the rising edge detection approach VI, the time shift between the two pulse trains associated with the signals' average rising edge times, $\Delta t_r\left(\overline{t_{i\text{OP}'}}\right)$, is calculated as:

$$\Delta t_r\left(\overline{t_{i\text{OP}'}}\right) = t_{i\text{OP}'_2} - t_{i\text{OP}'_1} \tag{12}$$

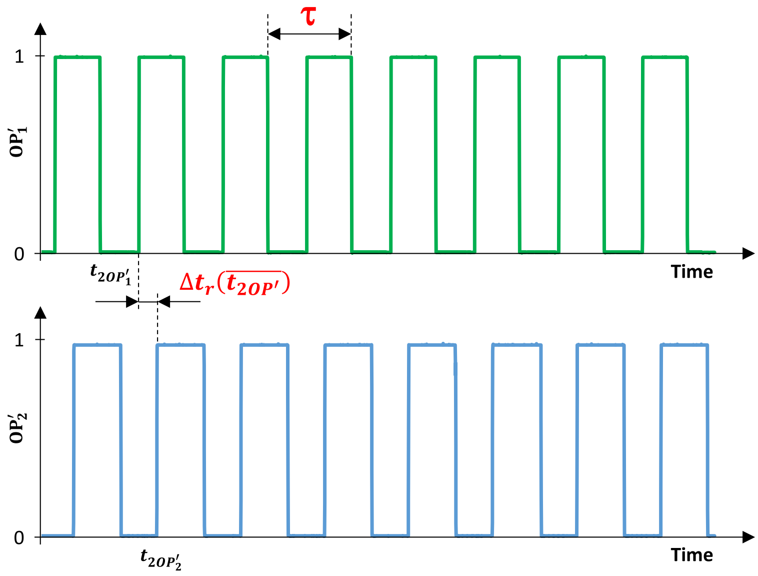

Figure 10. Phase shift estimation through the rising edge detection approach.

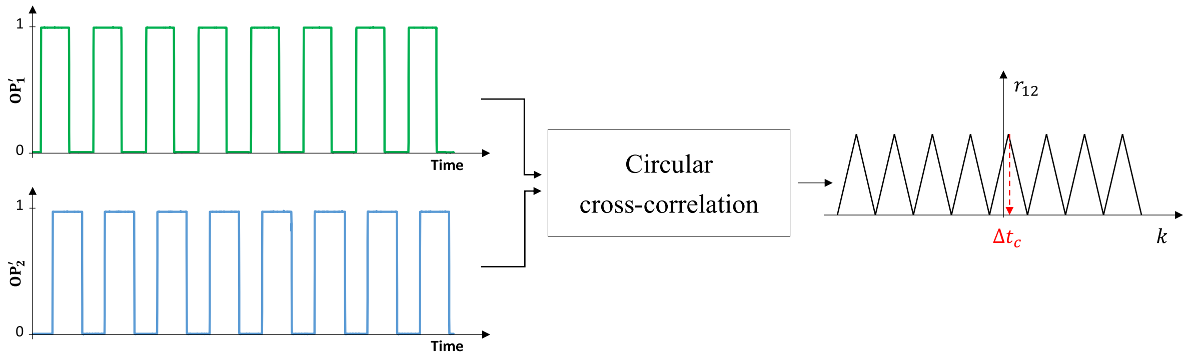

Figure 11. Phase shift estimation through the cross-correlation approach.

where $i = 1,\ldots.., m$ and $\overline{t_{i\mathrm{OP}'}}$ is defined as:

$$\overline{t_{i\mathrm{OP}'}} = \frac{t_{i\mathrm{OP}_1'} + t_{i\mathrm{OP}_2'}}{2}. \tag{13}$$

As already pointed out, tangential and radial displacements between shaft and OPs, typically caused by vibrations or shaft deformation, introduce noise in timing of pulses. This noise is expected to be periodic, at the rotational frequency or its harmonics. Therefore, a moving average filter is implemented to measure a time delay averaged over a full revolution $\overline{\Delta t_{\mathrm{r}}}\,(t_j)$. This is implemented as moving average filter over the eight delays $\Delta t_{\mathrm{r}}\,(\overline{t_{i\mathrm{OP}'}})$ measured during a full revolution, with seven-point overlap over time, allowing the calculation of an averaged delay for each pulse, that is one value per zebra tape pulse.

The eight-point averaged time shift, $\overline{\Delta t_{\mathrm{r}}}\,(t_j)$, is calculated as:

$$\overline{\Delta t_{\mathrm{r}}}\,(t_j) = \sum_{i=j+1-\left|\frac{ppr}{2}\right|_{\mathrm{up}}}^{j+\left|\frac{ppr}{2}\right|_{\mathrm{down}}} \frac{\Delta t_{\mathrm{r}}\left(\overline{t_{i\mathrm{OP}'}}\right)}{ppr}. \tag{14}$$

3.3.3.2.Time shift measurement by cross-correlation. The cross-correlation approach allows the measurement of the similarity of the two time series, OP_1' and OP_2', as a function of the time-lag applied to one of them. Unlike the rising edge detection approach, the cross-correlation VI uses the full initialised signals OP_1' and OP_2' to estimate their time shift and not only the times at which the rising edges occur (figure 11).

Cross-correlation is implemented according to [28], as circular cross-correlation, defined as:

$$r_{12}\,(k) = \frac{1}{N}\sum_{n=0}^{N-1} \mathrm{OP}_1'(n)\,\mathrm{OP}_2'(k-n) \tag{15}$$

where $k = 0,\ldots, N-1$ and N, the length of the two signals, is chosen equal to the shaft revolution. This algorithm does not require zero padding, but considers the pulse train to be periodic.

Circular cross-correlation provides an output with 8 peaks, equal to the number of pulses per revolution (figure 11), that correspond to 8 possible time delays, as usual in a periodic function. The delay of interest is the smallest one, Δt_{c}, provided that the zebra tape period is larger than the maximum shift, as discussed in section 3.1, equation (5). The other peaks appear because the train of pulses is a periodic function.

The signals OP_1' and OP_2' are progressively circular cross-correlated giving one value of the time shift per zebra tape pulse, $\Delta t_c(t_j)$, similarly to the case of the rising edge detection approach $\overline{\Delta t_r}(t_j)$.

In both approaches, the calculated time shifts, $\overline{\Delta t_r}(t_j)$ and $\Delta t_c(t_j)$, respectively, depend on the shaft speed. According to equation (4), they are converted into shaft absolute angular shifts, $\theta_{a\_r}(t_j)$ and $\theta_{a\_c}(t_j)$, respectively, by:

$$\theta_{a\_r}(t_j) = \frac{2\pi}{60} n(t_j) \overline{\Delta t_r}(t_j) \tag{16}$$

$$\theta_{a\_c}(t_j) = \frac{2\pi}{60} n(t_j) \Delta t_c(t_j). \tag{17}$$

3.4. Range, resolution and sampling frequency

For a given zebra tape design (ppr), shaft speed (n) and OP sampling frequency (f_{OP}), the non-intrusive torque measurement system features are:

$$\text{Range:} \qquad \theta_{RANGE} = [-\theta_{full_{scale}}, \theta_{full\_scale}] = \left[-\frac{\pi}{ppr}, \frac{\pi}{ppr}\right] \tag{18}$$

$$\text{Resolution:} \qquad \delta\theta = \frac{2\pi n}{60} * \frac{1}{f_{OP}}. \tag{19}$$

Using the calibration curve, $\theta = m * T$, where m is the calibration line slope, equations (18) and (19) allow the estimation of the corresponding torque range T_{RANGE} and resolution δT.

$$T_{RANGE} = \frac{\theta_{RANGE}}{m} \tag{20}$$

$$\delta T = \frac{\delta\theta}{m} \tag{21}$$

$$\text{Sampling Frequency:} \qquad f_c = \frac{2\pi n}{60} * \frac{ppr}{2\pi} = \frac{n * ppr}{60}. \tag{22}$$

Torque samples are then obtained at a non-constant frequency which is dependent on the shaft speed.

4. Calibration and uncertainty analysis

4.1. System calibration

The non-contact optical torque system was calibrated against reference torque measurements from the in-line torque transducer in order to fully characterise the torque-twist angle relationship described by equation (1). The calibration curve allows the estimation of the torque acting along the shaft by simply recording the zebra tape pulse trains, calculating their time shift and hence the shaft angular shift, using either method.

Steady state tests were performed on the test rig at four different shaft speeds: 1600, 1700, 1800 and 1900 rpm. For each speed, the calibration procedure consisted of the following steps:

(1) Run the motor to the required testing speed.
(2) Record the signals from both the OPs and the torque transducer at no-load (0 V applied to the generator stator) for around 10 s.
(3) Vary the generator stator voltage to increase the shaft torque in steps of 2 N m, starting from an initial torque value of 1 N m in the case of the tests run at 1600 and 1800 rpm and 2 N m in the case of the tests run at 1700 and 1900 rpm. For each speed, to avoid damage to the generator during operation, the stator voltage was varied up to a precautionary safety limit of its armature winding current of 8 Amps; this determined the maximum operational torque. Given the available experimental set-up, the calibration range was limited to 16 N m, even though the zebra tape had been designed with a period allowing measurements up to 62 N m, which therefore represents its full-scale input range.
(4) Record the signals from both the OPs and the torque transducer for around 10 s for each applied torque level.
(5) Post-process the OP pulse data and calculate the shaft twist using the rising edge detection and cross-correlation approaches presented in section 3.3.
(6) Build calibration curves by plotting the shaft relative twist, calculated according to equation (4), against the corresponding reference torque measured by the in-line transducer, whose signal was resampled to match the time delay sampling frequency.

The calibration curves resulting from the rising edge and the cross-correlation approaches are shown in figures 12 and 13, respectively, and compared in table 2. They result from the linear regression of experimental data by a straight line using the least square method. As predicted by equation (1), the torque-twist trend is linear under steady state conditions. The two calibration curves show a similar trend with satisfactory R-squared levels, indicating a good fit of the experimental data by the regression line. A difference in sensitivity of around 2% is observed.

4.2. Measurement uncertainty evaluation

The measurement uncertainty has been estimated according to the ISO GUM (Guide to the expression of uncertainty in measurement). The statistical processing of series of experimental data obtained in the laboratory conditions has allowed a Type A uncertainty estimation. A more comprehensive Type B analysis has been performed using the Monte Carlo method, where a number of influencing parameters and disturbances which could affect the measurement system in a real-world application has been considered.

4.2.1. Type A uncertainty. The regression of calibration data has allowed the statistical estimation of the Type A uncertainty of measurement, U_{exp} (table 2), with respect to the maximum torque achievable during operation (16 N m), which corresponds to 26% of the torque meter full operating range.

For each case, the standard deviation of the input torque, s_T, has been estimated by statistical analysis of the residuals of the M calibration data with respect to their interpolating line as:

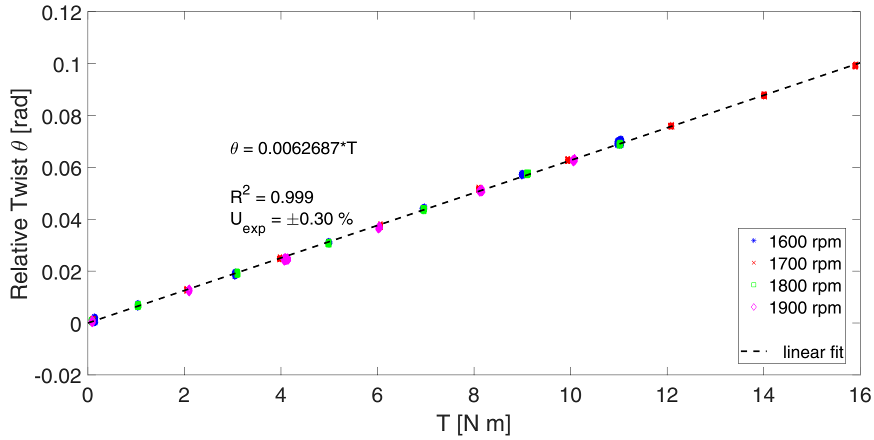

Figure 12. Calibration curve: Rising edge detection approach.

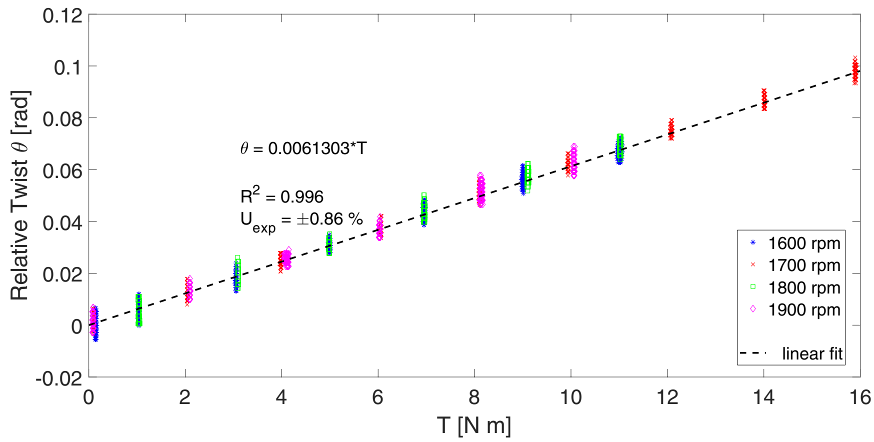

Figure 13. Calibration curve: cross-correlation approach.

Table 2. Parameters of the two calibration curves and their Type A expanded uncertainty relative to the system full-scale torque, U_{exp}.

Method	Linear fit equation	R^2	U_{exp} (%)
Rising edge	$\theta = 6.2687\ 10^{-3} * \mathrm{T}$	0.999	±0.30
Cross-correlation	$\theta = 6.1303\ 10^{-3} * \mathrm{T}$	0.996	±0.86

$$s_{\mathrm{T}} = \sqrt{\frac{1}{M-2}\sum_{k=1}^{M}\left(\frac{\theta_k}{m} - T_k\right)^2} \tag{23}$$

where θ is the shaft relative twist predicted by the calibration line. The type A uncertainty relative to the system full-scale torque, U_{exp}, associated with each approach has then been calculated, in compliance with the ISO GUM:1995 [29], as expanded uncertainty with a coverage factor $k = 2$, allowing for a 95% confidence level, as:

$$U_{\text{exp}}(\mathrm{N\,m}) = ks_{\mathrm{T}} \tag{24}$$

and expressed as a percentage of the measurement system full-scale torque, $T_{\text{full\_scale}}$, as:

$$U_{\text{exp}}(\%) = \frac{u_{\text{exp}}(\mathrm{N\,m})}{T_{\text{full\_scale}}(\mathrm{N\,m})}100 \tag{25}$$

where:

$$T_{\text{full\_scale}} = \frac{\theta_{\text{full\_scale}}}{m} \tag{26}$$

and $\theta_{\text{full\_scale}}$ is the measurement system full-scale twist output given in table 1.

In this analysis, the same statistical uncertainty has been assumed all over the entire operating range, even if this has been estimated by using available experimental data referring to the first 26% of the torque meter design range.

The type A uncertainty analysis has taken into account experiments at various speed and torque levels, which were repeated over several days and performed by different operators. This provides information on repeatability and reproducibility of the proposed method.

For the experimental set-up used in this work, the maximum measurable angular shift of the system corresponds to the full-scale input torque $T_{\text{RANGE}} = 62$ N m, which is approximately four times larger than the calibration range. Within this range the system has a resolution δT of 0.27 N m if only one rising edge is used; however, the resolution decreases by *ppr* if the angular shift is determined by averaging a series of *ppr* angular shifts. In this case *ppr* = 8 was used.

Unexpectedly, the cross-correlation approach results show a higher dispersion around their best fit curve when compared to the rising edge detection approach, resulting in higher uncertainty of the method (table 2). Cross-correlation underperforms

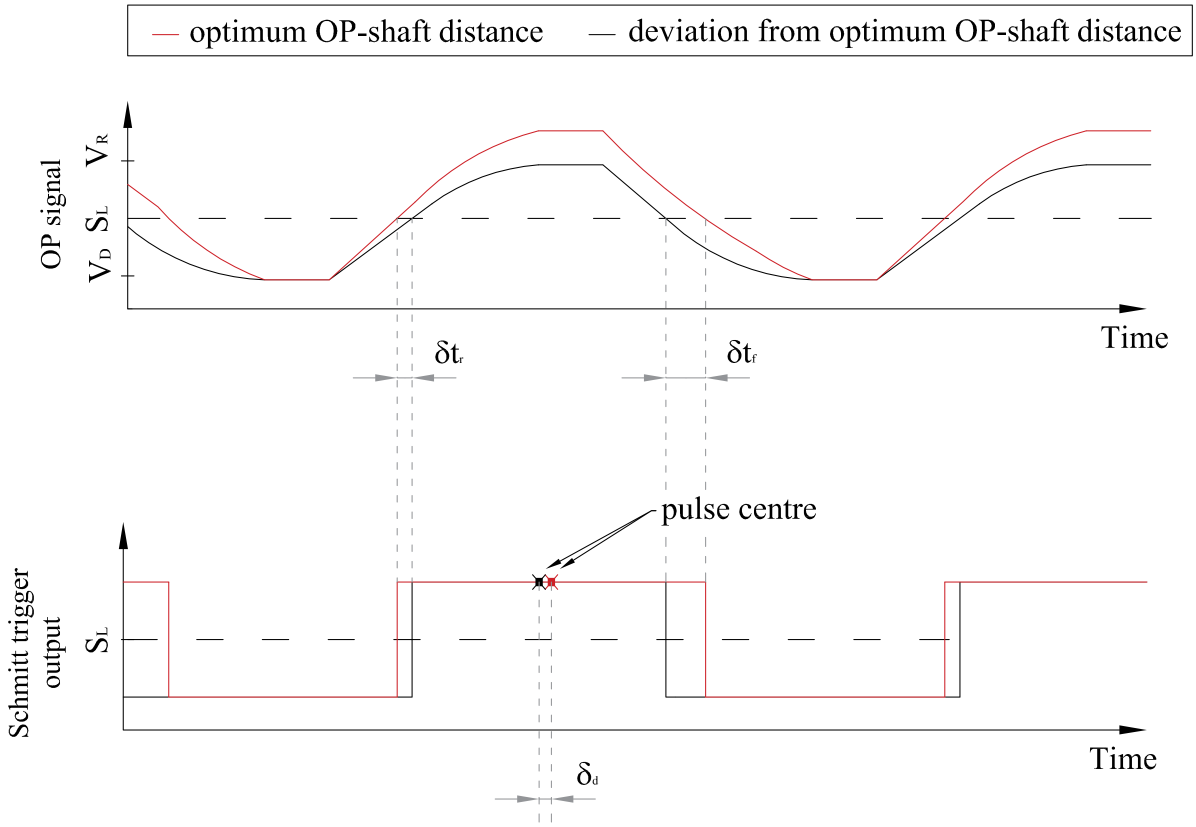

Figure 14. Effect of sensor to shaft distance variation on the OP output.

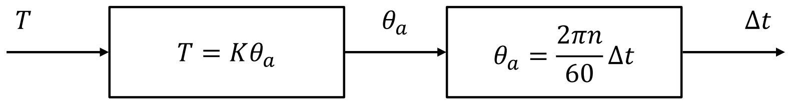

Figure 15. Zebra tape torque meter model.

with respect to direct timing because of the changes in duty cycle throughout one shaft revolution and the time shift introduced by the Schmidt trigger operating on an amplitude modulated photodetector signal. As mentioned, amplitude modulation may affect the optical signal because of possible vibrations, shaft misalignment or bending; all these phenomena would affect the sensor to shaft distance during shaft rotation. In these conditions, after the Schmidt trigger, the variation of duty cycle and time shift causes a displacement of the pulse centre equal to $\delta_d = (\delta t_r + \delta t_f)/2$, as shown in figure 14.

Cross-correlation is more sensitive to pulse shape than rising edge timing. Moreover, cross-correlation is intrinsically sensitive to the position of the centre of each square pulse. These effects together explain the larger dispersion of data seen for cross-correlation whenever the optical signal experiences amplitude modulation and a Schmidt trigger is applied. It would therefore be expected that cross-correlation would better perform on the original photodetector signal, before being squared by the Schmidt, but this has not been implemented in this paper.

4.2.2. Uncertainty analysis using Monte Carlo method (MCM). The propagation of distributions through a mathematical model of the zebra tape torque meter system has been implemented by MCM for the evaluation of uncertainty of measurement according to the GUM:1995 Supplement 1 [30].

Table 3. Measurement system model equations.

Method	Model
Rising edge detection	$T = K\frac{2\pi n}{60}\overline{\Delta t_r}$
Cross-correlation	$T = K\frac{2\pi n}{60}\Delta t_c$

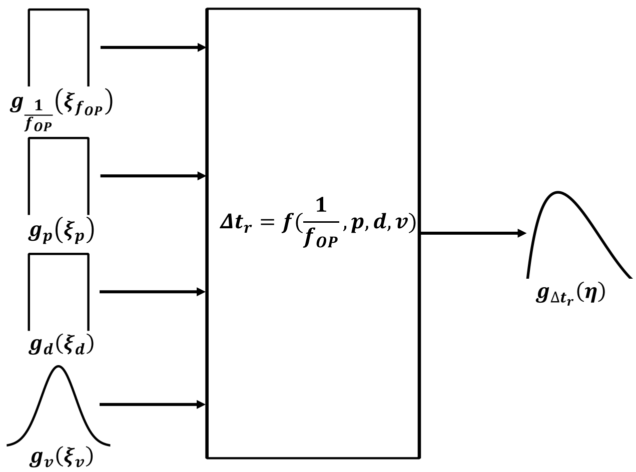

Figure 16. PDF propagation of the four independent input quantities to provide the PDF of Δt_r (Adapted with permission from [30]. Permission to reproduce extracts from ISO publications is granted by BSI Standards Limited (BSI) on behalf of International Organization for Standardization (ISO). No other use of this material is permitted.)

Table 4. Uncertainties and sensitivity analysis of the quantities contributing to $u_{\Delta t_r}$.

X_j				
Symbol	Name	Standard deviation s_j	Half-width tolerance a_j	Sensitivity analysis $\left(\frac{d\hat{f}}{dx_j}\right)^2 ux_i^2$
$\frac{1}{f_{OP}}$	OP sampling frequency		$4.00 * 10^{-6}$ (s)	$1.33 * 10^{-12}$ (s)
p	Zebra tape laser-printing		$2.12 * 10^{-5}$ (m)[a]	$2.76 * 10^{-7}$ (s)
d	Shaft cylindricity error		$33 * 10^{-6}$ (m)[a]	$4.30 * 10^{-7}$ (s)
v	Shaft movements	$60 * 10^{-6}$ (m)[a]		$5.63 * 10^{-10}$ (s)

[a] Model assumption.

The measurement uncertainty evaluation has been performed with respect to a shaft rotational speed of 1700 rpm at which the maximum torque achievable during operation (16 N m) was measured.

A mathematical model of the zebra tape torque meter, shown schematically in figure 15, has been built to relate the output quantity T (i.e. the quantity intended to be measured) with the input quantities $\boldsymbol{X}$ (i.e. K, n and Δt) upon which T depends. Table 3 summarises the model equations for the two approaches.

The shaft torsional stiffness, K, has been estimated as the inverse of the slope of the rising edge calibration linear fit equation and its standard deviation, s_K, has been computed by Type A method according to the GUM [29], that is by performing a statistical analysis of the residuals of the M calibration data with respect to its inverse interpolating line $T = K\theta$ as:

$$s_K = \sqrt{\frac{M s_T^2}{M \sum_{j=1}^{M} \theta_j^2 - \left(\sum_{j=1}^{M} \theta_j\right)^2}}. \tag{27}$$

The uncertainty of the shaft angular speed n is computed by Type A method, by performing a statistical analysis of the time series of experimental data from the torque test rig at steady state, according to the GUM [29]. The standard uncertainty s_n is therefore computed as standard deviation of n, and results to be:

$$s_n = 0.23\ (\text{rpm}). \tag{28}$$

In the case of the rising edge approach, the probability density function (PDF) for the time shift measured by direct timing of each pair of rising edges, $g_{\Delta t_r}(\eta)$, has been computed through MCM, where 10^6 simulations have been performed to deliver a 95% coverage interval for the output quantity according to [30]. In this case $g_{\Delta t_r}(\eta)$ depends on the propagation through the model of the PDFs of the following independent input quantities (figure 16), each with its own statistical dispersion:

- the time interval between the OP samples, with an associated rectangular PDF and $2a_{\frac{1}{f_{OP}}}$ width, where:

$$a_{\frac{1}{f_{OP}}} = \frac{1}{2 * f_{OP}} \tag{29}$$

- the zebra tape laser-printing resolution, with an associated rectangular PDF and $2a_p$ width, where, assuming a 1200 dpi laser printer, the printing tolerance, a_p, is given by:

$$a_p = \frac{(25.4 * 10^{-3})}{1200} = 2.128 * 10^{-5}\ (\text{m}) \tag{30}$$

- the shaft cylindricity error, with an associated rectangular PDF and $2a_d$ width, where, assuming an IT8 tolerance class of the shaft, its dimensional tolerance, a_d is given by [31];
- the shaft radial movements (possibly due to vibrations), assumed to act in the direction perpendicular to the optical sensor axis, with associated Gaussian PDF and an assumed standard deviation of:

$$s_\nu = 60 * 10^{-6}\ (\text{m}). \tag{31}$$

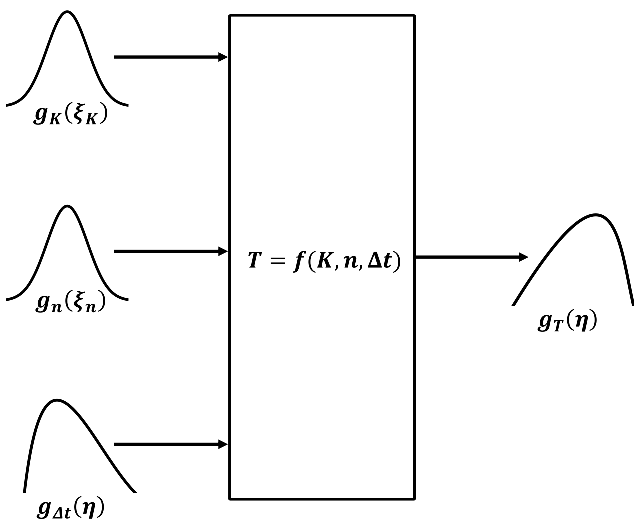

Figure 17. PDF propagation of K, n and Δt to provide the PDF of T through the zebra tape torque meter model (Adapted with permission from [30]. Permission to reproduce extracts from ISO publications is granted by BSI Standards Limited (BSI) on behalf of International Organization for Standardization (ISO). No other use of this material is permitted.)

Table 4 summarises the input parameters contributing to the uncertainty of Δt_r, $u_{\Delta t_r}$, each with its associated uncertainty intervals used in the model. The amplitude of these intervals has been assumed based on knowledge of the technology implemented in the system; it is either the width of a flat PDF or the standard deviation of a Gaussian PDF, depending on the type of parameter. The table also provides a sensitivity

Table 5. Uncertainties and sensitivity analysis of the quantities contributing to u_T.

X_j			Standard deviation s_j	Sensitivity analysis	
Symbol	Name	Value		Rising edge	Cross-correlation
K	Shaft torsional stiffness	159.523 N m rad^{-1}[a]	0.0077 N m rad^{-1}[a]	$5.965 * 10^{-7}$ (N m)	$5.965 * 10^{-7}$ (N m)
n	Shaft rotational speed	1700 (rpm)[a]	0.23 (rpm)[a]	$4.686 * 10^{-6}$ (N m)	$4.686 * 10^{-6}$ (N m)
$\overline{\Delta t_r}$	Time shift measurement by direct timing of rising edges	$5.634 * 10^{-4}$ (s)[a]	$1.272 * 10^{-5}$ (s)[b]	0.131 (N m)	
$\overline{\Delta t_c}$	Time shift measurement by cross-correlation	$5.509 * 10^{-4}$ (s)[a]	$1.273 * 10^{-5}$ (s)[b]		0.137 (N m)

[a] Experimental result.
[b] MCM result.

Table 6. Torque meter system Type B expanded uncertainty relative to the system full-scale torque, U_{MCM}.

Method	U_{MCM} (%)
Rising edge	±1.17
Cross-correlation	±1.19

analysis, that is an estimate of the contribution to the overall uncertainty budget for each input parameter, showing that the zebra tape laser-printing and the shaft cylindricity errors are the major contributors to $u_{\Delta t_r}$.

Within each shaft revolution, the standard deviation of $\overline{\Delta t_r}$, $s_{\overline{\Delta t_r}}$, has then been then obtained through MCM as the average of the eight pulse train rising edges, Δt_r, and their PDFs, $g_{\Delta t_r}$.

In the case of the cross-correlation approach, the same Gaussian PDF, with uncertainty $u_{\Delta t_r}$, has been assumed for all the time shifts measured between the rising and falling edges, respectively. Unlike the rising edge detection approach, in this case the standard deviation of Δt_c, $s_{u_{\Delta t_c}}$, has been obtained by type B analysis [29] as:

$$s_{\Delta t_c} = \frac{u_{\Delta t_r}}{\sqrt{2ppr}}. \tag{32}$$

The PDF for T, $g_T(\eta)$, depends on the propagation through the model of the PDFs of the independent input quantities, K, n and Δt ($\overline{\Delta t_r}$ or Δt_c, depending on the approach adopted) as described in figure 17.

Table 5 summarises the quantities used for the estimation of the uncertainty of T, u_T, and their sensitivity analysis, showing that, in both approaches, the estimation of Δt is the major contributor to u_T.

For both approaches, table 6 shows the torque measurement type B expanded uncertainty at 95% confidence level (i.e. corresponding to two standard deviations) obtained by applying the MCM in compliance with the ISO GUM [30] and expressed as a percentage of the system full-scale torque T_{full_scale}.

In both cases, the results show that the application of the MCM to a simplified model of the measurement system overestimates the overall uncertainty when compared to the type A uncertainty obtained by experimental results, as reported in table 2. The rising edge detection approach shows the larger difference between the values of U_{MCM} and U_{exp}. Indeed, it is reasonable that a type A evaluation based on laboratory data underestimates uncertainty, given that MCM takes into account all possible sources of uncertainty which may occur in real-world applications and not in the controlled laboratory environment. This explains the lower value of uncertainty obtained through statistical processing of the experimental data. Therefore, the uncertainty estimated by MCM sets the maximum value of the system uncertainty attainable in practical applications.

5. Results

Tests have been performed to validate the proposed zebra-tape torque meter under both static and variable conditions. The torque measurements obtained by the zebra tape torque meter have been compared with measurements from the in-line torque transducer (Magtrol) which has been assumed as the reference system for all the experimental work, being a well-established state-of-the-art technique. Shaft speed was also recorded by the zebra tapes.

5.1. Steady state tests

Figure 18 shows speed and torque results for two steady state tests performed at 1700 rpm, 4 N m and 1900 rpm, 10 N m.

Both the cross-correlation (azure solid line) and rising edge (red solid line) approaches show good agreement, on average, with reference transducer measurements (black dotted line) however the zebra tape data appears noisier. This is particularly apparent for torque measurements obtained by cross-correlation. The causes of noise in this data have been already outlined when showing the calibration results however it should also be noted that the reference transducer is sampled at a much lower rate, possibly reducing its own noise levels. The frequency at which noise appears for the optical system is significantly higher than any relevant frequencies expected in the mechanical torque signal therefore such noise could be reduced by low pass digital filtering.

5.2. Variable torque and speed tests

Finally, variable torque and speed tests have been performed to evaluate and compare the response of the two approaches. Figure 19 shows the effects of sharp step changes in torque.

The shaft speed was initially set at around 1715 rpm and the torque first increased and then decreased in steps of approximately 2 N m, in the 0–15 N m operating range. Changes in

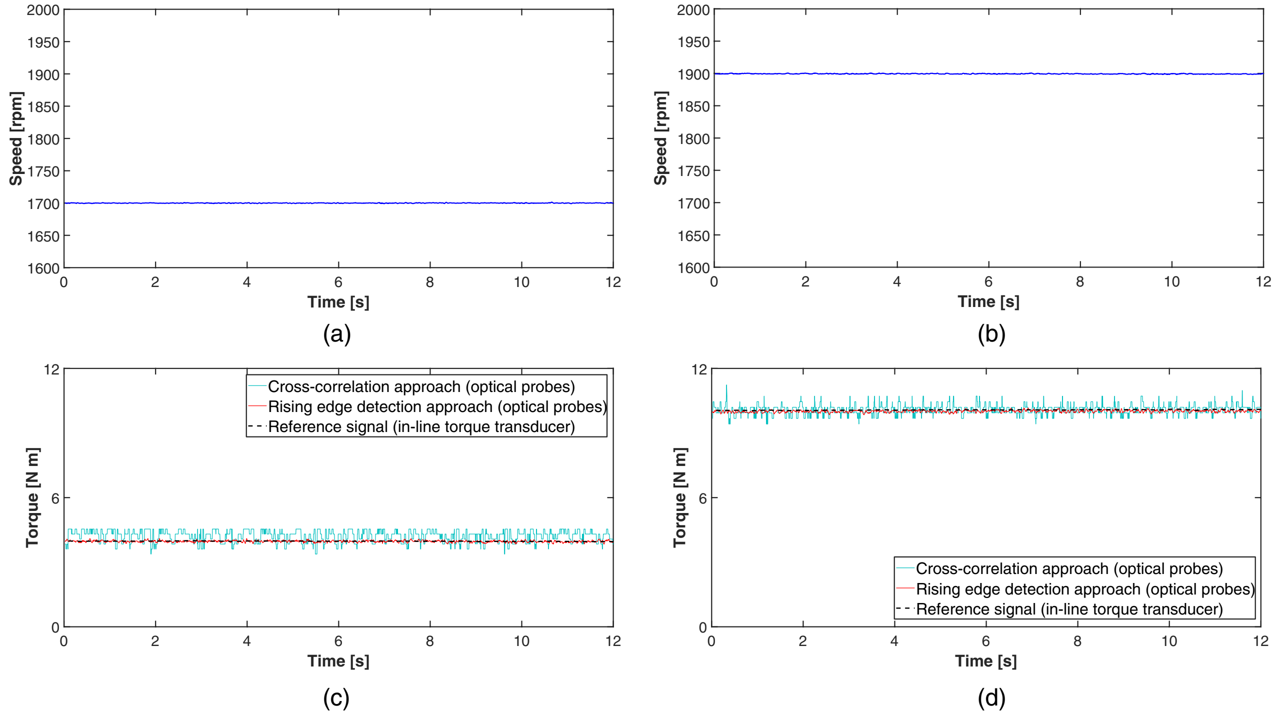

Figure 18. Optical system speed and torque measurement under steady state conditions: (a) and (c) 1700 rpm and 4 N m; (b) and (d) 1900 rpm and 10 N m.

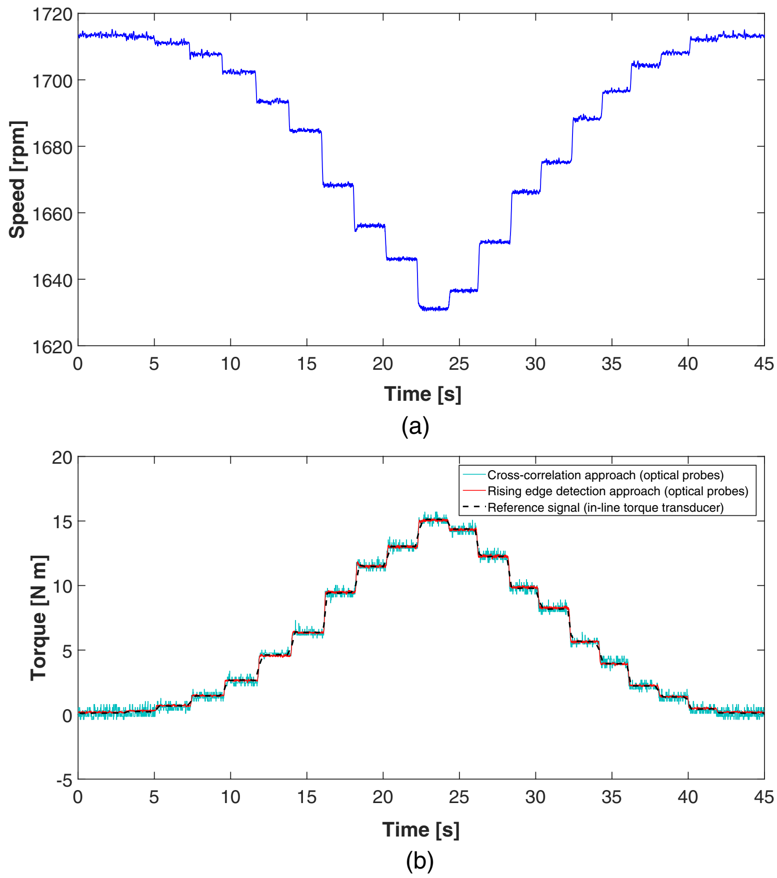

Figure 19. Optical system speed (a) and torque (b) measurements under sharp step torque changes.

speed are the result of applied torque that were not countered by the variable speed drive. The zebra tape measurements allow tracking of the rotational frequency as well as the torque during the whole transient. The response of the zebra tape torque meter under variable torque and speed test conditions is sufficient to track the torque variations imposed on the shaft.

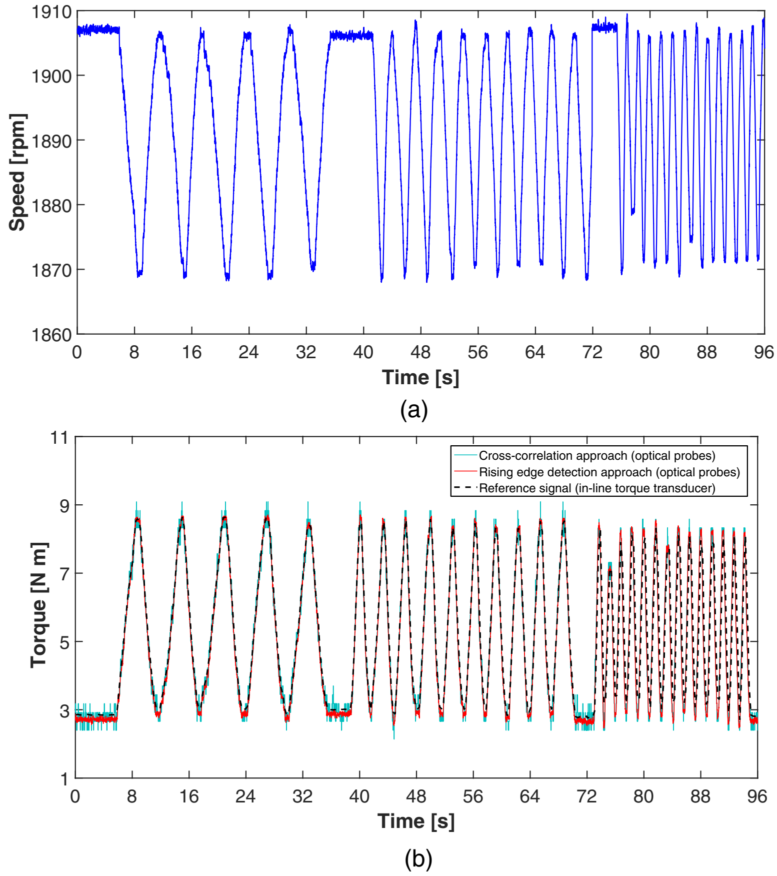

Figure 20. Optical system speed (a) and torque (b) measurements under torque varying at three different frequencies (0.17 Hz, 0.30 Hz and 0.63 Hz).

Both the rising edge and cross correlation torque estimations follow the step changes well and without any timing delay. However, as already noted, the outputs are noisier, especially when the cross-correlation approach is applied. Low pass filtering would reduce this noise without affecting torque meter response in the band of frequencies of interest for mechanical torque measurements.

Additional variable torque and speed tests have been performed by applying a harmonic input torque at three different frequencies (0.17 Hz, 0.30 Hz and 0.63 Hz) and at a peak-to-peak amplitude of approximately 6 N m (figures 20(a) and (b)), within experimental limitations. Again, the zebra tape torque meter shows a good response under harmonic changes of input torque, even if affected by greater high frequency noise in the case of the cross-correlation approach.

6. Comparison with conventional twist angle measurement methods

Similarly to the conventional twist angle measurement methods [7, 13–15], the time shift between the signals recorded by the two zebra tape torque meter OPs is a function of the twist of the shaft due to the applied torque. However, the non-intrusive system presented in this paper has the significant advantages of using less-intrusive, cheaper, easier and quicker to install equipment, making it suitable for a larger range of industrial applications, even in confined, challenging or sensitive operating environments, without any significant impact on shaft design and mechanical integrity. In addition to torque measurement, the zebra tape torque meter provides the shaft rotational speed, which allows the measurement of the mechanical power transmitted by the shaft. This results in a reduction in the number of sensors in the system and hence saving in space, weight and complexity, which is particularly important for many industrial applications, such as in the naval and wind energy sectors. The measurement system is reliable, robust and straightforward to use. The zebra tapes can be designed to be fitted or retrofitted on any shaft diameter and material, while all the electronic components remain on the static part of the system, making the system compatible with harsh and polluted environments. High measurement accuracy and resolution can be achieved by accurately designing the width of the zebra tape black and white stripes to suit the particular application. Thanks to the easy glue-on installation of the zebra tapes, the measurement system can be moved to other similar installations easily in a very short amount of time. This is ideal when torque monitoring forms part of the final check-out of multiple machines. By simply modifying the separation distance of the two zebra tapes along the shaft, when its length allows, different measurement sensitivities can be achieved according to the field application requirements. This would generally result in sensitivities higher than conventional optical torque measurement systems.

7. Conclusions

This paper presents a non-intrusive technique for shaft speed and torque measurement consisting of a set of two zebra tapes and OPs, one at each end of the shaft. The method has been experimentally implemented and validated under both static and variable conditions. The following specific conclusions arise:

- As the shaft rotates, each optical sensor generates a pulse train signal proportional to the light intensity reflected by the zebra tape stripes. Shaft rotational speed has been calculated by measuring the times at which the rising edges of the pulse trains occur.
- Torque has been estimated by measuring the angle of twist from the pulse train time shift measurements through the application of rising edge detection and cross-correlation approaches.
- The contactless, optical torque measurement system performance has been demonstrated by comparing the results from both approaches against reference measurements from an in-line torque transducer mounted on the test bench shaft.
- Experimental measurements under steady state conditions, performed to calibrate the contactless system, show a linear relationship between torque and twist, in perfect agreement with theoretical predictions.
- Uncertainty has been estimated according to the ISO GUM. Type A analysis of experimental data has provided an expanded uncertainty relative to the system full-scale torque, of $\pm 0.30\%$ for the rising edge approach and $\pm 0.86\%$ for the cross-correlation approach. Statistical variations of the parameters affecting system performance under real-world operating conditions have been simulated through the Monte Carlo method providing, in the worst case, an estimation of the system expanded uncertainty of $\pm 1.19\%$.
- The higher uncertainty associated with the cross-correlation method is shown to be due to the combined effect of its higher sensitivity to the pulse shape and to the position of its centre. Low pass digital filtering would reduce the noise associated with the cross-correlation approach without affecting the torque meter response.
- The rising edge and the cross-correlation torque measurements correlate closely with the in-line transducer measurements under both steady state and variable test conditions, although showing a higher level of noise.
- Unlike conventional in-line torque transducers and the conventional strain gauge technique, the proposed zebra tape torque meter does not require costly embedded sensors, electronics or wires on the rotating shaft. Comparing with conventional twist angle measurement methods, the proposed methodology is less intrusive, simpler and cheaper to implement, making it suitable to a larger variety of engineering applications. Measurement accuracy and resolution can be easily adapted to the field application requirements by carefully designing the zebra tapes and their separation along the shaft.

Acknowledgments

This work was funded as part of the UK EPSRC SUPERGEN Wind Hub, EP/L014106/1. The data presented in this paper are available from the Durham Research Online Data Depository at https://doi.org/10.15128/r1v979v306n.

ORCID iDs

D Zappalá https://orcid.org/0000-0002-8283-5102
C J Crabtree https://orcid.org/0000-0003-0109-5323
N Paone https://orcid.org/0000-0002-1228-8967

References

[1] van Millingen R D and van Millingen J D 1991 Phase shift torquemeters for gas turbine development and monitoring *Proc. ASME Int. Gas Turbine and Aeroengine Congress and Exposition (Orlando, FL, 3–6 June)* vol 5 (https://doi.org/10.1115/91-GT-189)

[2] Petek J and Hamilton P 2005 Performance monitoring for gas turbines *Orbit* **25** 65–74

[3] Vath A and Grimm S 2015 Reliability and energy yield increase of wind turbines as a benefit of dynamic load reduction operation *Proc. Scientific Track of the European Wind Energy Association Conf. (Paris, France, 17–20 November 2015)*

[4] Hackl C M and Schechner K 2016 Non-ideal feedforward torque control of wind turbines: impacts on annual energy production & gross earnings *J. Phys.: Conf. Ser.* **753** 1–10

[5] Soong W and Ertugrul N 2002 Field-weakening performance of interior permanent-magnet motors *IEEE Trans. Ind. Appl.* **38** 1251–8

[6] Boyer F, Porez M and Khalil W 2006 Macro-continuous computed torque algorithm for a three-dimensional eel-like robot *IEEE Trans. Robot.* **22** 763–75

[7] Austin C and Rojon I 2014 *Ship Performance Management* (Windsor: Fathom)

[8] Fleming W J 1982 Automotive torque measurement: a summary of seven different methods *IEEE Trans. Veh. Technol.* **3** 117–24

[9] Guy B 2015 Measurement and traceability of torque on large mechanical drives *Proc. AMA Conf.—SENSOR 2015 and IRS2 2015 (Nuremberg, Germany, 19–21 May 2015)* pp 44–5

[10] Cichowicz J, Gerasimos T and Dracos V 2015 Dynamic energy modelling for ship life-cycle performance assessment *Ocean Eng.* **110** 49–61

[11] Nazar Ul Islam M, Cheng P and Oelmann B 2016 Method of torque measurement based on volumetric strain *Proc. SICE Annual Conf. (Tsukuba, Japan, 20–23 September 2016)* pp 116–23

[12] Lee K-E, Kim J-W, Kim C-Y and Ahn S-H 2009 Development of micro torque measurement device using strain gauge *Proc. IEEE Int. Symp. on Assembly and Manufacturing, ISAM 2009 (Suwon, Korea, 17–20 November 2009)* pp 101–6

[13] de Silva C W 2015 *Sensors and Actuators: Engineering System Instrumentation* 2nd edn (Boca Raton, FL: CRC Press)
[14] Shams S, Lee J Y and Han C 2012 Compact and lightweight optical torque sensor for robots with increased range *Sensors Actuators* A **173** 81–9
[15] Hazelden R J 1993 Optical torque sensor for automotive steering systems *Sensors Actuators* A **37–8** 193–7
[16] Wilmshurst T H, Rothberg S J and Halliwell N A 1991 Laser torquemeter: a new instrument *Electron. Lett.* **27** 186–7
[17] Tullis I D C, Halliwell N A and Rothberg S J 1996 Laser torquemeter: effects of axial shaft vibration *Proc. SPIE* **2868** 449–57
[18] Tullis I D C, Halliwell N A and Rothberg S J 1998 Shaft tilt sensitivity of the laser torquemeter *Proc. SPIE* **3411** 309–16
[19] Garinei A and Marsili R 2017 Development of a non-contact torque transducer based on the laser speckle contrast method *J. Sensors Sensor Syst.* **6** 253–8
[20] Hajdu F and Horváth P 2012 Contactless torque sensor development *Acta Tech. J.* **5** 115–20
[21] Angleviel D, Frachon D and Masson G 2006 Development of a contactless hall effect torque sensor for electric power steering *Proc. SAE 2006 Automotive Dynamics Stability and Controls Conf. and Exhibition (Novi, Michigan, 14–16 February 2006)* (https://doi.org/10.4271/2006-01-0939)
[22] Seidlitz S, Kuether R J and Allen M S 2016 Experimental approach to compare noise floors of various torsional vibration sensors *Exp. Tech.* **40** 661–75
[23] Janssens K, Van Vlierberghe P, D'Hondt P, Martens T, Peeters B and Claes W 2011 Zebra tape butt joint algorithm for torsional vibrations *Structural Dynamics* (*Conf. Proc. of the Society for Experimental Mechanics Series* vol 3) ed T Proulx (New York: Springer) (https://doi.org/10.1007/978-1-4419-9834-7_19)
[24] Friswel M I, Penny J E T, Garvey S D and Lees A W 2010 *Dynamics of Rotating Machines* (Cambridge: Cambridge University Press) (https://doi.org/10.1017/CBO9780511780509)
[25] Sue P, Wilson D, Farr L and Kretschmar A 2012 High precision torque measurement on a rotating load coupling for power generation operations *Proc. IEEE Int. Instrumentation and Measurement Technology Conf. (I2MTC) (Graz, Austria, 13–16 May 2012)* pp 518–23
[26] Janssens K and Britte L 2014 Comparison of torsional vibration measurement techniques *Advances in Condition Monitoring of Machinery in Non-Stationary Operations* eds G Dalpiaz *et al* (Berlin: Springer) pp 453–63
[27] Vishay Application of optical reflex sensors document number 80107, 02-02 (www.vishay.com/docs/80107/80107.pdf) (Last Accessed: 18 May 2017)
[28] Oppenheim A V, Schafer R W and Buck J R 1999 *Discrete-Time Signal Processing* (Upper Saddler River, NJ: Prentice Hall)
[29] ISO/IEC 2008 *Guide 98-3:2008 Uncertainty of Measurement—Part 3: Guide to the Expression of Uncertainty in Measurement (GUM:1995)* (International Organisation for Standardization)
[30] ISO/IEC 2008 *Guide 98-3:2008/Suppl.1:2008 Uncertainty of Measurement—Part 3: Guide to the Expression of Uncertainty in Measurement (GUM:1995)—Supplement 1: Propagation of Distributions using a Monte Carlo Method* (International Organisation for Standardization)
[31] UNI EN ISO 286-1 2010 *Geometrical Product Specifications (GPS)-ISO Code System for Tolerances on Linear Sizes—Part 1: Basis of Tolerances, Deviations and Fits* (International Organisation for Standardization)

IET Power Electronics

Special Section: Selected papers from the 8th International Conference on Power Electronics, Machines and Drives (PEMD 2016)

Impact of wind conditions on thermal loading of PMSG wind turbine power converters

ISSN 1755-4535
Received on 7th October 2016
Revised 12th April 2017
Accepted on 24th May 2017
E-First on 10th July 2017
doi: 10.1049/iet-pel.2016.0802
www.ietdl.org

Christopher J. Smith[1], Christopher J. Crabtree[1] ✉, Peter C. Matthews[1]
[1]*School of Engineering and Computing Sciences, Durham University, South Road, Durham, UK*
✉ *E-mail: c.j.crabtree@durham.ac.uk*

Abstract: Power converter reliability is critical for permanent magnet synchronous generator (PMSG) wind turbines. Converter failures are linked to power module thermal loading but studies often neglect turbine dynamics, control and the impact of wind speed sampling rate on lifetime estimation. This study addresses this using a 2 MW direct-drive PMSG wind turbine model with a two-level converter, and simulating junction temperatures (T_j) using a power module thermal equivalent circuit under various synthetic wind speed conditions. These synthetic wind conditions include constant and square wave profiles representing stable and gusty wind conditions. Responses to square wave wind speeds showed that the lower the gust frequency, the higher ΔT_j becomes, demonstrating that low turbulence sites have greater thermal variation in the converter. In contrast, wind speed variations with frequencies >0.25 Hz deliver only small increases in ΔT_j. It is concluded that reasonable approximations of T_j profiles can be made with 0.25 Hz wind speed data, but that lower data rate wind measurements miss essential, damaging characteristics.

1 Introduction

To meet EU renewable energy targets for 2020 and beyond, the levelised cost of energy (LCoE) of offshore wind must be reduced to below £100/MWh [1]. Operation and maintenance (O&M) accounts for ∼30% of the LCoE [2]. A key aspect of O&M is turbine sub-system reliability. By understanding which components have the greatest impact on downtime and power production, O&M resources can be focused to minimise turbine disruption and reduce the LCoE of offshore wind.

1.1 Wind turbine power converter reliability

Numerous studies have explored the reliability of wind turbine sub-systems using operational data. Carroll *et al.* [3] examined a large dataset for offshore wind turbines with mixed turbine technology to determine the main causes of failure and concluded that power converters had a typical failure rate of ∼0.2 failures/turbine/year, much lower than the highest failure rate of > 1 failure/turbine/year for pitch systems. However, a more focused study on turbine type [4] found that the failure rate of fully-rated converters (FRC) in permanent magnet synchronous generator (PMSG) turbines was 0.593 failures/turbine/year compared with 0.106 failures/turbine/year for partially-rated converters in doubly fed induction generator turbines. This suggests that the unique operating conditions of PMSG-FRCs are causing higher failure rates. Furthermore, Spring *et al.* [5] examined large wind turbine datasets and used expert knowledge to determine the impact of component failure to turbine downtime, compiling a top 30 list of failure sources. It was concluded that power converters were the highest source of turbine downtime, with their failure modes occupying the top 15 positions. Converter reliability must, therefore, be examined with a focus on the FRC in PMSG turbines.

Of the failures outlined in [4], power module failure is the failure mode for nearly all major converter repairs. Traditionally, power module failure has been linked to power module thermal loading, where the variation of temperature in the insulated gate bipolar transistors (IGBT) and diode cases causes fatigue through expansion and contraction between package layers (Fig. 1*a*). The temperature used for reference is the virtual junction temperature, ($\Delta T_{j,\mathrm{IGBT}}$, $\Delta T_{j,\mathrm{diode}}$), which is a virtual representation of the chip p–n junction temperature (Fig. 1*b*).

1.2 Power converter reliability studies

This approach has been applied in a number of studies to explore the expected reliability of power converters in wind turbines [7–16]. However, these studies often have limitations. Some studies neglect the impact of wind turbine dynamics and control, so wind speed inputs are directly converted into a T_j [7–9], which will deviate significantly from the true T_j profile in the converter. The use of wind speed distributions [8, 10] and large time steps, e.g. 3-hourly [11] neglects the impact of wind speed history, which has been shown to have a large impact on the current loading, and subsequently, the thermal loading of the converter [17]. For example, the use of supervisory control and advisory data acquisition (SCADA) data may only provide a mean and maximum wind speed over a 10 min period, which may hide a large amount of variation that is causing damage to the converter.

Some studies have included both realistic wind speed profiles and drive train models [12–15]. However, only two have studied a PMSG wind turbine [14, 15], and these two studies disagree whether high-frequency wind speed events impact the thermal loading of the converter significantly. There is therefore a need for a detailed study into the impact of operating conditions on power converter reliability to help inform how the turbine should be operated in order to extend its life and reduce the LCoE.

1.3 Research contributions

These limitations mean that operational profiles and failure data may not be representative of converter operation in the field, and there is no consensus on the required wind speed data frequency for accurate thermal simulation. This paper addresses these limitations by identifying the temporal fidelity over which wind events (such as gusts) cause the highest thermal variation. The minimum wind speed sampling frequency that will still provide accurate thermal profile simulation can then be determined. The impact of modelling assumptions on the estimated T_j profiles is also explored. These results will provide guidance for future simulation and experimental studies to improve converter reliability analysis accuracy, with an aim of improving best practice in both academia and industry.

To simulate these thermal loading profiles, a drive train model (Section 2.1), power loss model (Section 2.2), thermal model

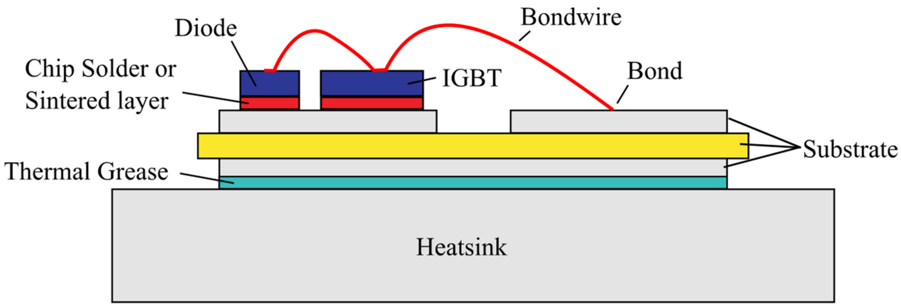

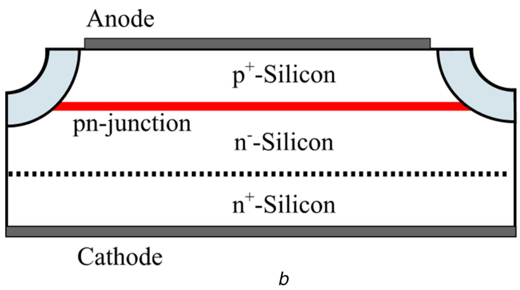

Fig. 1 *Chip layout and packaging for typical power module devices. Figures adapted from [6]*
(a) Typical IGBT power module packaging with no base plate. Areas of fatigue include the bondwire, the bondwire bonds, and the chip solder/sintered layer, ***(b)*** Internal structure of a typical p–n diode chip showing the location of the p–n junction used as the virtual reference point for $T_{\text{j,diode}}$

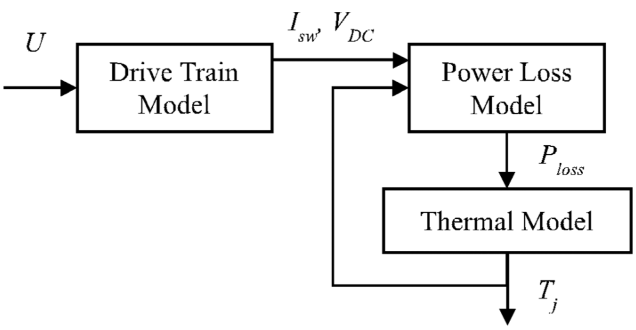

Fig. 2 *Summary of drive train and converter thermal model*

(Section 2.3), and wind inputs (Section 2.4) are required. The impacts of temporal fidelity and modelling assumptions were explored through an analysis of individual T_{j} cycles (Section 3.1), comparison of constant wind speed results with a comparable study (Sections 3.2 and 3.3) and analysis of the converter response to synthetic wind speed time series (WSTS) (Section 3.4). A summary of the main findings is given in Section 4.

2 Approach

First, an approach to identifying the thermal loading of a wind turbine power converter was developed as follows:

- Modelling of a wind turbine drive train to provide the current throughput of the converter.
- Modelling of the resultant power losses in the converter due to the current throughput.
- Modelling the power module thermal processes in response to the power losses.
- Simulation of power module thermal response to selected wind speed inputs.

Fig. 2 illustrates the full-system model. U is the incoming wind speed, I_{sw} is the converter switch current, V_{DC} is the DC link voltage, and P_{loss} is the power module device switching losses.

This section outlines the details of each of the sub-systems.

2.1 Drive train model

The drive train model developed for this work was a 2 MW FRC-PMSG, direct-drive turbine. The model was split into five sub-systems: rotor power extraction, drive train dynamics, generator, machine-side converter (MSC), and turbine control. Fig. 3 provides a summary of the drive train model. T_{t} is the turbine torque extracted from the wind, T_{m} is the mechanical torque resulting from the shaft stiffness and damping, T_{g} is the electromagnetic torque, ω_{t} is the turbine rotational speed, ω_{g} is the generator rotational speed, β is the pitch angle, β_{ref} is the reference pitch angle, I_{abc} is the generator output current, $V_{\text{t},abc}$ is the generator terminal voltage applied by the MSC, and $V_{\text{ref},abc}$ is the reference MSC output voltages.

This section outlines the core aspects of each sub-system. Detailed descriptions can be found in [17, 18].

2.1.1 Turbine power extraction:

T_{t} from the wind is calculated using the following equation:

$$T_{\text{t}} = \frac{0.5 C_{\text{p}} \rho \pi r^2 U^3}{\omega_{\text{t}}} \tag{1}$$

C_{p} is the power coefficient, ρ is air density, and r is the turbine radius.

C_{p} depends on the tip speed ratio (λ) and β. The C_{p}, λ, and β relationship is turbine specific but it is typical to use a numerical approximation (2) and (3) [19], with λ calculated using (4)

$$\frac{1}{\lambda_i} = \frac{1}{\lambda + H_{\text{t}}\beta} - \frac{K_{\text{t}}}{\beta^3 + 1} \tag{2}$$

$$C_{\text{p}} = A_{\text{t}}\left(\frac{B_{\text{t}}}{\lambda_i} - C_{\text{t}}\beta - D_{\text{t}}\beta^{E_{\text{t}}} - F_{\text{t}}\right)\text{e}^{(-G_{\text{t}}/\lambda_i)} \tag{3}$$

$$\lambda = \frac{\omega_{\text{t}} r}{U} \tag{4}$$

A_{t} to F_{t} and K_{t} are turbine specific constants. The values used can be found in the Appendix.

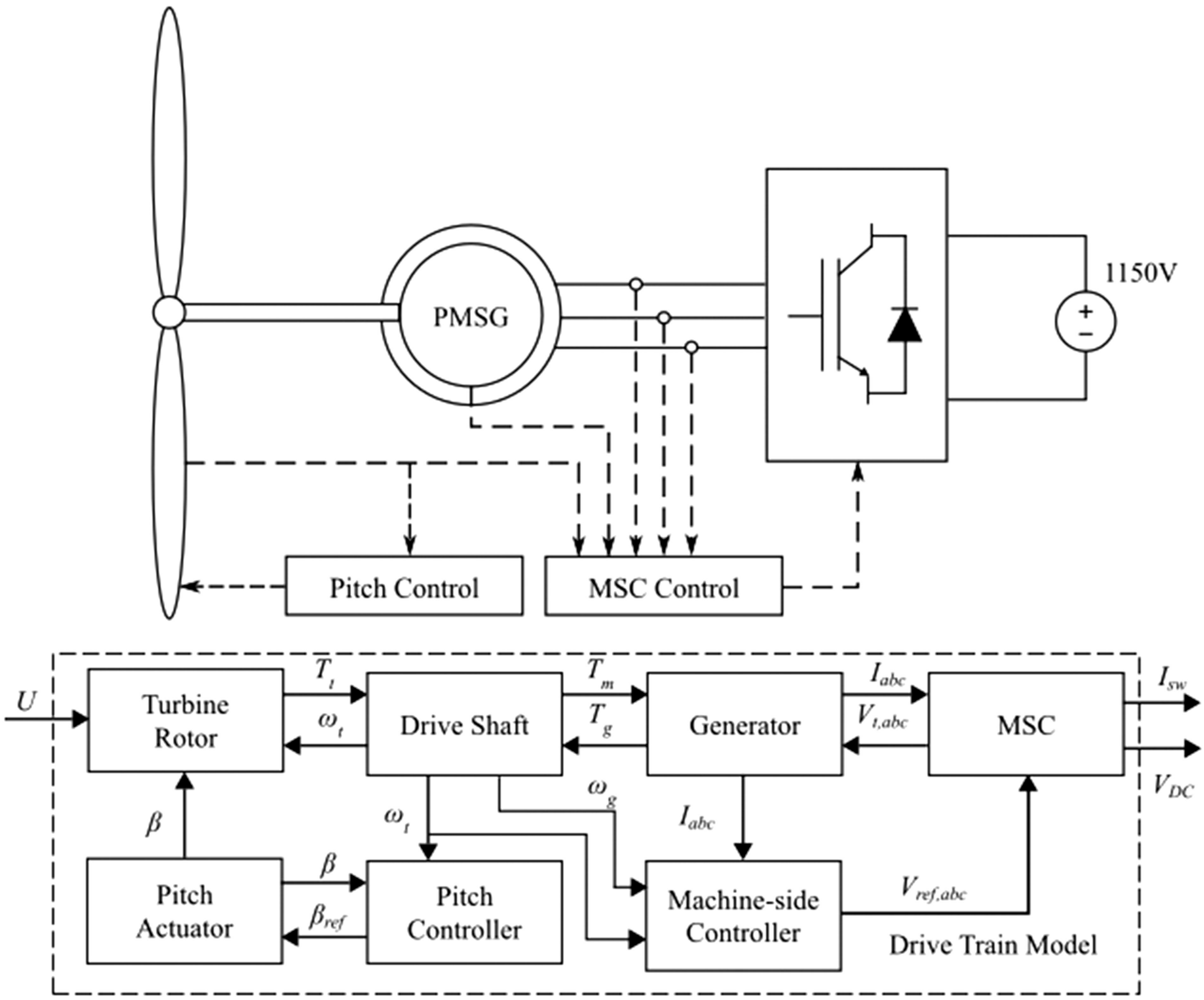

Fig. 3 *Drive train model summary*

2.1.2 Drive train dynamics: T_t is applied to the drive shaft. The drive train can be modelled as a mechanical mass-spring-damper system which dynamically impacts the T_m applied to the generator.

The drive train was modelled as a two-mass system, rather than a lumped-mass system, to include the dynamic effects of shaft stiffness and damping. The two-mass system is defined by the following equation [20]:

$$\begin{bmatrix} J_t & 0 \\ 0 & J_g \end{bmatrix} \begin{Bmatrix} \alpha_t \\ \alpha_g \end{Bmatrix} + \begin{bmatrix} C_d & -C_d \\ -C_d & C_d \end{bmatrix} \begin{Bmatrix} \omega_t \\ \omega_g \end{Bmatrix} + \begin{bmatrix} K & -K \\ K & -K \end{bmatrix} \begin{Bmatrix} \theta_t \\ \theta_g \end{Bmatrix} = \begin{Bmatrix} T_t \\ T_g \end{Bmatrix} \quad (5)$$

J_t, J_g are the moments of inertia of the turbine and generator, respectively, θ_t, θ_g are the rotational displacements of the turbine and generator, respectively, C_d is the shaft damping coefficient, K is the shaft stiffness, and α_t, α_g are the rotational accelerations of the turbine and generator, respectively. The expanded matrix can be solved numerically, with T_m calculated using the following equation:

$$T_m = (\omega_t - \omega_g)C_d + (\theta_t - \theta_g)K \quad (6)$$

2.1.3 Generator: The generator model used is a second-order non-salient PMSG in the $dq0$ reference frame [21] with a current rating of 1868 A_{rms}. The mechanical component was modelled with the torque swing equation. The generator parameters can be found in the Appendix.

2.1.4 MSC: In a typical wind turbine, the converter is comprised of an MSC and grid-side converter (GSC). The role of the MSC and GSC differs depending on control strategy but the MSC typically controls the speed of the wind turbine for optimum power production whilst the GSC controls power export to maintain the DC-link voltage.

Due to the turbine's variable speed operation for maximum power extraction, the MSC experiences a more varied operating profile compared with the GSC, which operates at fixed frequency. The MSC is consequently of greater interest for reliability analysis. Here, only the MSC is modelled while the GSC is replaced with a constant voltage source of 1150 V_{DC} (± 575 V_{DC}).

The MSC parameters were based on the power modules found in the SEMIKRON SKSB2100GD69/11-MAPB stacks [22]. These stacks have a maximum DC voltage of 1200 V and a maximum current of 1000 A_{rms}. The stacks use SKiiP2013GB172-4DWV3 half-bridge integrated power modules [23].

The voltage output of the MSC is determined by $V_{abc,\mathrm{ref}}$ from the machine-side controller (Section 2.1.5). Pulse width modulation (PWM) converts the modulated $V_{abc,\mathrm{ref}}$ (V_m) into a switching pattern for the IGBTs in order to produce the three-phase converter output voltage ($V_{c,abc}$). Space vector PWM was chosen and therefore V_m was calculated using the following equation:

$$V_m = \frac{\sqrt{3}}{V_{DC}} V_{abc,\mathrm{ref}} \quad (7)$$

The current through the devices is split between diode and IGBT depending on the current polarity. Since two parallel stacks are required to reach the current rating of the turbine (Section 2.1.3), this current is split equally between stacks [24].

2.1.5 Turbine control: Power extraction is controlled in two ways depending on operating region. Maximum power point tracking (MPPT) is used for below rated speed, while active pitch control is used above rated speed to limit power.

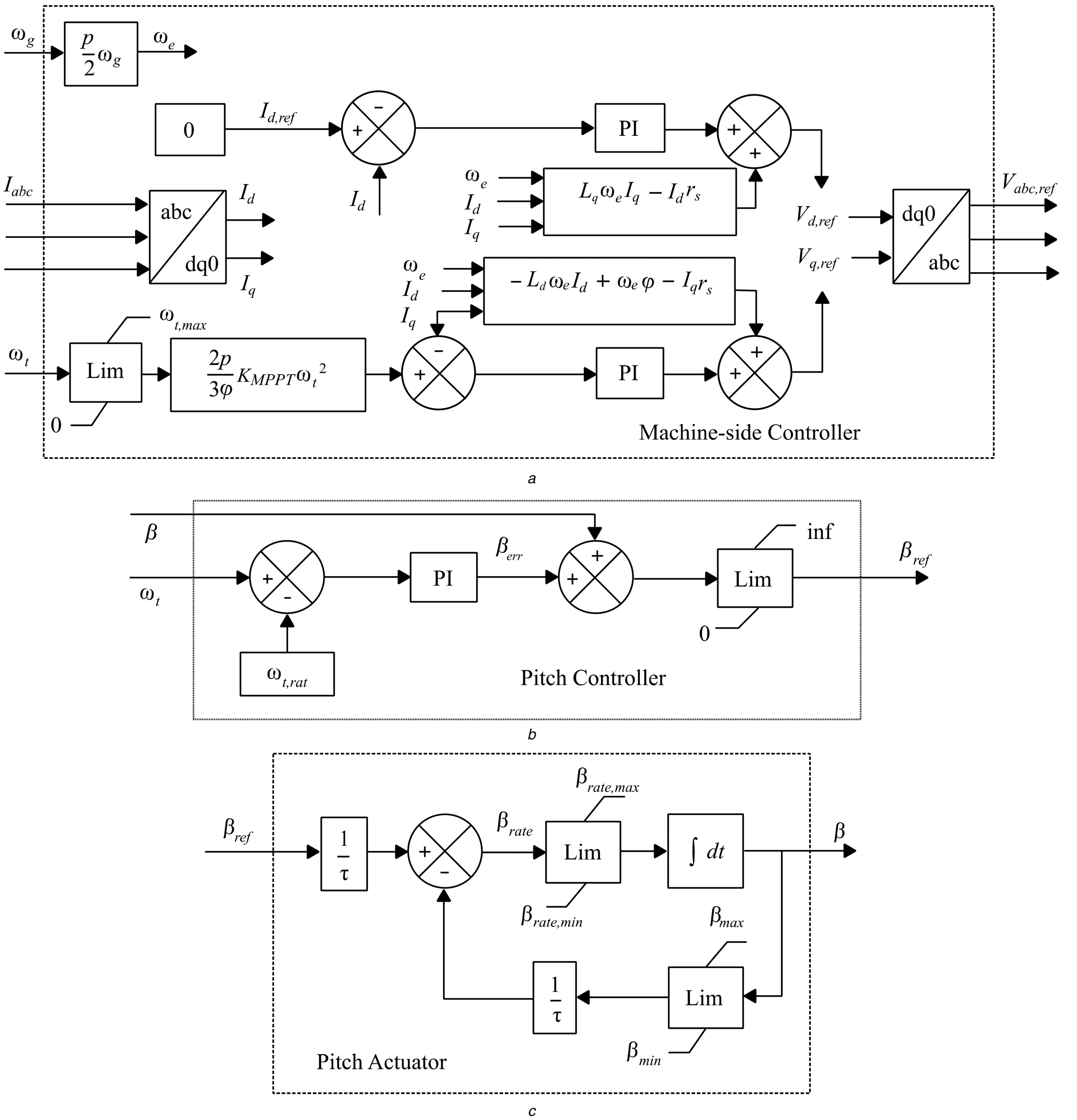

Fig. 4 *Schematics of*
(a) Machine side controller, ***(b)*** Pitch controller, ***(c)*** Pitch actuator

For MPPT, C_p must be maximised ($C_{p,\max}$). By controlling ω_t, the optimum λ can be maintained (λ_{opt}) when below rated wind speed

$$\omega_{t,\,\text{opt}(u)} = \frac{U\lambda_{\text{opt}}}{r} \tag{8}$$

$\omega_{t,\text{opt}(u)}$ is the optimum turbine rotational speed at a given wind speed.

As U is not measured in this control strategy, $\omega_{t,\text{opt}}$ is unknown. Instead ω_t is varied until the turbine reaches steady state, which occurs when $\omega_{t} = \omega_{t,\text{opt}}$. ω_t is varied via T_g, which is carried out using direct-quadrature-zero current (I_{dq0}) control applied to the MSC. Fig. 4*a* illustrates the machine-side control algorithm. $V_{d,q}$ are the *d,q* reference frame voltages, $V_{d,q,\text{ref}}$ are the required *d,q* terminal voltages, $I_{d,q,\text{ref}}$ are the reference $I_{d,q}$, r_s is the PMSG stator phase resistance, $L_{d,q}$ are the PMSG *d,q* armature inductances, φ is the permanent magnet flux linkage, K_{MPPT} is a turbine specific constant, $\omega_{t,\max}$ is the maximum turbine rotational speed considered by the controller, and ω_e is the magnetic field rotational speed, which is related to ω_g via the generator pole pairs.

To determine the required generator currents, ω_t is related to the required T_g (T_{ref}) via the turbine power curve using a turbine specific constant K_{MPPT} (9) and (10). The reference I_q is calculated using a known relationship between I_q and T_g in the generator (11). I_d is maintained at 0 A [25]. These currents are achieved by applying a controlled voltage on the generator terminals using the MSC

$$T_{\text{ref}} = K_{\text{MPPT}}\omega_t^2 \tag{9}$$

$$K_{\mathrm{MPPT}} = 0.5C_{p,\max}\rho\pi r^2\left(\frac{r}{\lambda_{\mathrm{opt}}}\right)^3 \tag{10}$$

$$I_{q,\mathrm{ref}} = \frac{2p}{3\varphi}T_{\mathrm{ref}} \tag{11}$$

To note, the machine-side controller is not constrained by the rated turbine rotational speed ($\omega_{\mathrm{t,rat}}$) but by a higher maximum ($\omega_{\mathrm{t,max}}$). This allows the machine-side controller to deal with sudden increases in wind speed for which the pitch controller is too slow to respond effectively. This provides a similar controller interaction to [26].

Pitch control limits power extraction when above rated wind speed by pitching the blades away from the optimum angle, reducing the turbine's C_{p}.

There are a number of pitch control methods available [27]. For this work, the difference in ω_{t} and rated ω_{t} ($\omega_{\mathrm{t,rat}}$) is used to produce a β error (β_{err}) (Fig. 4*b*). β_{err} is added to the current β to produce a reference β (β_{ref}) and applied to the pitch actuator (Fig. 4*c*). The pitch actuator is modelled as a first-order dynamic system [28] with limits on β and the rate of change of β (β_{rate}). These values can be found in the Appendix.

2.1.6 Drive train model summary: The drive train model consists of the following key features:

- Modelled as a direct-drive 2 MW PMSG wind turbine to align with modern turbine technology with sufficient data for modelling.
- Mechanical drive train modelled as a two-mass model to capture the critical dynamics of a wind turbine drive train.
- FRC with MSC based on SEMIKRON Renewable Energy stacks to provide realistic converter parameters.
- GSC modelled as an ideal DC link to isolate impacts of wind on the MSC.
- Turbine controlled using ω_{t} as the reference signal, with both MPPT and active pitch control as in the majority of modern wind turbines.

2.2 Converter power loss model

To convert the current throughput into T_{j} profiles, power losses must be calculated, specifically:

- The IGBT and diode conduction losses.
- The IGBT switching losses and diode reverse recovery (RR) losses.

The conduction and switching losses are summed for each device. The power loss model used is based on [29, 30].

2.2.1 Conduction losses: Conduction losses depend on device internal resistance so are calculated using the device voltage and current

$$P_{\mathrm{C,IGBT}} = V_{\mathrm{ce}}\, I_{\mathrm{c}} \tag{12}$$

$$P_{\mathrm{C,diode}} = V_{\mathrm{f}}\, I_{\mathrm{f}} \tag{13}$$

$P_{\mathrm{C,IGBT}}$ and $P_{\mathrm{C,diode}}$ are the IGBT and diode conduction losses, respectively, V_{ce} is the IGBT collector–emitter voltage, V_{f} is the diode forward voltage, I_{c} is the IGBT collector current, and I_{f} is the diode forward current.

I_{c} and I_{f} are the input currents. V_{ce} and V_{f} are functions of I_{c} and I_{f}, respectively, and the device T_{j}. The functions are given in the manufacturer's data sheet [23] for a T_{j} of 25 and 125°C. V_{ce} and V_{f} are calculated by interpolating between the values given at these reference temperatures.

2.2.2 Switching/RR losses: Switching and RR losses occur when there is a change in direction of voltage and current. Device response is not instantaneous but occurs over nanoseconds [29]. Nanosecond simulation is impractical for run times longer than a few seconds and the energy loss information given in manufacturer's datasheets is not detailed enough for accurate temporal loss simulation. For example, the energy loss during switch on (E_{on}) and switch off (E_{off}) are not given separately, but reported as a summation of the two ($E_{\mathrm{on+off}}$) [23]. As such, a simplified approach has to be taken.

It has been assumed that the energy loss is given by the conditions at the first low-high (L-H) switching instance. The energy is modulated over the switching cycle (between L-H and the next L-H) to provide a constant switching power loss. This was deemed acceptable as the device thermal time constants (µs-ms) will dominate the thermal profile [29].

With the above assumptions, the switching/RR losses were found by

(i) Determining the energy losses at L-H switching events. The switching/RR energy loss is given as a function of input current at two reference V_{DC} [23] and is assumed to be linear. The IGBT energy loss is $E_{\mathrm{on+off}}$, whilst the diode energy loss is twice the reverse energy loss (E_{rr}).

(ii) Calculating the equivalent modulated power losses over the switching cycle using the following equations [30]:

$$P_{\mathrm{sw}}\big(t{:}T_{\mathrm{s,th}}{:}(t + T_{\mathrm{p,sw}}(t))\big) = \frac{E_{\mathrm{on+off}}(t)}{T_{\mathrm{p,sw}}(t)} \tag{14}$$

$$P_{\mathrm{rr}}\big(t{:}T_{\mathrm{s,th}}{:}(t + T_{\mathrm{p,rr}}(t))\big) = \frac{E_{\mathrm{rr}}(t)}{T_{\mathrm{p,rr}}(t)} \tag{15}$$

$$P_{\mathrm{sw},T_{\mathrm{j}}}(t) = \big(1 + TC_{E\mathrm{sw}}\big(T_{\mathrm{j,IGBT}}(t) - T_{\mathrm{ref}}\big)\big)\,P_{\mathrm{sw}}(t) \tag{16}$$

$$P_{\mathrm{rr},T_{\mathrm{j}}}(t) = \big(1 + TC_{E\mathrm{rr}}\big(T_{\mathrm{j,diode}}(t) - T_{\mathrm{ref}}\big)\big)\,P_{\mathrm{rr}}(t) \tag{17}$$

P_{sw} is the IGBT switching power loss, P_{rr} is the diode RR power loss, t is the time step, $T_{\mathrm{s,th}}$ is the thermal sampling time, $T_{\mathrm{p,sw}}$ is the IGBT switching time period, $T_{\mathrm{p,rr}}$ is the diode RR time period, $P_{\mathrm{sw},Tj}$, $P_{\mathrm{rr},Tj}$ are the T_{j} corrected P_{sw} and P_{rr}, respectively, $\mathrm{TC}_{E\mathrm{sw}}$, $\mathrm{TC}_{E\mathrm{rr}}$ are the switching loss and RR temperature coefficients, respectively, and T_{ref} is the reference temperature of the energy loss look-up tables (LUTs).

2.3 Thermal loss model

Converter thermal modelling can be carried out in three ways:

- Thermal equivalent circuits using resistor–capacitor (RC) networks [8, 10–12, 14–16].
- Thermal diffusion equations [13].
- Finite-element analysis [7].

As the RC network data was readily available, a common practice approach of thermal equivalent circuit modelling was used.

The data given in [23] is for a Foster RC network. To provide a more accurate half-bridge temperature profile the Foster thermal resistance ($R_{\mathrm{th,f}}$) and time constant (τ) parameters were converted into RC parameters [31], and then converted into Cauer RC parameters to provide a more realistic thermal profile throughout the device [32]. Fig. 5 gives the half-bridge Cauer RC network. The parameters are available in the Appendix.

The power losses (P_{loss}) are dependent on T_{j} and therefore the power loss and thermal sub-systems must be run concurrently. Due to the power-thermal inter-dependency, the initialisation of C_{th} temperatures was solved iteratively. The steady-state temperatures are related to the R_{th} only [30]. Therefore, initial temperatures were set throughout the device, and then the power losses and

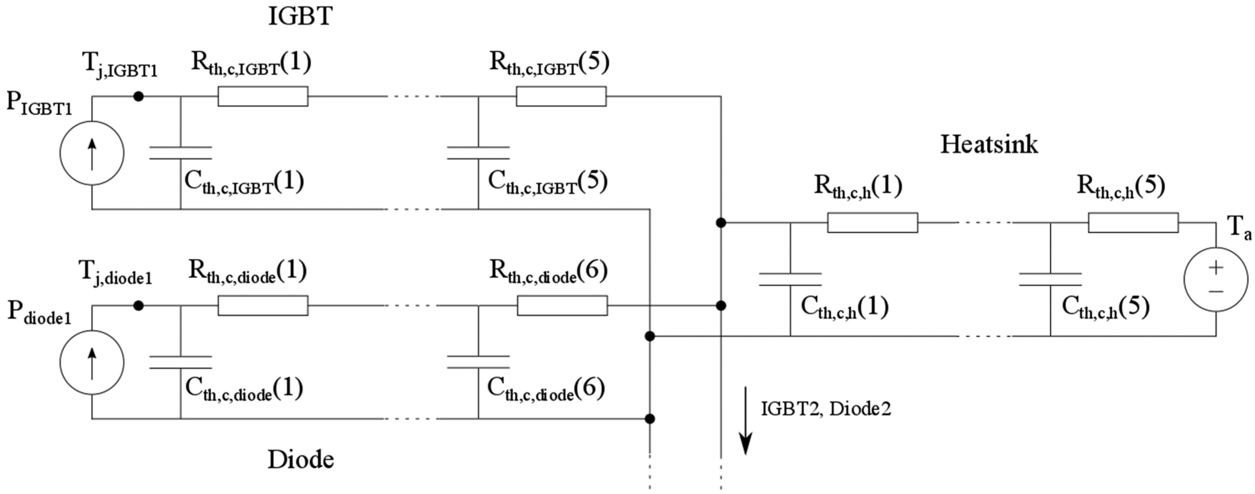

Fig. 5 *Half-bridge Cauer RC network (one IGBT and diode represented). P_{IGBT1} is the IGBT power loss, P_{diode1} is the diode power loss, $R_{th,c}$ is the Cauer thermal resistance, and $C_{th,c}$ is the Cauer thermal capacitance*

temperatures were iteratively updated until steady state was reached.

2.4 Wind speed inputs

Wind speed and converter current throughput are partly decoupled by the drive train inertia and control [17]. As such, it can be challenging to determine which characteristics of a WSTS have the largest impact on thermal loading.

To address this, experiments have been constructed which use synthetic WSTS to isolate potential wind speed characteristics and determine their impact on thermal loading. Square waves have been used to represent sudden changes in wind speed, which was validated against high-frequency wind speed data. The tests are carried out over 65 s, with the first 5 s carried out at constant wind speed to minimise the impact of variations in the input current. For the square wave tests this constant wind speed represents the average power wind speed, which is slightly higher than the average wind speed. The model time step is also much smaller than the test period to ensure it does not influence the results; 5×10^{-6}s for the drive train, and 5×10^{-5}s for the thermal simulation.

2.5 Summary

To summarise, a Simulink model of a wind turbine drive train and power converter thermal network has been constructed. This allows for any wind speed profile to be entered and the corresponding power module thermal profiles be produced.

3 Results and discussion

This section outlines the analysis performed on T_j profiles produced in response to constant and square wave WSTS.

3.1 Individual T_j cycles

The power loss and temperature profiles over individual power cycles were examined. Fig. 6 compares the diode and IGBT current T_j profiles at a constant 12.7 m/s. The T_j profile for the diode (Fig. 6*d*) is comparable with the expected response found in Fig. 5.2.13 in the manufacturer's handbook [30], although it should be noted that the manufacturer's data considers only the average power loss of the switching cycle, rather than individual switching events. This simulation output can show higher frequency temperature variation than revealed in the manufacturer's data.

This higher frequency temperature variation becomes most apparent in the IGBT (Fig. 6*c*), particularly in the first half of the current cycle. This can be attributed to the converter being connected to a PMSG. The PMSG reactance causes the current to be out-of-phase with the voltage, and therefore the switching cycles are not distributed symmetrically over the input current, with a period of low voltage (Fig. 6*a*). The low voltage means the IGBT has a smaller duty cycle. Where there is infrequent current due to a low duty cycle (Fig. 6*a*), T_j varies more (Fig. 6*c*). This effect is not seen in the diode as the current not flowing through the IGBT must pass through the diode, creating a near continuous current throughput (Fig. 6*b*) and therefore a smooth T_j response (Fig. 6*d*).

3.2 Constant wind speeds

Fig. 7 shows the thermal response to constant WSTS for an IGBT and diode with an ambient temperature (T_a) of 40°C [8]. The mean T_j increases non-linearly as wind speed increases due to the cubic relationship between wind speed and power. The ΔT_j also increases due to the higher power loss per cycle, and the ΔT_j frequency increases due to the higher generator rotational speed.

The diode temperatures T_j and ΔT_j (Fig. 7*b*) are consistently higher than the IGBT (Fig. 7*a*). This is due to the higher power losses experienced by the diodes and the higher R_{th} of the diodes. The higher diode R_{th} (K/W) means that for every watt of heat loss, the diode experiences a greater rise in temperature than the IGBT. This is then coupled with the greater power losses due to the more continuous current flow through the diode (Section 3.1), causing the higher T_j and ΔT_j. This was also found for the MSC devices in [14] and suggests that the diode is more vulnerable to thermal cycling, with both higher mean T_j and ΔT_j.

3.3 Study comparison

The results in Figs. 7*a* and *b* were compared with the 1.55 MW turbine in [14] (Fig. 7*c*); it is assumed the scaled power ratings would have limited impact on the thermal loading as the converter rating would also be scaled, leading to comparable T_j profiles for a given wind speed. However, whilst it was found that the ΔT_j for both IGBTs and diodes was comparable at a given wind speed, the mean T_j for a given wind speed was higher in this study than in [14], despite T_a being 10°C lower. This is in part is due to the lack of R_{th} value for the heatsink in [14]. At steady-state conditions this will create a higher case temperature (T_c) and therefore higher mean T_j. The mean T_j change from 12 to 8.5 m/s is also much lower in [14]. This suggests that the MSC in this work is more susceptible to T_j rises due to the higher R_{th} values in the devices. This highlights three key conclusions that must be made.

- The ΔT_j magnitude for IGBT and diodes is consistent with those found in [14], but there is greater variation in mean T_j between wind speeds in this study.
- The value of T_a can have a large impact on the mean T_j value.

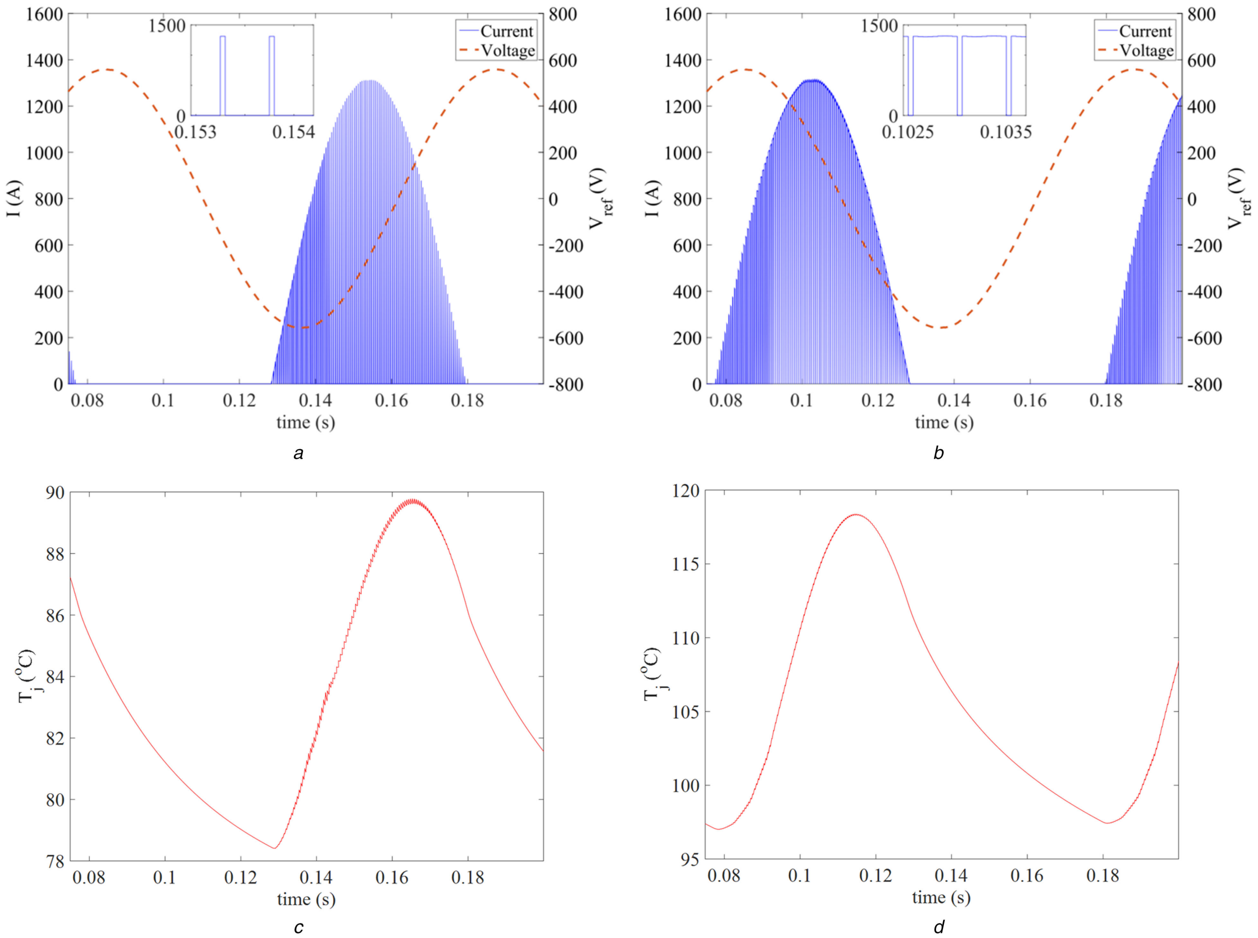

Fig. 6 *Cycle view of*
(a) IGBT current with the current waveform peak magnified, ***(b)*** Diode current with the current waveform peak magnified, ***(c)*** IGBT T_j, ***(d)*** Diode T_j at a constant 12.7 m/s

- The inclusion of the heatsink thermal parameters in the model causes a significant increase in the mean T_j.

3.4 Response to varying wind speed input

The T_j response of the power module to a range of square wave WSTS is detailed to understand what might be masked by using SCADA data in lifetime/temperature swing calculations. For comparison, the maximum T_j swing over the simulation period (max ΔT_j) have been plotted for square gust amplitudes of 1 and 2 m/s, for varying frequencies and mean wind speeds, for both IGBT and diode (Fig. 8).

In general, the higher the frequency of wind speed variation, the lower ΔT_j becomes. This is as the turbine inertia acts as a low-pass filter, restricting the high-frequency wind speed variation being transmitted as current variation. Indeed, wind speed variations with frequency >0.25 Hz lead to a minimal increase in ΔT_j compared with the constant wind speed case (0 Hz). Therefore, reasonable approximations of T_j profiles can be made (within 1°C) with 0.25 Hz wind speed data. Furthermore, these results imply that lower turbulence wind farm sites, such as offshore, have more damaging thermal profiles in the converter than higher turbulence onshore sites.

There are exceptions to this trend. ΔT_j becomes relatively consistent below 0.03 Hz. This is because the turbine has time to respond to the change of wind speed and reaches its steady operating state. The turbine is then at this steady-state condition long enough for T_j to reach its maximum before the wind speed reduces. Lower frequencies will increase the number of times that the maximum T_j is reached during a particular gust, but will not affect the maximum T_j. The same will also be true for the minimum T_j. Therefore, gust frequencies of 0.03 Hz and below provide the maximum ΔT_j.

These results show that the use of one wind speed data point for a long time period, e.g. 10 min SCADA data, 3 hourly data found in [11], or the use of a wind speed distribution in [8, 10], can mask a large amount of information and will underestimate the T_j variation significantly; in Fig. 8*d* the diode ΔT_j at U_m of 12 m/s increases by up to 71%. Therefore, these results agree with the conclusions in [15] that higher frequency wind speed data is required for accurate T_j profile estimation, and it is suggested that a minimum WSTS frequency of 0.25 Hz is required, though it is recognised that this will not always be available/practical. This, however, would reduce the amount of data required for studies such as in [12–15]. The results at higher U_m also indicate that the unique operating conditions may have a significant effect on the T_j profile experienced by the power converter, and therefore the lack of drive train dynamic modelling in [7–9] will change the T_j profiles significantly.

4 Conclusions

The power converter is reliability critical for FRC-PMSG wind turbines. Converter failures are typically linked to the thermal loading of the power module. This paper models the converter thermal loading when the turbine is subjected to various synthetic WSTS to explore and demonstrate the impact of the frequency of wind speed variation on power converter thermal loading.

The thermal simulation has three main parts: a PMSG drive train model, a converter power loss model based on conduction and switching/RR, and a thermal equivalent circuit model. Both constant and square wave WSTS were tested to replicate real wind characteristics. From the results, it can be concluded that:

- At high wind speeds the switching pattern of the IGBT causes intermittent T_j profiles.

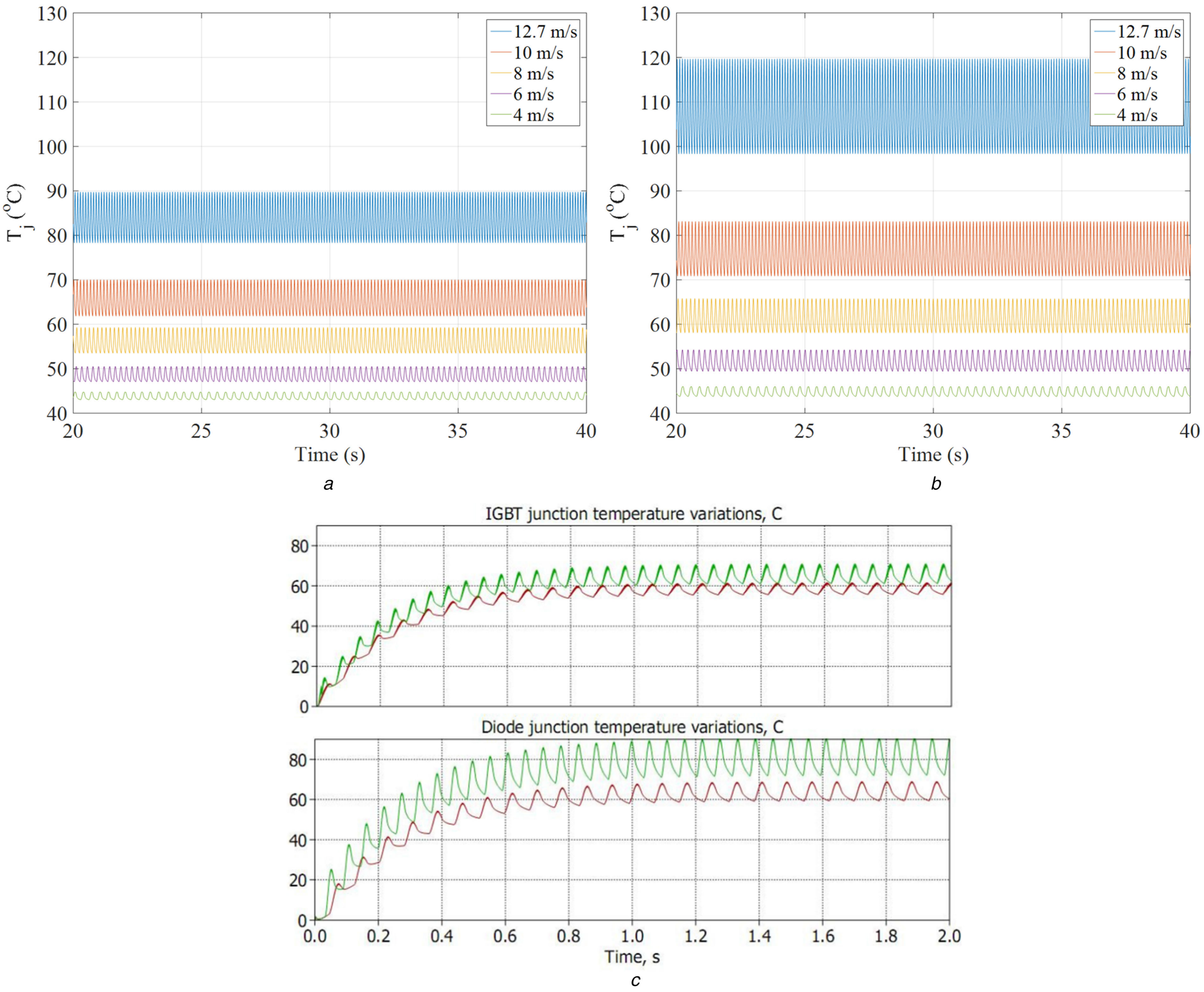

Fig. 7 *T_j response to constant wind speeds in the MPPT region for*
(a) IGBT, ***(b)*** Diode, ***(c)*** Results found in [14] for a 12 m/s input

- The diodes experience greater thermal loading than the IGBTs in all comparative cases.
- A comparison with another study showed that the inclusion of heat sink thermal parameters and ambient temperature are important for providing accurate T_j profiles.
- The lower the frequency of wind speed variation, the higher ΔT_j becomes, implying that low turbulence sites such as offshore have greater thermal variation, and therefore damage, in the converter.
- For the first time, the minimum wind speed data frequency for accurate converter thermal simulation has been determined. Wind speed variations with frequency >0.25 Hz have a small increase in ΔT_j and therefore reasonable approximations of T_j profiles can be made with 0.25 Hz wind speed data. Wind speed data at lower frequencies allow simulations to overlook damaging temperature variations.

5 Acknowledgments

This work was supported by the EPSRC SUPERGEN Wind project (grant number EP/L014106/1).

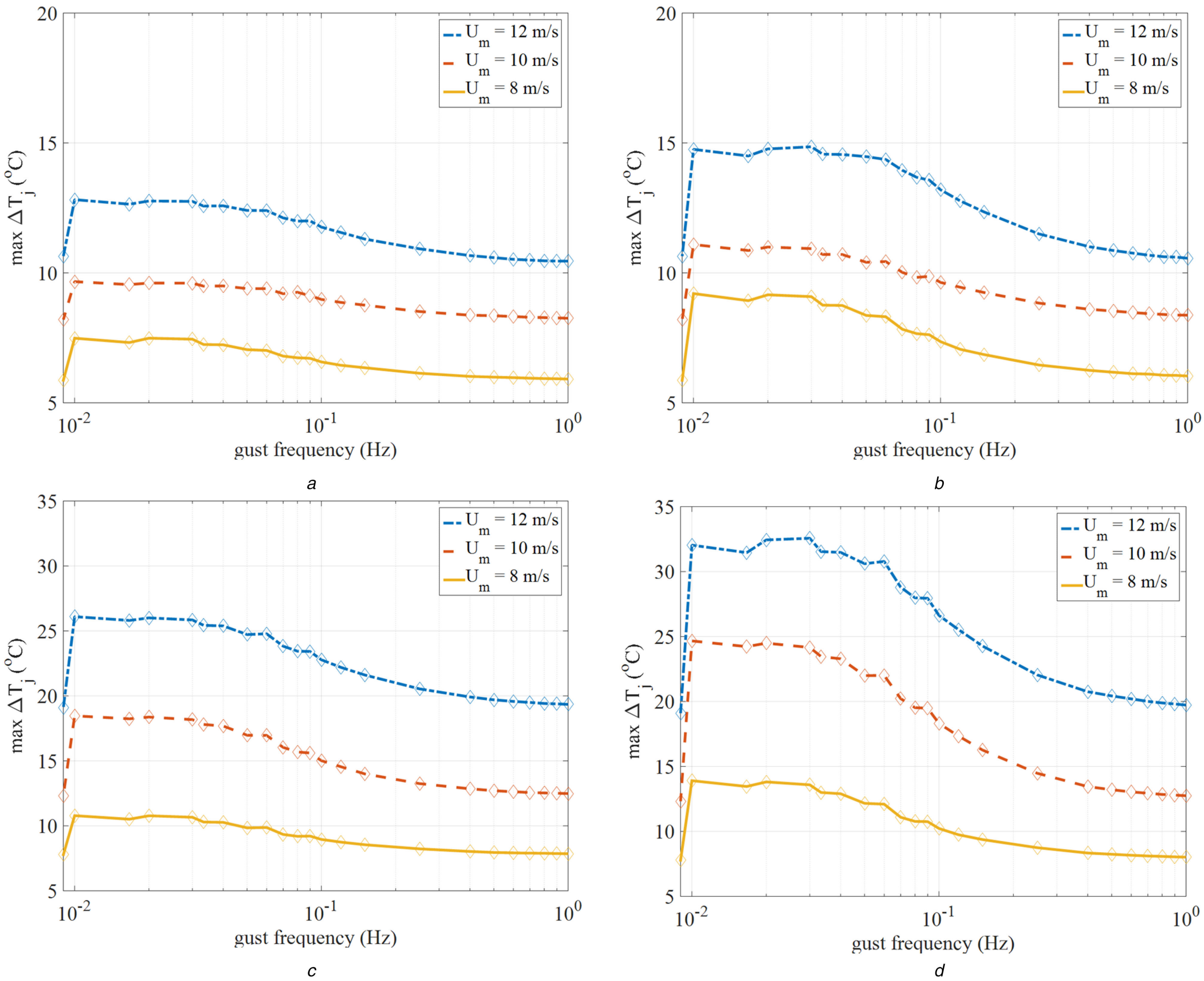

Fig. 8 *Max ΔT_j over varying mean wind speeds (U_m) and square gust frequencies for*
(a) IGBT for ΔU of 1 m/s, ***(b)*** IGBT for ΔU of 2 m/s, ***(c)*** Diode for ΔU of 1 m/s, ***(d)*** Diode for ΔU of 2 m/s

6 References

[1] 'Offshore Wind Cost Reduction, Pathways Study. Available at http://www.thecrownestate.co.uk/media/5493/ei-offshore-wind-cost-reduction-pathways-study.pdf, accessed 19 July 2016

[2] 'Large-Scale Offshore Wind Power in the United States: Assessment of Opportunities and Barriers'. Available at http://www.nrel.gov/docs/fy10osti/40745.pdf, accessed 19 July 2016

[3] Carroll, J., McDonald, A., McMillan, D.: 'Failure rate, repair time and unscheduled O&M cost analysis of offshore wind turbines', *Wind Energy*, 2015, **19**, (6), pp. 1107–1119

[4] Carroll, J., McDonald, A., McMillan, D.: 'Reliability comparison of wind turbines with DFIG and PMG drive trains', *IEEE Trans. Energy Convers.*, 2015, **30**, (2), pp. 663–670

[5] Spring, M., Davies, P., Gaal, G., *et al.*: 'Top 30 Chart for wind turbine failure mechanisms'. EWEA Annual Event, Paris, France, November 2015

[6] 'Application Manual Power Semiconductors'. Available at https://www.semikron.com/dl/service-support/downloads/download/semikron-application-manual-power-semiconductors-english-en-2015, accessed 8 September 2016

[7] Bartram, M., De Doncker, R.: 'Doubly-fed-machines in wind-turbine systems: is this application limiting the lifetime of IGBT-frequency-converters?'. IEEE PESC, Aachen, Germany, June 2004, pp. 2583–2587

[8] Fuchs, F., Mertens, A.: 'Steady state lifetime estimation of the power semiconductors in the rotor side converter of a 2 MW DFIG wind turbine via power cycling capability analysis'. EPE, Birmingham, UK, August 2011

[9] Weiss, D., Eckel, H.: 'Fundamental frequency and mission profile wearout of IGBT in DFIG converters for windpower'. EPE, Lille, France, September 2013

[10] Zhou, D., Blaaberg, F., Franke, T., *et al.*: 'Reliability and energy loss in full-scale wind power converter considering grid codes and wind classes'. IEEE ECCE, Pittsburgh, USA, September 2014, pp. 3067–3074

[11] Kostandyan, E., Ma, K.: 'Reliability estimation with uncertainties consideration for high power IGBTs in 2.3 MW wind turbine converter system', *Microelectron. Reliab.*, 2012, **52**, (9), pp. 2403–2408

[12] Ma, K., Liserre, M., Blaabjerg, F., *et al.*: 'Thermal loading and lifetime estimation for power device considering mission profiles in wind power converter', *IEEE Trans. Power Electron.*, 2015, **30**, (2), pp. 590–602

[13] Mussallam, M., Johnson, C.: 'Impact of different control schemes on the life consumption of power electronic modules for variable speed wind turbines'. EPE, Birmingham, UK, August 2011

[14] Baygildina, E., Peltoniemi, P., Pyrhönen, O., *et al.*: 'Thermal loading of wind power converter considering dynamics of wind speed'. IEEE IECON, Vienna, Austria, November 2013, pp. 1362–1367

[15] Isidoril, A., Rossi, F., Blaaberg, F., *et al.*: 'Thermal loading and reliability of 10-MW multilevel wind power converter at different wind roughness classes', *IEEE Trans. Ind. Appl.*, 2014, **50**, (1), pp. 484–494

[16] Senturk, O., Munk-Nielsen, S., Teodorescu, R., *et al.*: 'Electro-thermal modeling for junction temperature cycling-based lifetime prediction of a press-pack IGBT 3L-NPC-VSC applied to large wind turbines'. IEEE ECCE, Phoenix, USA, September 2011, pp. 568–575

[17] Smith, C., Wadge, G., Crabtree, C., *et al.*: 'Characterisation of electrical loading experienced by a nacelle power converter'. EWEA Annual Event, Paris, France, November 2015

[18] Smith, C., Crabtree, C., Matthews, : 'Impact of wind conditions on thermal loading of PMSG wind turbine power converter'. IET PEMD, Glasgow, UK, April 2016

[19] Heier, S.: '*Grid integration of wind energy: onshore and offshore conversion systems*' (John Wiley & Sons, 2014, 3rd edn.)

[20] Rao, S., Yap, F.: '*Mechanical vibrations*' (Addison-Wesley, 1995)

[21] Wu, B., Lang, Y., Kouro, S.: '*Power conversion and control of wind energy systems*' (John Wiley & Sons, 2011)

[22] 'SKS B2 100 GD 69/11 - MA PB Datasheet'. Available at http://www.semikron.com/dl/service-support/downloads/download/semikron-datasheet-sks-b2-100-gd-69-11-ma-pb-08800565, accessed 7 December 2015

[23] 'SKiiP 2013 GB172-4DW V3 Datasheet'. Available at http://www.semikron.com/dl/service-support/downloads/download/semikron-datasheet-skiip-2013-gb172-4dw-v3-20451248, Accessed 8 December 2015

[24] 'Optimised Converter for Solar and Wind'. Available at http://www.semikron.com/dl/service-support/downloads/download/semikron-flyer-semistackre-2014-04-08, accessed 14 September 2015

[25] Anaya-Lara, O., Jenkins, N., Ekanayake, J., *et al.*: '*Wind energy generation: modelling and control*' (John Wiley & Sons, 2009)

[26] Hansen, A., Sorensen, P., Iov, F., *et al.*: 'Control of variable speed wind turbines with doubly-fed induction generators', *Wind Eng.*, 2004, **28**, pp. 411–432

[27] Zhang, J., Cheng, M., Chen, Z., *et al.*: 'Pitch angle control for variable speed wind turbines'. DPRT, Nanjuing, China, April 2008, pp. 2691–2696
[28] Bianchi, F., De Battista, H., Mantz, R.: '*Wind turbine control systems: principles, modelling and gain scheduling design*' (Springer Science & Business Media, 2006)
[29] Wyllie, P.: 'Electrothermal modelling for doubly fed induction generator converter reliability in wind power'. Durham University thesis, 2014
[30] Wintrich, A., Nicolai, U., Tursky, W., *et al.*: 'Application manual power semiconductors' (SEMIKRON International GmbH, 2015)
[31] 'AN11261: Using RC Thermal Models: Application note'. Available at http://www.nxp.com/documents/application_note/AN11261.pdf, accessed 9 December 2015
[32] 'Convert Foster Network to Cauer'. Available at http://uk.mathworks.com/matlabcentral/fileexchange/46348-convert-foster-network-to-cauer/content//fostercauer.m, accessed 9 December 2015
[33] Slootweg, J., Polinder, H., Kling, W.: 'Dynamic modelling of a wind turbine with doubly fed induction generator'. PESSM, Canada, July 2001, pp. 644–649
[34] Akhmatov, V.: 'Analysis of dynamic behaviour of electric power systems with large amount of wind power'. Technical University of Denmark thesis, 2003
[35] Sim, J., Kim, K., Son, R., *et al.*: 'Ride-through of PMSG wind power system under the distorted and unbalanced grid voltage dips', *J. Electr. Eng. Technol.*, 2012, **7**, (6), pp. 898–904
[36] Leithead, W., Connor, B.: 'Control of variable speed wind turbines: dynamic models', *Int. J. Control.*, 2000, **73**, (13), pp. 1173–1188
[37] Gonzalez-Longatt, F., Wall, P., Terzija, V.: 'A simplified model for dynamic behavior of permanent magnet synchronous generator for direct drive wind turbines'. IEEE PES PowerTech, Trondheim, June 2011, pp. 1–7

7 Appendix

$P_{t,rat}$ is the rated turbine power, f_{rat} is the rated frequency, U_{rat} is the rated wind speed, $V_{l,rat}$ is the rated line voltage, I_{rat} is the rated current, T_{rat} is the rated torque, V_f is the IGBT forward voltage, V_{fd} is the diode forward voltage, $T_{f,t}$ is the IGBT fall time and tail time, respectively, R_{on} is the IGBT on-state slope resistance, $P_{p,id,iq}$ are the proportional gains for the pitch, I_d, and I_q controllers, respectively, $I_{p,id,iq}$ are the integral gains for the pitch, I_d, and I_q controllers, respectively, and f_{sw} is the switching frequency (see Table 1).

Table 1a *Continued*

Parameter	Value	Reference
A_t	0.22	[33]
B_t	116	[33]
C_t	0.4	[33]
D_t	0	[33]
E_t	0	[33]
F_t	5	[33]
G_t	12.5	[33]
H_t	0.08	[33]
K_t	0.035	[33]
$P_{t,rat}$	2.0 MW	[21]
$\omega_{t,rat}$	22.5 rpm	[21]
f_{rat}	9.75 Hz	[21]
λ_{opt}	6.3	—
$C_{p,max}$	0.438	—
U_{rat}	12.7 m/s	—
r	34 m	—
ρ	1.225 kg/m^3	[25]
J_t	2.92×10^6 kg/m^2	[34]
J_g	200 kg/m^2	[35]
K	4.0×10^7 Nm/rad	[34]
C_d	6.72×10^6 Nms/rad	—
$V_{l,rat}$	690 $V_{(rms)}$	[21]
$I_{,rat}$	1867.76 $A_{(rms)}$	[21]
T_{rat}	848.826 kNm	[21]
R_s	8.21×10^{-4} Ω	[23]
L_d	1.5731 mH	[23]
p	52	[23]
φ	8.24 Vs (peak)	[23]
V_f	0.95 V	[23]
V_{fd}	1.9 V	[23]
R_{on}	0.925 mΩ	[23]
V_{DC}	1150 V	—
β_{max}	45°	[36]
β_{min}	0°	[36]
$\beta_{rate,max}$	8°/s	[36]
$\beta_{rate,min}$	−8°/s	[36]
τ	0.5 s	[37]
P_p	3.357	—
I_p	0.012	—

Table 1b *Drive train parameters*

Parameter	Value	Reference
P_{id}	−0.148	—
I_{id}	−5.377	—
P_{iq}	−0.155	—
I_{iq}	−2.689	—
f_{sw}	2 kHz	[22]
$R_{\mathrm{th},c,\mathrm{IGBT}}(1)$	1.5×10^{-3} K/W	—
$R_{\mathrm{th},c,\mathrm{IGBT}}(2)$	7.3×10^{-3} K/W	—
$R_{\mathrm{th},c,\mathrm{IGBT}}(3)$	5.9×10^{-3} K/W	—
$R_{\mathrm{th},c,\mathrm{IGBT}}(4)$	2.5×10^{-3} K/W	—
$R_{\mathrm{th},c,\mathrm{IGBT}}(5)$	0.37×10^{-3} K/W	—
$C_{\mathrm{th},c,\mathrm{IGBT}}(1)$	0.55 Ws/K	—
$C_{\mathrm{th},c,\mathrm{IGBT}}(2)$	3.61 Ws/K	—
$C_{\mathrm{th},c,\mathrm{IGBT}}(3)$	35.90 Ws/K	—
$C_{h,c,\mathrm{IGBT}}(4)$	476.61 Ws/K	—
$C_{h,c,\mathrm{IGBT}}(5)$	4.81×10^{3} Ws/K	—
$R_{\mathrm{th},c,\mathrm{diode}}(1)$	2.8×10^{-3} K/W	—
$R_{\mathrm{th},c,\mathrm{diode}}(2)$	10.2×10^{-3} K/W	—
$R_{\mathrm{th},c,\mathrm{diode}}(3)$	10.5×10^{-3} K/W	—
$R_{\mathrm{th},c,\mathrm{diode}}(4)$	11.9×10^{-3} K/W	—
$R_{\mathrm{th},c,\mathrm{diode}}(5)$	8.6×10^{-3} K/W	—
$R_{\mathrm{th},c,\mathrm{diode}}(6)$	0.94×10^{-3} K/W	—
$C_{\mathrm{th},c,\mathrm{diode}}(1)$	0.773 Ws/K	—
$C_{\mathrm{th},c,\mathrm{diode}}(2)$	1.45 Ws/K	—
$C_{\mathrm{th},c,\mathrm{diode}}(3)$	4.90 Ws/K	—
$C_{\mathrm{th},c,\mathrm{diode}}(4)$	36.07 Ws/K	—
$C_{\mathrm{th},c,\mathrm{diode}}(5)$	577.76 Ws/K	—
$C_{\mathrm{th},c,\mathrm{diode}}(6)$	1.60×10^{4} Ws/K	—
$R_{\mathrm{th},c,h}(1)$	0.79×10^{-3} K/W	—
$R_{\mathrm{th},c,h}(2)$	3.1×10^{-3} K/W	—
$R_{\mathrm{th},c,h}(3)$	4.3×10^{-3} K/W	—
$R_{\mathrm{th},c,h}(4)$	0.88×10^{-3} K/W	—
$R_{\mathrm{th},c,h}(5)$	0.14×10^{-3} K/W	—
$C_{\mathrm{th},c,h}(1)$	337.28 Ws/K	—
$C_{\mathrm{th},c,h}(2)$	409.76Ws/K	—
$C_{\mathrm{th},c,h}(3)$	1.37×10^{3} Ws/K	—
$C_{h,c,h}(4)$	1.91×10^{4} Ws/K	—
$C_{h,c,h}(5)$	1.30×10^{4} Ws/K	—
TC_{Esw}	0.003	[30]
TC_{Err}	0.006	[30]
T_{ref}	125°C	—

Journal of Physics: Conference Series

PAPER • **OPEN ACCESS**

Monitoring Wind Turbine Loading Using Power Converter Signals

To cite this article: C A Rieg *et al* 2016 *J. Phys.: Conf. Ser.* **749** 012018

Monitoring Wind Turbine Loading Using Power Converter Signals

C A Rieg[1], C J Smith[1], C J Crabtree[1]

[1]School of Engineering and Computing Sciences, Durham University, Lower Mountjoy, South Road, Durham, DH1 3LE, UK

c.j.crabtree@dur.ac.uk

Abstract. The ability to detect faults and predict loads on a wind turbine drivetrain's mechanical components cost-effectively is critical to making the cost of wind energy competitive. In order to investigate whether this is possible using the readily available power converter current signals, an existing permanent magnet synchronous generator based wind energy conversion system computer model was modified to include a grid-side converter (GSC) for an improved converter model and a gearbox. The GSC maintains a constant DC link voltage via vector control. The gearbox was modelled as a 3-mass model to allow faults to be included. Gusts and gearbox faults were introduced to investigate the ability of the machine side converter (MSC) current (I_q) to detect and quantify loads on the mechanical components. In this model, gearbox faults were not detectable in the I_q signal due to shaft stiffness and damping interaction. However, a model that predicts the load change on mechanical wind turbine components using I_q was developed and verified using synthetic and real wind data.

1. Introduction

Extreme wind conditions such as gusts can lead to very large loads on the turbine that cause fatigue, shut-downs and damage to components such as the gearbox [1]. In response the condition of wind turbine components is monitored so that a developing fault can be detected and appropriate action taken. This allows maintenance to be scheduled before the impact on the system has become too large, resulting in lower downtimes and lower cost of energy (CoE) [2].

Condition monitoring (CM) techniques such as vibration and strain measurement require expensive sensors that are often impractical in the high-torque applications of wind turbines [3]. Using readily available signals from other areas of the turbine could prove an inexpensive alternative CM approach.

The power converter could provide this information for CM applications; the converter should respond to any disturbances and therefore its signals should show the drive train response. For example, the quadrature-axis component of the machine side converter (MSC) current signal (I_q) controls the real power flow and contains torsional information from the drive train. Monitoring I_q could provide useful information about torsional loads on components that could be used for early fault detection without extra sensors.

This investigation focuses on whether power converter signals can be used for CM with a focus on two potential applications:

1. Gear tooth failure detection.
2. Mechanical load estimation from damaging gusts.

2. Approach

To carry this work out a drive train model was required. The model developed at Durham in Simulink [4] was used. It is a drivetrain model of a fully rated, direct-drive 2MW permanent magnet synchronous generator (PMSG) wind turbine with two voltage sources connected to ground simulating the DC link. To make this model suitable for this study the following modifications were made:

1. A full grid-side converter (GSC) was added for a more realistic converter model.
2. A gearbox was added.
3. A gearbox fault model was used to provide fault conditions.
4. A gust model was added to provide data for load prediction.

A schematic of the final model is shown in figure 1. This section outlines how these aspects were modelled. Modifications to the PMSG and MSC as a result of including a gearbox are also detailed.

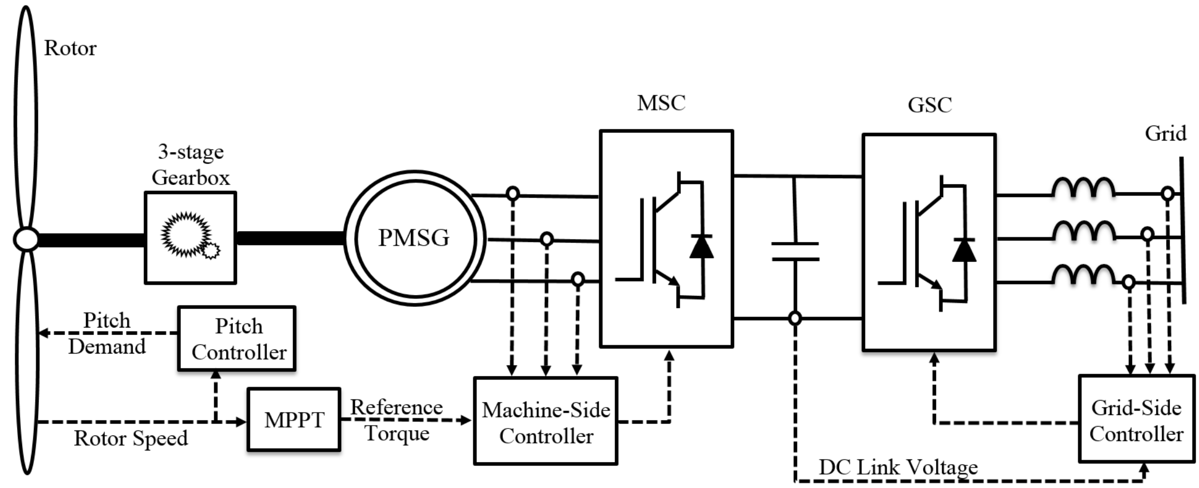

Figure 1. Schematic of the 2MW geared PMSG wind energy conversion system. MPPT stands for maximum power point tracking.

2.1. Grid-Side Converter

The main objective of the GSC is to control power flow between converter and grid to maintain a constant DC link voltage regardless of the power input from the MSC (figure 1). In this configuration the GSC acts as an inverter and the MSC acts as a rectifier. The GSC was modelled as a 2-level insulated-gate bipolar transistor (IGBT)/diode pair active inverter. In the model the 'Universal Bridge' block from the Simulink library was used with the power electronic device set to 'IGBT/Diodes'. It is controlled using the 'PWM Generator (2 level)' block that takes the voltage from the grid side controller as the modulating input signal. The DC-link voltage is $1150V_{DC}$. The grid is represented as ground connected to a three phase programmable voltage source connected to the GSC via inductors.

To control the GSC, vector control was chosen as it is able to respond to transient events more robustly than load angle control [5]. Figure 2 outlines the control schematic for the GSC. I_d is the direct-axis current, V_d is the direct-axis voltage, ω is the grid frequency (rad/s), L is the grid inductance, V_{DC_link} is the DC-link voltage, V_q is the quadrature-axis voltage, $V_{d,r}$ is the converter reference V_d, $V_{q,r}$ is the converter reference V_q, and V_0 is the 0-component voltage. To convert between 3-phase sinusoidal and direct-quadrature-zero (dq0) reference frames the Park and inverse Park transforms were used.

2.2. Gearbox Model

The gearbox is connected to the hub via the low-speed shaft and to the generator via the high-speed shaft. It increases the speed of the incoming turbine speed to the desired generator speed while reducing the torque by a gear ratio N_{GB}. The dynamic interactions of the rotor, gearbox and generator were modelled as a 3-mass model. Higher order models were considered, however no data was found and the 3-mass model represents the dynamic interactions of the rotor, gearbox and generator adequately for this project. The 3-mass model is shown in figure 3. J_R is the rotor moment of inertia, J_{GB} is the gearbox moment of inertia, $J_{m1,2}$ are the equivalent moments of inertia for the low and high speed gear sections respectively, $T_{m1,2}$ are the equivalent mechanical torques for the low and high shafts respectively and J_g is the generator moment of inertia.

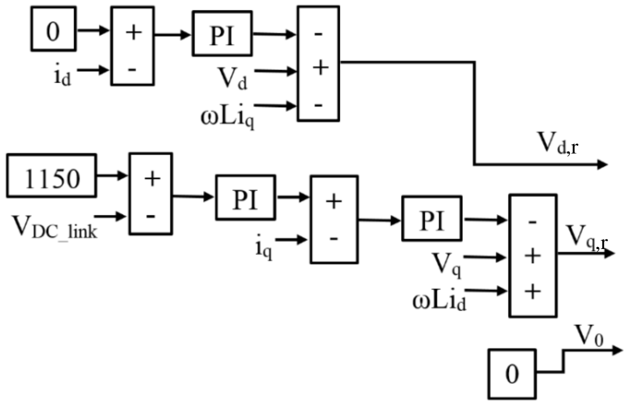

Figure 2. Vector control scheme for the GSC.

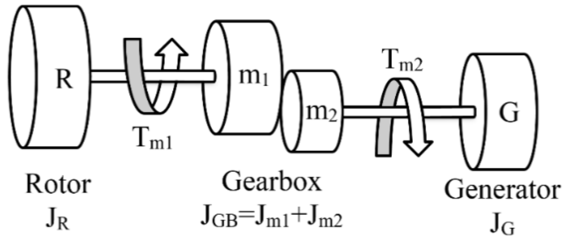

Figure 3. Schematic of the 3-mass model dynamics.

The first mass in the rotor, the second mass is the gearbox and the third mass is the generator. The model uses the principles of a mass-spring-damper system where each mass has inertia J and each shaft a stiffness K and viscous damping B. The second mass (gearbox) is divided into two parts that are related through N_{GB} to represent the difference in speeds of each gear. As such the resulting $T_{m1,2}$ and rotational speeds of the various components (ω) can be represented using equations (1-6).

$$T_{m1} = B_1(\omega_r - \omega_{m1}) + K_1 \int (\omega_r - \omega_{m1}) \mathrm{d}t \tag{1}$$

$$T_{m2} = B_2\left(\omega_{m2} - \omega_g\right) + K_2 \int \left(\omega_{m2} - \omega_g\right) \mathrm{d}t \tag{2}$$

$$\omega_r = \int \frac{T_r - T_{m1}}{J_r} \mathrm{d}t \tag{3}$$

$$\omega_{m1} = \int \frac{T_{m1} - T_g N_{GB}}{J_{GB}} \mathrm{d}t \tag{4}$$

$$\omega_{m2} = \int \frac{T_{m2} - T_r / N_{GB}}{J_{GB}} \mathrm{d}t \tag{5}$$

$$\omega_g = \int \frac{T_e - T_{m2}}{J_g} \mathrm{d}t \tag{6}$$

Where $B_{1,2}$ are the viscous damping of the low and high-speed shaft respectively, $K_{1,2}$ are the shaft stiffnesses of the low and high-speed shafts respectively, ω_r is the rotational speed of the rotor, $\omega_{m1,2}$ are the rotational speeds of the low and high-speed gear components respectively, ω_g is the generator rotational speed. T_r is the rotor torque, T_g is the generator torque, and T_e is the electromechanical torque.

The torque and speed across the rotor and generator are related through the gearbox ratio, N_{GB} using equation (7).

$$N_{\mathrm{GB}} = \frac{\omega_{\mathrm{g}}}{\omega_{\mathrm{t}}} = \frac{T_{\mathrm{r}}}{T_{\mathrm{e}}} \tag{7}$$

Due to the new torque and speed in the generator from [4], changes of the PMSG were made to accommodate the current and voltage requirements. To keep the current and voltage outputs the same equations (8) and (9) were used. The number of poles was reduced to 4 because the generator has a rotational speed of 1500rpm. The flux density was changed to 1.611Vs and the armature inductance was changed to 0.4mH.

$$I_{\mathrm{q}} = \frac{4T_{\mathrm{m2}}}{3p\varphi} \tag{8}$$

$$V_{\mathrm{d},m} = L_{\mathrm{d}}\omega I_{\mathrm{q}} - I_{\mathrm{q}}R_{\mathrm{s}} \tag{9}$$

p is the number of generator poles, φ is the generator flux linkage, $V_{d,m}$ is the MSC direct-axis voltage, L_d is the direct-axis generator inductance, and R_s is the stator resistance. The data for the 3-mass model has been taken from research papers and is given in Appendix B.

2.3. Gearbox Fault Model

The most severe gearbox failure modes that arise from extreme wind conditions have been identified as fretting corrosion and high cycle bending fatigue [6]. Fretting corrosion is the deterioration of contacting gear tooth surfaces as a result of vibratory motion between teeth and is this study's focus.

The gear friction coefficient varies according to three different types of surface structure: adhesion, unevenness and wear [7]. Friction losses in the gears are part of the normal force exerted by each gear at the point of contact F_{N} as a friction factor μ. Due to difficulties involved in the estimation of the μ with lubrication it is often assumed constant [8] and was not used in this project due to a lack of relevant experimental data in the literature. As gears are well lubricated this assumption was deemed satisfactory.

Instead, the gear wear impact on stiffness was considered. The effect of tooth wear on the mechanics of the system has previously been examined and it was found that gear tooth wear causes a reduction in the stiffness of the gear. It was found that it can be modelled as a rectangular pulse wave or a half sine function. The half sine wave function is used in detailed gearbox models that include the gear meshing process in their calculations [9]. For this model the rectangular pulse function was chosen as it represents the fault accurately for the purpose of this investigation.

The reduction of the gear tooth stiffness can be calculated according to equation (10).

$$K_{\mathrm{wear}} = K_{\mathrm{g}} l_{\mathrm{w}} A \tag{10}$$

Where K_{wear} is the wear stiffness, K_{g} is the hertz contact stiffness, l_{w} is the wear length and A is the amplitude of wear.

Typical values of l_{w} are between 1 and 2mm and A typically has a value between 0 and 1 [9]. The contact stiffness with a wear fault present, $K_{\mathrm{g,wear}}$, is given as the difference between the non-faulty gear stiffness and the wear stiffness as in equation (11) [9].

$$K_{\mathrm{g,wear}} = K_{\mathrm{g}} - K_{\mathrm{wear}} \tag{11}$$

The relationship between the contact stiffness of the gears and the stiffness of the shaft can be modelled as springs connected in series. The total stiffness K_{Total} is calculated from K_{g} and the shaft stiffness K_{S} as in equation (12).

$$K_{\mathrm{Total}} = \frac{1}{\frac{1}{K_{\mathrm{g}}} + \frac{1}{K_{\mathrm{s}}}} \tag{12}$$

The effect of tooth wear in the gearbox was modelled as a reduction in the total stiffness every time there is contact with a worn gear tooth as shown in figure 4. The total stiffness is applied across the shaft in the model.

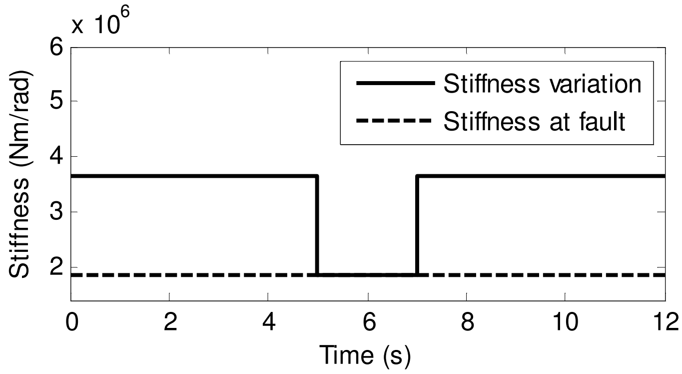

Figure 4. The stiffness relationship in a worn gear.

Other faults such as gear cracks have been modelled using a periodic cosine based variation in shaft stiffness given in (13) where K_{crack} is the reduction in shaft stiffness due to the crack that can be calculated using finite element analysis [9, 10]. The underlying calculations for a crack fault and a wear fault are very similar as they both rely on a periodic reduction in the shaft stiffness due to a fault.

$$K_{\mathrm{s}} = \frac{1-\cos\left(\omega t\right)}{2} K_{\mathrm{crack}} \tag{13}$$

Gearbox faults are often modelled as a periodic variation in tooth stiffness to indicate the presence of a fault. As a widely used, well-established method of modelling faults and experimental data available, it was chosen in this project.

A typical gearbox in a wind turbine has 3-stages with a planetary gearbox at the first stage, coupled to two parallel gearboxes at the second and third stage [11]. Due to the speed dependency of the gear fault model, faults can be introduced into any of the gear stages. Appendix A gives a summary of the gear ratios and output speeds corresponding to the individual stages.

2.4. Gust Model

Existing gust models rely on real wind data to model the amplitude, duration and gust shape introduced along with a running average wind speed [12, 13]. These wind gust profile characteristics can be extracted and applied using square or cosine shaped wind profiles that have a gust amplitude, duration and frequency. The maximum gust speed ($U_{\mathrm{G,max}}$) in a given time period is calculated from the gust factor $G(t)$ in equation (14). An expression for the gust factor is given in equation (15) [14].

$$U_{\mathrm{G,max}} = G\left(t\right)U_{\mathrm{W}} \tag{14}$$

$$G\left(t\right) = 1 + 0.42 I_{\mathrm{u}} \log_{\mathrm{e}}\left(\frac{3600}{t_G}\right) \tag{15}$$

Where U_w is the mean wind speed, I_{u} is the longitudinal turbulence intensity, and t_G is the gust duration.

The International Electrotechnical Commission (IEC) has divided the value for turbulence intensity into three categories - higher, medium and lower turbulence characteristics with values of 0.16, 0.14 and 0.12 respectively [15]. The underlying square wave gust characteristic was used as the basis for all gust analysis.

For the load prediction model gust, 10 gust categories were defined, each representing a reduction in the gust wind speed (table 1).

Table 1. Gust category assignment.

Gust Category	U_G	Gust Category	U_G
1	$(U_G+U_W) + U_W$	6	$[(U_G + U_W)/2.25] + U_W$
2	$[(U_G + U_W)/1.25] + U_W$	7	$[(U_G + U_W)/2.5] + U_W$
3	$[(U_G + U_W)/1.5] + U_W$	8	$[(U_G + U_W)/3] + U_W$
4	$[(U_G + U_W)/1.75] + U_W$	9	$[(U_G + U_W)/4] + U_W$
5	$[(U_G + U_W)/2] + U_W$	10	$[(U_G + U_W)/6] + U_W$

3. Results

The section presents and discusses the results of gearbox fault detection using converter signals (section 3.1), and estimating turbine drive train loads from gusts using converter signals (section 3.2).

3.1. Gearbox Fault Detection

Gearbox wear faults were introduced using the method outlined in section 2.3. The first fault was introduced as a wear fault with wear amplitude 0.5 and wear length 1mm present on every other tooth, giving a fault frequency of 1.72Hz. The incoming wind speed was constant at 7m/s. The parameters used to introduce the first fault in the second gearbox stage of the gearbox are detailed in Appendix B.

By taking the Fast Fourier Transform (FFT) of the MSC I_q signal the frequency spectrum was computed to identify differences between the 'healthy' (no fault) and faulty spectrum. Figure 5 shows the frequency response of the MSC I_q signal in its 'healthy' and faulty state as well as the amplitude difference between the healthy and faulty state. It can be seen that there is no clear difference in the spectrum at the fault frequency. There is a small difference at 2Hz, where both the healthy and the faulty spectrum show a spike due to control errors.

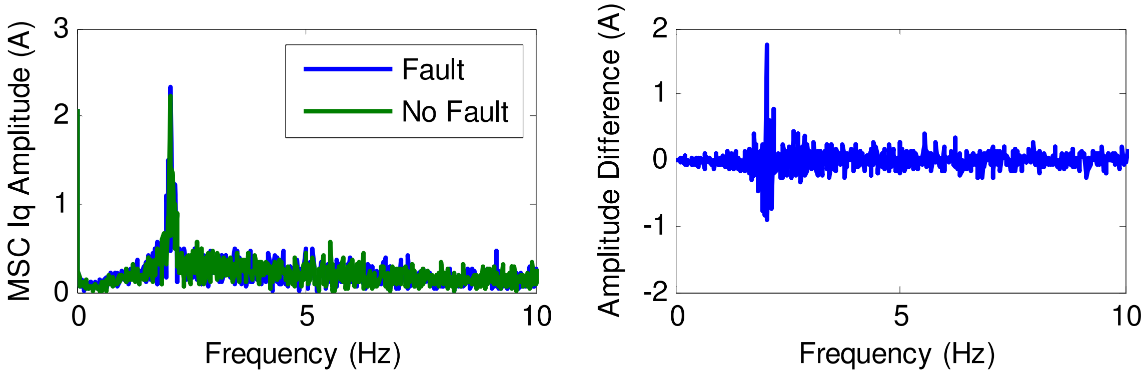

Figure 5. MSC I_q frequency response

It was investigated why the fault does not appear in the MSC I_q frequency spectrum by looking at the frequency spectrum of the relevant torque components. The torque across the high speed shaft is an input to the PMSG and is used to determine the MSC I_q and is result of the addition of the torque due to stiffness (T_K) and the torque due to damping (T_B). Figure 6 shows the frequency spectrum of each of these individual torque signals in their 'healthy' state and their faulty state. It can be seen that the fault is visible in the frequency spectrum of T_K and T_B (figure 6), yet is no longer visible in the resulting total torque spectrum (figure 5).

To understand the impact of the damping and stiffness components on the fault frequency response, the time sequence of T_K and T_B was monitored with the fault present (figure 7). The time sequences showed that the oscillatory motion of T_K due to the fault is counteracted by an opposite oscillatory motion from T_B removing the oscillation due to the fault from the frequency spectrum.

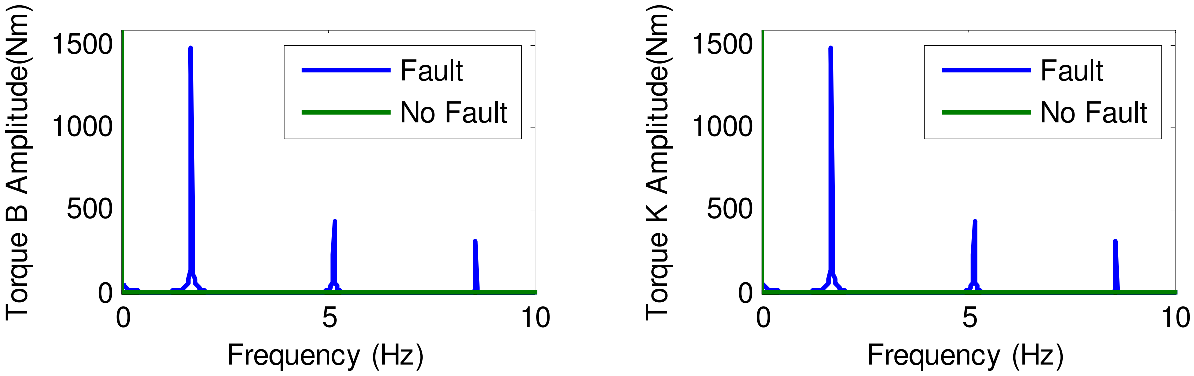

Figure 6. Frequency spectrum of mechanical torque components.

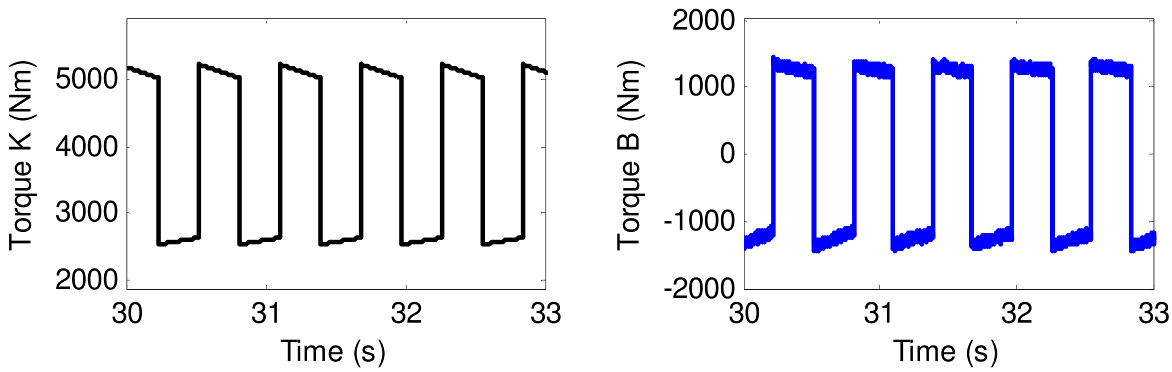

Figure 7. Temporal spectrum of mechanical torque components.

The amplitude of the torque due to damping counteracts the amplitude of the torque due to stiffness exactly, resulting in a critically damped system. The gearbox was modelled analogous to a mass-spring-damper system. In this system the role of the damper is to reduce or prevent oscillations. The fault amplitude was varied in the full range of 0 to 1 and the wear length was varied in the full range of 1mm to 2mm and the input speed was varied. However in each case the system remained critically damped, resulting in the fault not appearing in the MSC signals.

In a real gearbox the torque due to damping and torque due to stiffness cannot be measured separately as they have been in this model. In a real gearbox the system parameters might not be as perfectly balanced as in this modelled system and the damping might not have the same effect as in this model. Thus there is a possibility that faults can be detected in the MSC I_q signal of a real gearbox system where the components and parameters are not as balanced as in this drive train model.

3.2. Load prediction on mechanical components using MSC signals

The MSC converter signal spectrum changes with the incoming wind speed and wind pattern. Wind gusts at varying frequencies appear clearly on the spectrum and can be monitored using the MSC signals. Figure 8 shows the variation of the frequency spectrum as the gust frequency of the incoming wind is varied at a mean wind speed of 7.5 m/s using the maximum gust speed.

Simulations were done at different speeds and constant gust frequency of 3Hz. A relationship between the MSC I_q amplitude and the difference in rotor torque magnitude was derived for each gust category using simulation results as data points. The result for the first, second and third gust categories are shown in Figure 9 with equations (16-18) representing their relationship respectively. ΔT_r is the change in mechanical load on the rotor in kNm.

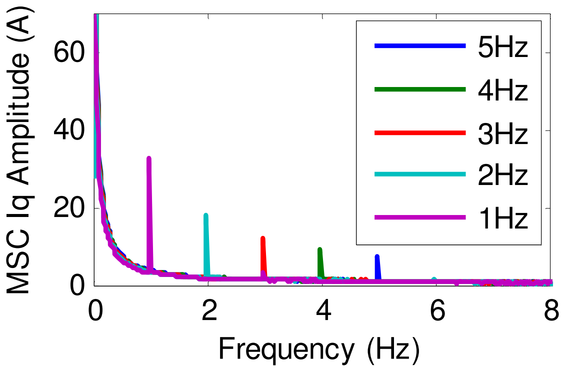

Figure 8. MSC I_q frequency spectrum for different gust frequencies.

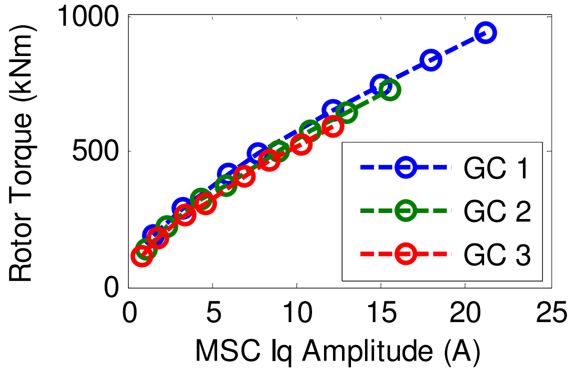

Figure 9. ΔT_r vs MSC I_q amplitude for different gust categories.

$$\text{GC 1: } \Delta T_r = 137.7 I_q^{0.6238} \tag{16}$$

$$\text{GC 2: } \Delta T_r = 130.21 I_q^{0.6206} \tag{17}$$

$$\text{GC 3: } \Delta T_r = 123.92 I_q^{0.6176} \tag{18}$$

With this information, a load prediction model can be constructed. The proposed model works on the basis that the wind speed and MSC signal amplitudes can be measured. A flowchart of its operating principle is illustrated in Figure 10. The wind is monitored and depending on the mean wind speed and gust magnitude it can be assigned a gust category. Each gust category has an equation relating the change in torque and the MSC current amplitude for an assigned frequency range.

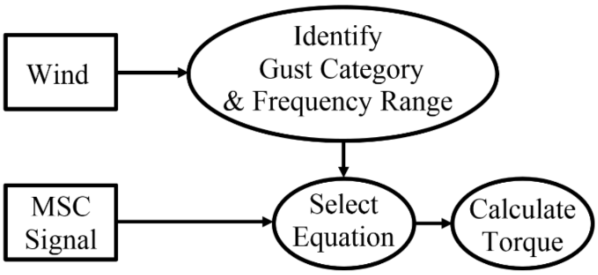

Figure 10. Flowchart of the load prediction model.

Depending on the gust category and gust frequency, an equation is selected from which ΔT_r can be calculated. The frequency ranges become smaller as the gust frequency decreases because the change in I_q amplitude increases. Severe load changes can then be counted to estimate the mechanical fatigue.

In order to verify the functionality of this method a variety of ideal category 1 gusts with different mean wind speeds were inputted into the model. The MSC I_q FFT amplitude was measured and the expected load on the rotor was calculated according to equation ($\Delta T_{r,est}$) (16). $\Delta T_{r,est}$ was compared to the measured torque from the simulation ($\Delta T_{r,sim}$) using the percentage error.

The results are summarised in table 2. The percentage error between the measured and the calculated error is very small, below 1%. This shows that the model is able to predict the load on the mechanical components in the wind turbine drive train through MSC signal measurements adequately.

The model was tested using real wind data from the anemometer on a 1.5MW variable speed wind turbine in order to investigate the accuracy of the model using a real, non-ideal wind characteristic. The data was identified as GC 10 and frequency 0.29Hz. The equation relating $\Delta T_{r,est}$ and MSC I_q in this case is given by (19). Table 2 gives a summary of the results.

Table 2. Model Verification and response to real wind input.

U_W (m/s)	MSC I_q (A)	$\Delta T_{r,est}$ (Nm)	$\Delta T_{r,sim}$ (Nm)	% Error
		Verification (GC 1)		
5.5	4.536	353636.5	350370	0.92
6.2	6.648	448868.5	445450	0.76
7	9.84	573264.2	568160	0.89
8.2	16.344	786715	780330	0.81
		Real wind input (GC 10)		
8.4	11.82	98978.5	104860	5.9

$$\Delta T_{r,est} = 15.739 I_q^{0.7445} \tag{19}$$

The percentage error for the real wind is higher than for the ideal wind. This is expected as the real wind gusts have a larger variation in duration and magnitude. The frequency of the gusts in the real wind characteristic is not as clear as in the ideal characteristic. The frequency categories allow for some variation that increases the percentage error. For a mean wind speed of 8.5m/s with gusts of frequency 0.29Hz the difference between the maximum (GC 1) and minimum (GC 10) change in rotor torque is 555910Nm. The difference between the calculated and measured rotor torque from Table 3 is 5881.9Nm, which is 100 times smaller than the difference between GC1 and GC10. This indicates that the model has the ability to estimate the change in load using real wind characteristics well.

4. Conclusion

CM of wind turbine components allows appropriate action to be taken to minimise the impact of developing faults but currently requires expensive sensors and data acquisition devices**.** This paper investigates whether converter signals, which are already monitored by turbine controllers, can be used for CM.

A drive train model was modified to include a gearbox, GSC and gearbox fault model to determine whether gearbox faults could be detected in the converter signals. Gusts were also modelled to determine if drive train mechanical loading could be predicted using converter signals. The conclusions from this study are:

- Gear wear cannot be detected in the MSC signals due to the model damping effects. However, physical testing should be carried out to explore the impact of non-ideal dynamics.
- A model using MSC signals successfully predicted the load changes in the turbine with a percentage error < 1% under ideal wind conditions, and <6% for a real wind speed case.

Further investigations into the magnitude of load changes that cause mechanical component damage could lead to the application of this accurate MSC-based load prediction model to prevent gearbox faults through turbine shutdown during damaging wind conditions.

Appendices

Appendix A. 3-stage gearbox gear ratios.

	Stage 1	Stage 2	Stage 3
Gear type	Planetary	Parallel	Parallel
Gear ratio	1:16.667	1:2	1:2
Output speed	375rpm	750rpm	1500rpm

Appendix B. Data for 3 mass model and gear faults.

Parameter	Value	Ref	Parameter	Value	Ref
J_r	2.92×10^6 kgm^2	[16]	K_2	2.29×10^8 Nm/rad	[18]
J_g	200 kgm^2	[17]	K_g	3.715×10^6 Nm/rad	[17]
J_{GB}	190 kgm^2	[17]	K_{wear}	1857.5 Nm/rad	(10)
B_1	6.72 Nms/rad	[4]	$K_{g,wear}$	3713143Nm/rad	(11)
B_2	6.72 Nms/rad	[4]	K_{Total}	3655585 Nm/rad	(12)
K_1	4.00×10^7 Nm/rad	[16]	$K_{Total,wear}$	1842070 Nm/rad	(12)

References

[1] Kanev S and van Engelen T 2010 Wind turbine extreme gust control *Wind Energy* **13** pp 18-35
[2] Han Y and Song Y 2003 Condition monitoring techniques for electrical equipment-a literature survey *IEEE Trans. Power Del.* **18**(1) pp 4-13
[3] Yang W, Tavner P, Crabtree C and Wilkinson M 2010 Cost-effective condition monitoring for wind turbines *IEEE Trans. Ind. Electron*. **57**(1), pp 263-71
[4] Smith C, Wadge G, Crabtree C and Matthews P 2015 Characterisation of electrical loading experienced by a nacelle power converter *EWEA Annual Event 17-20 Nov. (Paris)*
[5] Anaya-Lara O, Jenkins N, Ekanayake J, Cartwright P and Hughes M 2009 *Wind Energy Generation: Modelling and Control* (West Sussex: Wiley)
[6] Sheng S and McDade M 2011 Wind turbine failure modes *IJTC 23-26 Oct. (Los Angeles)*
[7] Mahdavian S and Mai Y 1984 Further study in friction, metallic transfer and wear debris of sliding surfaces *Wear* **95** pp 35-44
[8] Brethee K, Gao J, Gu F and Ball A 2015 Analysis of frictional effects in the dynamic response of gear systems and the implications for diagnostics *ICAC 11-12 Sep. (Glasgo*w)
[9] Cui L and Cai C 2015 Nonlinear Dynamics of a Gear-Shaft-Bearing System Breathing Crack and Tooth Wear Faults *Open Mech J* **9** pp 483-491
[10] Kidar T, Thomas M, El Badaoui M and Guibault R 2013 Control of phases by ESPRIT and WLSE methods for the early detection of gear cracks *3rd International Congress on Engineering Industrial Risk 3-5 Jul. (Riems)*
[11] Feng Y, Li J, Qiu Y, Yang W and Infield D 2014 Study on order analysis for condition monitoring wind turbine gearbox *RPG 24-25 Sep. (Naples)*
[12] Sheridan P 2011 Review of techniques and research for gust forecasting and parameterization *Forecasting Research Technical Report 570* (Exeter: Met Office)
[13] Verheij F, Cleijne J and Leene J 1992 Gust modelling for wind loading *J WIND ENG IND AEROD* **42**(1-3) pp 947-958
[14] Burton T, Jenkins N, Sharpe D and Bossanyi E 2011 *Wind energy handbook* (West Sussex: Wiley).
[15] IEC 2005 Wind turbines-Part 1: design requirements *IEC 61400-1:2005(E)*
[16] Akhmatov V 2003 Analysis of dynamic behaviour of electric power systems with large amount of wind power *Electric Power Engineering Ørsted-DTU Thesis*
[17] Jiang B 2010 Modelling of dynamics of driveline of wind stations *Chalmers University of Technology Master's Thesis*
[18] Ackermann T 2005 *Wind power in power systems* (West Sussex: Wiley)

www.ietdl.org

Published in IET Renewable Power Generation
Received on 10th June 2013
Revised on 19th November 2013
Accepted on 28th November 2013
doi: 10.1049/iet-rpg.2013.0177

Special Issue: European Wind Energy Association 2013

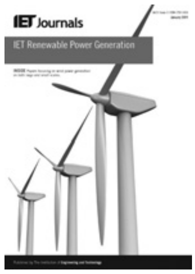

ISSN 1752-1416

Side-band algorithm for automatic wind turbine gearbox fault detection and diagnosis

Donatella Zappalá[1], Peter J. Tavner[1], Christopher J. Crabtree[1], Shuangwen Sheng[2]
[1]School of Engineering and Computing Sciences, Durham University, Durham, DH1 3LE, UK
[2]National Wind Technology Center, National Renewable Energy Laboratory (NREL), Golden, Colorado 80401, USA
E-mail: donatella.zappala@durham.ac.uk

Abstract: Improving the availability of wind turbines is critical for minimising the cost of wind energy, especially offshore. The development of reliable and cost-effective gearbox condition monitoring systems (CMSs) is of concern to the wind industry, because the gearbox downtime has a significant effect on the wind turbine availabilities. Timely detection and diagnosis of developing gear defects is essential for minimising an unplanned downtime. One of the main limitations of most current CMSs is the time consuming and costly manual handling of large amounts of monitoring data, therefore automated algorithms would be welcome. This study presents a fault detection algorithm for incorporation into a commercial CMS for automatic gear fault detection and diagnosis. Based on the experimental evidence from the Durham Condition Monitoring Test Rig, a gear condition indicator was proposed to evaluate the gear damage during non-stationary load and speed operating conditions. The performance of the proposed technique was then successfully tested on signals from a full-size wind turbine gearbox that had sustained gear damage, and had been studied in a National Renewable Energy Laboratory's (NREL) programme. The results show that the proposed technique proves efficient and reliable for detecting gear damage. Once implemented into the wind turbine CMSs, this algorithm can automate the data interpretation, thus reducing the quantity of the information that the wind turbine operators must handle.

1 Introduction

The European Wind Energy Association estimates that by 2020, 230 GW of wind capacity will be installed in Europe and 735 GW will be installed by 2050 [1]. These targets cannot be met without a large-scale offshore wind development in increasingly remote and hostile locations. In these environments, installation is more difficult and expensive and access to the wind farms for maintenance is also limited. Owing to the reduced site accessibility and the high cost of specialist personnel and equipment involved, the offshore operation and maintenance (O&M) costs can be quantified as three to five times higher than those on land [2]. O&M costs are estimated to account for up to 30% of the energy generation costs, with a considerable part, about 70%, caused by unexpected failures [3]. These high figures make the energy produced less competitive compared with the conventional sources and emphasise the need for optimising the O&M strategy for the offshore wind farms to reduce the turbine downtime and increase the availability. Achieving high wind turbines availability is paramount to providing affordable and cost-effective wind energy. The reactive maintenance strategies that are often employed onshore are largely impractical offshore because of difficulties in accessing wind farms in harsher environmental conditions. The adoption of a condition-based maintenance (CBM) can contribute significantly to minimising the offshore O&M costs by lowering the number of inspection visits and corrective maintenance actions [4]. This maintenance approach involves the repair or the replacement of parts based on their actual condition and the individual operating history of the particular machine, rather than on a schedule based on the predicted operating conditions of the average machine [5]. The development of reliable and cost-effective condition monitoring techniques, with automatic damage detection and diagnosis of the wind turbine components, plays a pivotal role in establishing technically and economically viable CBM strategies, especially for the unattended wind turbines located in remote and difficult-to-access locations. Autonomous on-line condition monitoring systems (CMSs) allow the early warning of mechanical and electrical defects to prevent major component failures. Faults can be detected while the defective component is still operational and thus necessary repair actions can be planned in time.

2 Wind turbine gearbox condition monitoring

Among the various wind turbine components, the gearbox has been shown to cause the longest downtime [6] and is the most costly to maintain throughout a turbine's 20-year-plus design life [7]. Gearbox faults, with high replacement costs, complex repair procedures and revenue loss caused by a long downtime, are widely considered a leading issue for the wind turbine drive train condition monitoring (CM) [5, 8, 9]. Common wind turbine gearbox failure modes are bearing faults and gear tooth damage [10]. The stochastically varying torque on the gearbox is considered to be a major root cause for bearing and gear wear, driving gearbox failure modes and affecting gearbox life. Typical gear faults include pitting, scuffing, chipping and more seriously, cracks [11]. In a recent study, Gray and Watson [12] have shown that the gearbox alone could be responsible for up to one-third of all the lost onshore wind turbine availability. This problem is exacerbated offshore where the harsh weather and sea conditions could prevent maintenance or component replacement for long periods of time. Few reliability data are still publicly available for the offshore wind turbines. However, 3 years of available data from the Egmond and Zee wind farm in the Netherlands show how the gearbox downtime caused 55% of the total wind farm downtime [13].

The main wind turbine operator concerns about gearbox reliability, particularly offshore, are:

- High replacement costs following a failure.
- Complex repair procedures that incur high logistics costs and require favourable weather conditions [10].
- High revenue losses caused by a long downtime between the failures and repair completion.

Consequently, the gearbox has become an essential subject for the current commercial wind turbine CMS. Timely and reliable detection and diagnosis of the developing gear defects within a gearbox is an essential part of minimising an unplanned downtime of the wind turbines. The wind turbine CMS application was requested by insurance companies in Europe in the late 1990s, following a large number of claims triggered by catastrophic gearbox failures [14], although these root causes have largely been eliminated by changes in the wind turbine design. Today, a number of commercial wind turbine CMSs are available to the wind industry and they are largely based upon the experience of monitoring the conventional rotating machines. A cost-benefit analysis has shown that the lifetime savings derived from an early warning and the avoidance of the impending failures of the critical wind turbine components would more than offset the lifetime cost of a CM system [11].

A survey conducted by the UK Supergen Wind Energy Technologies Consortium [15] shows that the most popular CM approach for the gearbox is vibration monitoring using traditional Fourier transform analysis of the high frequency data to detect the fault-specific frequencies. However, applying the vibration-based CM to the wind turbines presents a few unique challenges. The wind turbines are variable load and speed systems operating under highly dynamic conditions, usually remote from technical support. This results in CM signals that are dependent not only on a component integrity but also on the operating conditions. One limitation of the conventional fast Fourier transform (FFT) analysis is its inability to handle non-stationary waveform signals that may not yield accurate and clear gearbox features. To acquire the directly comparable data and to allow the spectra to be recorded in apparently stationary conditions, a number of commercial CMSs can be configured to collect the vibration spectra within limited, pre-defined speed and power ranges [15]. To overcome the problems of the conventional FFT-based techniques and find improved solutions for the wind turbine CM, a number of advanced signal processing techniques, including wavelet transforms, time–frequency analysis and artificial intelligence techniques, have been also researched recently [8, 16–18]. However, most new techniques are unsuitable for an online CM use, because they are computing intensive, and have not been demonstrated yet in the operating wind turbines.

One major limitation of the current commercially available CMSs is that very few operators make use of the alarm and the monitoring information available to manage their maintenance because of the volume and the complexity of the data. In particular, the frequent false alarms and the costly specialist knowledge, required for a manual interpretation of the complex vibration data, have discouraged the wind turbine operators from making a wider use of the CMSs. This happens despite the fact that these systems are fitted to the majority of the large wind turbines (>1.5 MW) in Europe [18]. Moreover, with the growth of the wind turbine population, especially offshore, a manual examination and comparison of the CM data will be impractical unless a simplified monitoring process is introduced.

Current efforts in the wind CM industry are aimed at automating the data interpretation and improving the accuracy and the reliability of the diagnostic decisions, especially in the light of impending large-scale, offshore wind farm generation. This paper attempts to target this research area by experimentally defining an algorithm that could be incorporated into the current CMSs for an automatic gear fault detection and diagnosis. This algorithm could reduce the quantity of the information that the wind turbine operators must handle, providing improved detection and timely decision-making capabilities.

The paper initially investigates the effect of the gear tooth fault severity on the gearbox vibration signature by using the experimental results obtained from the 30 kW wind turbine Condition Monitoring Test Rig (WTCMTR) at Durham University. A frequency tracking algorithm that automatically detects and diagnoses the gear tooth faults is proposed and discussed. The performance of the proposed technique is then tested by using 750 kW gearbox datasets from the National Renewable Energy Laboratory's (NREL) wind turbine Gearbox Condition Monitoring Round Robin project [19]. These vibration signals were collected from a real wind turbine gearbox that had sustained gear damage during its field test.

3 Experimental methodology

3.1 Durham WTCMTR

Experimental research was performed on a 30 kW WTCMTR at Durham University, shown in Fig. 1, which has been designed to act as a model for a wind turbine drive train. The rig features a 54 kW DC motor driving a 3-phase, 4-pole, 30 kW wound rotor induction generator (WRIG) through a two-stage helical-gear parallel shaft gearbox. The first low-speed (LS) stage teeth 66/13 and the second high-speed (HS) stage 57/58 provide an overall gear ratio of 5:1 (4.9894:1). A complete description of the test rig and instrumentation can be found in [20].

The WRIG has external variable resistors connected to the rotor circuit that allowed a super-synchronous generator speed variation of 100 rev/min, from 1500 to 1600 rev/min, with a corresponding maximum power output of 3.6 kW. The DC motor was driven at constant and wind-like variable speed conditions to cover the allowed speed range. Variable speed machine testing was performed by using the driving data derived from a 2 MW wind turbine model [20]. Vibration

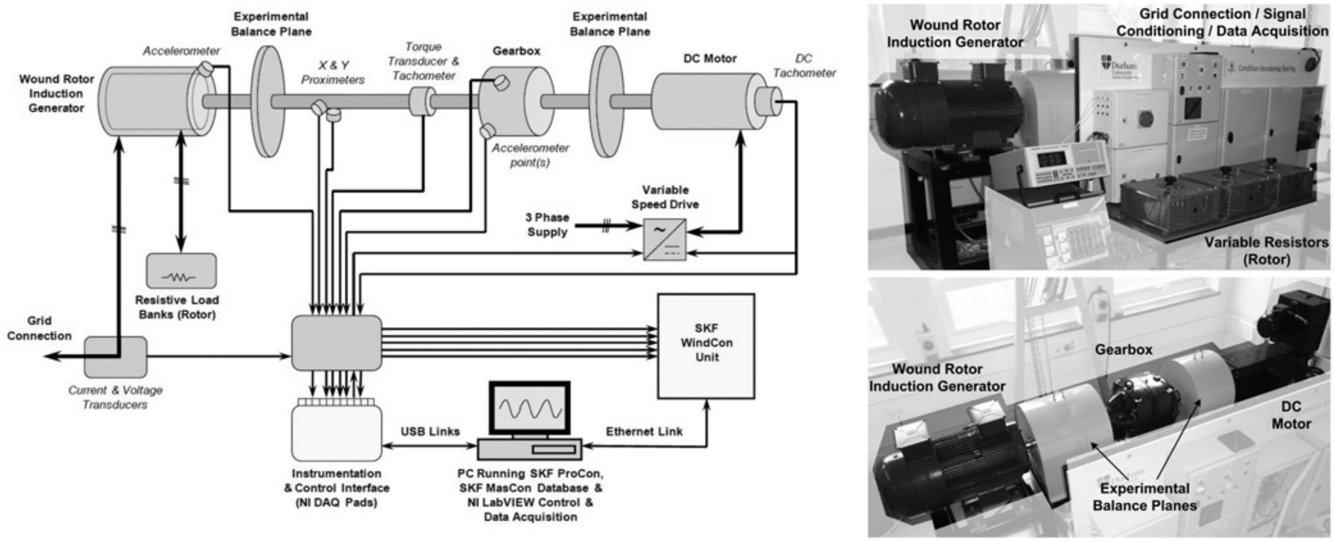

a *b*

Fig. 1 *Durham WTCMTR:*

a Schematic diagram
b Main components, instrumentation and control systems [20]

data from a single axis, vertically mounted accelerometer located on the gearbox HSS were processed by using an SKF WindCon unit 3.0, a commercial CMS producing FFT spectra, as currently used on the full size operational wind turbines. The sensor used was a piezoelectric accelerometer with integral electronics and a sensitivity of 500 mV/g.

3.2 Experimental procedure and data observation

In a geared transmission system, the main vibration source is the meshing action of the gears. The geometry of the gear profile has a crucial effect on the vibration behaviour. In practice, as the teeth deform under load, a meshing error is introduced even when the tooth profiles are perfect. In addition, there are geometric deviations from the ideal profiles, because of the gear manufacturing errors [16]. The most important components in the gear vibration spectra are the tooth meshing frequencies and their harmonics, together with the sidebands (SBs) caused by the modulation phenomena because of mean geometric errors on the tooth profiles, machining errors and wear. The gear meshing frequency is defined as the product of the number of the teeth on the gear and its turning speed. For the gearboxes in good condition, the SB level generally remains constant with time. Therefore an increment in the number and the amplitude of such SBs may indicate a fault condition [17]. Local tooth damage produces short-duration effects that add amplitude and frequency modulation effects to the meshing vibration, and in turn generate a higher level of SBs around the mesh harmonics. Moreover, the spacing of the SBs is related to their source and thus contains important diagnostic information [21]. In particular, the localised modulation effect takes place only during the engagement of the faulted teeth, but is repeated once in each revolution of the gear. As a consequence, the spectrum presents a large number of SBs of the tooth meshing frequency and its harmonics spaced by the faulted gear rotational frequency. Typically, the more damage that occurs, the more energy there is in the SBs [22]. In particular, the previous literature on the vibration analysis has shown that monitoring the second harmonic of the gear mesh and its SBs allows early detection of gear wear [23].

Experiments were conducted to investigate the progression of a tooth defect on a high-speed shaft (HSS) pinion, which was introduced into the WTCMTR at variable speed and generator load. The behaviour of a healthy pinion and of four faults of increasing severity were investigated by introducing progressive damage to the leading contact edge of one tooth of the gearbox pinion. These are called seeded fault tests. Fig. 2*a* shows the healthy pinion, Figs. 2*b–d* show the early stages of tooth wear, while Fig. 2*e* depicts the entire tooth missing. The vibration data from the accelerometer were processed by WindCon assuming a fixed sampling frequency and producing the FFT spectra with an overall frequency range of 5 kHz in the 1500–1600 rev/min HSS active range. The accelerometer measurement point in WindCon has been configured to provide the vibration spectra which refer to a measurement time window of 1.28 s. The produced spectra have 6400 resolution lines for a 5 kHz bandwidth with a resulting frequency resolution of 0.78125 Hz/line. WindCon's built-in diagnostic tools have been used to assist with the analysis of the spectra by tracking the machine component-specific, speed-dependent fault frequencies, their harmonics and SBs.

Normalised order spectra (X) were used to facilitate the comparison of the spectra and to identify the effect of a faulty tooth on the 30 kW gearbox vibration signature. A local gear defect, such as a cracked tooth, generates a disturbance in each revolution. Basically, a spectral order is introduced as a non-dimensional frequency parameter. If the frequency axis is normalised to the shaft rotation frequency any cyclic event synchronised with the shaft rotation will produce a spectral component at a fixed position even under the variable speed conditions. The advantage of this approach is that it is easier to focus on a specific cyclic mechanism. During the tests performed on the Durham WTCMTR the HSS speed signal was recorded simultaneously with the vibration data by the WindCon software. WindCon's frequency unit has a built-in tool allowing the operator to switch easily and automatically between Hz or order frequency units. This is done by dividing the FFT frequency in Hz by the HSS rotational speed, f_{HSS}, at which the

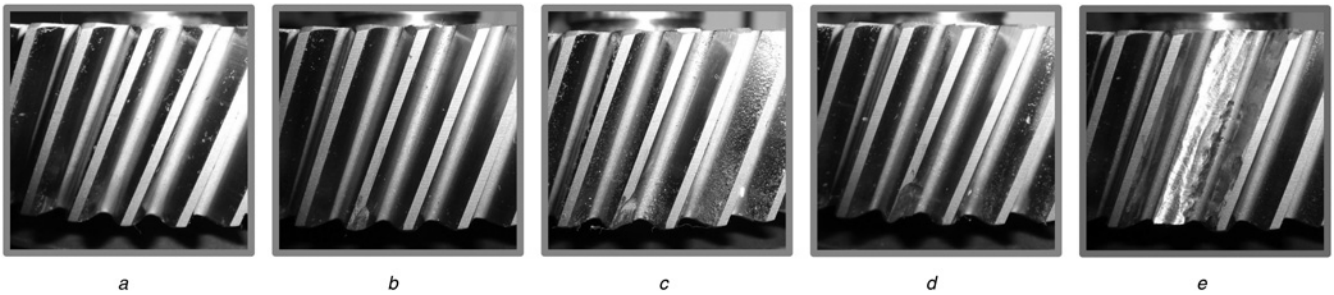

Fig. 2 *HSS pinion conditions investigated during the seeded fault tests*

a Healthy
Early stage of tooth wear
b 3-mm × 2-mm chip
c 5-mm × 5-mm chip
d 7-mm × 5-mm chip
e Missing tooth

spectrum was collected. The FFT spectra produced were compared under similar machine operating conditions. The measured data showed that the presence of an HSS pinion faulty tooth results in clear and prominent $f_{\rm HSS}$ SB components of the HS stage meshing frequency second harmonic, $2xf_{\rm mesh,HS}$, vibration signal. For this reason, monitoring the second harmonic narrowband window has been assumed as the most reliable and consistent indicator of the HSS pinion fault [24]. Fig. 3 shows the zoom-in view of the measured HSS order vibration spectra around the $2xf_{\rm mesh,HS}$ second harmonic, given by

$$2xf_{\rm mesh,HS} = 116X \tag{1}$$

for the healthy, early stages of tooth wear and the missing tooth conditions at a typical operating speed of 1560 rev/min and 51% of the maximum generator output. The spectra show an increase in the signal harmonic content as a result of the abnormal gear-set behaviour caused by the progressive damage introduced to the gearbox HSS pinion. The presence of the faulty pinion can be clearly seen in the $2xf_{\rm mesh,HS}$ harmonic which is heavily modulated by the HSS speed, $f_{\rm HSS}$, given by

$$f_{\rm HSS} = 1X \tag{2}$$

Ten SBs of the $2xf_{\rm mesh,HS}$ harmonic, SB_i, calculated as

$$\text{SB}_i = \left(2xf_{\rm mesh,HS} \pm i\right)X \tag{3}$$

where $i = \pm 1,\ \pm 2,\ \pm 3,\ \pm 4,\ \pm 5$, are visible in the spectra. The severity level of the tooth damage affects the SB amplitudes. Furthermore, the gear mesh centre harmonic, surrounded by the SBs, denotes which gear mesh the damaged gear is passing through. These two pieces of information indicate

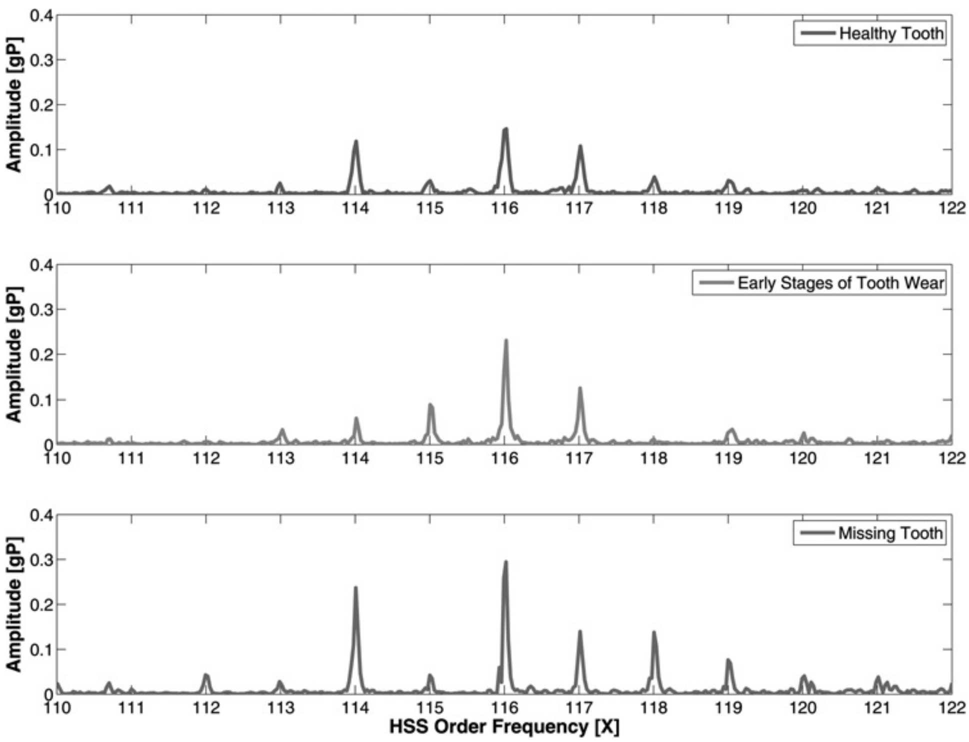

Fig. 3 *30 kW gearbox FFT vibration spectra during the seeded fault tests in the [110–120] X HSS order frequency bandwidth*

doi: 10.1049/iet-rpg.2013.0177

that the damaged component is passing through the HS stage gear mesh and is mounted on the HSS shaft.

3.3 Algorithm definition

The seeded fault tests conducted in this paper show that the presence of the meshing frequency harmonic SBs and their amplitudes could be valuable for detecting and diagnosing the gear defects. However, a manual analysis of the spectra, needed to compare the changes in the amplitudes for different conditions, requires significant time-consuming work because of the great number of frequency bands to be monitored. This calls for intelligent monitoring strategies that are able to detect the faulty signal in an automatic way. The suggestion is to track the overall power of the spectra associated with the $2xf_{\text{mesh,HS}}$ SB frequency window. Based on the experimental evidence, a gear condition indicator, the SB power factor (SBPF) algorithm, has been proposed to evaluate the gear damage during the wind turbine non-stationary load and speed operating conditions [24]. The SBPF algorithm sums the power spectrum amplitudes of the HS stage meshing frequency second harmonic and its first 5 SB peaks on each side. It has been calculated by using

$$\text{SBPF} = \text{PSA}\left(2xf_{\text{mesh,HS}}\right) + \sum_{i=-5}^{+5} \text{PSA}(\text{SB}_i) \tag{4}$$

where $\text{PSA}(2xf_{\text{mesh,HS}})$ and $\text{PSA}(\text{SB}_i)$, with $i = \pm1, \pm2, \pm3, \pm4, \pm5$, being the power spectrum amplitudes of the $2xf_{\text{mesh,HS}}$ harmonic and of its first 5 SBs spaced at the HSS rotational speed, respectively, shown in Fig. 4. The proposed algorithm facilitates the monitoring analysis, reducing each FFT spectrum to only one parameter for each data acquisition and avoiding a time consuming manual spectra comparison.

3.4 Results

The influence of the fault severity and the variable load operating conditions on the SBPF values has been investigated by performing variable speed tests on the WTCMTR at a load of up to 3.6 kW. The resulting SBPF values are shown in Fig. 5 against the load, expressed as a percentage of the maximum generator output in this condition, for the HSS pinion healthy conditions, for the early stages of tooth wearing and for a missing tooth. No frequency averaging has been performed on the data before the extraction of the SBPF values.

The results show that the SBPF magnitude is proportional to the magnitude of the gear fault level. This is because as damage develops on a gear tooth passing through the gear mesh, the SBs increase in amplitude, resulting in the larger SBPF values. The trend of the obtained SBPF values can be fitted by an exponential curve, relating vibration spectra power increase with machine load. In the full range of the load investigated, the SBPF values for the missing tooth case are higher than both the healthy and the early tooth wear cases, indicating a clear fault detection. The proposed algorithm works successfully even at the early stages of the tooth failure, showing a higher effectiveness at the percentage loads above 20%.

4 Algorithm validation

4.1 NREL wind turbine Gearbox Condition Monitoring Round Robin project

To validate the performance and the reliability of the proposed SBPF algorithm on a full size gearbox, the algorithm has been tested on the data from the NREL wind turbine Gearbox Condition Monitoring Round Robin project [19]. Vibration data collected from two identical 750 kW wind turbine gearboxes, tested on the NREL dynamometer test stand in Fig. 6, were used in this paper. A complete description of the NREL test-bed and instrumentation can be found in [25]. The gearboxes have an overall ratio of 1:81.491 and feature one low-speed (LS) planetary stage and two parallel stages, an intermediate-speed (IS) and HS, respectively. Table 1 provides the details of the NREL gearbox nomenclature for the internal elements and the gear teeth number.

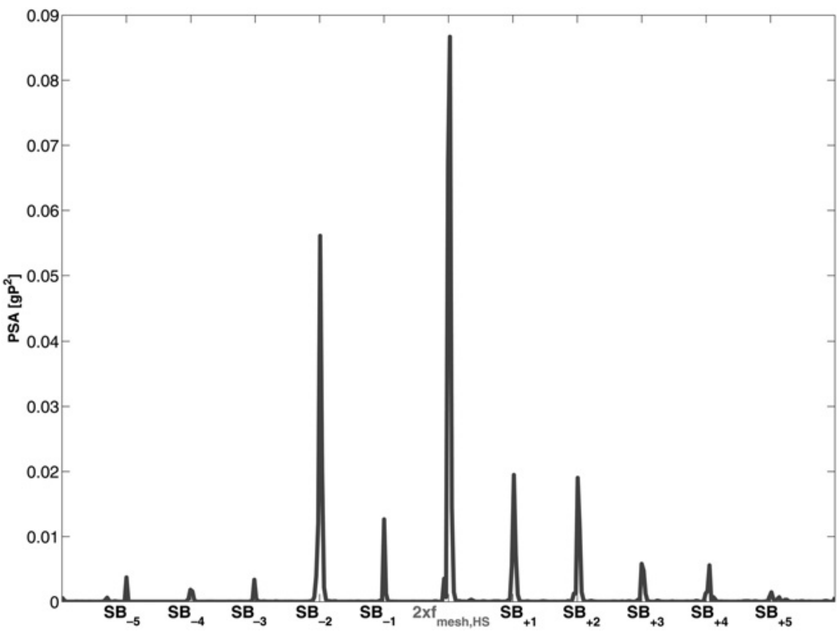

Fig. 4 *Typical FFT power spectrum around the $2xf_{mesh,HS}$ harmonic in the case of a faulty HSS pinion*

IET Renew. Power Gener., 2014, Vol. 8, Iss. 4, pp. 380–389
doi: 10.1049/iet-rpg.2013.0177

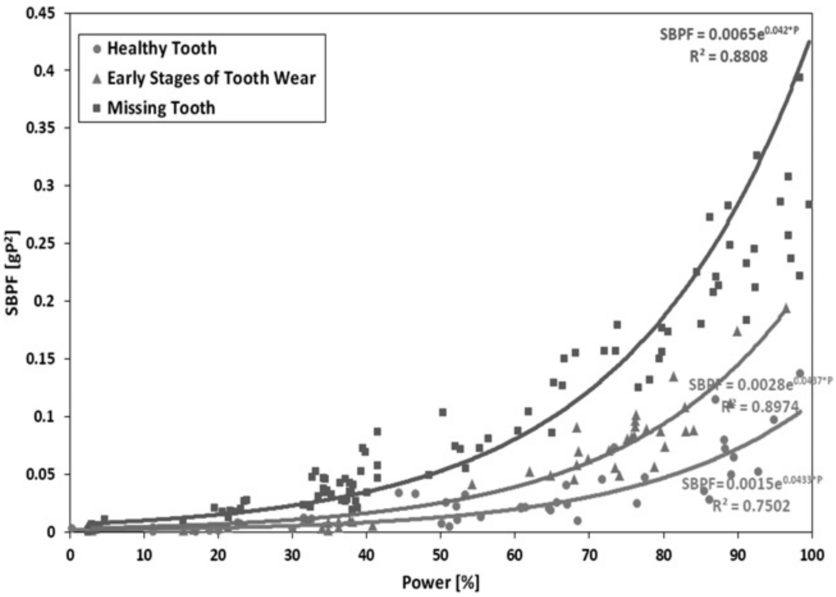

Fig. 5 *Influence of the fault severity and the variable load operating conditions on the SBPF values during the seeded fault tests*

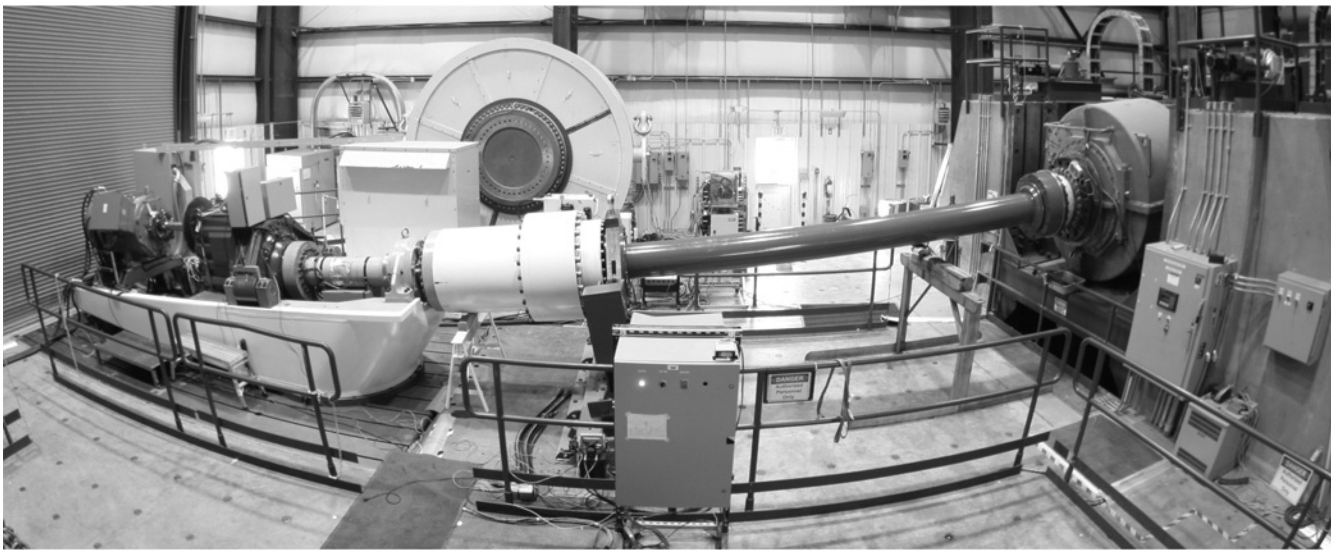

Fig. 6 *NREL dynamometer test stand with a 750 kW gearbox installed*
Photo by Lee Jay Fingersh/NREL 16913

Baseline data were collected on the dynamometer test stand from a healthy test gearbox, which had no operational experience. Data then were collected from the dynamometer retest of an identical gearbox after its internal components had sustained damage from its field test. This gearbox first finished a run-in in the NREL dynamometer and was then sent to a nearby wind farm for a field test. The test gearbox was installed on a three-blade, stall-regulated, upwind wind turbine with a rated power of 750 kW and a rated wind speed of 16 m/s, respectively. In the field, two oil loss events occurred and led to some damage to the gears and the bearings inside the test gearbox. The gearbox was then removed from the field and retested under controlled conditions in the NREL test stand. During the retest, various condition monitoring data were collected, including the measurements of vibration and oil debris. Once the dynamometer retest was completed, the gearbox was disassembled and a detailed failure analysis was conducted [26]. Severe scuffing of the HS shaft gear set was one of the 12 instances of damage found during a failure analysis. Fig. 7 shows the damaged HSS pinion.

4.2 Vibration data analysis

The task of this paper was to validate the SBPF analysis of the vibration data to detect and diagnose the HSS pinion damage by using the data collected by two independent accelerometers, AN6 and AN7, mounted radially on the gearboxes intermediate-speed shaft (ISS) and HSS, respectively. Both these sensors were integrated-circuit piezoelectric-type accelerometers with a sensitivity of 100 mV/g.

The available dataset refers to an HSS speed of 1800 rev/min and to 50% of the rated power, which is the highest

doi: 10.1049/iet-rpg.2013.0177

Table 1 NREL 750 kW gearbox nomenclature and teeth number

Gear element	Location	Number of the teeth	Mate teeth	Ratio
ring gear	LS planetary stage	99	39	—
planet gear	LS planetary stage	39	99	—
sun pinion	LS planetary stage	21	39	5.71
intermediate gear	IS parallel stage	82	23	—
intermediate pinion	IS parallel stage	23	82	3.57
HS gear	HS parallel stage	88	22	—
HS pinion	HS parallel stage	22	88	4.0
overall ratio:				81.491

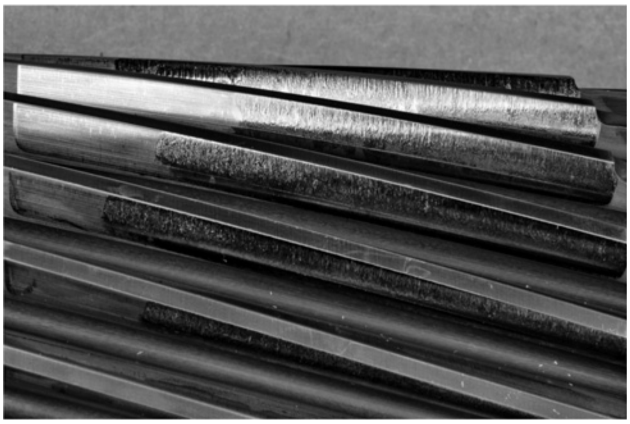

Fig. 7 *Pinion damage on a 750 kW gearbox HSS*
Photo from GEARTECH/NREL 19743

test load applied to reduce the chances of a catastrophic gearbox failure. For each accelerometer, it contains:

- For the healthy gearbox: 1 single FFT spectrum collected by a commercial CMS at 5 kHz for a duration of 1.6 s.
- For the faulty gearbox: 40 kHz raw vibration data collected continuously for 10 min.

The dataset presented some challenges for deriving an SB amplitude comparison system baseline. This was overcome by the windowing data from the faulty gearbox through a 1.6 s time window and then processing the data by using the built-in FFT algorithm in MATLAB. For each accelerometer, the resulting 375 FFT spectra have then been consistently compared against the available healthy spectrum, presenting the same frequency resolution. Figs. 8*a* and *b* show an example of the zoom-in view of the healthy and the faulty HSS order vibration spectra around the HS stage meshing frequency second harmonic, $2xf_{\text{mesh,HS}}$, given by

$$2xf_{\text{mesh,HS}} = 44X \qquad (5)$$

for the AN6 and the AN7 accelerometer data, respectively.

In both the cases, when comparing the degraded gearbox with the nominal baseline healthy gearbox, the increase in the energy content of the $2xf_{\text{mesh,HS}}$ harmonic and its SBs can be clearly seen. In the faulty spectrum, the HS meshing frequency second harmonic is heavily modulated by the HSS rotational speed, $f_{\text{HSS}} = 1X$. The SB spacing indicates severe damage in the HSS pinion.

4.3 Algorithm implementation

To quantify these observations from the vibration data, SBPF values were extracted from the baseline spectrum and the 375 degraded gearbox spectra. The results are shown in Figs. 8*c* and *d* for AN6 and AN7, respectively. In both the cases, the SBPF magnitude is much larger for the degraded gearbox compared with the baseline gearbox, representing an average value of 0.021 $(\text{gP})^2$ and 0.013 $(\text{gP})^2$, respectively. From the SBPF methodology, there is a strong indication that there is damage on the high-speed shaft pinion. These results, on a full-size 750 kW gearbox, provide further credibility to the SBPF algorithm, already proven on the 30 kW WTCMTR, for a timely detection and a diagnosis of gear damage.

In this case, the use of the vibration signals collected from two independent accelerometers located at strategic positions on the gearbox casing improves the confidence in the SBPF fault detection and diagnosis capability, eventually reducing the false alarms. This is particularly interesting when considering that one issue around the CMS data interpretation is to rely on a single signal, which could lead to false alarms from the monitoring process [10].

5 Discussion

Experimental work on the low-power Durham WTCMTR has allowed the implementation of the repeated seeded-fault conditions under controlled conditions. The developed SBPF algorithm allows the assessment of a gear fault severity by tracking a progressive tooth gear damage during the variable speed and load operating conditions of the test rig. The performance of the proposed technique has then been successfully tested on the signals from a field test of a full size wind turbine gearbox that has sustained gear damage.

The SBPF detection sensitivity to the tooth damage has been calculated by determining, for each load condition, the percentage change of the SBPF value. For each case, the SBPF detection sensitivity (%SBPF) between the faulty and the healthy conditions has been defined as

$$\%\text{SBPF} = \frac{\text{SBPF}_{\text{f}} - \text{SBPF}_{\text{h}}}{\text{SBPF}_{\text{h}}} \times 100 \qquad (6)$$

where SBPF_{h} and SBPF_{f} are the SBPF values for the healthy and the faulty cases, respectively. Table 2 summarises the average SBPF detection sensitivities to the HSS pinion damage for the 30 kW Durham gearbox and the 750 kW NREL gearbox datasets.

In the case of the Durham 30 kW gearbox dataset, the sensitivity analysis shows that the SBPF technique proves successful in the detection of both the early and the final stages of the gear tooth damage, with average detection sensitivities of 100 and 320%, respectively. The influence of the fault severity on the SBPF detection sensitivity values is evident; the more damaged the pinion the easier it is to discriminate the fault.

In the case of the NREL dataset, although the gearbox damage was more complex than in a typical operational wind turbine [19] and the dataset provided refers to only

IET Renew. Power Gener., 2014, Vol. 8, Iss. 4, pp. 380–389
doi: 10.1049/iet-rpg.2013.0177

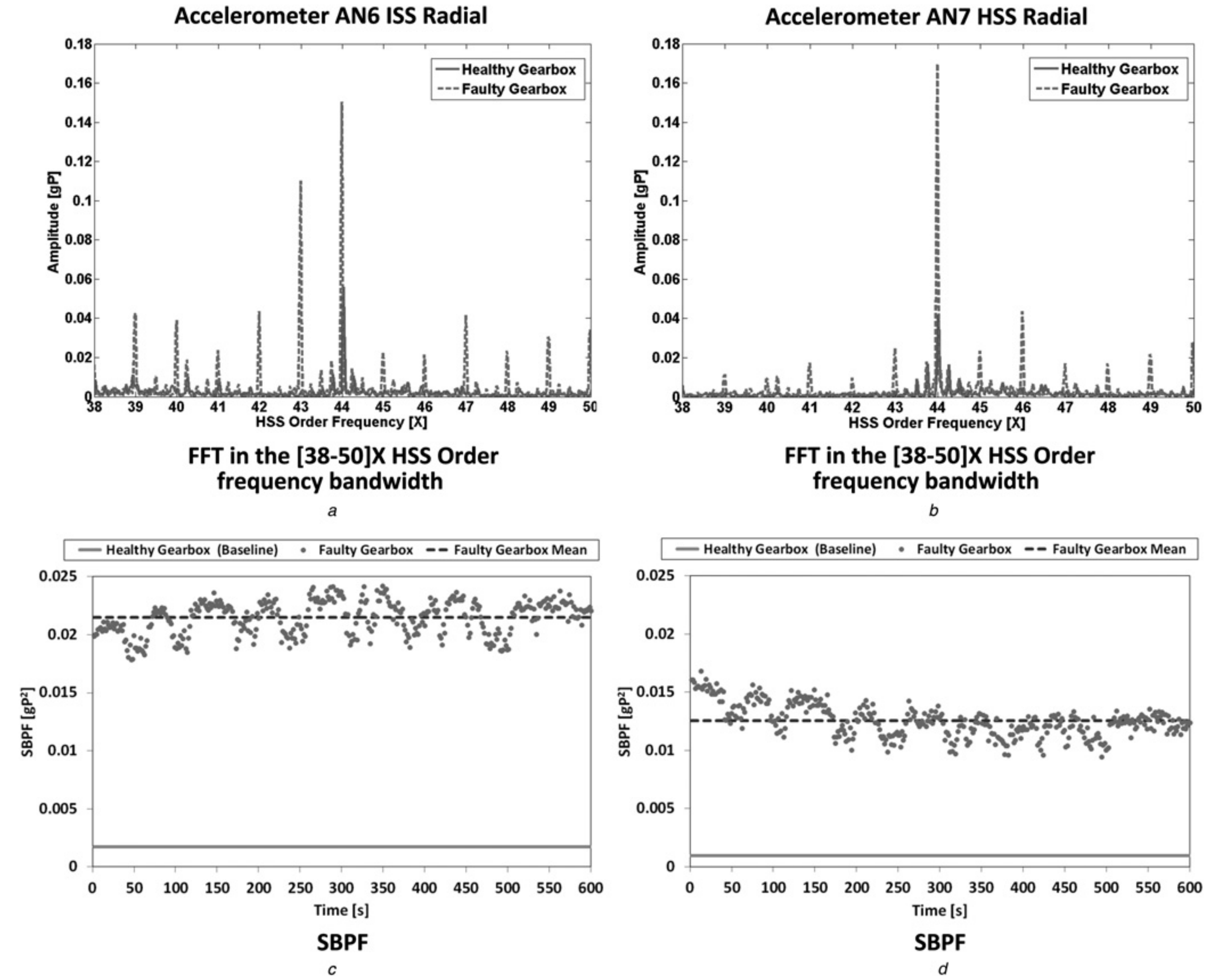

Fig. 8 *Vibration FFT spectra and the SBPF plots for two accelerometer positions on healthy and faulty identical 750 kW gearboxes*

a Accelerometer AN6 ISS Radial, FFT spectrum
b Accelerometer AN7 HSS Radial, FFT spectrum
c Accelerometer AN6 ISS Radial, SBPF plot
d Accelerometer AN7 HSS Radial, SBPF plot

Table 2 Durham (30 kW) and NREL (750 kW) gearbox average SBPF detection sensitivities

Gearbox	HSS pinion fault severity	Accelerometer location	Average % SBPF
Durham – 30 kW seeded fault tests	early stages of tooth wear	HSS vertical	100
	missing tooth	HSS vertical	320
NREL – 750 kW gear box datasets	severe scuffing	AN6 ISS radial	1140
	severe scuffing	AN7 HSS radial	1251

one speed and load operational condition, the SBPF detection and diagnostics technique proves successful in the detection of the HSS pinion damage, with an average detection sensitivity of 1140 and 1251% for the AN6 ISS radial and the AN7 HSS radial accelerometers, respectively. Since the analysed dataset contains multiple gearbox progressed faults, it is believed that the SBPF diagnostic performance could be improved when deployed in the field, bearing in mind the smaller number of the faults usually present during the early stages of the gearbox fault evolution.

The proposed SBPF algorithm facilitates the monitoring analysis, reducing each FFT spectrum to only one parameter for each data acquisition. By automating the condition monitoring of the gears, the SBPF reduces the quantity of the vibration information that the wind turbine operators must handle, providing improved detection and timely decision-making capabilities. The SBPF can be monitored over time, trended and compared with one or more predetermined threshold levels to provide warnings and alarms to the operators.

The knowledge of the gearbox load is fundamental to apply effectively the SBPF technique. The current commercially available CMSs usually provide information on the turbine load. This will allow the SBPF technique to work in context with the gearbox load. Otherwise, in case the turbine load is not available, the operator has to take the SBPF measurements only when the machine is at its full load.

The SBPF methodology, based on the analysis of the dynamics of the gears, can easily be scaled to the higher wind turbine power levels. However, this would probably imply an increase in the spectral background noise because of the higher complexity of the wind turbine drive trains compared with the small-scale WTCMTR.

For the gearbox parallel stages, the SBPF is easily applicable to the harmonics of each fundamental gear mesh frequency using both the gear and the pinion SBs, once the multistage gearbox configuration and the number of the teeth of each gear element are known. This information allows for the calculation of the gear damage features, such as the meshing frequencies, their second harmonic and the spacing of the SBs because of the gear wear modulation phenomena for each stage, and the extraction of the corresponding SBPF values. For the planetary stages, the analysis of the SB patterns could be more complicated because of a low mechanical transmissibility from the gear components and the multiple contact points between each planet gear meshing and the sun and ring gears.

6 Conclusions

This paper has proposed an experimental sideband algorithm for an automatic wind turbine gear tooth fault detection and diagnosis, which has been validated by analysing the vibration signals from a full size wind turbine gearbox with the HSS pinion faults. The following specific conclusions arise:

- The SBPF algorithm proved effective in detecting the presence of the gear damage introduced into a 30 kW Test Rig gearbox, that is, damage location, and in identifying the precise damaged gear, that is, damage diagnosis, with a detection sensitivity of 100–320%.
- The SBPF successfully allowed the assessment of a gear fault severity on the test rig by tracking a progressive tooth damage, from the early stages of development, during the variable speed and load conditions.
- The experimentally defined SBPF technique has also been successfully tested against the vibration data from an NREL 750 kW wind turbine gearbox, which had experienced severe high-speed shaft gear set scuffing, with detection sensitivities of 1140 and 1251%.
- Confidence in the NREL gearbox results is enhanced by a strong SBPF detection and diagnosis evidence from two independent accelerometers.
- The proposed methodology is relatively simple to implement into a commercial wind turbine CMS for an automatic gear fault detection and diagnosis.
- The generation of the SBPF trends from the vibration spectra and the definition of the magnitude thresholds for the fault severity levels could indicate to a wind turbine operator when a maintenance action needs to be performed.
- The SBPF can be easily adapted to detect gear damage on all the wind turbine gearbox parallel stages, while its applicability to the planetary stages still requires more investigation.
- Compared with the conventional FFT approach used in the current commercial vibration-based CMSs, requiring a time consuming visual spectra analysis, the SBPF approach enables an automatic detection and diagnosis of the gear faults with a low risk of false alarms. This will lead to an increased accuracy of the wind turbine drive-train vibration-based condition monitoring.

7 Acknowledgments

This work was funded as part of the UK EPSRC Supergen Wind Energy Technologies programme, EP/H018662/1. The authors thank NREL for its support for this work and for providing the vibration data used for the validation of the SBPF algorithm.

8 References

1 EWEA: 'Wind Energy, Statistics & Targets'. European Wind Energy Association Report, 2013, available at http://www.ewea.org/fileadmin/files/library/publications/statistics/Factsheets.pdf, last accessed 23 April 2013
2 McMillan, D., Ault, G.W.: 'Quantification of condition monitoring benefit for offshore wind turbines', *Wind Eng.*, 2007, **31**, (4), pp. 267–285
3 Walford, C.A.: 'Wind turbine reliability: understanding and minimizing wind turbine operation and maintenance costs'. Sandia National Laboratories Report SAND2006–1100, March 2006, available at http://prod.sandia.gov/techlib/access-control.cgi/2006/061100.pdf, last accessed 20 April 2013
4 Wiggelinkhuizen, E., Verbruggen, T., Braam, H., Rademakers, L., Xiang, J.P., Watson, S.: 'Assessment of condition monitoring techniques for offshore wind farms', *Trans. ASME, J. Sol. Energy Eng.*, 2008, **130**, (3), p. 9
5 Hyers, R.W., McGowan, J.G., Sullivan, K.L., Manwell, J.F., Syrett, B.C.: 'Condition monitoring and prognosis of utility scale wind turbines', *Energy Mater., Mater. Sci. Eng. Energy Syst.*, 2006, **1**, (3), pp. 187–203
6 Faulstich, S., Hahn, B., Tavner, P.J.: 'Wind turbine downtime and its importance for offshore deployment', *Wind Energy*, 2011, **14**, (3), pp. 327–337
7 Sheng, S.: 'Investigation of various condition monitoring techniques based on a damaged wind turbine gearbox'. Proc. Eighth Int. workshop on Structural Health Monitoring, Condition-based Maintenance and Intelligent Structures, Stanford, California, 13–15 September 2011
8 Hameed, Z., Hong, Y.S., Cho, Y.M., Ahn, S.H., Song, C.K.: 'Condition monitoring and fault detection of wind turbines and related algorithms: a review', *Renew. Sustain. Energy Rev.*, 2009, **13**, (1), pp. 1–39
9 Wilkinson, M.R., Spinato, F., Tavner, P.J.: 'Condition monitoring of generators and other subassemblies in wind turbine drive trains'. IEEE Int. Symp. on Diagnostics for Electric Machines, Power Electronics and Drives, SDEMPED 2007, 6–8 September 2007
10 Feng, Y., Qiu, Y., Crabtree, C.J., Long, H., Tavner, P.J.: 'Monitoring wind turbine gearboxes'. Wind Energy, Article first published online: 16 July 2012, DOI: 10.1002/we.1521
11 Walford, C., Roberts, D.: 'Condition monitoring of wind turbines: technology overview, seeded-fault testing and cost-benefit analysis'. EPRI Report No. 1010419, 2006
12 Gray, C.S., Watson, S.J.: 'Physics of failure approach to wind turbine condition based maintenance', *Wind Energy*, 2012 **13**, (5), pp. 395–405
13 Crabtree, C.J.: 'Operational and reliability analysis of offshore wind farms'. Proc. Scientific Track of the European Wind Energy Association Conf., Copenhagen, Denmark, 16–19 April 2012
14 Tavner, P.J.: 'Offshore wind turbines: reliability, availability and maintenance' (The Institution of Engineering and Technology, 2012, 1st edn.)
15 Crabtree, C.J., Zappalà, D.: 'Survey of commercially available condition monitoring systems for wind turbines'. Supergen Wind Energy Technologies Consortium Report, 2012, available at http://www.supergen-wind.org.uk, last accessed 2 September 2012
16 Randall, R.B.: 'Vibration-based condition monitoring: industrial, aerospace and automotive applications' (John Wiley & Sons, Ltd, 2011)
17 García Márquez, F.P., Tobias, A.M., Pinar Pérez, J.M., Papaelias, M.: 'Condition monitoring of wind turbines: techniques and methods', *Renew. Energy*, 2012, **46**, (0), pp. 169–178
18 Yang, W., Tavner, P.J., Crabtree, C.J., Feng, Y., Qiu, Y.: 'Wind turbine condition monitoring: technical and commercial challenges'. Wind Energy, Article first published online: 1 August 2012, DOI: 10.1002/we.1508
19 Sheng, S.: 'Wind turbine gearbox condition monitoring round Robin study – vibration analysis'. NREL Report No. TP-5000-54530, 2012, available at http://www.nrel.gov/publications/, last accessed 26 November 2012

20 Crabtree, C.J.: 'Condition monitoring techniques for wind turbines'. PhD thesis, Durham University, UK, 2011
21 Randall, R.B.: 'A new method of modelling gear faults', *Trans. ASME, J. Mech. Des.*, 1982, **104**, (2), pp. 259–267
22 Goldman, S.: 'Vibration spectrum analysis: a practical approach' (Industrial Press Inc., 1999, 2nd edn.)
23 Mobley, R.K.: 'Vibration fundamentals' (Newnes/ Butterworth-Heinemann, 1999, 1st edn.)
24 Zappalà, D., Tavner, P.J., Crabtree, C.J.: 'Gear fault detection automation using windcon frequency tracking'. Proc. Scientific Track of the European Wind Energy Association Conf., Copenhagen, Denmark, 16–19 April 2012
25 Musial, W., McNiff, B.: 'Wind turbine testing in the NREL dynamometer test bed'. Proc. American Wind Energy Association's WindPower 2000 Conf., Palm Springs, CA, 30 April–4 May 2000
26 Errichello, R., Muller, J.: 'Gearbox reliability collaborative gearbox 1 failure analysis report'. NREL Report NREL/SR-5000-530262, 2012, available at http://www.nrel.gov/docs/fy12osti/53062.pdf, last accessed 15 September 2012

www.ietdl.org

Published in IET Renewable Power Generation
Received on 7th October 2013
Revised on 10th February 2014
Accepted on 13th February 2014
doi: 10.1049/iet-rpg.2013.0324

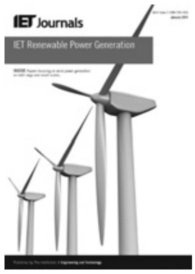

ISSN 1752-1416

Detection of rotor electrical asymmetry in wind turbine doubly-fed induction generators

Mahmoud Zaggout[1,2], Peter Tavner[1], Christopher Crabtree[1], Li Ran[3]

[1]School of Engineering and Computing Sciences, Durham University, Durham, DH1 3LE, UK
[2] Department of Electrical Engineering, Faculty of Engineering, Misurata University, Misurata, Libya
[3]School of Engineering, University of Warwick, Coventry, CV4 7AL, UK
E-mail: m.n.zaggout@durham.ac.uk

Abstract: This study presents a new technique for detecting rotor electrical faults in wind turbine doubly-fed induction generators (DFIGs), controlled by a stator field-oriented vector control scheme. This is a novel method aimed at detecting and identifying rotor electrical asymmetry faults from within the rotor-side inverter control loop, using the error signal, to provide a future method of generator condition monitoring with enhanced detection sensitivity. Simulation and experimental measurements of the proposed signals were carried out under steady-state operation for both healthy and faulty generator conditions. Stator current and power were also investigated for rotor electrical asymmetry detection and comparison made with rotor-side inverter control signals. An investigation was then performed to define the sensitivity of the proposed monitoring signals to fault severity changes and a comparison made with previous current, power and vibration signal methods. The results confirm that a simple spectrum analysis of the proposed control loop signals gives effective and sensitive DFIG rotor electrical asymmetry detection.

1 Introduction

Over the last 15 years, variable speed wind turbines (WTs) with doubly-fed induction generators (DFIGs) have become the most applied WT technology and the drive train choice for up to 60% of large, >1.5 MW WTs [1]. The typical configuration of these WTs consist of a wound rotor induction generator (WRIG) with stator winding connected directly to the grid, whereas the rotor winding is connected via slip-rings to a partially rated back-to-back converter and operating as a DFIG, as shown in Fig. 1*a*. In this system, the variable speed range is approximately ±25% of the synchronous speed, as shown in Fig. 1*b*. The rating of the power electronic converter is only 30% of the generator capacity, which makes this concept attractive and popular from an economic point of view.

From Fig. 1*b*, whenever the wind speed is below the rated the WT-DFIG operates at variable speed, under the control of the converter. However, when the wind speed reaches the rated, the WT-DFIG delivers full power, fixed at the top of its speed range, subject to variations because of wind turbulence.

Like every electrical machine, these generators are prone to electromechanical faults and require attention at the incipient fault stage to avoid fault escalation leading to breakdown. However, a survey to compare the failure rates of WT induction generator (IG) with other machines in industrial applications based on data reported in [2–7] has shown the significance of WT generator failures, which are mainly concentrated in the rotor, stator and machine bearings, as shown in Fig. 2.

The study also showed that the failures associated with the rotor and other parts contribute significantly to the total number of induction machine failures, particularly in wind applications, ranging from 12 to 50% of generators failures. Owing to these percentages, WT-IG rotor fault diagnosis has received considerable attention and WT DFIG rotor asymmetry has been shown to be a significant indicator of WT generator faults, caused by either rotor winding or brush-gear defects. Previous work investigated the effects of induction machine rotor faults on the machine electrical signals [8–9] or mechanical signals [10]. Each method has its advantages but it is essential that the selected method should have a high sensitivity to incipient faults and prevent unexpected breakdown or total destruction of the machine.

Nowadays, in most applications the induction machine is part of a complex system with closed-loop control. In this case, condition monitoring techniques usually applied to line-fed, open-loop machines may be ineffective, as the control modifies the behaviour of machine signals and masks their information. Therefore other signal behaviours should be investigated and more sophisticated procedures adopted to find better indices to assess machine condition. Consequently a number of authors have investigated fault detection in closed-loop induction machines using machine control loop signals. Based on simulation and experimental investigation, frequency analyses of control current signals have been presented in [11] to diagnose the stator and rotor faults of controlled squirrel cage induction motors (SCIMs). A new online method based on measured torque control

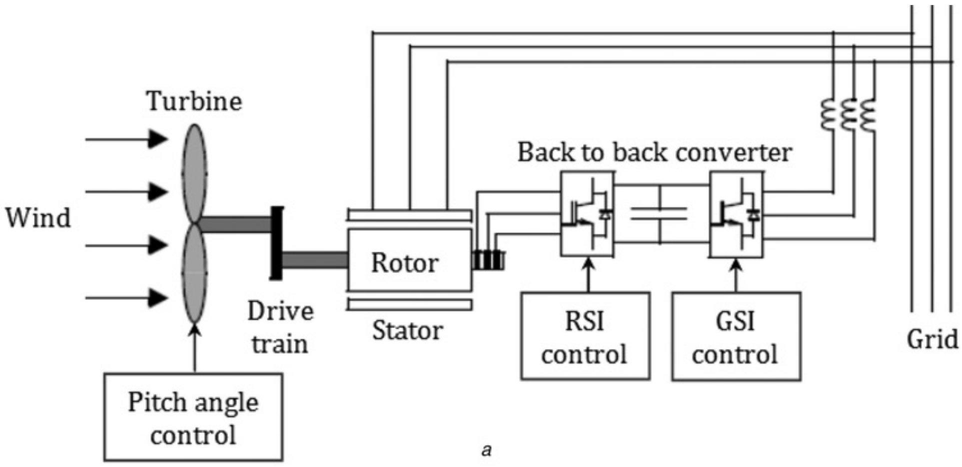

a

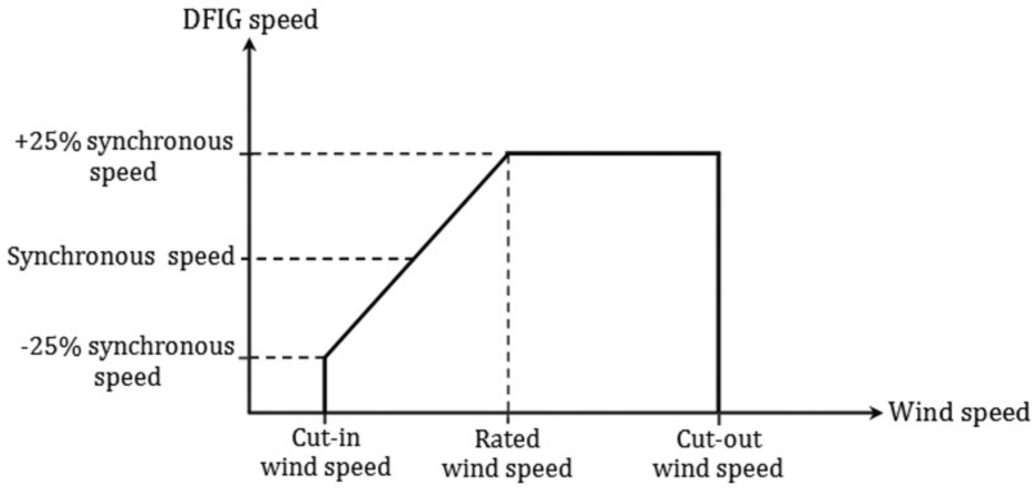

b

Fig. 1 *Typical configuration of WTs.*
a Variable speed WT with DFIG controlled with a partial-scale power converter
b Generator speed against wind speed

current component and calculated slip frequency was proposed in [12]. Later, diagnosis of SCIM rotor faults through current controller error signals, current controller output signals and the estimated rotor flux analyses were studied in [13]. Another investigation of rotor faults in

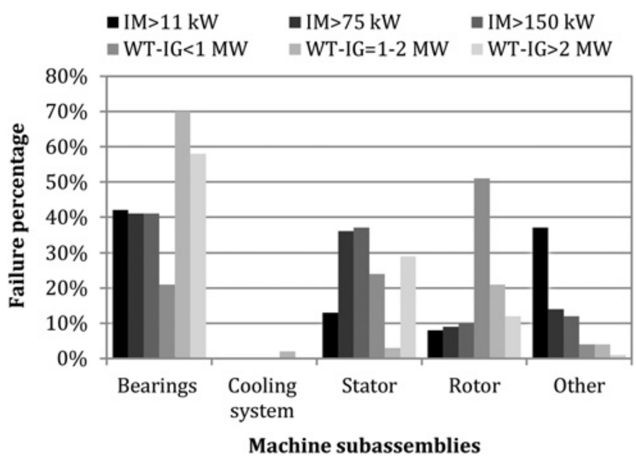

Fig. 2 *Distribution of failed subassemblies in induction machines based on data reported in [2–7]*

different controller topologies, particularly in IM open or closed speed loop control, was presented in [14]. More recently, this research was developed [15] to include a SCIM with direct torque control.

However, understanding the influence of WT-IG failures on different generator control variables and using these signals for monitoring the WT-IGs has received little research attention. A simulation and experimental study was presented in [16] to identify the best diagnostic procedure for unbalanced DFIG phase fault detection. It was confirmed that the current signature analysis technique could be utilised, but a more interesting technique would be to use rotor modulation signal spectral analysis. More recently, the sensitivity of rotor modulation signal spectra, with respect to the variation of current loop bandwidth, was evaluated in [17] as a new and reliable diagnostic index.

The work described in this paper extends previous WT-IG failure diagnosis research in [8], based on stator current and total power spectra, to consider WT-DFIG fault detection using generator control loop signals. It particularly concentrates on the rotor side inverter (RSI) and compares the effectiveness of control loop fault detection signals with stator current, total power and vibration signals. Frequency analysis of the RSI current control error signal is proposed as an effective new diagnostic index for

WT-DFIGs. Using such signals will improve WT condition monitoring because:

- Control error signals are dominated by the fault effect and their spectra clearly show faulty harmonics allowing them to be detected more clearly, compared to generator signal spectra.
- These signals are already available for control purposes and can easily be measured, giving them an advantage over some conventional techniques, which require costly additional instrumentation and data processing.

The novelty of the paper is its consideration of control signals for condition monitoring of a variable speed WT-DFIG, demonstrated by simulation and verified on a realistic Test Rig. The rest of the paper is organised as follows: Section 2 gives an in-depth investigation of the influence of rotor electrical asymmetry on RSI control signals. Section 3 describes the overall simulation and experimental tools. Section 4 presents the RSI control scheme. Section 5 describes the simulation results for the proposed signals, and then confirmed by experimental results. The improvement in condition monitoring detection performance with the proposed method has been demonstrated in comparison with previous stator current, power and vibration analysis methods. These comparisons will demonstrate that the proposed method can reliably detect rotor fault, regardless of fault severity.

2 Rotor electrical asymmetry

Generator rotor faults, because of the increasing resistance or open-circuit of one or more of the rotor windings or brush-gear circuits, results in rotor electrical asymmetry. Such faults are caused by a combination of magnetic, thermal and mechanical stresses acting on the rotor, varying dynamically with loading and environmental conditions. Although rotor asymmetries do not initially cause a machine to fail, they can have serious secondary effects, increasing losses, reducing efficiency and lowering generator and turbine reliability. However all of this could be avoided if the machine was supervised by an appropriate condition monitoring system.

2.1 Basic derivation of electrical frequencies

The sequence of electromagnetic and mechanical phenomena due to asymmetry in the stator or rotor of an induction machine was explained in [18]. They give rise to a series of harmonic components in the rotor current at frequencies $-sf, \pm 3sf, \ldots, \pm isf$, where s is the generator slip, f is the stator frequency and $i = 1, 3, 5, \ldots$ Although the RSI controller is designed and implemented for a healthy generator, its closed-loop action attempts to ensure a correct operation even in the presence of any rotor asymmetry. In this case, the PI current control loops try to impose balanced rotor current references by applying unbalanced voltages to the rotor winding. Therefore typical generator current faulty harmonics might become less visible because of the compensating action of the RSI controller. In contrast, these fault-components should remain clearly observable in the error signals inside rotor current PI controller, allowing these signals to be considered as new effective diagnostic indices.

The rotor faulty harmonics ($\pm isf$) will be transferred into RSI control loop signals and are expected to produce a relevant harmonic in the d- and q-rotor currents (i_{dr} and i_{qr}) at $\pm 2msf$ where $m = 1, 2, 3, \ldots$ Under rotor fault condition, the d- and q-rotor currents, in the stator flux linkage reference frame, can be written as

$$i_{dr}(t) = I_{dr_0}(t) + \sum_{m=1}^{\infty} I_{dr_{\pm 2m}} \cos(2\pi(\pm 2m\mathrm{s}\mathrm{f})t + \text{Ø}_{dr_{\pm 2m}}) \quad (1)$$

$$i_{qr}(t) = I_{qr_0}(t) + \sum_{m=1}^{\infty} I_{qr_{\pm 2m}} \cos(2\pi(\pm 2m\mathrm{s}\mathrm{f})t + \text{Ø}_{qr_{\pm 2m}}) \quad (2)$$

where I_{dr} and I_{qr} are the harmonic magnitudes of d- and q-rotor currents, Ø_{dr} and Ø_{qr} are the harmonic phase shifts of d- and q-rotor currents. Subtracting (1) from the d-rotor reference current ($i_{dr\ \mathrm{ref}}$) and (2) from the q-rotor reference current ($i_{qr\ \mathrm{ref}}$), the error signals (εi_{dr} and εi_{qr}) inside PI control loops is obtained. Theoretically $i_{\mathrm{dr\ ref}}(t) \cong I_{\mathrm{dr}_0}(t)$ and $i_{qr\ \mathrm{ref}}(t) \cong I_{qr_0}(t)$. Then, the error signals can be written as

$$\mathcal{E}i_{dr}(t) \cong -\sum_{m=1}^{\infty} I_{dr_{\pm 2m}} \cos(2\pi(\pm 2m\mathrm{s}\mathrm{f})t + \text{Ø}_{dr_{\pm 2m}}) \quad (3)$$

$$\mathcal{E}i_{qr}(t) \cong -\sum_{m=1}^{\infty} I_{qr_{\pm 2m}} \cos(2\pi(\pm 2m\mathrm{s}\mathrm{f})t + \text{Ø}_{qr_{\pm 2m}}) \quad (4)$$

From (3) and (4), as mentioned before, the current error signals are expected to contain mainly the faulty harmonics, which will dominate the error signal spectrum and can be detected by applying a simple FFT algorithm. In this work, the used FFT algorithm analyse the component signals in both the positive and negative sequence, plotting both on the positive axis of the spectrum. Therefore attention will be focused only on the $2sf$ component inside the control signals, as well as the $2sf$ and $(1\text{–}2s)f$ in the total power and stator current, respectively.

2.2 Fault representation

In order to test several fault situations in a machine operating as IG in a WT system, the main problem is to realise a fault situation similar to reality. In practice, rotor electrical asymmetries can be modelled by inserting an additional resistance in series with the rotor phase windings. In this research, the rotor asymmetry was created on an experimental Test Rig, by means of external variable resistor (R_{ex}) connected into one phase of the rotor circuit via the machine slip rings. This allows different asymmetry levels to be introduced in a controlled fashion. When R_{ex} is greater than zero the faulted phase resistance is present. For clarity, the asymmetric rotor resistance is given as a percentage of the balanced phase resistance, where rotor asymmetry, ΔR, in percent, is

$$\Delta R(\%) = \frac{R_{\mathrm{ex}}}{R_{\mathrm{r}}} \times 100 \quad (5)$$

where R_{r} is the healthy rotor phase resistance. The values of R_{ex} and ΔR depend on the unbalance severity. Note that rotor unbalance can be in one phase or more and it will produce the same relative frequency harmonics in the machine or control signals. In the same way, the fault can be applied to a MATLAB model of the Test Rig.

IET Renew. Power Gener., 2014, Vol. 8, Iss. 8, pp. 878–886
doi: 10.1049/iet-rpg.2013.0324

3 Investigation tools

The proposed technique in this paper has been validated experimentally on a Durham Test Rig which was designed to investigate and monitor various WT drive-train failure modes. Over the last few years, this Rig has been used to develop a number of WT generator condition monitoring algorithms [8, 19, 20]. Fig. 3 shows the block diagram of the Test Rig developed to operate as a WT-driven DFIG. It comprises a 4-pole, 30 kW WRIG driven through a 5:1 gearbox by a 54 kW DC motor, which simulates the WT. The stator windings of the WRIG were directly connected to the grid whereas the rotor windings were fed from a PWM-RSI controlled by an xPC TargetBox real-time system. The DC Link was provided by a battery, to avoid any interaction from the GSI. Therefore the machine operates as a DFIG, whose details are given in the Appendix. The RSI control algorithm is designed based on a stator field-oriented vector control scheme. The controller model was represented initially in the MATLAB Simulink and when the operator is ready to run the controller, the model can be simply compiled to be executable and loaded onto the xPC TargetBox. However, because of the limitations of the xPC TargetBox hardware in synchronising the generated phase PWM signals both the DC-link voltage and the stator voltage were purposely reduced, compared to the generator and converter rating, to provide lower distortion control and generator signals and increase safety. This voltage reduction lowered the machine flux density. This was not expected to affect the prospective accuracy of a proposed rotor asymmetry detection technique on a WT-DFIG operating at normal operating voltage and flux density, when the PWM signals are perfectly synchronised. The Test Rig was used to obtain the measured results presented in this paper.

A mathematical model of the experimental Test Rig was built in MATLAB Simulink by the authors to represent all the mechanical and electrical parts of the Rig, as well as the grid and losses. The validity of the experimental results, in time and frequency domains, was verified by comparison with this model, which was used to obtain all the simulated results presented in this paper.

4 Rotor-side inverter controller

Similar to a real WT-DFIG, the rotor is associated with a back-to-back converter and the stator directly connected to the grid in the closed-loop Test Rig configuration. The RSI is controlled in a synchronously rotating *dq*-axis frame, with the *d*-axis oriented along the stator flux vector position and the *q*-axis leading the *d*-axis by 90°. In this way, a decoupling between the electrical torque and the rotor excitation current is obtained in order to control stator active power. The stator currents are assumed to be positive when flowing from the grid into the machine. Since the stator is connected to the grid, and the influence of the stator resistance is small, the stator magnetising current can be considered constant. Under stator-flux orientation, the active and reactive powers (P_s and Q_s) delivered by the stator of the machine can be written as a function of *dq*-rotor current components and stator voltage magnitude ($|V_s|$) as [1]

$$P_s \cong -1.5 \frac{L_M}{n_{sr} L_s} |V_s| i_{qr} \tag{6}$$

$$Q_s \cong 1.5 \frac{L_m}{L_s} |V_s| \left(\frac{|V_s|}{\omega L_m} - \frac{i_{dr}}{n_{sr}} \right) \tag{7}$$

where L_m and L_s are the generator magnetising and stator self-inductances, n_{sr} is the stator–rotor turns ratio and ω is the stator flux speed. By assuming the stator voltage magnitude and frequency are constant, the stator active power can be considered proportional to the *q*-axis rotor current component and the stator reactive power related to the *d*-axis rotor current component.

5 Results

In order to verify the proposed detection method several tests were carried out on the physical Test Rig and its MATLAB Simulink model under both healthy and faulty conditions. The analysis was achieved by comparing the harmonic spectra of stator current and power with those of *d*- and

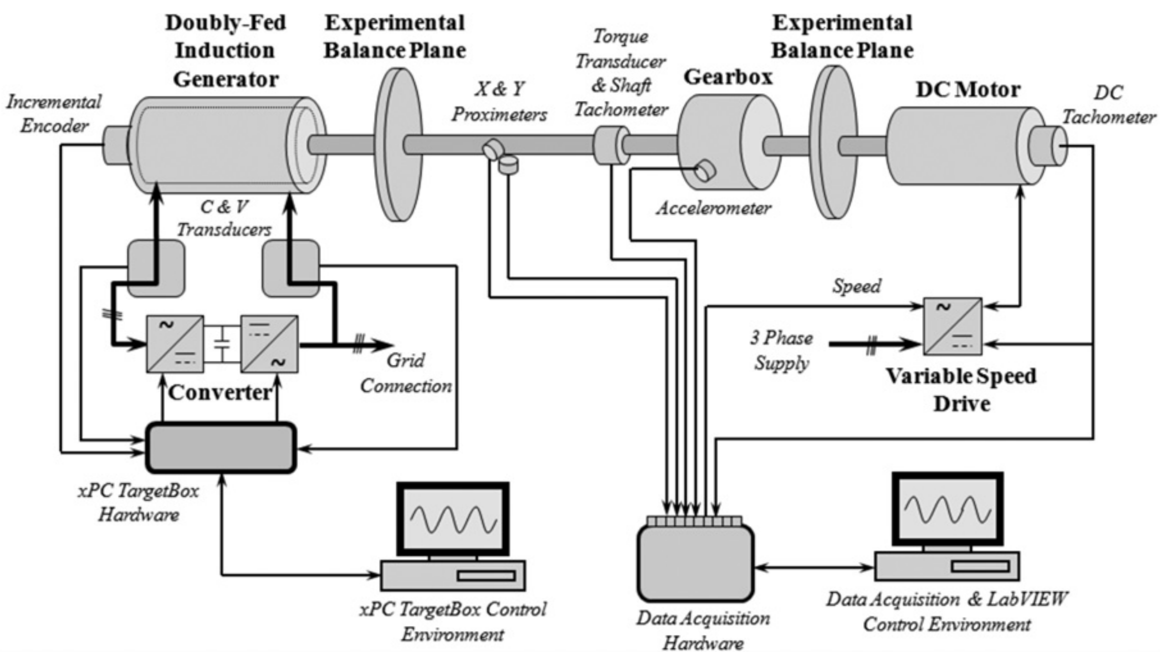

Fig. 3 *Schematic diagrams of the WT drive train Test Rig with DIFG*

doi: 10.1049/iet-rpg.2013.0324

q-rotor current error signals. The harmonic spectra were obtained by applying an FFT algorithm to instantaneous values of the monitored variables which were sampled at 5 kHz.

5.1 Fixed speed operation

In both the simulation and experimental environments, the system was run at super-synchronous fixed speed of 1600rev/min, with the generator delivering 4.7 kW and absorbing 1.95 kVAr, under healthy or faulty conditions. This speed Test Rig operation was undertaken with the speed of the Test Rig DC drive motor controlled by a turbine model, developed, tested and verified by Strathclyde University, representing a WT operating above rated wind speed at its rated power, as shown in Fig. 1*b*. The speed of the Test Rig was approximately constant, but varied because of turbulence of the wind driving the turbine model and the action of the DFIG RSI control loop to maintain speed constant. The effect of any rotor electrical asymmetry on the WT generator speed would have been negligible, as the turbine and generator inertia damp this effect. The healthy rotor resistance, including internal winding resistance, was 0.235 Ω per phase and additional resistance up to 0.047 Ω was successively added to one phase to give 20% unbalance. To simplify the presentation of results, all signal spectral analyses have been normalised to 0 dB at the highest harmonic component magnitude, depending on the signal type.

5.1.1 Simulated results: Simulations were carried out operating the machine in a noise-free environment. For balanced and unbalanced operations, the dq-rotor error current spectra are presented in Fig. 4. The healthy current spectra, Figs. 4*a* and *c*, indicate the fundamental harmonic at 0 Hz, 0 dB and a set of harmonics at 19.5, 39, 58.5, 78 and 97.5 Hz, produced by the PWM process used in the RSI. This set of harmonics is less visible in the faulty spectra shown in Figs. 4*b* and *d*. The faulty spectra show a significant rise in the magnitude of the $2sf$ component at frequency at 6.5 Hz, as expected, which dominate the whole two spectra.

Simulated healthy and faulty stator current and total power spectra for this condition are shown in Fig. 5. Only one phase current signal is presented and analysed here, as is usually the case for Motor Current Signal Analysis (MCSA). The healthy current spectrum in Fig. 5*a* indicates the fundamental harmonic at 50 Hz whereas the power spectrum in Fig. 5*c* indicates the fundamental harmonic at 0 Hz. They show that the reflection of rotor switching harmonics is not visible in the stator current compared to the total power. The faulty stator current and total power spectra in Figs. 5*b* and *d* show visible harmonics related to the fault at 56.5 Hz and 6.5 Hz with magnitudes of −66 dB and −71 dB. Note that, both the total power and stator current faulty harmonics are not as large in magnitude as in the case of error signals, Fig. 4.

It can be observed that the harmonic spectra of the d- and q-rotor current error signals show larger amplitude harmonic components than at other fault-related frequencies, giving a better fault indication. Thus, the proposed method is interesting and could be adopted for improved condition monitoring.

5.1.2 Measured results: For comparison with simulated results, in the physical Test Rig the RSI controller and DFIG measured signals were collected, with rotor circuits balanced or unbalanced, from the xPC TargetBox. However, the measured signals now incorporate higher levels of noise than the simulated signals. This noise was caused experimentally by

- The small but continuous grid frequency fluctuation, between 49.9 and 50.1 Hz;
- DFIG stator magnetising unbalance;
- University site grid voltage unbalance which, although small, contributes to stator unbalance and noise.

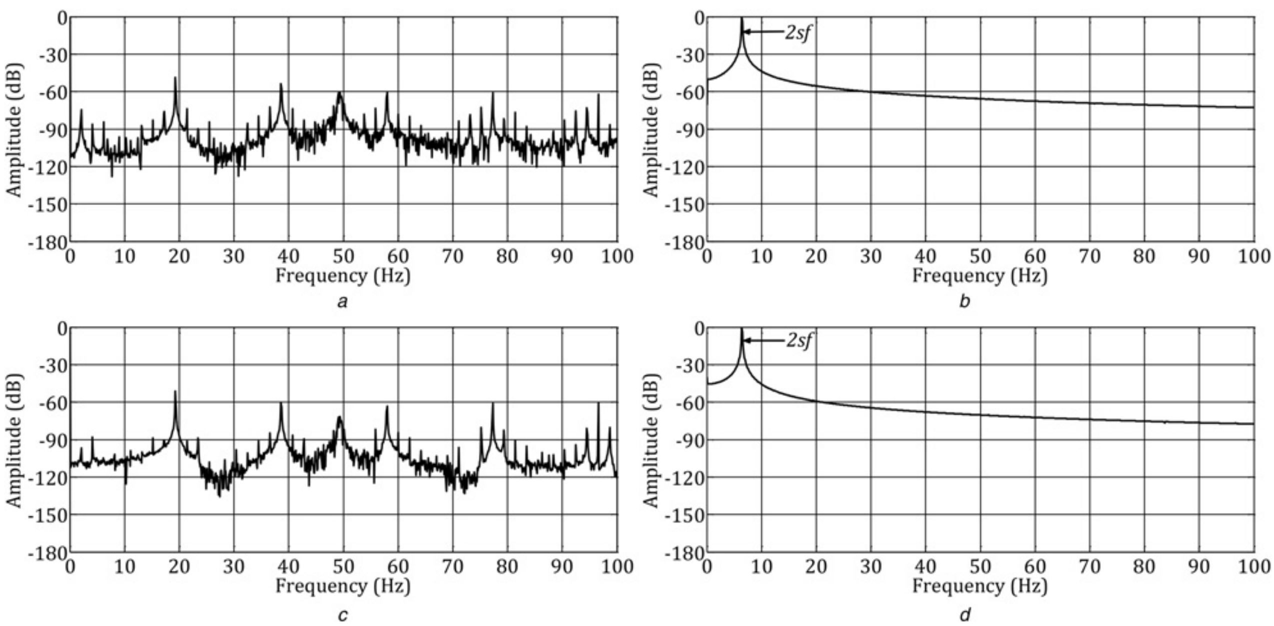

Fig. 4 *Healthy and faulty simulated spectra for generator control signals*

a d-rotor current error-healthy condition
b d-rotor current error-faulty condition
c q-rotor current error-healthy condition
d q-rotor current error-faulty condition

doi: 10.1049/iet-rpg.2013.0324

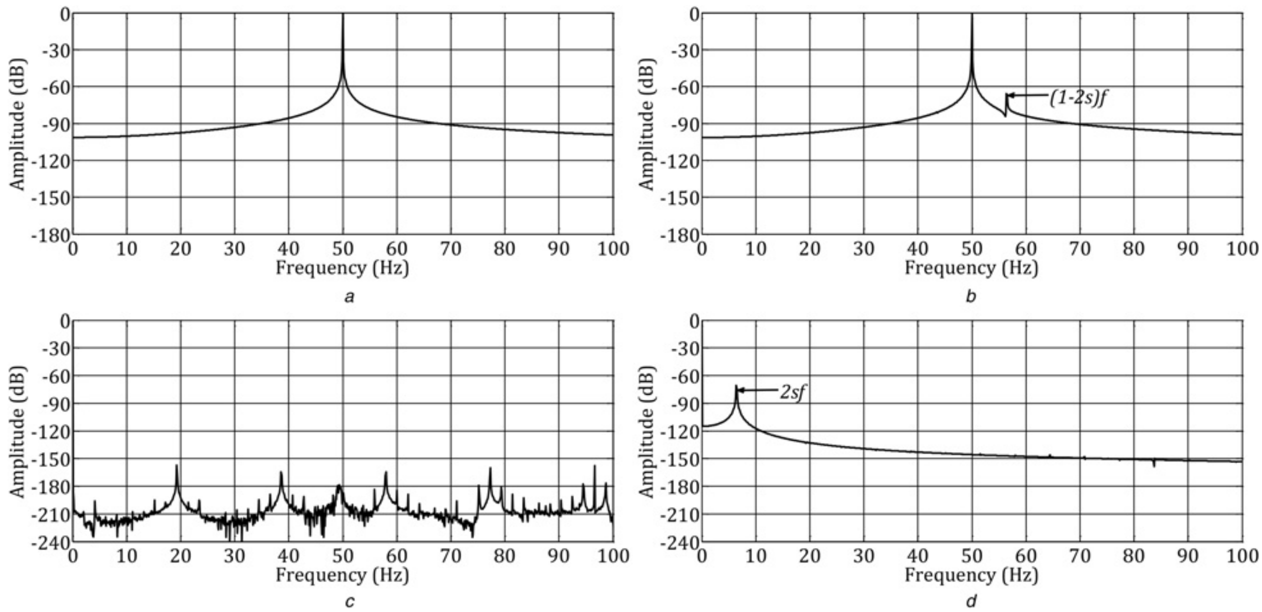

Fig. 5 *Healthy and faulty simulated spectra for stator current and total power signals*

a Stator current-healthy condition
b Stator current-faulty condition
c Stator total power-healthy condition
d Stator total power-faulty condition

These noise sources were unavoidable in the current measurements from the physical Test Rig; however, they are not specific only to the Test Rig but would also be present in a real WT-DFIG, so any functioning condition monitoring system needs to accommodate them.

Frequency analysis of the error signals is shown in Fig. 6. From these figures, the harmonic $2sf$ related to the fault presence is located at 6.5 Hz with a magnitude of −28 and −22 dB for *d*-and *q*-rotor error current spectra, respectively. However, comparing with the simulation results in Fig. 4, it can be seen that these magnitudes are not the highest values in this case and the highest magnitudes appear at 100 Hz in both spectra. These harmonics, as explained above, are related to the stator fault contributed by a little grid voltage unbalance.

The stator current harmonic spectra are presented in Figs. 7*a* and *b*. The magnitude of the faulty harmonic is less visible with a value of −47 dB for the stator current at

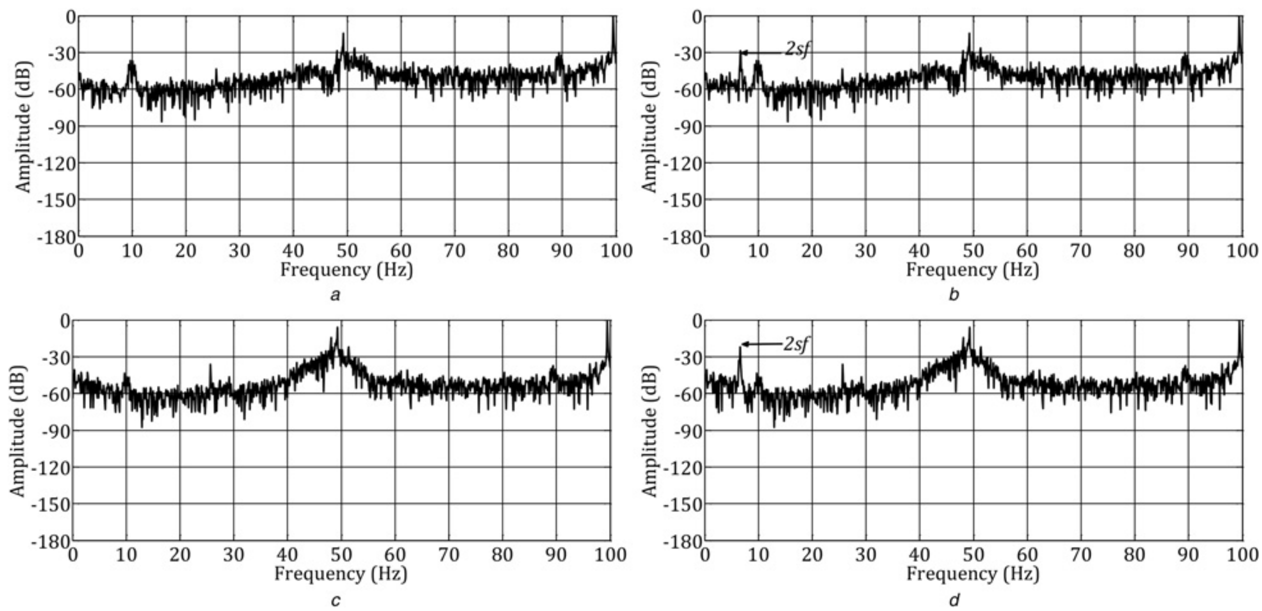

Fig. 6 *Healthy and faulty measured spectra for generator control signals*

a d-rotor current error-healthy condition
b d-rotor current error-faulty condition
c q-rotor current error-healthy condition
d q-rotor current error-faulty condition

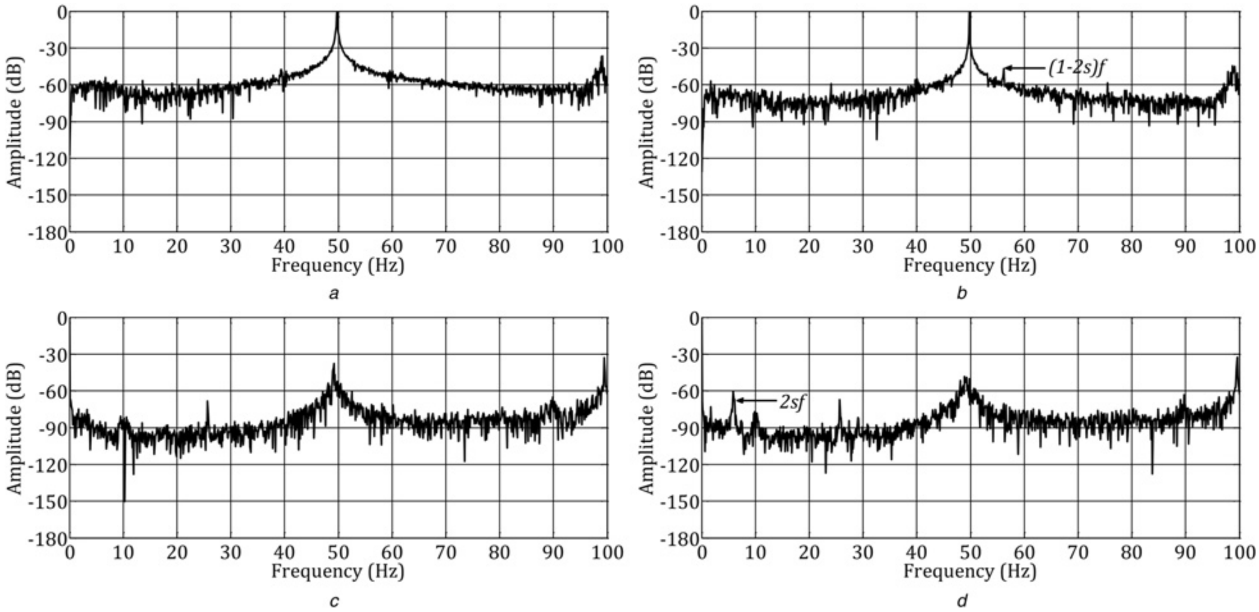

Fig. 7 *Healthy and faulty measured spectra for stator current and total power signals*

a Stator current-healthy condition
b Stator current-faulty condition
c Stator total power-healthy condition
d Stator total power-faulty condition

56.5 Hz (1–2s)*f*. The total power harmonic spectra are presented in Figs. 7*c* and *d* and the faulty harmonic component magnitude at 6.5 Hz (2*sf*) is −60 dB.

Again, these experimental results confirm that the control error signals have faulty component magnitudes at frequency (2*sf*) much higher than the other signals used in this research. This shows that the proposed technique has the potential to detect an incipient electrical asymmetry fault on a WT-DFIG, since the magnitude of the characteristic harmonic frequency can be easily detected.

5.2 Signal sensitivity on faulty detection

From the simulation and experimental results, it can be observed that all signal frequency analyses show an increase in the power level of the fault-frequency components. However, the signal that provides the best fault detection depends not only on the faulty harmonic magnitude but also on its sensitivity. The higher the sensitivity, the better the fault signature resolution. To verify the sensitivity achievable using the control and other signals as diagnostic indices, further simulation and experimental tests were carried out with the Test Rig DFIG in a 1400 rev/min steady-state condition at various fault-severities. The sensitivity values are obtained from the simulated and measured results by

$$\mathrm{Sensitivity(dB)} = 10\log_{10}\left(\frac{A_\mathrm{f} - A_\mathrm{h}}{A_\mathrm{h}}\right) \quad (8)$$

where A_f and A_h are the magnitudes of the faulty and healthy harmonic components. Complete results of the sensitivity for

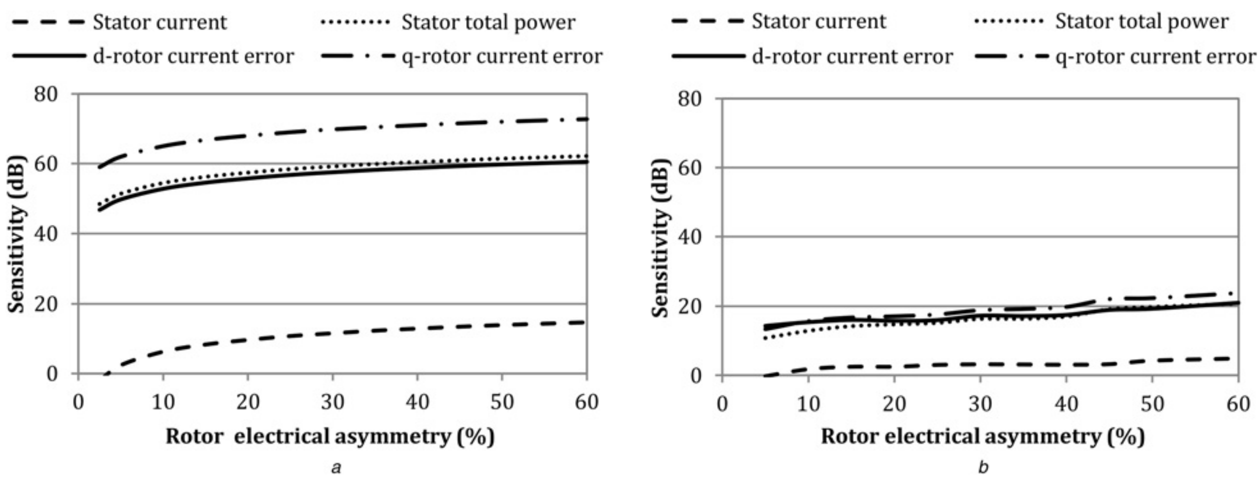

Fig. 8 *Sensitivity from*

a Simulation data
b Measured Test Rig data

doi: 10.1049/iet-rpg.2013.0324

Table 1 Comparison of fault detection sensitivities between open- and closed-loop Test Rig

Test Rig system	Closed-loop system		Open-loop system				
signal type	current error signals inside RSI		stator current		stator total power		vibration
	εi_{dr}	εi_{qr}					
frequency analysis	FFT		frequency tracking algorithm				SBPF
fault type	20% rotor electrical asymmetry		23% rotor electrical asymmetry				missing tooth of high speed shaft pinion
harmonics of interests	$2sf$		$(1-2s)f$	$(3-2s)f$	$2sf$	$(2-2s)f$	$2f_{mesh,HS}$ and its first five sideband peaks on each side
stator voltage	78 V		230 V				
sensitivity calculated at 1550 rev/min	14.3 dB	15.2 dB	3.0 dB	4.7 dB	6.7 dB	4.9 dB	5.1 dB
sensitivity calculated at 1600 rev/min	14.6 dB	15.3 dB	3.7 dB	6.9 dB	7.3 dB	6.0 dB	4.6 dB

the four signal types are summarised and compared in Fig. 8. It can be seen that the sensitivity of all signals, both simulated and measured, increased with fault severity. From Fig. 8*a*, the sensitivities of the simulated control error signals had high values with the ability to detect even small fault severities. However, the *q*-rotor current error sensitivity was higher than the *d*-rotor current error sensitivity as well as those of the stator

The measured results, Fig. 8*b*, again show that despite the experimental effects of noise the *q*-rotor current error signal still has higher sensitivity over the other signals. They show a decreased sensitivity compared with simulation results, because of the noise in the measured signals, however, the results still show a significant and usable sensitivity for condition monitoring purposes.

From these results, it is evident that control signals, *d*- and *q*-rotor current errors, are sensitive to any rotor electrical asymmetry, with an advantage to the *q*-rotor current error compared to *d*-rotor current error, stator power or current.

Further tests have also been carried out with the Test Rig operating as when the WT was operating below rated wind speed and therefore rated power, see Fig. 1*b*, operating under full variable speed conditions. The results are similar to those presented here but have been omitted from this paper because of limitations of space.

5.3 Test Rig open and closed-loop fault detection sensitivities

As mentioned in Section 3, the open-loop Test Rig has been used in previous work to develop other techniques for WT-IG fault detection. One of these techniques is the frequency tracking algorithm based on stator line current and total power analysis [8], which investigated rotor electrical asymmetry detection for faults similar in magnitude to this paper. More recently, another technique was introduced in [21] based on the sideband power factor (SBPF) algorithm for WT gearbox fault detection by vibration analysis. The SBPF was successful in detecting gearbox tooth faults on a high speed shaft pinion. New work is being done to extend the vibration analysis for rotor electrical asymmetry detection in WRIG but results are not yet available. Therefore only the vibration analysis results for gearbox fault detection are presented in this comparison. Table 1 shows an experimental comparison between fault detection sensitivities on the closed-loop Test Rig using RSI control signals and open-loop Test Rig using stator current, power and vibration signals.

As can be seen from Table 1, the RSI control current error fault sensitivity is much higher than the frequency tracking algorithm with the same fault magnitude. This comparison confirms that the closed-loop detection sensitivities, even in the presence of noise, are considerably greater than they were achieved open loop with current, and power signals. This is because, as shown in (3) and (4), the *d*- and *q*-current error signals in the closed-loop system are mainly the reflection of rotor health condition changes whereas in the open-loop system the fault-related response is influenced by more factors than the fault. A direct comparison with the SPBF vibration results for electrical fault detection will be possible once more results are available.

6 Conclusions

This paper has demonstrated a new WT-DFIG rotor fault detection technique based on frequency analysis of the *d*- and *q*-rotor error current signals inside the DFIG RSI controller loop.

- The development of fault harmonics inside the proposed signal spectra has been explained.
- An RSI stator flux-oriented vector control scheme has been set up to verify this technique.
- A set of simulated and measured results have been obtained from a physical Test Rig and its validated model under fixed speed operating conditions, representing the conditions when the WT would be at full power.
- It has been shown that *d*- and *q*-rotor current error signals have characteristic frequencies that are a strong diagnostic index for rotor electrical asymmetry.
- The study has also clearly shown that the proposed *q*-control error signal provides better sensitivity to faults than stator current or total power signals and is a successful diagnostic even for small faults.
- Fault detection sensitivity in the closed-loop WT-DFIG Test Rig from the RSI control signals has a better sensitivity than previously published fault detection on an the open-loop WT-IG Test Rig from vibration, current and power signals.
- This technique is simple, attractive and could easily be extended to diagnose other generator or embedded turbine faults.
- Because of limitations of space in this paper, investigation of the method under full variable speed conditions, when the WT is below rated power, will be reported in a later publication.

• This study has shown that the measured results gave a lower sensitivity to faults than simulated results because of noise in the experimental system, which requires future investigation.

7 Acknowledgments

This work was supported by the UK EPSRC as part of the Supergen Wind Consortium under grant EP/D034566/1 and the Libyan Government by a PhD scholarship for the first author. The authors would like to thank the National Renewable Energy Centre, Blyth, for their assistance in the original provision of the Test Rig.

8 References

1 Zaggout, M.: 'Wind turbine generator condition monitoring via the generator control loop', *PhD thesis, School of Engineering and Computing Sciences*, Durham University, 2013
2 Motor Reliability Working Group: 'Report of large motor reliability survey of industrial and commercial installations, Part I', *IEEE Trans. Ind. Appl.*, 1985, **IA-21**, (4), pp. 853–864
3 Motor Reliability Working Group: 'Report of large motor reliability survey of industrial and commercial installations, Part II', *IEEE Trans. Ind. Appl.*, 1985, **IA-21**, (4), pp. 865–872
4 Motor Reliability Working Group: 'Report of large motor reliability survey of industrial and commercial installations, Part III', *IEEE Trans. Ind. Appl.*, 1987, **IA-23**, (1), pp. 153–158
5 Albrecht, P., Appiarius, J., McCoy, R., Owen, E., Sharma, D.: 'Assessment of the reliability of motors in utility applications-updated', *IEEE Trans. Energy Convers.*, 1986, **EC-1**, (1), pp. 39–46
6 Thorsen, O., Dalva, M.: 'A survey of faults on induction motors in offshore oil industry, petrochemical industry, gas terminals, and oil refineries', *IEEE Trans. Ind. Appl.*, 1995, **31**, (5), pp. 1186–1196
7 Alewine, K., Chen, W.: 'Wind turbine generator failure modes analysis and occurrence'. NREL, Lecture notes, September 2011
8 Djurovic, S., Crabtree, C., Tavner, P., Smith, A.: 'Condition monitoring of wind turbine induction generators with rotor electrical asymmetry', *IET Renew. Power Gener.*, 2012, **6**, (4), pp. 207–216
9 Ceban, A., Pusca, R., Romary, R.: 'Study of rotor faults in induction motors using external magnetic field analysis', *IEEE Trans. Ind. Electron.*, 2012, **59**, pp. 2082–2093
10 Li, W., Mechefske, C.: 'Detection of induction motor faults: A comparison of stator current, vibration and acoustic methods', *J. Vib. Control*, 2006, **12**, (2), pp. 165–188
11 Bellini, A., Filippetti, F., Franceschini, G., Tassoni, C.: 'Closed-loop control impact on the diagnosis of induction motors faults', *IEEE Trans. Ind. Appl.*, 2000, **36**, (5), pp. 1318–1329
12 Serna, E., Pacas, J.: 'Detection of rotor faults in field oriented controlled induction machines'. Proc. IEEE Industrial Applications Conf. 41st IAS Annual Meeting, Tampa, FL, 2006, pp. 2326–2332
13 Cruz, S., Cardoso, A.: 'Fault indicators for the diagnosis of rotor faults in FOC induction motor drives'. Proc. IEMDC, Antalya, May 2007, vol. 2, pp. 1136–1141
14 Concari, C., Franceschini, G., Lorenzani, E., Tassoni, C., Toscani, A.: 'Severity assessment of rotor faults in closed loop induction drives by different approaches'. Proc. SDEMPED, Cracow, 2007, pp. 309–315
15 Concari, C., Franceschini, G., Tassoni, C.: 'Rotor fault detection in closed loop induction motors drives by electric signal analysis'. Proc. ICEM, Vilamoura, 2008
16 Stefani, A., Yazidi, A., Rossi, C., Filippetti, F., Casadei, D., Capolino, G.: 'Doubly fed induction machines diagnosis based on signature analysis of rotor modulating signals', *IEEE Trans. Ind. Appl.*, 2008, **44**, (6), pp. 1711–1721
17 Casadei, D., Filippetti, F., Rossi, C., Stefani, A.: 'Closed loop bandwidth impact on doubly fed induction machine asymmetries detection based on rotor voltage signature analysis'. Proc. 43rd UPEC, Padova, 2008, pp. 1–5
18 Filippetti, F., Franceschini, G., Tassoni, C., Vas, P.: 'AI techniques in induction machines diagnosis including the speed ripple effect', *IEEE Trans. Ind. Appl.*, 1998, **34**, (1), pp. 98–108
19 Watson, S., Xiang, B., Yang, W., Tavner, P., Crabtree, C.: 'Condition monitoring of the power output of wind turbine generators using wavelets', *IEEE Trans. Energy Convers.*, 2010, **25**, pp. 715–721
20 Yang, W., Tavner, P., Wilkinson, M.: 'Condition monitoring and fault diagnosis of a wind turbine synchronous generator drive train', *IET Renew. Power Gener.*, 2009, **3**, (1), pp. 1–11
21 Zappala, D., Tavner, P., Crabtree, C., Sheng, S.: 'Sideband algorithm for automatic wind turbine gearbox fault detection and diagnosis'. Proc. EWEA, Vienna, February 2013, pp. 1–10

9 Appendix: DFIG parameters

Ratings: $P_s = 30$ kW, $f = 50$ Hz and $V_s = 230$ V
Pole pairs: $p = 2$
Stator–rotor turns ratio: $n_{sr} = 1.272$
Stator and rotor resistances: $R_s = 0.079$ and $R_r = 0.044\ \Omega$
Stator and rotor self-inductances: $L_s = 0.031$ mH and $L_r = 0.019$ mH
Magnetising inductance: $L_m = 0.031$mH
Stator voltage: $V_s = 78$ V
DC-link voltage: $V_{DC} = 48$ V

doi: 10.1049/iet-rpg.2013.0324

Automated Fault Detection in Wind Turbine Induction Generators with Rotor Electrical Asymmetry

Katharine Brigham, Donatella Zappalá, Christopher J. Crabtree, Christopher Donaghy-Spargo

Durham University, Department of Engineering, Durham, UK. Contact: katharine.brigham@durham.ac.uk

Keywords: automatic fault detection, condition monitoring.

Abstract

This paper presents an automated fault detection scheme for wind turbine (WT) induction generators with rotor electrical asymmetries. Fault indicators developed in previous works have made use of the presence of significant spectral peaks in the upper sidebands of the supply frequency harmonics; however the specific location of these peaks may shift depending on the speed of the wind turbine. As wind turbines tend to operate under variable speed conditions, it may be difficult to predict where these fault-related peaks will occur. To circumvent this issue, a set of bandpass filters is proposed to capture the fault-related spectral information to train a classifier for automatic detection. Several different system parameters were tested (e.g., the number of bandpass filters) to empirically determine reasonable parameter values. The overall fault detection system was then tested on 'unseen' data and yielded a high classification accuracy of 97.4%, demonstrating the efficacy of the proposed approach.

1 Introduction

Reliability surveys [1,2] have reported that rotor winding unbalance, caused by brush-gear or slip-ring wear/fault or winding electrical faults, makes a large contribution to WT generator failure rate. Prior works [3,4] have shown that the spectral content of the stator currents and the total power can contain significant information with regards to certain faults in wind turbine induction generators in both the doubly-fed (DFIG) and wound rotor (WRIG) configurations. In particular, rotor imbalance has been shown to induce a change in the generator electrical signature at slip-dependent sidebands of the dominant supply frequency and slotting frequency harmonic components. Closed-form analytical expressions have been derived as to the specific locations of these sidebands [5]. Fault indicators have previously been developed to aid in the automatic detection of rotor asymmetry by extracting and summing the spectral amplitudes at the speed-dependent sideband frequencies of interest [6]. However, in practice, wind turbines operate at variable speed conditions, and in faulty spectra this variability will cause the corresponding peak in the sidebands to shift along the frequency axis to different locations. Further to this, if the speed is unknown, it may not be possible to predict where these fault-related peaks will occur.

This work proposes an implementation for an automated fault detector of induction generator rotor electrical asymmetry that is invariant to the issue of shifting peaks in the spectra. In general, the approach for developing an automated detection / classification system is to first extract a set of "features" from input data (e.g., images, speech signals), and then use these features to train a classifier. Subsequent data can then be classified by applying the same feature extraction approach, and then inputting the features into the previously trained classifier to arrive at a decision / categorization about the class of the input data (e.g., healthy or faulty). The selection of an appropriate set of features is undoubtedly critical in this process towards implementing a successful detection system, as it is possible to extract features that do not contain information relevant for classification. Therefore, the suitability of the proposed set of features for automated fault detection will also be investigated by applying a form of supervised dimensionality reduction to allow for both visual and numerical analyses of experimental "healthy" and "faulty" data. The applicability of the proposed approach to detecting different fault levels will also be explored.

2 Feature Extraction and Dimensionality Reduction

Given the findings in previous works [5,6] regarding the manifestation of significant spectral peaks due to rotor asymmetry and the variability of the peak locations, the extracted features should incorporate information across the various frequency bands of interest. To this end, a set of bandpass filters is proposed (hereafter referred to as a filter bank), where the cutoff frequencies of the bandpass filters are determined based on an expected range of slip-dependent sideband peak locations, derived from both theory and actual experimentation. The average spectral magnitude contained in each frequency band of the filter bank is computed and concatenated to form a vector of features, whose vector length is equal to the number of bandpass filters.

To investigate the suitability of these features for classification / detection, Fisher's Linear Discriminant (FLD) will be applied to the features since its usage will permit visualisation of the proposed features in a lower dimensional subspace, and can help identify whether or not a distinct separation between healthy and faulty data can be attained. With FLD, the ability to achieve the desired distinctive separations can also be further analysed to determine whether or not such linear classifiers may be capable of detecting faults at multiple levels (e.g., the fault detector should ideally be capable of detecting various levels of rotor imbalances). FLD is a tool that is primarily used for dimensionality reduction, and computes a linear function of the input data as follows:

$$y = \mathbf{w}^T \mathbf{x} \quad (1)$$

where y is the (one-dimensional) FLD output, $\mathbf{w}$ is an N-dimensional weight (i.e., projection) vector, and $\mathbf{x}$ is an N-dimensional input vector (e.g., a feature vector derived from an input data sample). The weight vector $\mathbf{w}$ is determined using labelled 'training' data to solve an optimisation problem that minimises the *within-class variability* (i.e., spread of the data) and maximises the *between-class separation* of the projected output data.

The within-class variability of the output from Eq. (1) for class C_k will be denoted as s_k^2 and can be defined as the total sample variance, which for FLD, is given by [7]:

$$s_k^2 = \sum_{n \in C_k} (y_n - m_k)^2 \quad (2)$$

where y_n is the projected data point of $\mathbf{x}_n$ using Eq. (1) for $n \in C_k$ (where k is the class index), and m_k is the mean of the set of projected data points for class C_k.

While FLD has a multi-class variant [7], for simplicity, the following description of FLD will be restricted to two classes. The between-class separation of the projected data for class 1 and class 2 will be denoted as m_{12}, and can be defined as a distance between the means of the projected data from each class as follows:

$$m_{12} = (m_1 - m_2)^2 \quad (3)$$

where m_1 and m_2 are the means of the projected data belonging to class 1 and 2, respectively, and are computed using their respective sample mean:

$$m_k = \frac{1}{N_k} \sum_{n \in C_k} y_n, \quad for\ k = 1,2. \quad (4)$$

To both maximise the between-class separation and minimise the within-class variability, a ratio between the two measures can be constructed to formulate the following optimisation function [7]:

$$J(\mathbf{w}) = \frac{(m_1 - m_2)^2}{s_1^2 + s_2^2} \quad (5)$$

The projected means and variances on the right-hand side of Eq. (5) can be rewritten in terms of the original data and the weight vector $\mathbf{w}$ (making the dependence of the function on the weight vector explicit) to obtain the following final form of the desired optimisation function:

$$J(\mathbf{w}) = \frac{\mathbf{w}^T (\mathbf{m}_1 - \mathbf{m}_2)(\mathbf{m}_1 - \mathbf{m}_2)^T \mathbf{w}}{\mathbf{w}^T \mathbf{S}_W \mathbf{w}} \quad (6)$$

where $\mathbf{m}_1$ and $\mathbf{m}_2$ (denoted by bold letters to indicate that these are vectors) are the sample means of the input data and are given by:

$$\mathbf{m}_k = \frac{1}{N_k} \sum_{n \in C_k} \mathbf{x}_n, \quad for\ k = 1,2 \quad (7)$$

and $\mathbf{S}_W$ is the total within-class covariance:

$$\mathbf{S}_W = \sum_{n \in C_1} (\mathbf{x}_n - \mathbf{m}_1)(\mathbf{x}_n - \mathbf{m}_1)^T + \sum_{n \in C_2} (\mathbf{x}_n - \mathbf{m}_2)(\mathbf{x}_n - \mathbf{m}_2)^T. \quad (8)$$

Maximizing $J(\mathbf{w})$ from Eq. (6) with respect to $\mathbf{w}$ results in the following closed-form solution for $\mathbf{w}$ [7]:

$$\mathbf{w} \propto \mathbf{S}_W^{-1}(\mathbf{m}_1 - \mathbf{m}_2) \quad (9)$$

An optimal threshold for separating the classes after applying Eq. (1) to the input (i.e., training) data using the weight vector $\mathbf{w}$ found from Eq. (9) can subsequently be determined from the resulting input data projections.

3 Experimental Setup

The proposed approach was tested using data collected from the Durham Wind Turbine Condition Monitoring Test Rig (WTCMTR), whose schematic diagram is shown in Figure 1. The Durham rig was designed to act as a model for a WT drive train with the purpose of producing signals comparable to those encountered on an operational WT. The Durham rig features a WRIG driven at either constant speed or at non-stationary, variable speed conditions to reflect the stochastic effects of wind torque driving. WRIGs used with power electronic converters in DFIG type-III configurations are the dominant market technology in currently installed MW size wind turbines [8]9]. Details of the test rig are given in [6,10]. Seeded-fault conditions can be induced or removed from the test rig drive train as required enabling several electrical and mechanical faults to be implemented repeatedly on demand and under controlled driving conditions. Rotor electrical asymmetry was simulated on the test rig WRIG by using a load bank externally connected to the rotor circuit via the machine slip-rings to vary the resistance into one rotor phase winding circuit. For experimental purposes, in order to represent the development of rotor electrical faults on an induction generator, such as brush-gear or slip-ring wear, two seeded-fault levels were implemented on the test rig by successively adding two additional external resistances to phase 1 of the rotor circuit through the external load bank. The corresponding levels of rotor electrical asymmetry, given as a percentage of the rotor balanced phase resistance, were 21% and 43%. These values compare very favourably with other studies such as [4,11].

Tests on the rig were performed at steady-state, constant speed conditions to extract features indicative of the developing fault and to design the detection algorithm. The WRIG was also driven at wind-like variable speed conditions according to speed profiles derived from a 2 MW variable speed WT model. In each constant speed test the rig was driven for 300 seconds, while in each variable speed test it was driven for 450 seconds to allow for sufficient data acquisition.

Data was collected at constant speeds ranging from 1520RPM to 1600RPM, and at variable speeds. Variable speed machine testing was performed by using the driving data derived from a WT model. This model, developed by the University of Strathclyde, as part of the SUPERGEN Wind Energy Technologies Consortium, incorporates the properties of natural wind and the mechanical behaviour of a 2 MW variable speed WT operating under closed-loop conditions.

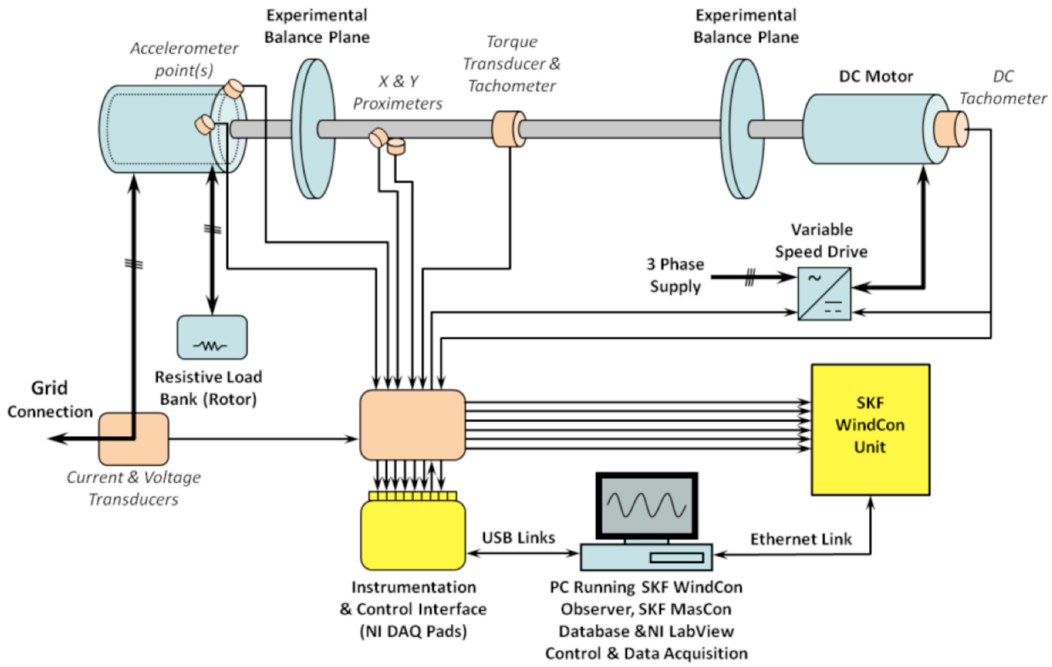

Figure 1. Schematic diagram of the Durham WTCMTR [6].

A variety of wind speeds and turbulence intensities, defined as the measure of the overall level of turbulence [12], were applied to the model. The driving conditions were then scaled to the test rig based on the generator speed data from the model [10]. The use of the 2 MW variable speed WT driving model has allowed the simulation of the different dynamic speed behaviours that a full-size WT 4-pole DFIG exhibits both below and above rated wind speed.

The scaled generator variable speed signals used for testing, shown in Figure 2, are:

1. 7.5 m/s mean, 6% turbulence intensity, representative of a low mean wind speed with low turbulence, with the WT operating at or below rated wind speed under generator speed control (hereafter denoted as '7.5m6t'); and
2. 15 m/s mean, 20% turbulence intensity, representative of a high mean wind speed with high turbulence, with the WT operating above rated wind speed under blade pitch control (hereafter denoted as '15m20t').

Three main sets of experimental data were curated and processed in this work that encompass a set of constant speeds spread across the experimental range and also includes variable-speed data. Table 1 shows the details of each experimental dataset. `TrainSet` is used to train FLD, `DevSet` is used to determine reasonable feature extraction parameters using the trained FLD weight vector, and `EvalSet` is used to test the final fault detection system.

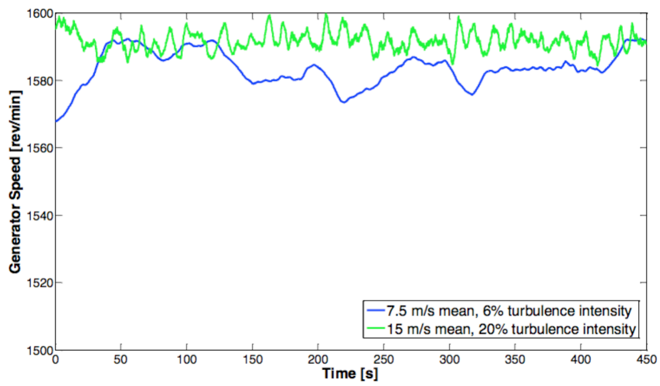

Figure 2. WTCMTR generator variable speed test conditions [6].

Dataset	*Speeds (RPM)*	*Fault Levels*
`TrainSet`	1520	none (healthy) 21% rotor asymmetry
`DevSet`	1525 1540 1553 1585 1600 variable (7.5m6t)	none (healthy) 21% rotor asymmetry 43% rotor asymmetry
`EvalSet`	1530 1555 1565 1590 variable (15m20t)	

Table 1. Speed and fault level details for the three curated datasets.

Note that during training, only the 'healthy' and '21% rotor asymmetry' data is used; this is to test how well the proposed fault detector can distinguish between different levels of fault (e.g., '43% rotor asymmetry') even when the different fault levels are not present in the training data.

For all data, features are extracted using the filter bank approach on the stator current spectra computed from 10-second windows of the stator current signal with the Hanning window applied. From [6], it is expected that in faulty spectra (compared to "healthy" spectra), higher amplitude peaks will appear at the $2sf$ upper sidebands of the supply frequency harmonics, where s is the machine slip and f is the supply frequency. Therefore, the filter bank will be constructed such that each bandpass filter encompasses the $2sf$ upper sideband of each supply frequency harmonic. Furthermore, since the expected frequency range of the expected sideband peaks can be computed from the given speed range of 1520-1600RPM, each bandpass filter will start at each supply frequency harmonic + 1Hz and have a range of 7Hz. The number of bandpass filters used is initially (arbitrarily) selected to be 10 (i.e., one filter is placed at the upper sideband of the 1st through 10th supply frequency harmonics).

In this feature extraction approach, there are several parameters that can be varied:

- Length of the analysis time window;
- Number of bandpass filters; and
- Frequency range of the bandpass filters.

These parameters will be tuned (i.e., the 'best' values will be determined) by using FLD to classify the data from the `DevSet`. The final set of selected feature extraction parameters will then be used to test the proposed approach on the `EvalSet`. Note that `EvalSet` is never used during training or "development" phase (during which the system parameters are tuned); the idea is that at least one dataset should be held out to test the generalisability of the proposed detection system (i.e., how does the detection system perform on never-before-seen data).

4 Results and Discussion

After training the FLD weight vector, the training data was projected to determine an appropriate threshold for classifying 'healthy' and 'faulty', which was selected as the halfway point between the means of each projected class. Numerical measures of the system performance were taken to be the system accuracy (i.e., the percentage of correctly identified samples) and the false positive rate (FPR) (i.e., the false 'alarm' rate), which is computed as the number of 'healthy' samples incorrectly categorized as 'faulty' over the total number of samples that were determined to be 'faulty'. The resulting classifications for the `DevSet` (categorising both '21%' and '43%' as faulty) are shown in Table 2 for the initially selected feature extraction parameters. The initial system accuracy and the false positive rate show the efficacy of the proposed solution in detecting faults in the stator current spectra as the resulting accuracy is quite high with a low false positive rate. Tables 3-5 show the system performance results for varying the length of the time window, the number of bandpass filters, and the frequency range of the bandpass filters, respectively.

Feature Extraction		*Accuracy*	*False Positive Rate (FPR)*
Parameter	*Value*		
Time Window	10s	98.8%	1.2%
# filters	10		
Freq. Range	7 Hz		

Table 2. `DevSet` accuracy and FPR for the initial set of feature extraction parameters.

Feature Extraction		*Accuracy*	*False Positive Rate (FPR)*
Parameter	*Value*		
Time Window	1s	77.6%	24.6%
	3s	75.3%	5.9%
	4s	83.2%	5.1%
	5s	98.8%	1.5%
	7s	98.8%	1.1%
	10s	98.8%	1.2%

Table 3. `DevSet` accuracy and FPR when varying the length of the time window. For the other parameters, 10 filters were used with a frequency range of 7 Hz each.

Feature Extraction		*Accuracy*	*False Positive Rate (FPR)*
Parameter	*Value*		
# filters	1	81.6%	21.7%
	2	84.7%	18.7%
	5	96.2%	5.4%
	7	96.6%	2.0%
	10	98.8%	1.1%
	15	98.8%	1.1%
	20	99.4%	0.87%
	25	85.8%	1.4%

Table 4. `DevSet` accuracy and FPR when varying number of bandpass filters. For the other parameters, a 7s time window was used (as this yielded a 'best' result shown in Table 3), and each filter had a frequency range of 7 Hz.

Feature Extraction		*Accuracy*	*False Positive Rate (FPR)*
Parameter	*Value*		
Freq. Range	5 Hz	69.2%	7.3%
	7 Hz	99.4%	0.87%
	9 Hz	89.8%	8.0%

Table 5. `DevSet` accuracy and FPR when varying the frequency range of the bandpass filters. Note that the lower cutoff frequency (the supply harmonic + 1Hz) is the same for all frequency ranges; it is only the higher cutoff frequency that is varied. For the other parameters, a 7s time window was used with 20 bandpass filters.

In varying the feature extraction parameters, from Table 3, it is evident that the length of the time window should be at least 5 seconds, as the system accuracy drops down significantly when the time window is less than 5 seconds. However, some improvement in the false positive rate can be gained by increasing the amount of time to 7 seconds, so a time window of 7 seconds was selected prior to varying the number of bandpass filters to produce the results shown in Table 4. The results shown in Table 4 demonstrates that the number of bandpass filters used does have a significant impact on the system performance, as a reduction in the number of filters also reduces the system accuracy, and an increase in the number of filters yields better system accuracy, up to a point (e.g., when using 25 bandpass filters) where the accuracy then drops. The drop in accuracy seen for a larger number of filters is likely due to noise as it is expected that there will be less actual 'information' present in the spectra at higher harmonics. Table 5 shows the resulting system performance when the frequency range of the filters is varied. It is clear that the original selected range was indeed the best choice as the performance is notably worse at other ranges. These results provide a sort of "sanity check" as the original selected frequency range was determined from the given speeds at which the experiments were run.

The resulting FLD projections for the `DevSet` are shown in Figure 3. A clear delineation between the healthy and faulty data can be seen. Of interest is also the faulty data with 43% rotor asymmetry can be seen at even a different level (i.e., range of projected values) compared with the '21% rotor asymmetry' data even though the '43%' data was not included during training. This result further highlights the potential generalisability of the proposed approach in even detecting alternate fault levels beyond those present during training.

Lastly, the proposed approach was tested on the `EvalSet` without any further system tuning. The resulting system performance is shown in Table 6, and the FLD projections for the `EvalSet` are shown in Figure 4.

Feature Extraction		*Accuracy*	*False Positive Rate (FPR)*
Parameter	*Value*		
Time Window	7s	97.4%	3.6%
# filters	20		
Freq. Range	7 Hz		

Table 6. `EvalSet` accuracy and FPR for the final selected set of feature extraction parameters.

The accuracy still remains relatively high, although the false positive rate has a significant increase. It can be seen in Figure 4 that one particular set of test data included in the `EvalSet` (namely the data on the left-hand side of Figure 4, which was collected at 1530RPM) does not exhibit as much of a separation between classes as can be seen in the rest of the `EvalSet` data. It is possible that the data collected at this particular speed contains more noise than the others; future investigations may include noise reduction techniques or more generalisable classifiers.

5 Conclusions

Overall, the proposed approach is shown to be promising for rotor electrical asymmetry detection under practical WT operating conditions. The usage of bandpass filters during feature extraction was robust against the effects of variable speeds. It was also found when varying the number of bandpass filters that there is significant information relevant

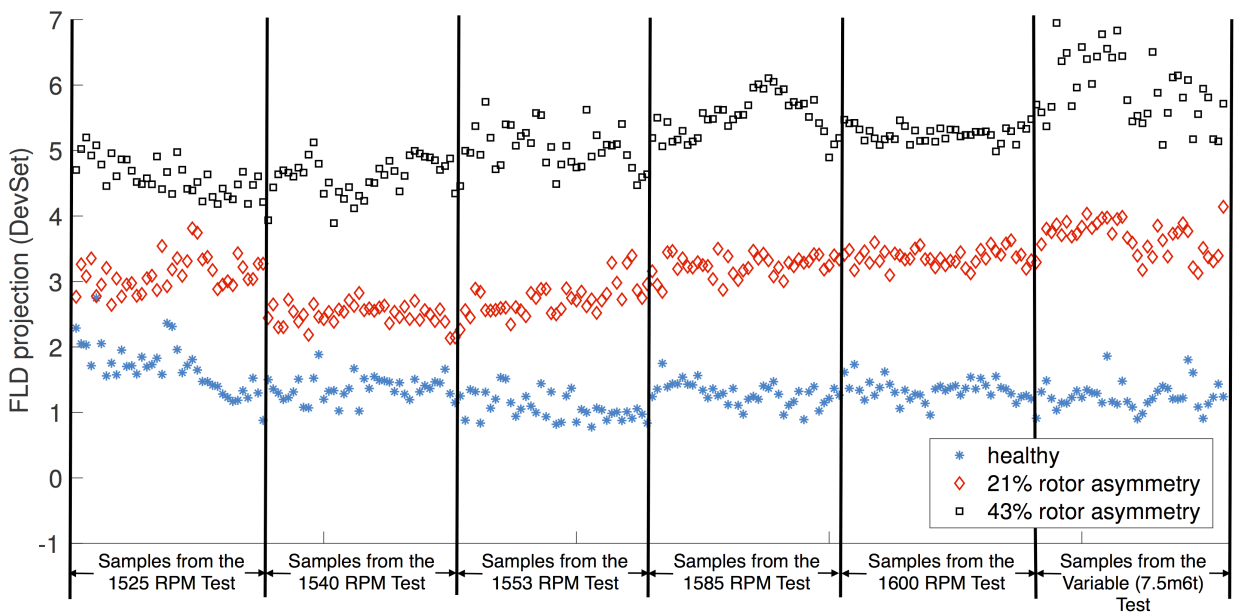

Figure 3. FDL Projection of the average spectral magnitudes of the stator current spectra computed in each bandpass filter for the **`DevSet`** containing speeds ranging from 1525-1600RPM, and a variable-speed dataset. These features were extracted using a 7 second time window and 20 bandpass filters with a frequency range of 7Hz.

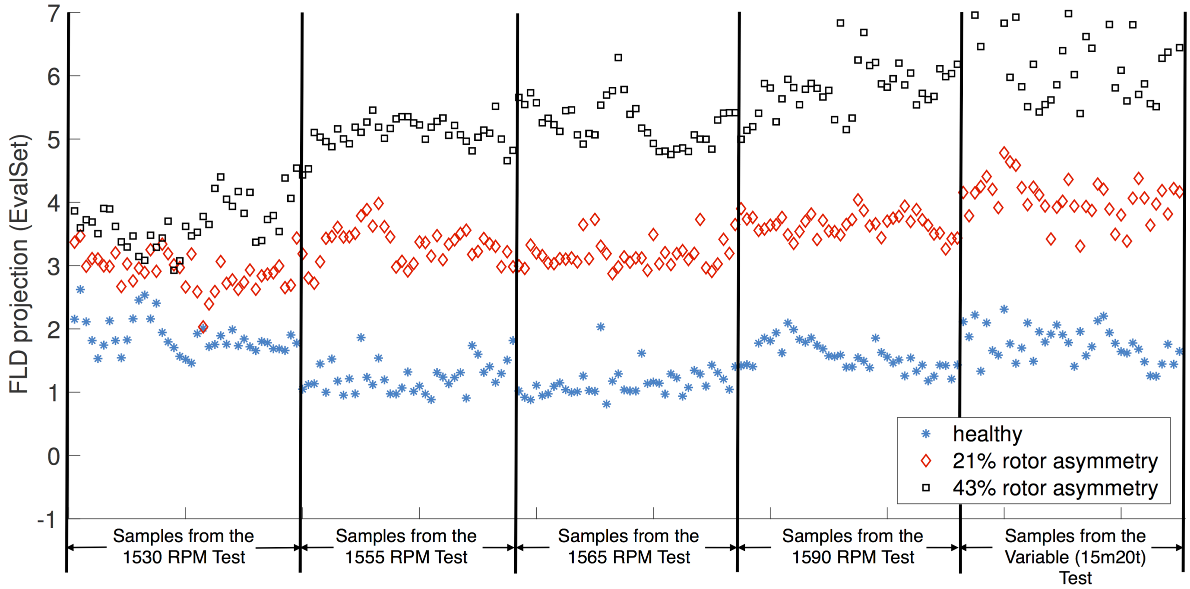

Figure 4. FDL Projection of the average spectral magnitudes of the stator current spectra computed in each bandpass filter for the **`EvalSet`** containing speeds ranging from 1530-1590RPM, and a variable-speed dataset. These features were extracted using a 7 second time window and 20 bandpass filters with a frequency range of 7Hz.

to fault detection contained in the slip-dependent upper sidebands of higher-order harmonics. The application of a dimensionality reduction technique enabled the visualisation of the proposed features where a clear delineation between separate classes can be observed. Of notable interest is the ability of the fault detector to also produce an observable difference between different levels of faults (21% rotor asymmetry vs. 43% rotor asymmetry). The proposed fault detection scheme may also be applicable to other machines for which the expected fault-related spectral content is known. Future work will consider noise reduction techniques, other faults that may also manifest in the frequency domain such as gearbox degradation, and the application of classifiers with known better generalisability such as Support Vector Machines.

References

[1] K. Alewine, W. Chen. “A Review of Electrical Winding Failures in Wind Turbine Generators”, *Proceedings of IEEE Electrical Insulation Conference* (*EIC*), Annapolis, MD, USA, pp. 392-397, (2011).

[2] J. Carroll, A. McDonald, D. McMillian. “Reliability Comparison of Wind Turbines with DFIG and PMG Drive Trains”, *IEEE Transactions on Energy Conversion*. 30, (2): pp. 663-670, (2015).

[3] P. J. Tavner, L. Ran, J. Penman, H. Sedding. “Condition Monitoring of Rotating Electrical Machines”, London: *Institution of Engineering and Technology*, (2008).

[4] S. Djurović, C. J. Crabtree, P. J. Tavner, A. C. Smith. “Condition Monitoring of Wind Turbine Induction Generators with Rotor Electrical Asymmetry”, *IET Renewable Power Generation*. 6(4): 207- 216, (2012).

[5] S. Djurović, D. S. Vilchis-Rodriguez, A. C. Smith. “Supply Induced Interharmonic Effects in Wound Rotor and Doubly-Fed Induction Generators”, *IEEE Transactions on Energy Conversion*. 30, (4): 1397 – 1408, (2015).

[6] D. Zappalá. “Advanced Algorithms for Automatic Wind Turbine Condition Monitoring”, Durham theses, Durham University. Available Online: http://etheses.dur.ac.uk/11059/, (2014).

[7] C. M. Bishop, “Pattern Recognition and Machine Learning”, Springer Verlag New York, 2006.

[8] P. J. Tavner, “Offshore Wind Turbines: Reliability, Availability & Maintenance”, London: *Institution of Engineering and Technology*, (2012).

[9] M. Edrah, K. L. Lo, O. Anaya-Lara. “Impacts of High Penetration of DFIG Wind Turbines on Rotor Angle Stability of Power Systems”, *IEEE Transactions on Sustainable Energy*. 6, (3), pp. 759-766, (2015).

[10] C. J. Crabtree. “Condition Monitoring Techniques for Wind Turbines”, Durham theses, Durham University. Available Online: http://etheses.dur.ac.uk/652/, (2011).

[11] A. Stefani, A. Yazidi, C. Rossi, F. Filippetti, D. Casadei, G. A. Capolino. “Doubly Fed Induction Machines Diagnosis Based on Signature Analysis of Rotor Modulating Signals”. *IEEE Transactions on Industry Applications*. 44(6): 1711-1721, (2008).

[12] Burton, T., Sharpe, D., Jenkins, N. and Bossanyi, E., “Wind Energy Handbook (2nd ed.)”, John Wiley & Sons, (2011).

Wind Turbine Non-Intrusive Torque Monitoring

Michael Secker, Christopher J. Crabtree, Donatella Zappalá
School of Engineering and Computing Sciences
Durham University, UK
m.p.secker@durham.ac.uk, c.j.crabtree@durham.ac.uk, donatella.zappala@durham.ac.uk

Abstract

Wind Turbine (WT) global installed capacity is expected to increase from 318GW to 596GW between 2013 and 2019, with an increasing proportion being from offshore wind farms. With up to 70% of Operations and Maintenance (O&M) costs coming from unplanned maintenance, the adoption of cost effective condition monitoring (CM) techniques is crucial for competitive development of offshore wind.

Monitoring the torque of a WT can provide much information about the WT's health and it has been shown to be successful in the detection of faults in the main drive train components. Although WT torsional effects are important, torque measurement on such a large, low speed, inaccessible machine is practically and logistically difficult, although it is possible using costly specialised intrusive in-line equipment.

This paper presents the development of a non-intrusive method for monitoring the drive train torque using timing differences between optical probe measurements along a shaft. An algorithm has been developed and initially verified using a simulated WT for speed and torque data. The algorithm torque was accurate to within ±3% of the input.

The initial performance of the proposed technique has been successfully tested experimentally under both steady and transient torque conditions**.** Experimental results show good agreement between the algorithm predictions and the measurements. The proposed algorithm successfully detects changes in shaft speed and torque, with the torque mean percentage error within 16-25%. Once implemented on a WT drive train, the proposed non-intrusive method can overcome the majority of problems limiting the industrial application of CM systems (CMSs) based on shaft torque measurements.

Keywords: Wind turbine, torque, non-intrusive measurement, condition monitoring.

1. Introduction

Wind energy is seeing huge increases in production with the Global Wind Energy Council reporting that global installed wind capacity has increased from 6.1 GW in 1996 to 318 GW in 2013, and is predicted to rise to 596 GW by the end of 2018 [1]. Offshore wind has significant generation potential, in particular in Europe, with increasingly large-scale sites identified as suitable for offshore development and benefiting from a favourable wind resource. Offshore wind is therefore expected to play a significant role in meeting this target, with projections of an increase in the proportion of offshore turbines from 2% to 10% of global wind capacity between 2015 and 2020 [2]. There any many advantages for going offshore including higher quality wind resources, less turbulence, larger WT ratings and less problematic visual intrusion. However, the harsher conditions offshore produce more significant variable loading along with difficult site accessibility for maintenance as favourable weather conditions and special service vessels are required for transportation of the maintenance team [3]. As large-scale wind farms (WF) move further offshore, achieving a high availability and capacity factor and ensuring that loss of energy and turbine downtime is minimised, are essential for a competitive cost of energy. The costs of offshore O&M have been quantified as three to five times higher than those onshore [4], with a considerable part, typically up to 65-70%, associated with unscheduled maintenance [5, 6], resulting in unexpected WT downtime, reduced availability and lost revenue. Repair costs are not the only consequence of maintenance as the time that is lost in which the turbine could have been generating energy and revenue must also be considered. These issues highlight the importance of O&M strategy within economic viability evaluation of large offshore WFs [7]. The adoption of cost effective condition monitoring (CM) techniques is crucial in reducing O&M costs, avoiding catastrophic failures and minimizing costly corrective maintenance. As the loading on the WT drive train components is highly variable the study of transient conditions is fundamental to the development of reliable CM techniques.

The potential of monitoring different WT drive train components using the shaft torque signal is significant as it contains information on the mechanical response to wind before any generator effects. Recent studies have shown the potential benefits of adopting condition monitoring systems (CMSs) based on the measurement of WT drive train shaft torque for the detection of rotor electrical asymmetry and machine winding faults [8-10], mass imbalance [11], gearbox failures [12], blade mass imbalance and aerodynamic asymmetry [13]. However, the measurement of shaft torque is largely limited to the laboratory environment. The major obstacle to industrial application is the costly and intrusive nature of the required measurement equipment, which is impractical for long-term use on operating WTs [14, 15].

This paper details research conducted on a low-cost, non-intrusive WT torque measurement method based on timing differences between optical probe signals along the shaft with a focus on tracking transient conditions for use in a CMS.

2. Theoretical Background

The torque applied to a rotating shaft is proportional to the twist angle between two points on the shaft [16]:

$$T = I\ddot{\theta} + C\dot{\theta} + K\theta \qquad (1)$$

where T is the applied torque (Nm), I is the shaft moment of inertia (kgm^2), C is the shaft damping coefficient (kgm^{2}s^{-1}rad^{-1}), K is the shaft torsional stiffness (Nm/rad) and θ is the relative twist angle (rad) given by:

$$\theta = \theta_a - \theta_0 \qquad (2)$$

where θ_a is the absolute twist angle and θ_0 is the no-load twist. θ_a can be calculated by measuring the timing difference and rotational speed between two points on the shaft [17]:

$$\theta_a = \frac{2\pi}{60}\omega\Delta t \qquad (3)$$

where ω is the shaft rotational speed (rpm) and Δt is the timing difference or phase shift (s). The no-load twist θ_0 is the absolute twist angle before torque has been applied to the system.

3. Non-Intrusive Torque Measurement Algorithm

The proposed non-intrusive torque measurement approach employs equation (1) to calculate the torque from the phase shift between the pulses generated by two bar codes and optical probes, one at each end of the shaft. The optical probes identify a black or white segment and produce a fixed voltage when reading white and zero volts when reading black, resulting in two pulse trains as the shaft rotates (Figure 1).

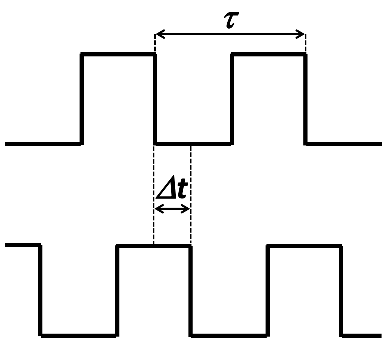

Figure 1: Typical pulse trains from the two shaft ends, where τ is the period and Δt is the phase shift.

The shaft rotational speed is calculated as:

$$\omega = \frac{60}{\tau p} \qquad (4)$$

where p is the number of pulses per shaft revolution and τ is the pulse train period (s).

For a given shaft stiffness, damping coefficient and moment of inertia, the measurement of the phase shift between two pulse trains Δt and the calculation of ω, allow the calculation of the shaft torque from equations (1)-(3).

4. Simulation Results

To validate the proposed approach, simulated WT drive train data were created using DNV GL's Bladed 4.6 software. The aim of using the Bladed simulations was to prove the effectiveness of the process of reconstructing the shaft speed and torque signals by using discrete pulse trains. The twist angle has been reconstructed from the simulation speed and torque data and used to generate an example pulse train. By analysing this pulse train, the ability of the algorithm to reverse the process could be tested. The main features of the reference example WT used in the simulations are shown in Table 1.

Table 1: WT parameters used in the simulations.

Blade Length (m)	38.75
Cut-In Speed (m/s)	4
Cut-Out Speed (m/s)	25
Gearbox Ratio	83.33

High speed shaft speed and torque data were collected at 20 Hz under a mean wind speed of 12m/s with 16% longitudinal turbulence intensity. The data were resampled to 50 kHz and interpolated to create pulse trains for the calculation of shaft speed and torque by using the shaft parameters of the example WT in Bladed. The resulting algorithm response compared to input data is shown in Figure 2.

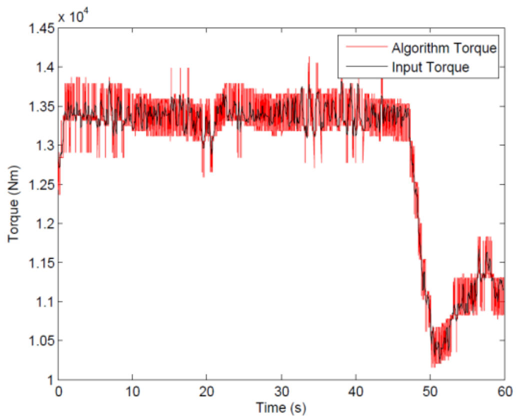

Figure 2: Algorithm response to WT simulation.

The trend of the input data simulated by Bladed is followed well by the algorithm output with a maximum percentage error noise associated of ±3%. The non-perfect reversibility between the original simulated signal and the one reconstructed by the algorithm introduces a slight reduction in the signal accuracy and the introduction of a certain level of noise.

An increase in the re-sampling frequency of the input data up to 100 kHz has shown a reduction of the noise levels to ±1.5%, suggesting that the sampling frequency and subsequent noise were issues requiring further investigation. The analysis of the pulse trains proved this to be correct as extra time steps at a higher sampling rate meant that the pulses were generated to a higher accuracy. The effect of resampling at a higher frequency is to produce signals which allow a smoother and continuous monitoring of the phase shift and period changes in the pulse trains. Consequently the algorithm measured the phase shift and period to a higher precision which produced a more accurate measurement.

5. Test Rig

Physical testing was performed to verify the proposed algorithm. Figure 3 provides a schematic of the torque test rig developed at Durham University and Figure 4 is a photo of the test stand which shows its main components and instrumentation system.

The test rig features a 4-pole 5 kW grid-connected induction generator driven by a 4-pole 5 kW induction motor. The motor shaft speed is varied via an inverter drive. The generator is connected to a VARIAC in order to vary the stator voltage and hence the shaft torque. An in-line Magtrol TM 212 torque transducer, measuring the shaft torque and speed, acts as a reference for comparison with the algorithm output. On either side of the transducer are the bar codes and OPTEK optical probes used to generate input data for the algorithm. Each bar code features 8 pulses per revolution and has been designed such that it divides into equal black and white segments, in both number and size, and that its total length fits exactly around the shaft. This design was selected so that the resulting pulses have a 50% duty cycle which makes phase shift measurement processing easier. The optical sensors consist of an Infrared (890nm) Light Emitting Diode (LED) and a NPN silicon Phototransistor, mounted side-by-side on converging optical axes. Couplings and bearings along the shaft ensure minimal radial shaft displacement helping to minimise a source of error when reading the bar codes.

Signals recorded from the optical probes are transmitted to a National Instruments data acquisition pad (USB-6009 DAQ pad) which is in turn connected by USB connection to the LabVIEW data acquisition environment. The probe sampling frequency was set at 24 kHz as this was the maximum possible for the NI USB-6009 data acquisition hardware. The torque transducer output is connected to a computer interface through the Magtrol Torque 1.0 data acquisition software and compared to the algorithm torque as verification.

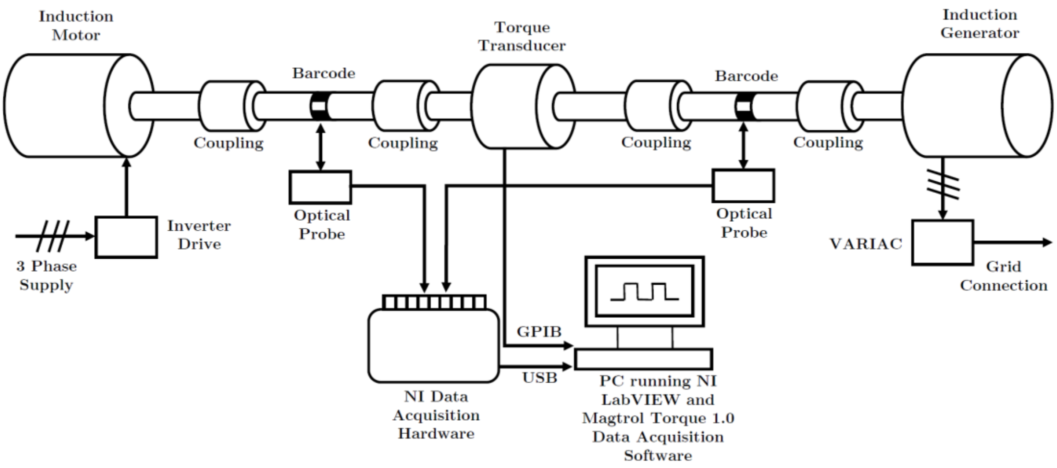

Figure 3: Schematic diagram of the torque test rig.

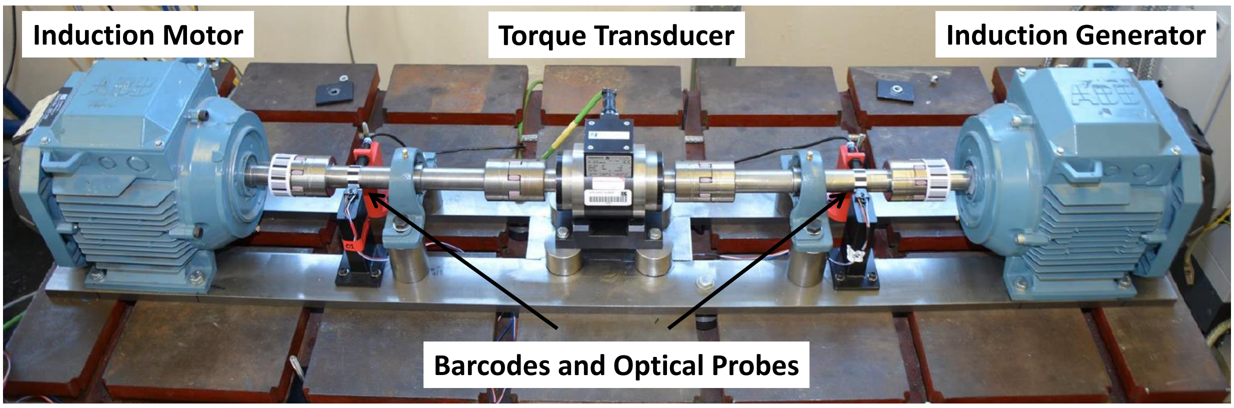

Figure 4 Torque test rig: main components and instrumentation.

6. Data Filtering

Data filtering has been performed on the signals recorded during the experiments in order to reduce the inherent systematic noise associated to the laboratory environment and to guarantee accuracy in the algorithm output.

Firstly a digital conversion was required to covert the optical probe voltage signals. A MATLAB code was implemented to convert any high voltage signal to a 1 and any low voltage signal to a 0. This conversion to a digital signal was performed in order to improve the algorithm train pulse edge detection and therefore the period and phase shift measurements.

Further filtering was carried out to ensure that any spikes in the middle of pulses were smoothed out. This was accomplished by comparing each data point with the previous 400µs of data as well along with following 400µs. If all of these data points matched except the one being examined, a noise spike was detected and converted to match the other 800µs of data points. Examination of these spikes showed they had a less than 40µs duration, therefore analysing each data point using a range ten times larger than this assures that checks are made on the digital state of the pulse rather than on noise spikes. A larger analysis period than 400µs risked analysing beyond a transition stage which means errors would not be detected through this method.

Preliminary experimental results showed that the physical optical probes did not display the transition in the pulse trains as a sharp edge but oscillated from previous to final state for up to 200µs before settling. A filter was then designed to detect any change in digital state between consecutive time steps. It inspected the state of the pulse in the previous 400µs and the state of the pulse for the next 400-800µs. A 400µs period was chosen for the same reason as mentioned above whilst analysing from 400µs after each state change was to ensure that the state of the pulse after a transition was checked rather than the state during a transition. At a transition, these two sets should give the exact opposite of each other (i.e. a set of 1's and a set 0's) and if this was detected, the entire oscillating transition period was converted into the final state of the transition. The importance of removing all the high frequency spikes was to avoid the algorithm using them to calculate extremely high erroneous speeds.

Finally, a low pass filter with cut-off frequency of 1 kHz was implemented to filter out periodic noise due to high frequency components in the signal.

7. Experimental Results

The algorithm has been fully developed by experimentally defining the relationship between torque and twist. Tests were performed according to the procedure below:

1) Run the motor up to 1600rpm;
2) Take a no-load measurement (0V applied to the generator stator using the VARIAC);
3) Record pulse and transducer data for 60s;
4) Use the VARIAC to apply a torque of -0.5Nm;
5) Record pulse and transducer data for 60s;
6) Repeat steps 4-5 for increasing magnitude of torque;
7) Repeat 1-6 for different super-synchronous speeds.

Pulse data were analysed using part of the algorithm to calculate the twist. For each 60s experiment, the means of the measured twist and torque were calculated and plotted to find the experimental relationship between torque and relative twist (Figure 5). The trend of the experimental data was then fitted by the following quadratic curve:

$$T = -80250^2 - 76\theta - 0.5453 \qquad (5)$$

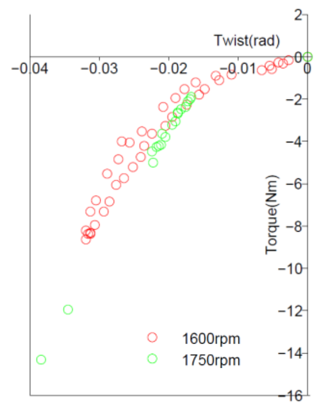

Figure 5: Test rig relationship between torque and twist.

The non-linear relationship between torque and twist described by equation (5) suggests that steady conditions during the experiments were not exactly obtained, especially at low magnitude torque values, and that dynamic conditions played a crucial role according to that predicted by the theoretical relationship (1).

Tests were then performed to validate the proposed algorithm under both steady state and transient conditions. The shaft speed and torque responses were calculated by implementing the proposed algorithm in MATLAB and compared with the transducer measurements. Figure 6 shows results for a steady state test at 1600 rpm and -3 Nm torque. The algorithm mean speed predictions show good agreement with transducer measurements with a percentage error of 0.06% and noise of ±0.3%. The algorithm mean torque predictions overestimate the transducer measurements by 44% with 200% noise. It is believed that the reason for the overestimation is due to the large amount of noise which occurred when calculating the twist, linked to the sampling frequency.

The proposed algorithm was then tested under transient conditions with the purpose of producing signals comparable to those encountered on an operational WT. Figure 7 shows results for transient conditions obtained by running the shaft up to 1600 rpm and smoothly varying the torque from 0 Nm to -10 Nm and back to 0 Nm. Both algorithm speed and torque track the transducer measurements well, particularly speed showing a percentage error of below 0.1%.

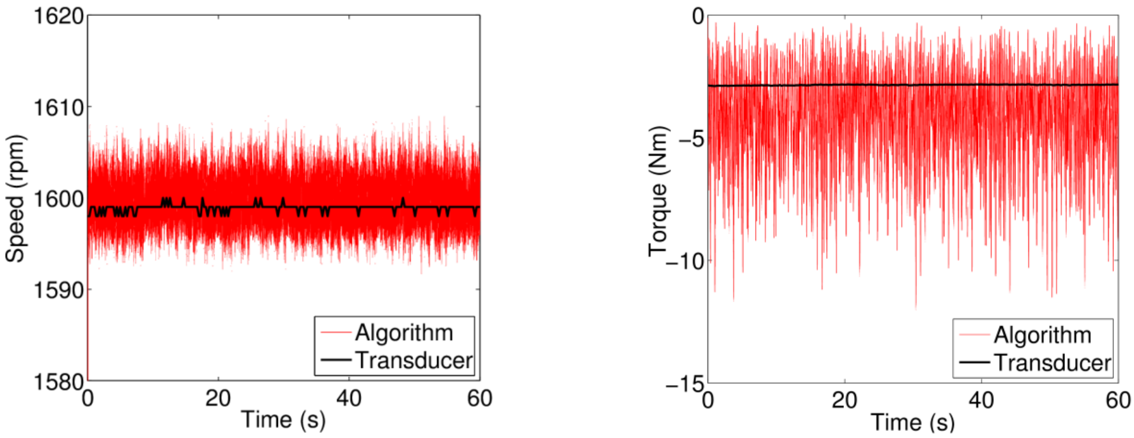

(a) (b)

Figure 6: Algorithm speed (a) and torque (b) response to steady state conditions of 1600 rpm and -3 Nm.

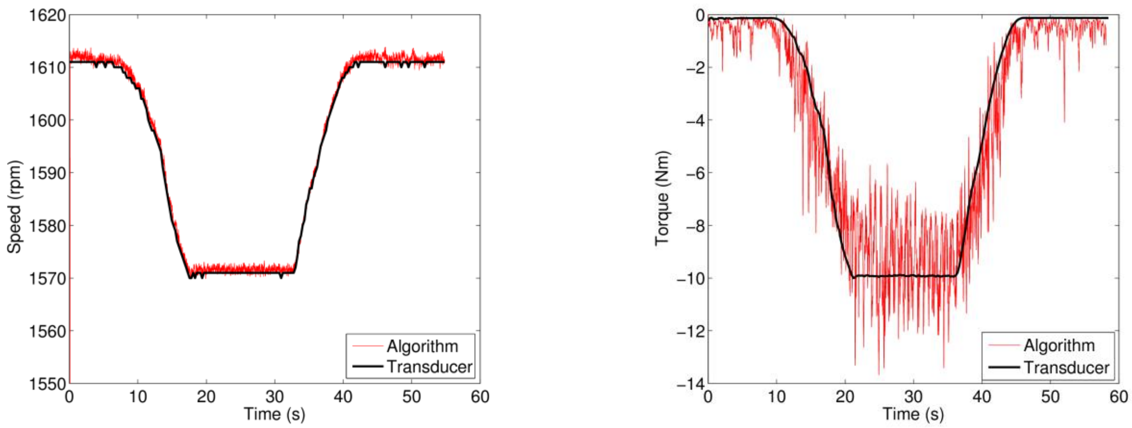

(a) (b)

Figure 7: Algorithm speed (a) and torque (b) response to shaft torque variations.

Figure 8 shows results for transient conditions obtained by keeping the generator stator voltage constant at 50% of the maximum whilst ramping the motor speed from 1525 rpm to 1750 rpm, holding for 30 s and then ramping back to 1500 rpm. The algorithm speed shows again good agreement with measurements with percentage errors less than 0.1%. For torque above 2 Nm, the average error was consistently around 25%, suggesting a systematic error was present. Figure 9 shows the effects of a step change in torque. The shaft speed was initially set at 1590 rpm and, starting from an initial torque of -3 Nm, four torque step changes were applied. The algorithm speed and torque follow the step changes well and without any timing delay. The algorithm predictions show good agreement with the measurements, with systematic errors lower than 0.1% for the speed and a torque mean percentage error of 16-25%. It is believed that the torque error is due to limitations in the signal sampling frequency. By increasing the sampling frequency during data acquisition it is expected that the systematic error associated with the measure of the phase shift between the two pulse trains would be reduced. This would result in improved predictions by the algorithm of the shaft twist angle, calculated by using equation (3), and of the relative torque values, calculated by using equation (5).

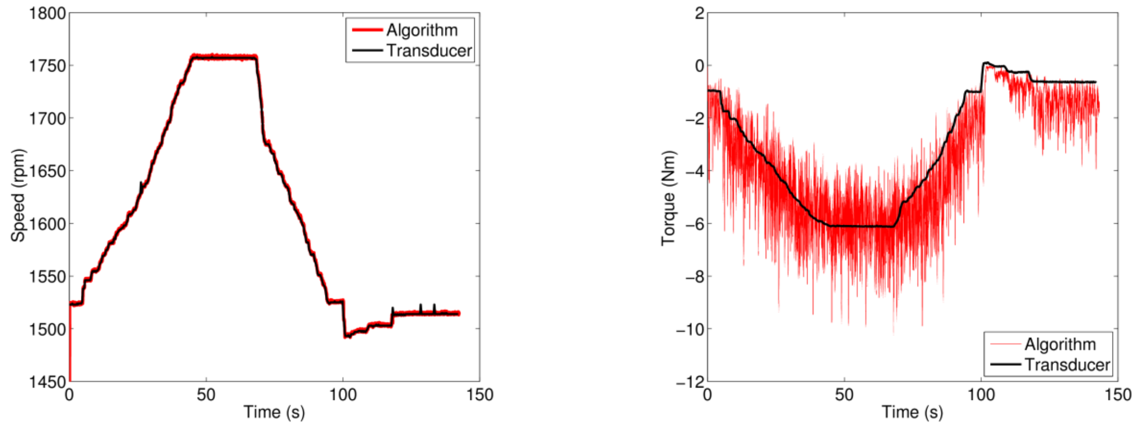

(a) (b)

Figure 8: Algorithm speed (a) and torque (b) response to motor speed variation at fixed generator voltage.

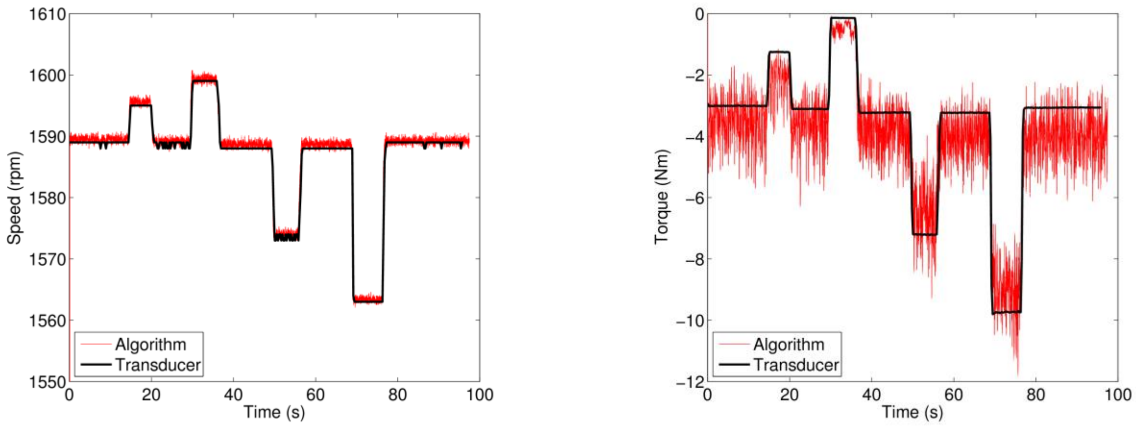

(a) (b)

Figure 9: Algorithm speed (a) and torque (b) response to step torque inputs.

8. Discussion

Although further investigation is required to reduce noise and tune the algorithm, the experimental results show that the proposed technique is successful in predicting changes in shaft speed and torque similar to those typically encountered by operating WTs.

Previous work has shown the strong potential of using the WT torque signal for CM purposes [8-13]. The major obstacle to its industrial application is the costly and intrusive nature of the required measurement equipment, which is impractical for long-term use on operating WTs. For this reason, in some cases, operators are only able to run short measurement campaigns by using specially installed torque transducers. Given the increasing awareness about the importance of long-term torque measurements for fully understanding the WT dynamics and for CM purposes, the wind industry is showing increasing interest in measuring the torque with cheap and non-intrusive techniques.

This work presents a novel approach to measure the drive train shaft torque by using a non-intrusive technique and could be a viable tool for WT CM. The proposed methodology is relatively simple and cheap to implement into a commercial WT CMSs for non-intrusive torque monitoring.

Although still at the small-scale stage implementation the economic benefits of the proposed technique, based on the use of two barcodes and two optical probe sensors, over the conventional in-line torque transducer are evident. While the non-intrusive equipment costs overall less than €100, the in-line sensor cost for a small shaft of 470 mm goes well beyond €5000. This difference in costs will be even larger in a commercial WT application due to the bigger WT drive train shaft diameter, which would increase the fitting cost of an in-line torque transducer.

The torque imposed on a rotating shaft has been measured in the past using strain gauges through a wireless telemetry or a slip ring system. However, the accuracy of the torque measurements provided by strain gauges often does not meet engineering requirements because the uncertainty of such measurements is rather large due to electromagnetic interference [17]. The results of the proposed non-intrusive technique correlate closely with the transducer measurements and it is believed that, once the sampling frequency of the data acquisition system will be increased and the main sources of signal noise and systematic errors removed, the algorithm should show a higher accuracy, compared to other methods, in predicting the speed and torque values during the WT operation.

Despite the promising results obtained in this study, the reliability of the proposed approach for CM purposes is currently under further investigation. In particular, drive train seeded-fault testing and analysis will be performed on the torque test rig with the aim of developing reliable torque signal processing algorithms for fault detection.

9. Conclusions

This paper presents a non-intrusive technique for torque measurement on a WT drive train. It can be concluded that:

- Torque measurement is achieved by measuring the angle of twist from the timing between pulse trains produced by two sets of bar codes and optical probes.
- The proposed algorithm was validated, computationally and through physical testing, under steady state and transient conditions. In both cases the derived algorithm torque correlated closely with the torque transducer measurements, with ±3% and 16-25% torque mean percentage errors, respectively.
- Higher sampling frequency of the data acquisition system is expected to reduce the noise and the systematic error associated with the algorithm output.
- Unlike conventional torque transducers, the proposed approach does not require any embedded sensors on the rotating shaft, overcoming the majority of problems limiting the industrial application of CMSs based on shaft torque measurements.
- Experimental investigation is currently carried out at Durham University with the aim to address the role played by the shaft moment of inertia, damping coefficient and torsional stiffness in controlling the torque predicted by the theoretical relationship given by equation (1), for both steady and transient conditions.
- Future work will focus on further validating the method using experimental data and developing suitable and reliable signal processing algorithms for fault detection.

Acknowledgements

This work was funded as part of the UK EPSRC Supergen Wind Energy Technologies programme, EP/H018662/1.

References

[1] Fried, L., Sawyer, S., Shukla, S., Qiao, L. (2014). 'Global Wind Report Annual Market Update 2013'. GWEC, available at http://www.gwec.net/wp-content/uploads/2014/04/GWEC-Global-Wind-Report_9-April-2014.pdf, last accessed 24th January 2015.

[2] GWEC. ‘Global offshore’: http://www.gwec.net/global-figures/global-offshore/. Last accessed on 16/03/15.

[3] Shafiee, M., Patriksson, M., Stromberg, A.-B., Bertling, L. (2013). A redundancy optimization model applied to offshore wind turbine power converters. In 2013 IEEE Grenoble PowerTech (POWERTECH), pages 1–6.

[4] McMillan, D., Ault, G.W. (2007). Quantification of Condition Monitoring Benefit for Offshore Wind Turbines. Wind Engineering. 31(4): 267-285.

[5] Walford, C.A. (2006). 'Wind Turbine Reliability: Understanding and Minimizing Wind Turbine Operation and Maintenance Costs'. Sandia National Laboratories SAND2006-1100, available at http://prod.sandia.gov/techlib/access-control.cgi/2006/061100.pdf, last accessed 21st February 2015.

[6] BVG Associates (2012). 'Pathways to Cost Reduction in Offshore Wind Technology: Technology workstream', available at http://www.bvgassociates.co.uk/Publications/BVGAssociatespublica%ADtions.aspx, last accessed 16th October 2015.

[7] Sheng, S., Veers, P. (2011). Wind Turbine Drivetrain Condition Monitoring - An Overview. Proceedings of Machinery Failure Prevention Technology (MFPT) Society 2011 Conference. Virginia Beach, Virginia.

[8] Yang, W., Tavner, P.J., Crabtree, C.J., Wilkinson, M. (2010). Cost-Effective Condition Monitoring for Wind Turbines. IEEE Transactions on Industrial Electronics. 57(1): 263-271.

[9] Abdusamad, K.B., Gao, D.W., Li, Y. (2014). Condition monitoring system based on effects of electrical torque pulsations of wind turbine generators. In PES General Meeting Conference Exposition, 2014 IEEE.

[10] Djurović, S., Vilchis-Rodriguez, D.S., Smith, A.C. (2012). Vibration Monitoring for Wound Rotor Induction Machine Winding Fault Detection. Proceedings of XXth International Conference on Electrical Machines, ICEM, Marseille, France.

[11] Wilkinson, M.R., Spinato, F., Tavner, P.J. (2007). Condition Monitoring of Generators & Other Subassemblies in Wind Turbine Drive Trains. Proceedings of 2007 IEEE International Symposium on Diagnostics for Electric Machines, Power Electronics and Drives (SDEMPED 2007). Cracow, Poland.

[12] Soker, H., Kieselhorst, S., Royo, R. (2004). Load monitoring on a mainshaft. A case study. German Wind Energy Conference DEWEK, Wilhelmshaven.

[13] Perišić, N., Kirkegaard, P.H., Pedersen, B.J. (2015). Cost-effective shaft torque observer for condition monitoring of wind turbines. Wind Energy. 18: 1-19.

[14] Lu, B., Li, Y., Wu, X., Yang, Z. (2009). A Review of Recent Advances in Wind Turbine Condition Monitoring and Fault Diagnosis. Proceedings of 2009 IEEE Symposium on Power Electronics and Machines in Wind Applications. PEMWA 2009. Lincoln, Nebraska.

[15] Yang, W., Tavner, P. J., Crabtree, C. J., Feng, Y., Qiu, Y. (2014). Wind Turbine Condition Monitoring: Technical and Commercial Challenges. Wind Energy. 17(5): 673-693.

[16] Friswell, M.I., Penny, J.E.T., Garvey, S.D., Lees, A.W. (2010). *Dynamics of Rotating Machines*. Cambridge University Press.

[17] Sue, P., Wilson, D., Farr, L., Kretschmar, A. (2012). High precision torque measurement on a rotating load coupling for power generation operations. In Instrumentation and Measurement Technology Conference (I2MTC), IEEE International.

Advanced Algorithms for Automatic Wind Turbine Generator Fault Detection and Diagnosis

Donatella Zappalá[1], Christopher J. Crabtree[1], Damian Vilchis-Rodriguez[2], Peter J. Tavner[1], Sinisa Djurovic[2], A.C. Smith[2]
[1] School of Engineering and Computing Sciences, Durham University, DH1 3LE, UK
[2] School of Electrical and Electronic Engineering, University of Manchester, Manchester M19 3PL, UK
donatella.zappala@durham.ac.uk, c.j.crabtree@durham.ac.uk, Damian.Vilchis-rodriguez@manchester.ac.uk, peter.tavner@durham.ac.uk, Sinisa.Durovic@manchester.ac.uk, sandy.smith@manchester.ac.uk

Keywords: Wind turbine, condition monitoring, generator faults, bearing faults, current signature analysis, vibration analysis,

Abstract

Previous wind turbine condition monitoring work identified signals and methods for wind turbine fault detection. This paper concentrates on raising sensitivity so that high reliability is achieved. This is done by adopting techniques of earlier papers but aggregating them in Side Band and Harmonic Power Factor algorithms that can be applied remotely and automatically to important WT drive train electrical and vibration signals. The process has already been demonstrated on a gearbox but has been extended here to consider generator electrical and vibration signals. The value of the algorithm and its detection sensitivity have been demonstrated by Test Rig results.

1. Introduction

Previous wind turbine (WT) condition monitoring work by the authors focused on developing automatic algorithms for improving detection sensitivity on disparate parts of the WT drive train and proving their efficacy on a Test Rig.

The aim of automatic fault detection with improved sensitivity was based upon a need, identified from offshore wind farm operators [1], to determine offshore WT condition remotely, so that the costly mobilisation of diagnosis specialists could be minimised only to serious, repairable WT faults.

The authors have been involved in developing the following techniques:

- WT generator electrical fault detection, through analysis of fault frequency components or side-bands in electrical current or power spectra[2];
- Enhancing WT generator electrical and mechanical fault detection sensitivity by variable speed tracking of fault frequency side-bands in electrical and vibration spectra [3];
- Extending WT generator fault detection to consider rolling element bearing faults [4];
- Enhancing WT gearbox fault detection sensitivity by collating fault frequency side-bands in vibration spectra, using a Side Band Power factor (SBPF) algorithm [5].

In each case the efficacy of the methods was tested on the Durham University Wind Turbine Condition Monitoring Test Rig (WTCMTR) or a similar Test Rig at Manchester University. In [5] that process was also extended to results from a full- WT gearbox, through the assistance of the National Renewable Energy laboratory (NREL) in the USA.

In the case of the WTCMTR it is possible to process the results in a commercial WT Condition Monitoring System (CMS), the SKF WindCon, further demonstrating the practicability of what was being proposed.

This paper presents combining and extending these methods, using SKF WindCon Observer for the electrical signals and a Bruel&Kjær Pulse system for the vibration signals, to produce higher detection sensitivities for WT variable speed generator electrical and mechanical faults. The algorithms have again been tested on the Durham WTCMTR and Manchester Test Rig. The Durham rig features a wound rotor induction generator (WRIG) with variable resistance in the rotor circuits, driven at either constant speed or with non-stationary, variable speed conditions. The Manchester rig operates as either a doubly-fed induction generator (DFIG) or WRIG at user-defined fixed speeds. Both machines operated synchronised with the grid with star connected rotor and stator windings. Details of the two test rigs are given in [2] and [5].

2. Electrical Signals

Experiments were conducted on the WTCMTR to investigate the progression of a generator rotor unbalance fault at variable speed and generator loads. Rotor asymmetry of 23% and 46% was applied to the test rig induction generator by means of external additional resistance into one rotor phase winding circuit via the machine slip rings.

An analysis of recorded generator current signals, using WindCon Observer, has shown that at different generator speeds and loads, in the case of an unbalanced generator rotor fault there are clear amplitude increases of the $|2s|f_s$ upper sidebands of the supply frequency 1st & 3rd harmonics, where s is the per unit slip and f_s is the stator supply frequency [2]. There is also clear dependence of the fault amplitude on the WT load, confirming what was shown for gearbox vibration signals in [5]. Similar results are expected in the power signals, down-shifted by the fundamental frequency close to DC.

Generator current simulations from Manchester have also shown that sidebands around the 1st and 3rd harmonics of the supply frequency are related to the rotor unbalance. Model predictions for balanced and unbalanced generator rotor line current spectra are shown in Figure 1 for an assumed mechanical speed of 1590 rpm and 23% rotor asymmetry.

The sideband on the 3rd harmonic is only present when the supply third order time harmonic exists in conjunction with the rotor electrical fault. These will be useful rotor unbalance detection indicators under practical WT operating conditions when supply unbalance is unavoidable.

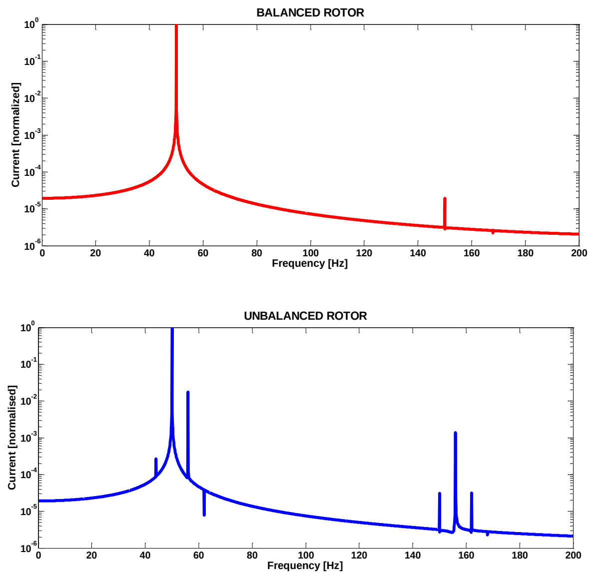

Figure 1: Line Current spectra simulation results at 1590 rpm for balanced (top) and unbalanced (bottom) generator rotor conditions.

Based on the simulation and experimental evidence, the two reported sideband frequencies have been used as a generator rotor unbalance fault indicator. The extraction and monitoring of the spectral components was achieved by a Side Band Power Factor (SBPF) algorithm similar to that proposed in [5] and the techniques presented in [3] to track and automate fault detection. The SBPF algorithm sums the Power Spectrum amplitudes of the $|2s|f_s$ upper sidebands of the supply frequency 1st & 3rd harmonics.

The influence of the fault severity and the variable load operating conditions on the SBPF values has been investigated by performing tests on the WTCMTR at a load up to 3.4 kW.

Figure 2 shows the SBPF values against the load, expressed as a percentage of the maximum generator output, for balanced rotor, 23% and 46% of unbalance level. The results show that the SBPF magnitude is proportional to the magnitude of the rotor fault level. For balanced rotor the SBPF magnitude does not vary significantly with the load. For faulty conditions the trend of the obtained SBPF values can be fitted by an exponential curve.

The results demonstrate effective operation of the SBPF for the full range of the investigated load levels. The algorithm is seen to enable clear fault detection, for both early and advanced stages of rotor fault.

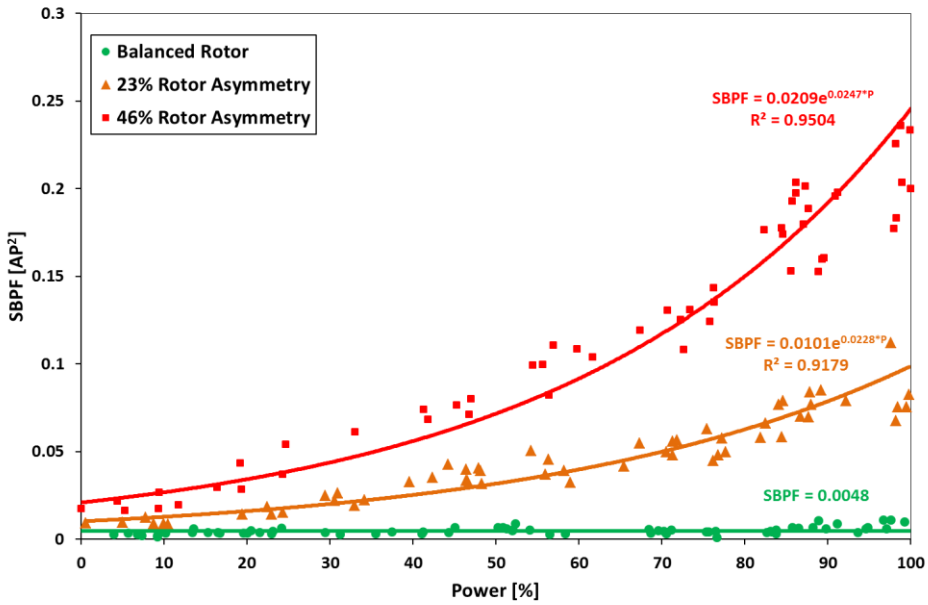

Figure 2: Influence of the fault severity and the variable load operating conditions on the SBPF values.

3. Vibration Signals

3.1. Rotor Electrical Unbalance

Based on the principles presented in [6], it follows that the rotor electrical unbalance will result in electromagnetic torque oscillations that can induce mechanical vibration at the same frequencies in the machine frame. Given the close relationship between torque and power the frequencies that appear in the torque spectrum, as consequence of rotor electrical unbalance, will also be present in the power signal. Therefore, the frequencies resulting from the rotor unbalance can be present in the power signal, as referred to in [2], and in the generator vibration signal [6].

A Bruel&Kjær Pulse system was used to record the vibration signal from two accelerometers fitted to the generator load side end-plate. The accelerometers were installed in two planes, vertically and horizontally, thus providing a comparison between fault effects in different positions on the stator frame. The vibration signals were recorded for a series of experiments at steady-state operating speeds of 1530, 1560 and 1590 rpm for balanced rotor, 23% and 46% rotor asymmetry conditions.

An analysis of recorded generator accelerometer data from the WTCMTR shows an amplitude increase, although not strong, of the $|2s|f_s$ upper sideband of the twice the fundamental supply frequency vibration component, $2f_s + |2s|$, when going from healthy to faulty conditions. Manchester has run similar rotor unbalance tests, to allow a comparison between the two test rig generators' vibration signatures under unbalanced rotor operation.

The vertically mounted accelerometer vibration frequency spectra around the $2f_s + |2s|$ frequency for a 1590 rpm speed and different fault severity levels are shown in Figure 3 for both test rigs. The results show a marked increase in the magnitude of the fault frequency for the most severe case.

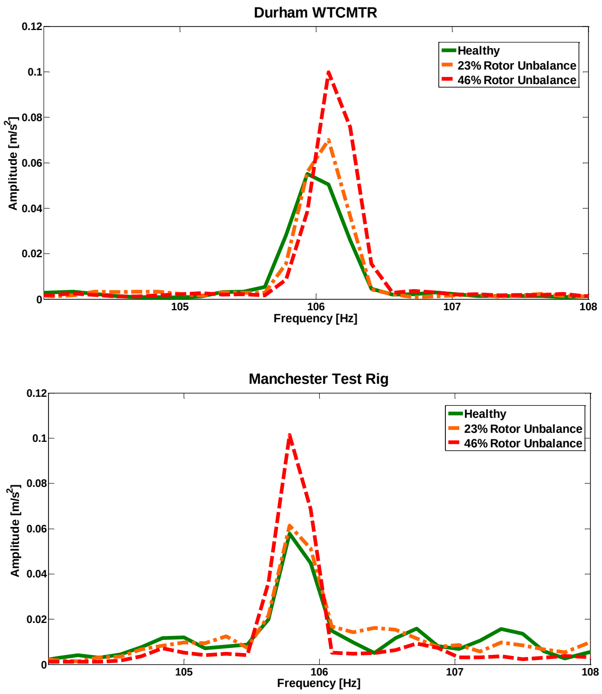

Figure 3: Vertical accelerometer vibration spectra around the $2f_s + |2s|f_s$ sideband (i.e. 106 Hz) for healthy and unbalanced rotor conditions from the Durham (top) and Manchester (bottom) test rigs at 1590 rpm.

As the investigated vibration signals are not rich in clearly detectable fault spectral signatures, only the $2f_s + |2s|f_s$ sideband can be used as generator rotor unbalance fault indicator. As a consequence, the SBPF algorithm, defined as a method of adding sideband powers [5], can not be used to enhance the sensitivity detection.

3.2. Bearing Faults

Bearing faults were experimentally simulated on the Manchester test rig by drilling a hole in the middle of the bearing outer race perpendicular to the race surface on the generator drive-end side bearing [4]. To simulate different levels of fault severity the diameter of the hole was varied from 3 to 12mm in steps of 3mm. For each considered hole dimension the faulted bearing was used to perform fault experiments and record the frame vibration signal. The machine bearing specifications are given in [4]. Bruel&Kjær Pulse system was used to record the vibration signals from the vertical and horizontal accelerometers fitted to the generator load side end-plate. The vibration signals were recorded for a series of experiments at the steady-state operating speeds of 1530, 1560 and 1590 rpm.

Analysis of recorded vibration signals has shown that at different generator speeds, the bearing faults result in clear amplitude increases of the first five outer race bearing fault frequency harmonics.

Based on the experimental evidence, a generator bearing outer race fault indicator, named the Harmonic Power Factor (HPF) algorithm, has been proposed. The HPF sums the Power Spectrum amplitudes of the first five outer race bearing fault frequency harmonics.

Figure 4 and Figure 5 show the HPF values versus considered values of rotor speed and for both vertical and horizontal axis frame vibration measurements.

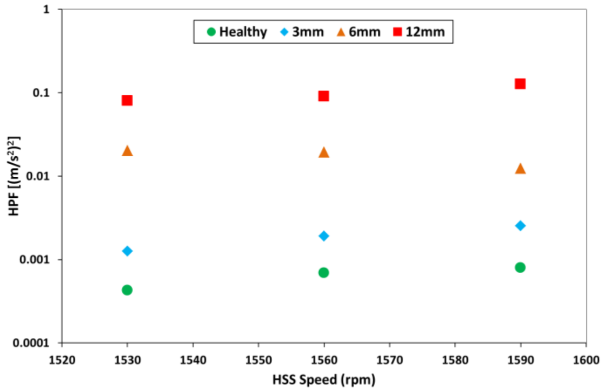

Figure 4: Influence of the fault severity and the speed operating conditions on the HPF values for the vertical accelerometer dataset.

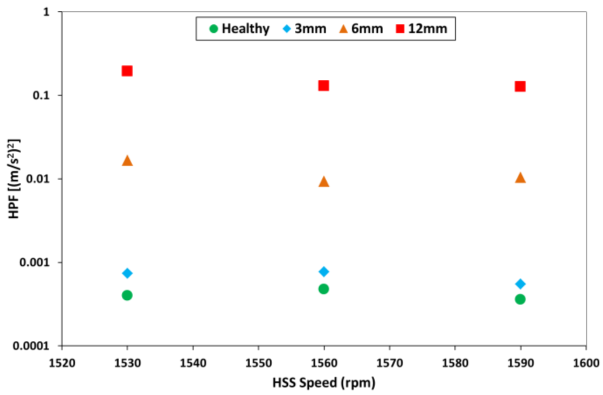

Figure 5: Influence of the fault severity and the speed operating conditions on the HPF values for the horizontal accelerometer dataset.

The results show that the HPF magnitude is proportional to the magnitude of the bearing fault level for both datasets. For the investigated operating conditions the proposed algorithm works successfully, achieving clear fault detection from early to more advanced levels of bearing fault.

4. SBPF and HPF Detection Sensitivity

In order to compare the results obtained for the two different generator faults and the relative monitoring signals investigated, the SBPF and HPF detection sensitivities, $\%SBPF$ and $\%HPF$ respectively, have been defined as

$$\%SBPF = \frac{SBPF_f - SBPF_h}{SBPF_h} * 100 \qquad (1)$$

$$\%HPF = \frac{HPF_f - HPF_h}{HPF_h} * 100 \qquad (2)$$

where $SBPF_h$ and HPF_h , $SBPF_f$ and HPF_f are the SBPF and HPF values for the healthy and faulty cases, respectively.

Table 1 and Table 2 summarise the average SBPF and HPF detection sensitivities, respectively, for the generator fault conditions investigated in this paper.

Table 1: Generator rotor unbalance average SBPF detection sensitivity.

Rotor Asymmetry	Average %SBPF
23%	743%
46%	1897%

Table 2: Generator drive-end side bearing damage average HPF detection sensitivity.

Bearing Fault Severity	Average %HPF	
	Vertical Accelerometer	Horizontal Accelerometer
3mm	197%	68%
6mm	2944%	2911%
12mm	15848%	36976%

The sensitivity analysis shows that both the SBPF and the HPF techniques prove successful in the detection of both early and final stages of fault level. It is evident the influence of the fault severity on the detection sensitivity values; the more damaged is the generator component the easier is to discriminate the fault.

5. Conclusions

This paper has shown that, for generator operation with rotor electrical unbalance or bearing fault, current and vibration signal spectrum contains identifiable fault frequencies, which could be tracked as the WT rotor speed varies.

High fault detection sensitivity algorithms, SBPF and HPF, can be configured to track the observed fault frequency magnitudes and sum their powers. This allows to significantly raise the detection sensitivity of the signals and to improve the reliability of detection.

The analysis of the generator vibration signature was shown to enable rotor electrical unbalance detection. However, in this case the application of the SBPF algorithm was prevented by the presence of only one relevant sideband fault frequency.

In the case of rotor electrical unbalance the results have also shown the benefit of tracking the SBPF as the WT load varies. These benefits have been demonstrated on WTCMTR under healthy and faulty conditions. In the case of bearing fault, the work presented in this paper clearly demonstrates the potential of developing real time tracking applications based on the HPF algorithm.

The proposed methodologies are relatively simple to implement into a commercial WT CMS, as the SKF WindCon, for automatic generator fault detection and diagnosis in the WT practical environment.

Such algorithms could be deployed for large offshore wind farms to reliably identify generator rotor winding and bearing problems, known to be a significant cause of down-time.

It is hoped that field measurements from real WTs can be made available to demonstrate the application of these methods to real data beyond that of the authors' Test Rigs.

The major learning outcomes of the paper are:

- To improve condition monitoring reliability using field fitted equipment;
- To devise automatic techniques that reduce the work-load on Wind Farm Operators;
- To develop more comprehensive techniques to monitor large offshore wind farms;
- To demonstrate that cheap and effective continuous condition monitoring is feasible on large offshore wind farms.

Acknowledgements

This work was funded by the UK EPSRC SUPERGEN Wind Energy Technologies programme, EP/H018662/1.

References

[1] Feng, Y., Tavner, P. J., Long, H., "*Early experiences with UK Round 1 Offshore Wind Farms*", Proc. Institution of Civil Engineers, Energy, Vol. 163, Iss. EN4 pp. 167-181, 2010.

[2] Djurovic, S., Crabtree, C. J., Tavner, P. J., Smith, A. C., "*Condition Monitoring of Wind Turbine Induction Generators with Rotor Electrical Asymmetry*", IET Renewable Power Generation, Vol. 6, Iss. 4, pp. 207-216, 2012.

[3] Yang, W, Tavner, P.J, Crabtree, C.J, Wilkinson, M.R, "*Cost-effective condition monitoring for wind turbines*", IEEE Transactions on Industrial Electronics, Vol. 57, Iss. 1, pp. 263-271, 2010.

[4] Vilchis-Rodriguez, D.S, Djurović, S, Smith, A.C, *"Wound rotor induction generator bearing fault modelling and detection using stator current analysis*", IET Renewable Power Generation, Vol. 7, Iss. 4, pp. 330-340, 2013.

[5] Zappala, D., Tavner, P. J., Crabtree, C. J., Sheng, S., "*Sideband Algorithm for Automatic Wind Turbine Gearbox Fault Detection and Diagnosis*", Proc. Scientific Track, EWEA 2013, Vienna, February 2013.

[6] Djurovic, S.; Vilchis-Rodriguez, D.; Smith, A. C., "*Vibration monitoring for wound rotor induction machine winding fault detection*", XXth International Conference on Electrical Machines (ICEM), pp. 1906,1912, 2-5 Sept. 2012.

ELECTRICAL FAULT DETECTION USING MECHANICAL SIGNALS

Christopher J. Crabtree, Donatella Zappalá, Peter J. Tavner, Simon I. Hogg
School of Engineering and Computing Sciences
Durham University, UK
c.j.crabtree@durham.ac.uk, donatella.zappala@durham.ac.uk
peter.tavner@durham.ac.uk, simon.hogg@durham.ac.uk

Keywords: Wind, condition monitoring, generator faults, frequency tracking.

Abstract

Wind turbine condition monitoring is gaining in importance as operators and developers move towards larger, further offshore, less accessible wind farms. However, condition monitoring is made highly challenging by the variable speed, variable load nature of wind turbines. Electrical faults, in the form of brush gear or slip ring damage contribute significantly to downtime yet operators have little experience of detecting these faults in the field. This paper subjects a physical test rig to rotor electrical unbalances and applies a frequency tracking algorithm to mechanical and electrical monitoring signals to compare the sensitivity of the various signals. The results shows that the total electrical power signal gives the clearest response to rotor electrical unbalance, as expected, but that torque measurements could be a viable alternative. Speed signal analysis showed much lower sensitivity to unbalance than torque or power measurements.

1. Introduction

As large-scale wind farms move further offshore into more inhospitable environments, achieving a high availability and capacity factor is essential in ensuring a competitive cost of energy. The cost of operations and maintenance (O&M) has been shown to be anything between 15% and 35% of the cost of energy from wind, with [1] giving a figure of 18% or £12 per MWh generated, making O&M a clear target for cost reduction. One approach to reducing the cost of O&M is to move away from reactive maintenance strategies to planned, proactive and preventative strategies. This requires the use of remote condition monitoring (CM) of individual wind turbines (WT) in order to inform operators of the health of each WT at any point in time. In order to allow for planned maintenance, a CM system (CMS) must be able to indicate the severity of a fault so that a judgement can be made as to when maintenance should take place. A particular challenge facing wind farm operators is that of automation of fault detection as manual interpretation of large amounts of data from multiple WTs is costly. Ideally, an automated system should present a clear detection or health signal to the operator who could then choose to examine a particular WT in more detail, if required.

The challenge of WT CM is aggravated by the operating conditions. Since the fuel is controlled, WTs are subject to highly non-stationary operating conditions with variable speed, power and torque over time. As a result, monitoring signals at two points in time cannot generally be directly compared to detect faults or establish fault severity.

This paper applies a frequency tracking algorithm, designed to reduce the effects of varying operating conditions, to mechanical and electrical monitoring signals from a laboratory test rig to examine how fault responses compare between signals when generator electrical faults are present. In particular, the relative sensitivities of the various signals are examined.

2. Monitoring Electrical Faults

Being such a key drive train component, faults in WT generators can have catastrophic effects resulting in costly and lengthy repairs. With reduced accessibility offshore, any downtime is significantly extended. Nevertheless, monitoring of electrical faults in generators has not yet become standard practice in the wind industry. Reliability studies [2] [3] have shown that generator defects make a significant contribution to WT downtime with [2] showing that 30% of total annual downtime results from power conversion system failures. Of this, 30% of the downtime resulted directly from generator failures. A recent survey of failed commercial generators [4] showed that brush-gear and slip-ring failures in wound rotor induction generators (WRIG) accounted for 16% of 2MW range generator failures. In smaller machines, 50% of failures originated from rotor unbalance.

Generator rotor electrical unbalances such as brush-gear and slip-ring damage have been shown to exhibit certain characteristics in the stator terminal electrical current and power signals [5] [6] for machines operating at constant speed and load. These signals can be analysed by Fourier transform approaches and give clear indications of the presence of electrical faults. However, the majority of modern WTs operate at variable speed and so current and power spectra change rapidly over time making conventional analysis challenging.

In WRIGs, electrical rotor unbalances manifest themselves as a function of the machine slip as shown in Table 1 where s is the per unit slip, f_s is the stator supply frequency (50 Hz) and f_c is the fault frequency of interest.

Table 1: Fault frequencies in stator electrical signals

Signal	Fault Frequency, f_c
Stator Total Power	$f_c = \lvert 2s \rvert f_s$
Stator Current	$f_c = \lvert 1 \pm 2s \rvert f_s$

In the majority of modern WTs, however, rotor current signals are only monitored for control purposes and operators often have difficulty in obtaining permission to use these signals for CM purposes. However, mechanical signals are much more commonly recorded by the CMS. Electrical unbalances manifest themselves as torque pulsations as they pass through the stator magnetic field and so can be expected to produce mechanical vibration. In the case of rotor electrical unbalance, the unbalance manifests itself in speed and torque signals at the same frequency as in the stator total power signal ($f_c = \lvert 2s \rvert f_s$).

3. Analysis Approach

3.1. Frequency Tracking

Research presented in [7] describes a frequency tracking approach which can be applied to non-stationary signals on the assumption that they are effectively stationary if examined over very short periods. The Iterative Localised Discrete Fourier Transform ($IDFT_{local}$) algorithm is discussed in detail in [7]. Importantly, the algorithm always analyses a fixed number of shaft rotations rather than a fixed length time series. This is a step towards taking into account the fact that the machine condition has changed.

The IDFT$_{local}$ algorithm is summarised as:

- Extract initial speed signal data point
- Calculate time length of the required number of machine revolutions and extract the relevant amount of data;
- Calculate sample mean speed;
- Calculate frequencies of interest;
- Calculate discrete constants from frequencies of interest;
- Calculate amplitudes for each constant;
- Extract maximum amplitude;
- Repeat the process starting with next unanalysed speed data point.

The IDFT$_{local}$ is expressed mathematically as:

$$A_i = \max_{k\in\left[k_{min\ i}, k_{max\ i}\right]} \left(\sum_{n=0}^{N_i-1} x\big((a_i+n)T\big) e^{-j2\pi nk\,\Delta fT} \right)$$

where x is the signal under analysis, T is the sampling period and A_i is the peak amplitude for the particular sample. The algorithm is derived and defined in full in [7] and is graphically represented in figure 1.

3.2. Detection Sensitivity

Given that any individual monitoring signal will have a different magnitude response to a particular unbalance level, it is useful to define a sensitivity function to compare results. Here, the percentage sensitivity of the response, $\%\,S$, is defined as:

$$\%\,S = \frac{A_f - A_h}{A_h} \times 100$$

where A_f and A_h are the signal amplitudes under unbalanced and healthy conditions respectively. This approach is consistent with that taken in [8] for monitoring for WT gearbox faults.

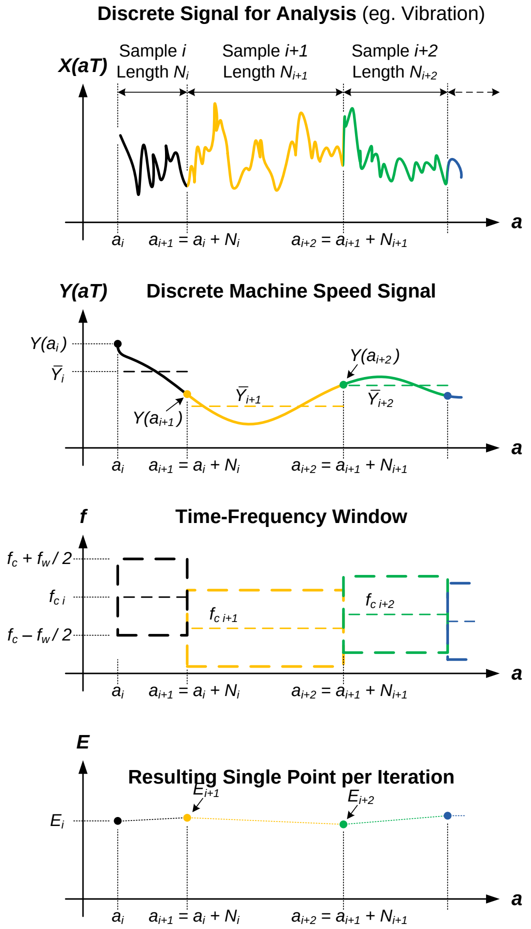

Figure 1: Graphical representation of the IDFT$_{local}$ algorithm

4. Physical Test Rig

Since CM data from large scale operational WTs is not readily available, due to operator concerns about confidentiality, the data used in the paper is recorded from a physical test rig at Durham University. Details of the test rig are given in [7] and [8]. The test rig, illustrated in figure 2, features a grid-connected 30kW wound rotor induction generator (WRIG) that is driven by a DC motor according to speed profiles derived from a WT model.

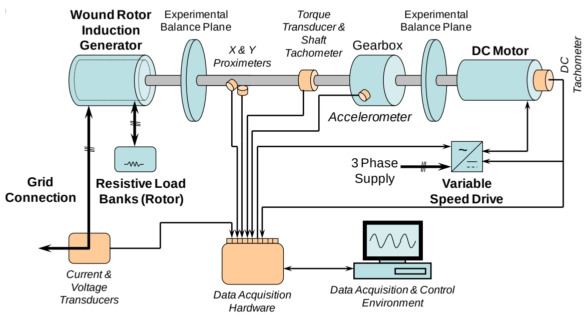

Figure 2: Schematic diagram of the Durham test rig

The driving conditions used in this paper are shown in figure 3. Rotor electrical unbalances are introduced as external resistances. A base resistance of 1.3Ω per phase is included to allow for a wide generator speed variation as would be found in a variable slip WRIG. Faults of 23% and 46% of the rotor phase resistance are then introduced as external resistances to represent the development of rotor electrical faults such as brush or slip ring damage. These values compare very favourably with other studies such as [9] which used external resistances of 25%, 50%, 75% and 100% of the rotor phase resistance.

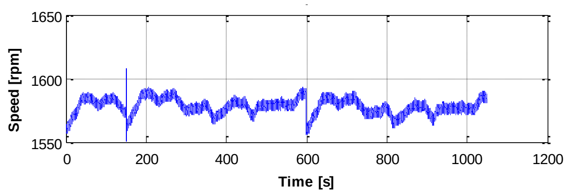

Figure 3: Generator variable speed profile

5. Results and Discussion

5.1. Electrical Signals

To verify the approach, measurements for the instantaneous generator stator total power were derived from stator current and voltage measurements sampled at 5kHz. The $IDFT_{local}$ algorithm was applied to the instantaneous power signal to extract the magnitude of the fault frequency defined in Table 1. Figure 4 shows the instantaneous frequency of interest, f_c , over time and the magnitude of that component as extracted from the total power signal.

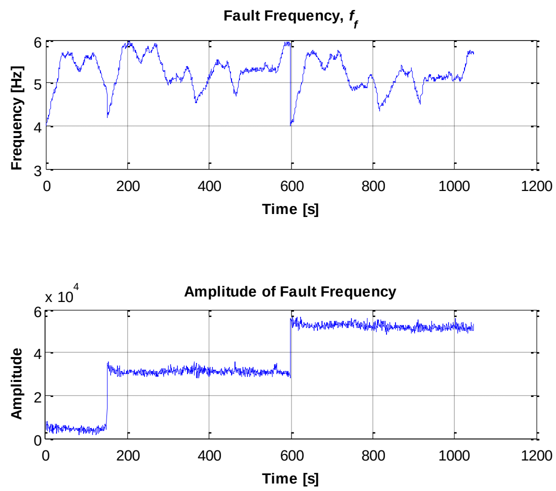

Figure 4: Frequency tracking of the stator total power signal

The point at which the unbalance level is changed from healthy to 23% to 46% is clearly visible. The combination of a low noise level and significant step change in the extracted result shows that the power signal is particularly sensitive to electrical faults, as would be expected.

This follows from earlier work [7] and suggests that the data is valid. It should be noted that the data was recorded in a noisy test environment as would be experienced on an operational WT so, with this in mind, the clarity of the results is very positive.

The frequency of interest over time and the extracted result for a single line current measurement are shown in figure 5. It is interesting to note that the result is subject to much greater inconsistency when compared to the power result in figure 4. The reasons for this are unclear however it is likely that much of the noise is cancelled when three currents are considered as the WRIG stator is star-connected.

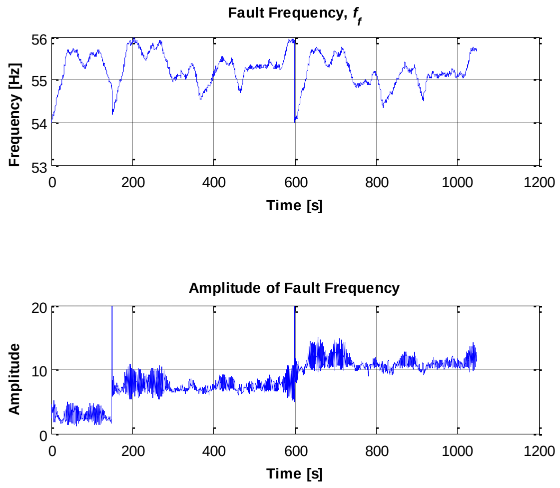

Figure 5: Frequency tracking of a stator line current signal

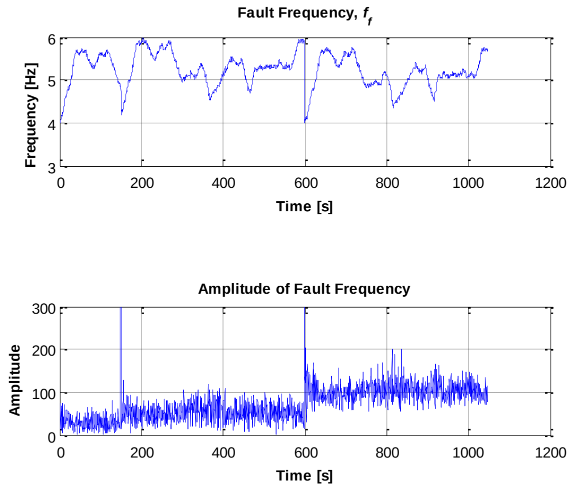

Figure 6: Frequency tracking of the generator speed signal

As would be expected, the electrical unbalances are clearly visible in the total power signal because of the direct link between the fault itself and the measured signals. However, in operational WTs, current and voltage measurements are not always available to operators for monitoring purposes and thus mechanical monitoring signals should be considered for detection of electrical faults.

5.2. Mechanical Signals

The same approach is now applied to the mechanical torque and speed measurements since these are generally more readily available to operators wishing to perform WT CM. The power frequency shown in Table 1 transforms directly into the mechanical signals for this machine so was taken as the fault frequency of interest for generator speed and shaft torque.

The frequency of interest over time and the extracted frequency tracking result for the machine speed signal are shown in figure 6.

The speed signal is extremely noisy in comparison to the power. This is aggravated by the fact that the measurement was taken by a digital tachometer whose digital signal was converted to an analogue signal for analysis. This would be the case in an operational WT and it introduces significant filtering even for high frequency pulse tachometers sampled at high frequencies.

Nevertheless, a change in fault frequency magnitude is visible in figure 6 as the unbalance level increases. Given the low power levels applied to the test rig, in the 5kW region, it is not unsurprising that this mechanical signal has not responded as strongly as the total electrical power signal.

However, the electrical unbalance leads directly to a reduced electromagnetic torque and therefore mechanical torque. Again, as the unbalance develops and increases in magnitude, it would be expected that the torque signal should offer a more sensitive detection signal than the speed. The frequency of interest over time and the extracted frequency tracking result for generator shaft torque are shown in figure 7.

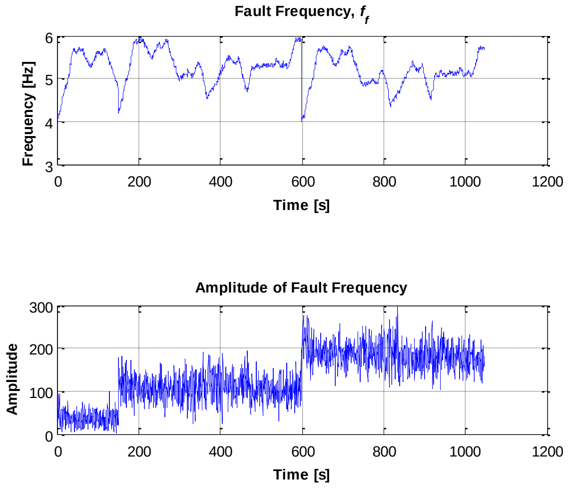

Figure 7: Frequency tracking of the generator shaft torque signal

The detection signal in figure 7 shows a marked change in magnitude as the unbalance level is increased. Whilst this is not as significant as for the electrical power signal shown in figure 4, it is distinct and clearly defined over time. It is expected that when higher generator powers are experienced, the torsional response will increase significantly but no data is yet available to test this.

5.3. Detection Sensitivity

The sensitivity calculation from section 3.2 was applied to results for each signal and each unbalance level to allow direct comparison between signals. The average sensitivities for the two unbalance levels are shown in Table 2.

Table 2: Signal sensitivities to different fault levels

	Sensitivity at:	
Signal	**23% Fault**	**46% Fault**
Speed	57%	215%
Torque	214%	414%
Total Power	675%	1200%

As expected, the total electrical power signal is most sensitive to rotor electrical unbalances. However, the torque signal has a high sensitivity albeit with a higher level of noise, as shown in figure 7. The speed signal sensitivity for the 46% unbalance is the same as that for the 23% in the torque signal. Overall, the torque signal presents itself as a possible option for machine monitoring if it could be measured easily in practice. However, further investigation is required to establish how the torque signal sensitivity varies as systems scale up to large-scale WTs.

6. Conclusions

This paper presents work completed at Durham University on the use of electrical and mechanical signals for the detection of generator electrical unbalances. It can be concluded that:

- Generator electrical unbalances cause electrical and mechanical torque pulsations that are detectable in both electrical and mechanical signals.
- Generator stator electrical power gives the most distinct response to changes in unbalance magnitude even for smaller fault magnitudes but this signal is not widely available in existing monitoring systems.
- Generator speed measurements show a change as unbalance is introduced but the low power levels on the test rig appear to limit the magnitude of the response and therefore results have poor sensitivity.
- Generator shaft torque measurements show a distinct change when electrical unbalance is present and the response would be expected to increase in magnitude for higher power machines.
- Electrical signals are the ideal monitoring medium however torque measurements could be a strong alternative.

Work is ongoing at Durham University to examine the sensitivity of mechanical signals to electrical faults in large-scale WTs.

Acknowledgements

This work was funded by the UK EPSRC SUPERGEN Wind Energy Technologies programme, EP/H018662/1.

References

[1] Feng, Y., Tavner, P. J., Long, H., "*Early experiences with UK Round 1 Offshore Wind Farms*", Proc. Institution of Civil Engineers, Energy, Vol. 163, Iss. EN4 pp. 167-181, 2010.

[2] M. Wilkinson, B. Hendriks, F. Spinato, E. Gomez, H. Bulacio, J. Roca, P. Tavner, Y. Feng, H. Long, "Methodology and Results of the Reliawind Reliability Field Study", Scientific Proc. European Wind Energy Conf. (EWEC), Warsaw, Poland, March 2010.

[3] F. Spinato, P. J. Tavner, G. J. W. Van Bussel, E. Koutoulakos, "*Reliability of Wind Turbine Subassemblies*", IET Renewable Power Generation, Vol. 3, Iss. 4, pp. 1-15, 2009.

[4] K. Alewine, W. Chen, "*Wind Turbine Generator Failure Modes Analysis and Occurrence*", Windpower 2010, Dallas, Texas, May, 2010.

[5] S. Djurović, S. Williamson, A. Renfrew, "*Dynamic Model for Doubly-fed Induction Generators with Unbalanced Excitation, both With and Without Faults*", IET Electric Power Applications, Vol. 3, Iss. 3, pp. 171-177, 2009.

[6] Djurovic, S., Crabtree, C. J., Tavner, P. J., Smith, A. C., "*Condition Monitoring of Wind Turbine Induction Generators with Rotor Electrical Asymmetry*", IET Renewable Power Generation, Vol. 6, Iss. 4, pp. 207-216, 2012.

[7] Crabtree, C. J., Tavner, P. J., "Condition Monitoring Algorithm Suited to Wind Turbine Use", IET Renewable Power Generation Conference, Edinburgh, September, 2011.

[8] Zappala, D., Tavner, P. J., Crabtree, C. J., Sheng, S., "*Sideband Algorithm for Automatic Wind Turbine Gearbox Fault Detection and Diagnosis*", Proc. Scientific Track, EWEA 2013, Vienna, February 2013.

[9] Stefani, A., Yazidi, A., Rossi, C., Filippetti, F., Casadei, D., Capolino, G. A., "*Doubly Fed Induction Machines Diagnosis based on Signature Analysis of Rotor Modulating Signals*", IEEE Trans. Industry Applications, Vol. 44, No. 6, pp. 1711-1721, 2008.